Analysis, Modeling, and Control of Thermoacoustic Instabilities

vorgelegt von
Diplom-Ingenieur
Jonas P. Moeck
aus Berlin

Von der Fakultät V – Verkehrs- und Maschinensysteme
der Technischen Universität Berlin
zur Erlangung des akademischen Grades

Doktor der Ingenieurwissenschaften
– Dr.-Ing. –

genehmigte Dissertation

Promotionsausschuss:

Vorsitzender:	Prof. Dr.-Ing. Utz von Wagner
Gutachter:	Prof. Dr.-Ing. Christian Oliver Paschereit
Gutachter:	Prof. Dr.-Ing. Rupert Klein (FU Berlin)
Gutachter:	Prof. Wolfgang Polifke, PhD (TU München)

Tag der wissenschaftlichen Aussprache: 22. September 2010

Berlin 2010

D 83

Vorwort

Die vorliegende Arbeit entstand während meiner Tätigkeit als wissenschaftlicher Mitarbeiter am Fachgebiet Experimentelle Strömungsmechanik des Instituts für Strömungsmechanik und Technische Akustik im Rahmen des von der Deutschen Forschungsgemeinschaft geförderten Sonderforschungsbereiches 557 „Kontrolle komplexer turbulenter Scherströmungen“ an der Technischen Universität Berlin.

Meinen besonders herzlichen Dank möchte ich meinem Doktorvater, dem Leiter des Fachgebietes, Prof. Dr.-Ing. Christian Oliver Paschereit, für den mir gewährten wissenschaftlichen Freiraum, das mir entgegengebrachte Vertrauen und nicht zuletzt für mein Wohlfühlen am Lehrstuhl aussprechen. Darüber hinaus bekam ich die Möglichkeit, auch neben dem Promotionsthema, eine Vielfalt an herausfordernden und spannenden Aufgaben zu bearbeiten. Auch hierfür bin ich äußerst dankbar.

Herrn Prof. Dr.-Ing. Rupert Klein danke ich für die Übernahme der Gutachtertätigkeit im Promotionsverfahren und für die gute Zusammenarbeit im Rahmen des SFBs, die sich hoffentlich auch weiterhin fortsetzt. Ebenfalls für die Gutachtertätigkeit möchte ich Herrn Prof. Wolfgang Polifke, PhD, danken, dessen Arbeiten ich seit Beginn meiner Tätigkeit bis heute immer aufmerksam verfolgt habe. Für die unkomplizierte Ausübung des Prüfungsvorsitzes während des Promotionsverfahrens bedanke ich mich bei Herrn Prof. Dr.-Ing. Utz von Wagner.

Michael Oevermann, Carsten Scharfenberg und Heiko Schmidt danke ich für die angenehme und aufschlussreiche Zusammenarbeit zur Hydrodynamik–Akustik Kopplung im Rahmen unseres SFB Projektes. Für die administrative Organisation des Sonderforschungsbereiches möchte ich mich bei Frau Steffi Stehr und für die Rolle als Sprecher des SFBs, die er in meinen Augen vorbildlich ausgeübt hat, bei Prof. Dr.-Ing. Rudibert King bedanken.

Bei zahlreichen Problemen mit Hard- und Software halfen mir Frank Bauermeister, Martin Franke, Nico Seifert und vor allem Angela Pätzold, wofür ich mich an dieser Stelle bedanken möchte. Der qualitativ außerordentlich hochwertigen Arbeit unserer Metallwerkstatt, vertreten durch Axel Bendiks, Thorsten Dessin, Horst Mettchen, Willi Postel und Manfred Ziehe, habe ich in wesentlichem Maße das Gelingen der experimentellen Teile der Dissertation zu verdanken. Bei allen elektrischen und elektronischen Aspekten konnte ich mich immer auf Heiko Stolpe verlassen, der darüber hinaus nie verlegen war, mir jegliche Schaltung bis ins kleinste Detail zu erläutern.

Mein Dank gilt außerdem der Lehrstuhlorganisation durch Kristin Halboth, Evelyn Kulzer, Navid Nayeri und besonders Lilli Lindemann für die unzähligen Hilfestellungen im Universitätsalltag.

Für die freundschaftliche, offene und hilfsbereite Atmosphäre möchte ich mich bei allen wissenschafltichen Mitarbeitern des Fachgebietes bedanken. Besonders die Zusammenarbeit mit meinen Büro- und Laborkollegen Mirko Bothien, Gregor Gelbert und Arnaud Lacarelle werde ich als außerordentlich inspirierend, produktiv und vor allem angenehm in Erinnerung behalten. Viele studentische Mit- und Diplomarbeiter waren mir bei einigen Teilen der Arbeit eine große Hilfe. Dafür möchte ich mich ebenfalls bedanken.

Für das Korrekturlesen von Teilen der Arbeit bedanke ich mich bei meinen Kollegen Bernhard Çosiç, Kilian Oberleithner, Christian Pfeifer und Yogesh Singh und für die Durchsicht des gesamten Manuskriptes ganz besonders bei Christina Schrödinger.

Schließlich möchte ich mich bei meinen lieben Eltern und bei meinem Bruder bedanken, auf deren Unterstützung ich mich jederzeit verlassen kann.

Berlin, im Oktober 2010 *Jonas Pablo Moeck*

Zusammenfassung

Moderne Gasturbinen werden mit magerer Vormischverbrennung betrieben, um niedrige Emissionsstandards zu erfüllen. Diese Art der Verbrennung ist jedoch äußerst anfällig gegenüber Störungen der Flamme durch akustische Schwankungen. Hierdurch entstehen sogenannte thermoakustische Instabilitäten, die sich durch außerordentlich hohe Druckpulsationen manifestieren. Diese selbsterregten Schwingungen werden durch die Interaktion der instationären Wärmefreisetzung in der Flamme mit den akustischen Moden der Brennkammer angetrieben. Neben erhöhtem Lärm führt dieses unerwünschte Phänomen zu einer Einschränkung des Betriebsbereiches der Maschine, so dass der angestrebte Wirkungsgrad und die niedrigst möglichen Schadstoffemissionen oft nicht erreicht werden können. Die Entwicklung von Methoden zur Voraussage und zur Kontrolle von Verbrennungsinstabilitäten ist daher für die Weiterentwicklung der Gasturbinentechnologie von enormer Wichtigkeit. Die vorliegende Arbeit trägt zu diesem Ziel bei.

Zuerst werden thermoakustische Instabilitäten in einem atmosphärischen Brennkammerprüfstand untersucht. Es wird ein Regelansatz vorgestellt, der unter Zuhilfenahme von verschiedenen Aktuationsmechanismen eine effiziente Kontrolle von thermoakustisch instabilen Moden erlaubt. Ein modellfreies, adaptives Regelungsverfahren wird im Prüfstand bei festen und variierenden Betriebsbedingungen eingesetzt und erreicht eine Reduktion der Schwingungsamplituden um nahezu zwei Größenordnungen. Subkritische Instabilitäten, die durch lineare Analysen nicht erfasst werden können und daher besonders schwer voherzusagen sind, werden im Experiment detailliert untersucht. Die Anregung von Grenzzyklusschwingungen in einem linear stabilen System sowie Hysterese bei einer Variation der Betriebsparameter werden demonstriert.

Eine effiziente Darstellung thermoakustischer Phänomene ist möglich, wenn man die Separation der Längenskalen in der Flamme–Akustik Interaktion ausnutzt. Hierauf basierend wird ein Modellierungsansatz vorgestellt, bei dem unterschiedliche Methoden zur Berechnung des hydrodynamischen und des akustischen Feldes verwendet werden. Dieser auf einer konsistenten Kopplung der beiden Berechnungsverfahren beruhende Ansatz wird anhand von einer einfachen Konfiguration vorgestellt und anschließend durch experimentelle Untersuchungen validiert. Komplexere Fälle einschließlich Regelung können ebenfalls simuliert werden.

Heutige Gasturbinen sind in den häufigsten Fällen mit Ringbrennkammern ausgestattet, in denen eine Vielzahl von Brennern in eine annulare Kammer feuert. Die akustischen Moden in diesen Geometrien weisen eine dominante Variation in Umfangsrichtung auf. Da sich die Großzahl an experimentellen und numerischen Untersuchungen an Einzelbrennerkonfigurationen, in denen nur rein longitudinale akustische Schwankungen auftreten, orientiert, sind an Umfangsmoden gekoppelte thermoakustische Instabilitäten weitaus weniger gut verstanden. Aus diesem Grund wird ein vereinfachtes, auf dem bekannten Rijke Rohr basierendes Ersatzsystem entwickelt, das eine grundlegende Untersuchung dieser Art von Schwingung im Detail erlaubt. Verschiedene instabile Umfangsmoden werden im Experiment beobachtet und durch ein Netzwerkmodell berechnet. Der Einfluss von Asymmetrien im System wird untersucht und ein modales Regelungsverfahren zur Kontrolle der Schwingungen angewandt.

Abstract

Modern gas turbine technology relies on lean premixed combustion to comply with low-emission standards. However, combustion systems operating in the lean premixed mode are highly susceptible to the excitation of high-amplitude pressure fluctuations commonly referred to as thermoacoustic instability. These self-excited oscillations are a result of the interaction between unsteady heat release in the flame and the acoustic modes of the combustion chamber. The main consequences of thermoacoustic instabilities are increased noise, reduced system performance, and reduced system durability. The capability to predict and to control combustion-driven oscillations, therefore, is of utmost importance for a further advance in gas turbine technology.

The present work contributes to the knowledge on thermoacoustic instabilities and their control in a number of ways. Combustion oscillations are investigated in an atmospheric single-burner test-rig. A multiple actuator scheme is developed that allows for efficient control of unstable acoustic modes, which is an important aspect in view of current actuator limitations. Model-free adaptive control is shown to be capable of mitigating strong pressure pulsations at varying operating conditions with peak amplitude reductions up to 40 dB. Subcritical instabilities, which are particularly dangerous because they are not accounted for in linear stability tools, are investigated in a detailed experimental study. Triggering of limit-cycle oscillations and hysteresis in operating parameter variations are demonstrated.

To exploit the separation of length scales inherent to flame–acoustic interactions in gas turbine combustors, a modeling approach based on separate descriptions of the hydrodynamic and the acoustic field is developed. This coupled method is demonstrated to be extremely efficient, and the computational results are validated with corresponding experiments in an elementary thermoacoustic configuration. It is shown that more complex cases can be handled as well and that active control schemes can be incorporated in this framework.

Thermoacoustic instabilities observed in modern gas turbines often exhibit a dominant circumferential variation of the fluctuating pressure field due to the ring-shaped geometry of the combustion chamber. In order to study these unstable azimuthal modes on a fundamental level, we devise a simplified surrogate system on the basis of the well-known Rijke tube. This mock-up mimics the multitude of flames in an annular combustor by simple heating grids; both feature a similar dynamic response to acoustic perturbations. The thermoacoustic dynamics in this set-up are investigated experimentally and by using a low-order, network-type model. Different unstable azimuthal modes are observed and characterized in detail. The effect of circumferential asymmetries in the heat sources is investigated and shown to be strongly related to the symmetry-induced degeneracy of the modes. A feedback control scheme, based on a modal decomposition of the measured pressure field, is set up and applied to the experimental configuration. This scheme is shown to be capable of controlling all unstable modes leading to a complete stabilization of the system.

Contents

List of Figures

Nomenclature

Vectors are printed in boldface italic. Matrices are denoted by boldface upright or by boldface calligraphic letters. Variables which have only very local usage are not included here but are defined in the text close to their appearance.

Latin letters

A	area; cross-sectional area of a duct
a	amplitude of sinusoidal signal
$\begin{smallmatrix}\mathbf{A} & \mathbf{B}\\ \mathbf{C} & D\end{smallmatrix}$	state-space matrices
a_m	modal coefficient of mth-order azimuthal mode
$\boldsymbol{b}_m^{c,s}$, $\boldsymbol{b}_m^{\pm}$	particular basis vectors in $\mathbf{B}_N$
$\mathbf{B}_N$	unitary transformation matrix of size N
C	center of gravity
c	speed of sound
c_k, c_τ	gain and characteristic time of heating grid transfer function
C_N	group of Nth-order discrete rotational symmetry with N additional reflection symmetries with respect to planes containing the symmetry axis
c_p	specific heat at constant pressure
e	forcing signal, control command
E_a	integral acoustic energy
e_a	acoustic energy density
F	cost functional
f	amplitude of downstream traveling wave
$F(\omega)$	transfer function
G	integrator gain
g	amplitude of upstream traveling wave
$g(\omega)$	speaker transfer function
$\mathbf{H}(\omega)$	6×12 plant transfer function
h	hub–tip ratio
$h_m(\omega)$	modal plant transfer function for mode m
i	$\sqrt{-1}$
I	global OH-chemiluminescence intensity
i_ac	acoustic intensity

$\mathbf{I}$	identity matrix
J_m	Bessel function of the first kind of order m
k	wavenumber (ω/c)
K	control gain
$\mathbf{K}$	6×12 control transfer function
k_{mn}	axial wavenumber associated with azimuthal and radial mode orders m and n
L	length
l	axial mode order
$\dot{m}$	mass flow
m	azimuthal mode order
M	Mach number
N	total number; in particular, number of tubes of the annular Rijke tube
$N(\omega, a)$	describing function
n	radial mode order
$\boldsymbol{n}$	outward pointing unit normal
P	electric power
P_0	thermodynamic pressure
p	acoustic pressure
Δp	burner pressure loss
Q	unsteady integral heat release rate
q	unsteady volumetric heat release rate
R	radius
R_g	specific gas constant
r	radial coordinate
s	source term
T	mean fluid temperature
$\mathbf{T}$	transfer matrix
t	time
u	axial velocity
$\boldsymbol{u}$	acoustic particle velocity
Δu	velocity divergence across heat source
V	volume
v, y	input and output of a static map
$W(\omega)$	compensator transfer function
$\mathbf{W}$	unitary discrete Fourier transform matrix
$\mathbf{X}$	diagonal matrix with ratios of characteristic impedances
x	axial coordinate

$\boldsymbol{x}$	coordinate vector
$\boldsymbol{x}$	state vector
Y_m	Bessel function of the second kind of order m
Y	mass fraction
y	transverse coordinate

Calligraphic letters, operators, and other symbols

$\mathcal{A}(\omega)$	specific admittance
$\boldsymbol{\mathcal{A}}(\omega)$	specific admittance matrix
$\mathcal{F}(\omega)$	heat release transfer function
$\boldsymbol{\mathcal{F}}(\omega)$	diagonal matrix with heat release transfer functions
$\boldsymbol{\mathcal{G}}(\omega)$	12×6 actuator transfer function
$\mathcal{H}$	Hilbert transform
$\mathcal{N}$	nonlinear operator mapping fluctuations in approach flow to velocity divergence
$\mathcal{R}(\omega)$	reflection coefficient
$\boldsymbol{\mathcal{R}}(\omega)$	reflection coefficient matrix
$\boldsymbol{\mathcal{S}}(\omega)$	system matrix
$\mathcal{Z}(\omega)$	specific impedance
$\boldsymbol{\mathcal{Z}}(\omega)$	specific impedance matrix
Im	imaginary part
Re	real part
$\partial_{(\cdot)}$	partial derivative with respect to $(\cdot)$
∇	nabla operator
∇^2	Laplacian
$\wp$	acoustic pressure divided by ρc

Greek letters

β_m	modal actuation command
γ	ratio of specific heats
Δ_m^{sp}	spin ratio of mth-order azimuthal mode
ε	perturbation parameter
ζ	pressure loss coefficient
ζ_α	modal damping term
θ	source term in Helmholtz equation
λ	acoustic wavelength
$\boldsymbol{\xi}$	acoustic scale ($\mathrm{M}\boldsymbol{x}$)
ξ	ratio of characteristic impedances

ρ	fluid density
σ	asymmetry parameter
τ	time lag
φ	angular coordinate
ϕ	equivalence ratio
ψ	eigenfunction
ω	angular frequency

Subscripts

a	analytic signal
ac	acoustic
cl	closed-loop
ds	downstream
exp	experiment
f	fundamental component
hp	high-pass
lmn	axial, azimuthal, and radial mode order
lp	low-pass
m	azimuthal mode order
mod	modeled
mn	azimuthal and radial mode order
n	tube number in annular Rijke tube configuration
ol	open-loop
osc	oscillation
pf	pilot fuel
ph	preheat
pl	phase-lead
p	perturbation
q	heat source
ref	reference
rms	root mean square
sp	speaker
s	source
us	upstream
x	axial component
α	multiindex, $\alpha = \{l, m, n\}$
η, μ	eigenfunction coordinates

ν	normal component

Superscripts

$(\cdot)'$	perturbation from mean; derivative of a function of a single scalar argument
$(\cdot)^*$	complex conjugate
$(\cdot)^+$	counter-clockwise spinning component of rotating wave
$(\cdot)^-$	clockwise spinning component of rotating wave
$(\cdot)^c$	standing wave basis, cosine component
$(\cdot)^s$	standing wave basis, sine component
$(\cdot)^T$	transpose of a matrix
$(\cdot)^\dagger$	Hermitian transpose
$(\cdot)^\star$	extremal value
$\bar{(\cdot)}$	mean state
$\dot{(\cdot)}$	(partial) derivative with respect to time
$\hat{(\cdot)}$	Fourier transform, oscillation amplitude
$(\cdot)^{\eta,\mu}$	eigenfunction coordinates

Abbreviations

CCD	**c**harge-**c**oupled **d**evice
DC	**d**irect **c**urrent
ESC	**e**xtremum-**s**eeking **c**ontrol
FEM	**f**inite **e**lement **m**ethod
LES	**l**arge **e**ddy **s**imulation
NOx	**n**itrogen **o**xides
PDF	**p**robability **d**ensity **f**unction
RMS	**r**oot **m**ean **s**quare
URANS	**u**nsteady **R**eynolds-**a**veraged **N**avier–**S**tokes

Chapter 1

Introduction

In this chapter, we introduce the phenomenon of combustion instabilities and illustrate its present and future relevance for the world's demand for energy and transport. Since combustion instabilities impede efficient and safe gas turbine operation, we have to both understand the process on a fundamental level and find countermeasures applicable to real configurations. A short overview how this thesis contributes to this task is given at the end of this chapter.

1.1 Background and Motivation

The increasing worldwide energy demand is one of the major challenges for the future. Although the use of renewable energy sources rapidly grows, fossil fuels will remain to be the major contribution in ensuring electric power and transport in the near future. The U. S. Energy Information Administration (2010) projects an 80 % contribution of coal, liquid fuels, and natural gas to the worldwide energy consumption at 2035 (Fig. 1.1), assuming no significant policy changes. The use of renewable energy sources in electric power production is anticipated to double, but natural gas consumption for electricity generation is still projected to increase by 44 % (U. S. Energy Information Administration 2010).

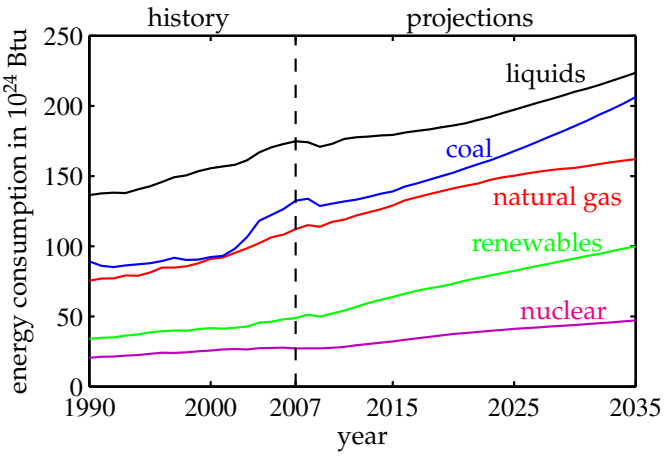

Figure 1.1: Past and projected worldwide energy use for different resources. The decline starting after 2007 is a result of the global economic recession but appears to have ended at the present time. Reproduced from data available from the U. S. Energy Information Administration (2010).

Maximizing the benefit of limited fossil fuel ressources is therefore imperative. Gas turbines play a significant role in this process, delivering a large part of the world's electricity (21 % in 2007 according to the International Energy Agency 2009, but the trend is progressive) and being the sole source for air transport. Increasing gas turbine efficiency is, however, constrained by the demand for lower emissions. While the greenhouse gas carbon dioxide eventually can only be reduced through an increase in efficiency, the emissions of nitrogen oxides (NOx), which are major contributors to acid rain, are strongly dependend on the details of the combustion process.

Since NOx production in stationary gas turbines for power generation is strongly temperature dependent, decreasing the stoichiometry is a viable means for a reduction of NOx emissions (Correa 1992). This was achieved by the gas turbine industry through the introduction of lean premixed combustion. In this burning mode, in contrast to the formerly used diffusion flames, air and fuel are well mixed before entering the flame, and in addition, the mixture has a low equivalence ratio, i.e., air excess. The lean premixed combustion mode was found, however, to be particularly susceptible to acoustic perturbations. Also, lower flame temperatures made convectively cooled combustion chambers more practical than the formerly used film-cooled type. The latter was associated with significantly higher acoustic damping.

As a result of the more susceptible lean premixed flames and the lower acoustic damping of the convectively cooled combustion chambers, combustion-driven oscillations became a serious problem for the gas turbine industry in the early 1990s. These so-called combustion – or thermoacoustic – instabilities result from the interaction of the perturbed flame and the acoustic field of the combustion chamber. Unsteady heat release acts as an acoustic source and, under unfavorable conditions, may excite an acoustic resonance of the chamber. The acoustic mode, in turn, perturbs the flame even stronger, and a feedback loop is established, which may lead to extraordinarily high pulsation amplitudes. In gas turbine combustors, the oscillation level can typically grow up to a few percent of the static pressure.

Combustion instabilities are an undesirable phenomenon in gas turbines for the following reasons:

- large amplitude pressure fluctuations can cause structural failure and enhance high-cycle fatigue;
- high levels of acoustic noise are unpleasant and damage human health;
- associated fluctuations of the flow field increase the heat transfer at the combustor walls, which increases the thermal load and has a negative impact on the efficiency;
- instabilities result in higher NOx emissions;
- strong oscillations of the flow field may lead to flame flashback or blow-off.

In fact, the major part of non-fuel costs in stationary gas turbine operation can be attributed to the repair and replacement of hot-section components, the cause of which often being related to combustion-driven oscillations (Lieuwen & Yang 2005). Even if hardware failure can be prevented by appropriate monitoring systems, combustion instabilities restrict the operating range of modern gas turbines so that optimum efficiency and emission levels cannot be realized.

Acoustically coupled instabilities in combustion technology have been known for quite some time. Active research to understand and control combustion dynamics began in the 1950s when problems in solid and liquid propellant rockets appeared (Crocco & Cheng 1956; Culick 1966). Although the pressure oscillation amplitudes associated with this type of instabilities are much larger than those encountered in gas turbine applications (up to the order of the mean pressure), and the impact on the structure is, accordingly, much more severe, this problem is still not solved today and remains an active topic of research. About a decade later, combustion-driven oscillations became an issue for industrial boilers and furnaces (Putnam 1971). In the 1980s, thermoacoustic instabilities were recognized to be a problem in ramjet-type jet engine augmentors, which motivated the work by Langhorne (1988) and Bloxsidge et al. (1988*a*,*b*). Combustion instabilities in civil aeroengine gas turbines are less frequently observed and not as severe as in the power generation case (Lieuwen & Yang 2005). It is to be expected, however, that this topic becomes more problematic in this application, too, because current and future emissions regulations eventually force the aeroengine industry to move towards lean-premixed-type combustion (Mongia et al. 2003).

Apart from the "large-scale" applications discussed above, thermoacoustic instabilities can appear in essentially every combustion device in which the flame is coupled to some kind of acoustic resonator (such as auxiliary heating devices for motor vehicles, Moeck et al. 2007*b*; Neunert 2009).

1.2 Scope of this thesis

We begin with a concise description of the fundamental theory and methods relevant to this work in Chapter 1. The contributions of this thesis are grouped into three main parts. While some of the chapters focus on experimental work, others tend to include more modeling. All of the work, however, is devoted to the analysis and control of combustion instabilities.

Part I is dedicated to the analysis and control of combustion instabilities in an atmospheric single-burner test-rig. The experimental set-up is briefly described in Chapter 2. Strong instabilities with pressure oscillations at frequencies close to 100 Hz occur in this configuration. We first apply a control methodology based on a combination of acoustic and secondary fuel actuation, while using a simple control law with empirically determined parameters (Chapter 4). Both actuators work well individually, but in combined mode, additional efficiency can be utilized.

The previous control approach is extended in Chapter 5 with an adaptive outer loop, based on an extremum-seeking scheme. This scheme tunes the control parameters with the aim to minimize the pressure oscillation amplitude in the combustor. The adaptive method is first demonstrated on the basis of an elementary model configuration and then applied in the test-rig. The adaptive controller is tested at different operating conditions and even at transient parameter variations. Finally, the ability of the extremum-seeking scheme to find the oscillation minimum in two-dimensional control parameter space is assessed.

The work presented in Chapter 6 constitutes a comprehensive experimental investigation of so-called subcritical instabilities that are observed in the test-rig for certain operating conditions. This type of instability is particularly dangerous because the oscillation amplitude may change discontinuously with variations in the operating parameters. Two stable system states exist in the subcritical regime and persist in a certain range of operating conditions. We study strongly nonlinear phenomena, such as triggering and hysteresis in the oscillation amplitude, and find a strong connection to a bistable flame-anchoring location of the burner–flame configuration. We set up a nonlinear low-order system model, partly based on experimentally identified data, that reproduces the phenomena observed in the test-rig.

Part II proposes an efficient modeling approach for the simulation of dynamic processes in thermoacoustic systems. Exploiting a distinct scale separation between the fluid-dynamic/combustion phenomena and the acoustic field, we derive a coupled representation for thermoacoustic systems in Chapter 7. A zero-Mach incompressible scheme is used for the small-scale hydrodynamic part, whereas network-type techniques for the acoustics are applied to the larger domain. Based on a consistent combination of the two models, a two-way coupling is achieved, which is extremely efficient. We illustrate the approach on the basis of an elementary model configuration. In Chapter 8, we apply the coupled method to an experimental system for validation purposes and give a detailed comparison of the measurement data and the computational results. Control applications are explored in a configuration with a two-dimensional flame in Chapter 9. Here, the flame is endowed with the acoustic environment of a combustor test-rig. Two types of control, utilizing different actuation mechanisms, are applied to this case.

Part III introduces an annular thermoacoustic surrogate system. Real gas turbine combustion chambers are typically of annular type. The acoustic modes that are often found to be unstable in these configurations have dominant circumferential variations and are therefore called azimuthal modes. These are not observed in purely longitudinal single-burner test-rigs. To study unstable azimuthal modes in a generic set-up, we devise an annular thermoacoustic system based on the well-known Rijke tube. Twelve ducts with heating grids, that mimic the flames in a gas turbine combustor, are coupled to a ring-shaped resonator. In contrast to a full annular combustion chamber, this system is easy to operate and has a clear definition. Chapter 10 gives a short overview on instabilities in annular configurations and introduces the experimental arrangement. Modeling tools for thermoacoustic systems in annular domains and, in particular, for our mock-up are developed in Chapter 11. A low-order model is built to predict mode stability and the effect of asymmetries in the configuration. In Chapter 10.3, a detailed experimental study of the unstable azimuthal modes in the set-up is performed. Based on the low-order model, a feedback controller is designed to mitigate the instabilities observed in the experiment.

A short summary of the main contributions with recommendations for extensions of this work follows at the end of the thesis.

Chapter 2

Fundamental Theory and Methods

Thermoacoustic instabilities are system instabilities that arise due to the coupling of flame, flow, and acoustics. As such, they span a wide range of physical processes that are all relevant to the problem. It may be this combination of often separately taught fields that has permitted this phenomenon to evade a general solution for a considerable period of time and despite an enormous effort by an abundance of industrial and academic research groups. (A recent review article by Huang & Yang 2009 comprises almost 600 references!) Covering all fundamental aspects of combustion instabilities and their control is not possible at this point. There are several review articles which can be consulted; we recommend Candel's work (Candel 2002, 1992) as general references, the book edited by Lieuwen & Yang (2005) with particular focus on gas turbines, and the comprehensive compilation by Culick (2006). The review article by Huang & Yang, mentioned above, is especially dedicated to combustion dynamics associated with swirl-stabilized burners.

In this chapter, we shall only give an overview of the relevant theory and methods and go into more detail at later instances whenever necessary. Since the Mach number M is small in the applications we consider, we use the acoustic equations for a quiescent medium.

2.1 Ducted sound fields

Neglecting heat conduction and viscous effects, linearized mass and momentum balances in a quiescent, source-free fluid read (Rienstra & Hirschberg 2006)

$$\partial_t \rho + \nabla\cdot(\bar{\rho}\boldsymbol{u}) = 0, \tag{2.1a}$$

$$\bar{\rho}\partial_t \boldsymbol{u} + \nabla p = 0, \tag{2.1b}$$

where $\bar{\rho}$ is the mean density (not necessarily constant in space), and ρ, $\boldsymbol{u}$, and p are the fluctuations in density, velocity, and pressure associated with acoustic wave propagation. Equations (2.1) are closed by employing energy and constitutive equations to relate pressure and density fluctuations by

$$\partial_t p = c^2\partial_t \rho + c^2\boldsymbol{u}\cdot\nabla\bar{\rho}, \tag{2.2}$$

where we assumed a uniform mean pressure and $c = \sqrt{\gamma R_g T}$ is the acoustic propagation speed of an ideal gas; γ, R_g, and T denote the ratio of specific heats, the specific gas constant, and the mean temperature of the fluid, respectively.[1] Although γ is a weak function of temperature, we consider it to be constant in the following.

With the pressure–density relation (2.2), the mass balance (2.1a) can be replaced with

$$\partial_t p + \bar{\rho} c^2 \nabla \cdot \boldsymbol{u} = 0. \tag{2.3}$$

Combination of Eqs. (2.1b) and (2.3) yields a wave equation for the acoustic pressure, viz.,

$$\partial_{tt} p = \nabla \cdot (c^2 \nabla p). \tag{2.4}$$

Upon introducing temporal Fourier transforms such that $\partial_t \mapsto \mathrm{i}\omega$, (2.4) can be reduced to the Helmholtz equation

$$\nabla \cdot (c^2 \nabla \hat{p}) + \omega^2 \hat{p} = 0, \tag{2.5}$$

where $\hat{(\cdot)}$ denotes the Fourier transform of a variable, and ω is the angular frequency, the Fourier transform variable.

In ducted configurations, the solution of the Helmholtz equation (2.5) can be given in terms of a superposition of *modes*, particular oscillation patterns characteristic to the problem. For hard-walled ducts with simple cross-sectional geometries (such as circular or rectangular) and uniform temperature, these modes are well-known (e.g., Morse & Feshbach 1953; Rienstra & Hirschberg 2006) and can be given in analytical form. We do not discuss the details of the modal pressure field at this point but postpone the description to Part III, where we need the higher-order modal content for our model of an annular system. Here, we shall content ourselves with a qualitative description.

2.1.1 Plane waves

Associated with each mode is an axial propagation constant that is either purely real or imaginary, depending on the angular frequency ω. If the propagation constant is purely imaginary, this particular mode is referred to as *cut-off* – or *evanescent* – because it decays exponentially in axial direction (Morse & Feshbach 1953; Rienstra & Hirschberg 2006). For characteristic acoustic wavelengths $\lambda = 2\pi c/\omega$ much larger than the characteristic transversal duct dimension, i.e., at low frequencies, only the plane, axisymmetric mode propagates. In a circular duct with radius R, this holds for frequencies smaller than $1.84\, c/(2\pi R)$ (Rienstra & Hirschberg 2006). Taking the duct's axis to be aligned in x-direction, the plane-wave pressure field takes the form

$$\hat{p} = \hat{f}\, \mathrm{e}^{-\mathrm{i}kx} + \hat{g}\, \mathrm{e}^{\mathrm{i}kx}, \tag{2.6}$$

where $k = \omega/c$ is the axial wavenumber, and $\hat{f}$ and $\hat{g}$ represent the complex amplitudes of down- and upstream traveling waves, the Riemann invariants of the acoustic field. With the Fourier transform of the linearized momentum balance (2.1b), the axial particle

[1] In the framework of linear acoustics, we will not encounter temperature fluctuations explicitly. Therefore, we use T solely as the mean temperature without an additional overbar. Likewise, c always denotes the mean speed of sound.

velocity u is found to satisfy

$$\hat{u} = \frac{1}{\bar{\rho}c}\left(\hat{f}\,\mathrm{e}^{-\mathrm{i}kx} - \hat{g}\,\mathrm{e}^{\mathrm{i}kx}\right). \tag{2.7}$$

In isothermal ducts, the inverse of the characteristic impedance can be absorbed into f and g. Then we have at the reference location $x = 0$, $\hat{\wp} = \hat{f} + \hat{g}$ and $\hat{u} = \hat{f} - \hat{g}$, where $\wp = p/(\bar{\rho}c)$ is the acoustic pressure scaled with the characteristic impedance of the medium.

For all ducted configurations we investigate in this work, except for that in Part III, we will only consider the plane wave mode to be relevant. This will be justified based on the characteristic transversal duct dimension. In Part III, in which we are explicitly dealing with thermoacoustic instabilities coupled to azimuthal modes, the circumferential pressure distribution is crucial.

2.1.2 Boundary conditions

To determine the acoustic field in a confined domain, boundary conditions have to be specified at the surrounding surface. At impermeable, rigid parts of this surface, the normal component of the acoustic velocity has to vanish, hence $\boldsymbol{u}\cdot\boldsymbol{n} = 0$, where $\boldsymbol{n}$ is the outward pointing unit normal. If the ambient pressure is imposed at a certain location, on the other hand, the pressure fluctuation has to be zero. A general acoustic boundary condition is typically formulated in frequency domain and relates the acoustic pressure and the normal component of the velocity through the acoustic impedance Z via

$$Z(\omega) = \frac{\hat{p}}{\hat{\boldsymbol{u}}\cdot\boldsymbol{n}} \tag{2.8}$$

or the inverse of Z, the admittance. In our case, it is often more convenient to work with specific impedance and admittance, denoted in the following by $\mathcal{Z}$ and $\mathcal{A}$. These are obtained from Z and Z^{-1} by scaling them with the characteristic impedance of the fluid $\bar{\rho}c$, hence $\mathcal{Z} = Z/(\bar{\rho}c)$ and $\mathcal{A} = \bar{\rho}cZ^{-1}$. We will be often using the negative of the specific admittance but denote it by $\mathcal{A}$ as well for convenience.

When working with the complex wave amplitudes $\hat{f}$ and $\hat{g}$, the acoustic boundary condition is commonly stated in terms of the reflection coefficient $\mathcal{R}(\omega)$, which is defined as the ratio of the reflected to the incident wave. For a boundary condition at $x = 0$, with the outward pointing normal aligned with the x-axis, the reflection coefficient is, accordingly, given by $\mathcal{R} = \hat{g}/\hat{f}$. Combination of Eqs. (2.6)–(2.8) then yields

$$\mathcal{R} = \frac{\mathcal{Z}-1}{\mathcal{Z}+1} \qquad \text{and} \qquad \mathcal{Z} = \frac{1+\mathcal{R}}{1-\mathcal{R}}. \tag{2.9}$$

The reflection coefficient is a clear indicator whether the associated boundary condition conserves energy: if the magnitude of the reflected wave amplitude is smaller than that of the one incident, in other words, if $|\mathcal{R}| < 1$, acoustic energy is dissipated or transmitted outside of the system.

One particular boundary condition we will often use is that of an unflanged, open end of a circular duct. According to Levine & Schwinger (1948), the specific impedance for this

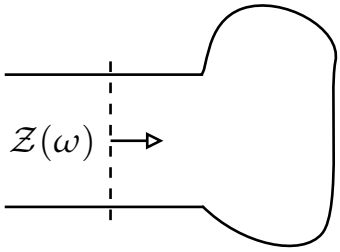

Figure 2.1: Schematic representation of a lumped boundary condition. The impedance $\mathcal{Z}$ contains the complete plane-wave response associated with the domain to the right of the dashed line.

case can be approximated for small duct Helmholtz numbers kR as

$$\mathcal{Z}_{\mathrm{LS}} = \tfrac{1}{4}(kR)^2 + \mathrm{i}\,0.61\,kR. \tag{2.10}$$

The imaginary part without the factor k is typically referred to as the *end correction* because it has the effect to shift the pressure node outside of the duct and thus makes it appear longer by an additional length of $0.61\,R$. The real part, the resistance, represents radiation away from the duct's end and increases with the square of the Helmholtz number. Since the associated energy is lost to the acoustic field in the duct, the corresponding reflection coefficient has a magnitude smaller than unity for $kR > 0$.

For a system in which the conditions for pure plane-wave propagation are satisfied at a certain location, we can actually represent larger subdomains, with possibly more complex geometries, by equivalent – or *lumped* – boundary conditions. This is illustrated in Fig. 2.1. The impedance at the indicated position represents the complete plane-wave response of the domain to the right of the dashed line. Here, it does not matter if there is a non-uniform temperature distribution or multi-dimensional effects beyond the dashed line. The impedance at the reference location gives a complete description whenever the acoustic dynamics in that domain are truly linear and time invariant.

The plane wave boundary condition can be measured with the so-called Multi-Microphone-Method. This will be an important aspect at various instances in this thesis. The experimental procedure is described in Appendix A.

2.2 The effect of unsteady heat release on the acoustic field

As mentioned in the beginning of this chapter, thermoacoustic instabilities arise as a result of a mutual coupling between the acoustic field and a source of unsteady heat release. This implies that the unsteady heat release has an effect on the acoustic field and vice versa. As it turns out, the second part, the unsteady response of the heat release to an acoustic perturbation, is much more complex. Therefore, we begin with a discussion of the first part, the excitation of acoustic waves by unsteady heat release, in this section.

In the presence of unsteady heat release, the pressure–density relation (2.2) does no longer hold but must be supplemented with the non-isentropic contribution, which is obtained from the entropy equation and the equation of state for an ideal gas (see, e.g., Dowling & Stow 2003), viz.,

$$\partial_t p = c^2 \partial_t \rho + c^2 \boldsymbol{u}\cdot\nabla\bar{\rho} + (\gamma - 1)q, \tag{2.11}$$

where q is the unsteady component of the volumetric heat release rate. Combining (2.11) with linearized mass and momentum balances (2.1), we obtain a wave equation for the acoustic pressure including the effect of unsteady heat release as

$$\partial_{tt} p = \nabla \cdot \left(c^2 \nabla p \right) + (\gamma - 1)\, \partial_t q, \tag{2.12}$$

or alternatively, the Helmholtz equation for the Fourier transform of the acoustic pressure

$$\nabla \cdot \left(c^2 \nabla \hat{p} \right) + \omega^2 \hat{p} = -\mathrm{i}\omega\, (\gamma - 1) \hat{q}. \tag{2.13}$$

Equation (2.12) is essentially a corollary of Lighthill's acoustic analogy (Lighthill 1952). Clearly, the unsteady heat release acts as a monopole-type source for the acoustic field.

Although (2.12) describes the evolution of the sound field, once supplemented with suitable boundary conditions, this equation cannot be solved unless the heat release q can be related to the acoustic variables. This turns out to be a rather complex task and is the subject of Section 2.3.

2.2.1 Compact heat sources

We consider now the case of a compact heat source, for which the spatial extent of q is much smaller than the acoustic length scale c/ω.[2] This requirement is commonly met in thermoacoustic instability problems. The exact distribution of q is then not important because it is confined to a region which is very small compared to the long acoustic wavelength. Integrating now the Helmholtz equation (2.13) over a volume containing q and using Gauss' theorem, we obtain

$$\int_{\partial V} c^2 \nabla \hat{p} \cdot \boldsymbol{n}\, \mathrm{d}A + \omega^2 \int_V \hat{p}\, \mathrm{d}V = -\mathrm{i}\omega(\gamma - 1)\, \hat{Q}, \tag{2.14}$$

where $Q = \int_V q\, \mathrm{d}V$ is the integral heat release and $\boldsymbol{n}$, as before, denotes the outward pointing unit normal. Now, since we essentially endowed q with δ-support, the integration volume can be made arbitrarily small so that the second term on the left hand side of (2.14) vanishes. Using further the linearized momentum balance to substitute the pressure gradient by the particle velocity yields

$$\int_{\partial V} \hat{\boldsymbol{u}} \cdot \boldsymbol{n}\, \mathrm{d}A = \frac{\gamma - 1}{\gamma P_0}\, \hat{Q}, \tag{2.15}$$

where we used the fact that $\bar{\rho} c^2 = \gamma P_0$ is constant (P_0 denoting the mean static pressure). Evidently, compact heat release acts as a volume source through unsteady expansion. Also note that (2.15) does not have an explicit frequency dependence, and therefore, holds also in time domain.

[2] If we were to include entropy perturbations in our analysis, the compactness condition would be much more stringent. Since entropy disturbances are simply advected by the mean flow, the characteristic wavelength is $\bar{u}/\omega$ ($\bar{u}$ denoting a characteristic convection speed). Accordingly, the width of a heat source distribution which can still be assumed to be compact decreases by a factor of the Mach number (Dowling 1995).

In a ducted configuration, for frequencies at which only the plane wave mode propagates, Eq. (2.15) takes the form

$$A(u_{\mathrm{ds}} - u_{\mathrm{us}}) = \frac{\gamma - 1}{\gamma P_0} Q, \tag{2.16}$$

where A is the cross-sectional area of the duct, and subscripts 'us' and 'ds' correspond to locations immediately up- and downstream of the heat source. Hence, the integral unsteady heat release induces a jump in the acoustic velocity across the heat source. Also note that even if q has δ-support, it follows from Eq. (2.13) that $\hat{p}$ is still continuous.

For the mean global heat release from the flame, we can write

$$\bar{Q} = \bar{\rho}_{\mathrm{us}} \bar{u}_{\mathrm{us}} A c_p (T_{\mathrm{ds}} - T_{\mathrm{us}}), \tag{2.17}$$

where c_p is the specific heat at constant pressure. Using this in (2.16), we find

$$u_{\mathrm{ds}} = u_{\mathrm{us}} + \left(\frac{T_{\mathrm{ds}}}{T_{\mathrm{us}}} - 1 \right) \frac{Q}{\bar{Q}} \bar{u}_{\mathrm{us}}. \tag{2.18}$$

2.2.2 Acoustic energy and Rayleigh's criterion

Whether the acoustic source actually enhances the fluctuation amplitudes or not is not apparent from the above discussion. This requires the introduction of the acoustic energy, which, in its most simple (local) form, can be defined as (Crighton et al. 1992; Rienstra & Hirschberg 2006)

$$e_{\mathrm{a}} = \tfrac{1}{2} \left(\bar{\rho} |\boldsymbol{u}|^2 + p^2 / (\bar{\rho} c^2) \right). \tag{2.19}$$

In non-isentropic flows, a consistent definition of the fluctuation energy must also include entropy perturbations (Chu 1965; Nicoud & Poinsot 2005). We do however, content ourselves at this point with the purely acoustic energy.

From the linearized mass and momentum equations (2.1) and the pressure–density relation (2.11), we obtain an evolution equation for the acoustic energy as

$$\partial_t e_{\mathrm{a}} + \nabla \cdot \boldsymbol{i}_{\mathrm{a}} = s, \tag{2.20}$$

where the energy flux $\boldsymbol{i}_{\mathrm{a}} = p\boldsymbol{u}$ is typically referred to as the acoustic intensity,[3] and the source term takes the form

$$s = \frac{\gamma - 1}{\gamma P_0} pq. \tag{2.21}$$

Integrating the acoustic energy equation (2.20) over a stationary volume, we obtain

$$\frac{\mathrm{d}}{\mathrm{d}t} E_{\mathrm{a}} = - \int_{\partial V} p\boldsymbol{u} \cdot \boldsymbol{n} \, \mathrm{d}A + \frac{\gamma - 1}{\gamma P_0} \int_V pq \, \mathrm{d}V, \tag{2.22}$$

where E_{a} denotes the integral acoustic energy in the domain. Clearly, the energy increases whenever the integral pressure–heat-release correlation is positive and exceeds the acoustic power flow lost at the system boundaries.

[3] Some authors define the intensity to be the time-average of $p\boldsymbol{u}$.

For oscillatory signals, it is instructive to consider the period-average of Eq. (2.22). Representing the time-domain signals by $z = \mathrm{Re}(\hat{z}\,\mathrm{e}^{\mathrm{i}\omega t})$ and averaging over one period of oscillation, we have

$$\Delta E_\mathrm{a} = -\frac{1}{2}\int_{\partial V} \mathrm{Re}(\hat{p}\hat{\boldsymbol{u}}^*\cdot\boldsymbol{n})\,\mathrm{d}A + \frac{1}{2}\frac{\gamma-1}{\gamma P_0}\int_V \mathrm{Re}(\hat{p}\hat{q}^*)\,\mathrm{d}V, \tag{2.23}$$

where $(\cdot)^*$ denotes the complex conjugate, and ΔE_a represents the change of the total acoustic energy over one period. From Eq. (2.23), we can most clearly identify Rayleigh's criterion (Rayleigh 1878): the unsteady heat release is destabilizing if it has an in-phase component with the fluctuating pressure because, in this case, energy is added to the acoustic field.

Since we shall not encounter any fluctuations in density from here on, we will drop the overbar from the mean density and denote it simply by ρ.

2.3 Flame response to acoustic perturbations

The excitation of heat release fluctuations by acoustic perturbations is an essential component in thermoacoustic phenomena because it closes the feedback loop between sound field and flame. This process is typically quantified in terms of the *flame transfer function*, which relates the Fourier transform of the normalized fluctuations in heat release rate to the Fourier transform of the fluctuations in approach flow velocity, mostly in a normalized form. In contrast to the excitation of the acoustic field by unsteady heat release, which has been described in the previous section and can be given to quite acceptable accuracy in analytical terms, this interaction mechanism is exceedingly complex. Yet, without knowledge on the heat release response to acoustic perturbations, no reliable statement about the stability of a thermoacoustic system can be made. Although various research groups are devoted to the analytical, numerical, and experimental investigation of flame transfer functions, only elementary configurations, like the laminar premixed Bunsen flame, seem to be comprehensively understood (Lieuwen 2003).

2.3.1 Mechanisms

For realistic flames, such as those used in gas turbine combustors, complete theoretical understanding and predictive modeling capabilities, even only for the linear regime, are far from being well developed. One reason for this is the sheer complexity of the possible interaction mechanisms in a technical burner–flame configuration (Paschereit et al. 2002; Sattelmayer 2003; Zinn & Lieuwen 2005).

In case of laminar premixed flames, acoustically induced oscillations in heat release are mainly a result of kinematic effects, i.e., wrinkling and movement of the flame, and the heat release perturbations are generally related to flame surface area variations (Ducruix et al. 2000; Fleifil et al. 1996; Schuller et al. 2002, 2003). The perturbation of the flame also includes the hydrodynamic field as an intermediate step. Velocity oscillations associated with the acoustic field excite receptive shear layers and trigger vortices that are convected into the flame and cause strong perturbations of the flame front. This vortex–flame interaction is particularly prominent in dump combustors, such as backward facing step

configurations (Ghoniem et al. 2005; Schadow & Gutmark 1992). Swirl-burners, which are commonly used in industrial gas turbines, exhibit pronounced flow instabilities, typically associated with helical structures, that cause fluctuations in the heat release and may couple to the acoustic field (Huang & Yang 2009; Paschereit et al. 1999*a*, 2000; Syred 2006; Thumuluru & Lieuwen 2009).

In gas turbine burners, air and fuel are not perfectly mixed when they reach the flame front. This would require a long mixing distance, which cannot be realized for safety reasons. For these partially – or technically – premixed flames, pressure and velocity oscillations at the location of fuel injection cause perturbations in the mixture fraction (Huber & Polifke 2009; Lieuwen et al. 2001). These perturbations are advected to the flame, subject to diffusion and dispersion (Polifke et al. 2001*a*; Sattelmayer 2003), and may generate large oscillations in the heat release rate. This is in particular so for the lean case, when flame properties, such as the burning velocity, become strongly susceptible to perturbations in the equivalence ratio (Lieuwen et al. 2001). Strong temporal variations in the mixture fraction may even lead to a dynamical displacement of the flame anchoring position, which then results again in the generation of unsteady heat release (Biagioli et al. 2008).

In general, the flame's response is understood to be mainly caused by velocity fluctuations (and possibly pressure perturbations at the fuel injector). However, since the chemical reaction rate is pressure dependent, there is, in principle, also a direct effect of the fluctuating pressure on the heat release. This mechanism was investigated theoretically some 20 years ago (Clavin et al. 1990; McIntosh 1991) with recent experimental (Wangher et al. 2008) and numerical results (Schmidt & Jiménez 2010). However, this so-called *direct pressure effect* is very small (by a factor of the Mach number smaller than heat release coupling by velocity fluctuations, Lieuwen 2003) and probably not one of the major driving mechanisms in typical combustion instabilities.

A technical burner–flame arrangement may generally exhibit all of the effects described above. Which ones are dominant depends on the particular set-up and the operating conditions so that it is difficult (or simply not possible) to make any general statements about the importance of the individual contributions. For liquid fuel flames, the interaction becomes even more complex because acoustic perturbations cause unsteadiness in the atomization and vaporization processes.

2.3.2 Models

Although the response of a flame to acoustic perturbations has quite different characteristics depending on the particular type and the operating conditions, two general properties have been identified: (i) low-pass, the response decreases with increasing forcing frequency; and (ii) time-lag, the phase shift between the forcing and the response signal increases approximately linearly with frequency. The time-lag characteristic of the flame response was introduced by Crocco & Cheng (1956) with the well-known n–τ model. Here, the combustion response is modeled as being proportional to $n\,f(t-\tau)$, where n is called the interaction index, τ is the time lag, and f represents the pressure or velocity perturbation at some reference position. The time lag τ is of crucial importance for stability because it controls the phase relationship of heat release and pressure perturbations. According to Rayleigh's criterion, this determines if the effect of the heat release–acoustic

interaction is destabilizing. Despite its simplicity, the n–τ model is still used today for fundamental studies.

Most of the modeling effort has so far been restricted to the linear regime. Typically, the desired relation is the flame transfer function $\mathcal{F}(\omega)$, a frequency-domain description that couples (normalized) perturbations in heat release to those in velocity via a linear time-invariant system. For premixed Bunsen-type and similar laminar flames, heat release fluctuations are predominantly caused by kinematic effects and can be modeled with a G-equation for the flame surface, which admits analytical solutions for linearized perturbations (Ducruix et al. 2000; Fleifil et al. 1996; Schuller et al. 2002, 2003).

Linear models for perfectly premixed industry-relevant swirl-stabilized flames were recently established (Hirsch et al. 2005; Komarek & Polifke 2010; Palies et al. 2010). Here, it was recognized that an acoustic wave impinging on the swirler generates a vorticity wave. In contrast to the longitudinal acoustic perturbation, which travels at the speed of sound, the vorticity wave is advected by the mean flow, and the heat release fluctuations generated by these two mechanisms may thus interfere constructively or destructively. This phenomenon explains large gain variations observed in measurements. A similar effect may result from the interference of velocity and mixture fraction disturbances in case of technically premixed flames (Schuermans et al. 2004*a*).

2.3.3 Finite-amplitude effects

Compared to the linearized case, the knowledge and modeling capabilities for the flame response at finite amplitude is significantly less developed. Experimental and numerical investigations show that nonlinear effects become important at velocity forcing amplitudes comparable to the mean flow (e.g., Bellows et al. 2007*a*). The effect of nonlinearity typically is to saturate the heat release response. Since nonlinear effects in the acoustic field can be generally assumed to be weak, it is the saturation in the heat release response that determines the final, steady-state oscillation amplitude.

Dowling (1997) used a simple limiter in combination with a time-lagged low-pass to model the nonlinear flame response of an afterburner configuration. As the heat release rate cannot become negative, Dowling argued, the amplitude has to be limited by half of the mean value. By combining this model with a linear description of the system acoustics, she was able to obtain limit-cycle oscillations in the simulations, showing good agreement with related experiments. In subsequent work, the nonlinear response was modeled by a G-equation for the flame front kinematics (Dowling 1999).

Technically premixed flames introduce an additional complexity also in the finite amplitude case because the rate of heat release depends on the mixture fraction in a nonlinear manner. Peracchio & Proscia (1999) modeled this effect explicitly through a nonlinear relation between the equivalence ratio and velocity perturbations (for the case of stiff fuel injectors) and a nonlinear dependence of the heat release rate on the mixture fraction. With this approach, they were able to reproduce the instability characteristics observed in a single-nozzle rig at engine conditions.

Experimental and numerical studies of the nonlinear flame response have been performed for various configurations (Armitage et al. 2006; Balachandran et al. 2005; Durox

et al. 2009; Lieuwen & Yang 2005) and have recently focused on measurements in swirl-burner configurations (Bellows et al. 2007*b*; Palies et al. 2009; Schimek et al. 2010). Nonlinear flame response measurements are typically performed for various forcing frequencies and amplitudes. These data sets then yield an amplitude-dependent transfer function that can be used in low-order models to estimate the oscillation amplitude in the unstable case (see next section). The development of nonlinear (reduced-order) models for the flame response is, however, not well advanced.

2.4 Linear instability and limit-cycle oscillations

As shown in the previous two sections, there is a two-way coupling between the acoustic field and the unsteady heat release in the flame. If the phase relationships of these processes match, as stated by Rayleigh's criterion, this interaction generates positive feedback so that the fluctuation energy increases in time. Typically, the oscillations observed in real applications as well as in test-rigs and numerical simulations are understood to be a result of linear instability. This means that positive feedback occurs already at small amplitudes. The steady, non-oscillating state is then unstable with respect to infinitesimal perturbations, and the fluctuation amplitudes grow exponentially in the initial phase. This linear instability can be calculated from a linearized system model. However, at large oscillation amplitudes, nonlinear mechanisms become important and typically have a saturating effect (see Section 2.3.3) so that the growth of the instability is limited. A finite-amplitude oscillation is then established, for which the energy gain through the Rayleigh term (see Eqs. (2.22) and (2.23)) is balanced by the power losses at the system boundaries and through dissipation inside the system. The system state is periodic with well-defined amplitude and frequency – a limit-cycle oscillation. Since this oscillation does not need any external forcing to be established, it is referred to as *self-excited*.

Figure 2.2 displays pressure data that was measured in a Rijke tube[4] to illustrate linear instability and the subsequent limit-cycle oscillation. The exponential growth marks the stage of linear instability. After a small overshoot, the oscillation settles on a finite amplitude, and the system state is periodic. This is evidenced by the phase-plane plot in Figure 2.2.

Consider now some system parameter, σ say, that controls linear stability. Then there is some critical value of that parameter, σ_{crit}, such that for $\sigma < \sigma_{\text{crit}}$, the system is stable and for $\sigma > \sigma_{\text{crit}}$, the system is linearly unstable, the oscillation amplitude growing continuously as σ is increased. This scenario corresponds to a supercritical Hopf bifurcation; a pair of complex eigenvalues of the linearized system crosses the imaginary axis with non-zero speed at σ_{crit} (Nayfeh & Balachandran 1995).

A stable limit-cycle oscillation can also be associated with a subcritical Hopf bifurcation. In this case, the system is not necessarily unstable for small amplitudes. There is a finite interval of σ values with $\sigma < \sigma_{\text{crit}}$ for which the steady state and the limit-cycle oscillation are both stable with respect to small perturbations. However, finite-amplitude perturbations can trigger a transition from one system state to the other. In contrast to

[4]The Rijke tube is the simplest device that exhibits thermoacoustic oscillations. Its set-up is very simple: a heated gauze is placed inside a tube open at both ends. A review on Rijke tubes and Rijke-like burners was given by Raun et al. (1993).

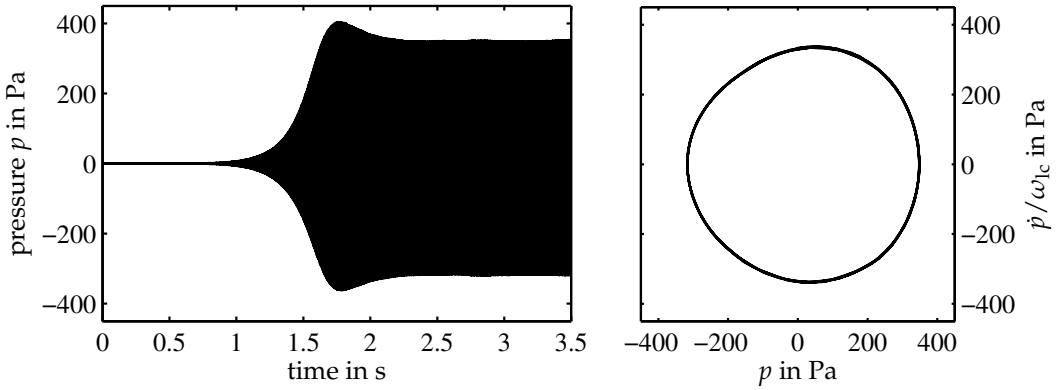

Figure 2.2: Linear instability and limit-cycle oscillation measured in a Rijke tube with 1 m length. Left: pressure history; right: p–$\dot{p}/\omega_{\mathrm{lc}}$ phase plane of the established oscillation. $\dot{(\cdot)}$ and ω_{lc} denote derivative with respect to time and limit cycle frequency (172 Hz), respectively.

the supercritical case, in which the system is linearly unstable, the finite-amplitude oscillations associated with subcritical instabilities are not self-excited but only self-sustained. This type of instability has been observed in various experimental studies of thermoacoustic oscillations (e.g., Knoop et al. 1997; Lieuwen 2002; Matveev & Culick 2003) and was also found in a recent theoretical investigation of a model of a Rijke tube with an electrically heated grid (Subramanian et al. 2010). A comprehensive investigation of this type of instability in an atmospheric test-rig combustor is the subject of Chapter 6, where in addition, more background information will be given and the results of previous studies in this field will be discussed.

It is also important to note that, although the heat-release–acoustic interaction is of distinctly local nature, being confined to a small region containing the flame, combustion oscillations are *system instabilities*. As such, stability of the steady state is influenced by the complete system configuration, up to a point where the boundary conditions can be unambiguously specified. This is because the acoustic field at the flame, which (i) generates the unsteady heat release and (ii) determines whether there is an energy gain through the Rayleigh term, depends on the complete geometry (and temperature distribution) and the boundary conditions. The dependence on the latter is evident from the global balance of acoustic energy (2.22); the whole system boundary is potentially decisive if oscillations grow (or not). This is in strong contrast to hydrodynamic stability problems of (nearly) parallel flows, in which stability can often be assessed on the basis of the local mean state (see, e.g., Schmid & Henningson 2001).

The strong dependence of system stability on the boundary conditions is a particularly problematic matter in the design of annular combustion chambers. Since experiments in full annular configurations are excessively expensive, most of the experimental development work is restricted to single-burner test-rigs. It is obvious, however, that the acoustic environment of an annular combustion chamber is quite different from a purely longitudinal set-up. For this reason, methods have been developed to adapt (at least part of) the acoustic boundary conditions to more engine-like conditions (Bothien et al. 2008; Mongia et al. 2003).

We shall also make a clear distinction between *combustion instabilities* and *combustion noise*. Although these terms are sometimes used interchangeably, it is reasonable to associate with each a distinct type of system behavior. When referring to combustion instabilities, we address a system state that exhibits coherent oscillations as a result of a linear or a subcritical instability. This oscillation state has a markedly concentrated spectral signature. Opposed to that, we use the term combustion noise for a system state that exhibits noticeable fluctuation amplitudes in pressure and heat release but not in a coherent manner. This signature corresponds to a lightly damped noise-driven system; the associated linearized model has a pair of eigenvalues close to the stability border, and high fluctuation amplitudes can be observed at the resonance frequencies. The spectral power distribution of a noise-driven system is typically broader than in the case of combustion instability. Although the fluctuation amplitudes can exceed the linear regime also in the noise-driven case, nonlinearity is not a necessary component to explain combustion noise. One way to distinguish between noise-driven and (noisy) limit-cycle oscillations in a test-rig experiment is to analyze the probability density function (PDF) of a representative system observable, typically the unsteady combustor pressure. As shown by Banaszuk et al. (1999*b*) and Lieuwen (2002), the pressure PDF of a limit-cycle oscillation has a characteristic bimodal shape, whereas a noise-driven system state gives rise to an approximately Gaussian PDF. For a stable linear system driven by Gaussian noise, the output signal, i.e., the pressure, would also have a Gaussian distribution. In case of a self-sustained oscillation, the bimodal PDF structure arises because the system spends more time at the extrema of the approximately sinusoidal state (Rowley et al. 2006).

2.5 Low-order modeling of thermoacoustic instabilities

Detailed numerical modeling of thermoacoustic oscillations is an inherently complex task due to their nature as system instabilities, as explained in the previous section. Representing all the participating physical mechanisms in an appropriate manner leads to a computationally expensive problem set-up. So-called *low-order models*, which are of much lower complexity and capture only the essential physics, often give remarkable insight and allow for a quick assessment of the stability of a particular system or the effect of parameter changes; the latter is particularly important in the industrial environment.

Traditionally, representing thermoacoustic systems with network models has been a frequency-domain approach, and accordingly, is primarily a linear tool. There are extensions to nonlinear frequency-domain methods and to time-domain simulations, which we shall also briefly discuss below.

2.5.1 Linear systems

One purpose of using low-order thermoacoustic models is to assess linear stability of a given system. Even if nonlinear oscillations are to be investigated, a major part of the model, typically the one that can be related to the acoustics only, will remain linear. For these reasons, linear systems form an essential part of a thermoacoustic network model, and we shall concisely summarize the types of representations we will be using in the following. These representations are for time-invariant systems only.

Representations

One component of a low-order thermoacoustic model can be typically characterized by some input–output relation that maps one or more input variables, u say, to one or more output variables y in a linear time-invariant manner. In frequency domain, this mapping can be represented by some complex-valued, frequency-dependent transfer function or matrix, viz.,

$$\hat{y} = F(\omega)\hat{u}, \tag{2.24}$$

where the number of columns and rows of F is equal to the number of inputs and outputs of the system, respectively. F is a complete characterization of the system; it is defined for frequencies in the whole complex plane and, therefore, also contains information on the transient dynamics.

Under certain conditions, which we will elaborate on below, an equivalent time-domain representation of the system can be given in standard state-space form as

$$\dot{\boldsymbol{x}} = \mathbf{A}\boldsymbol{x} + \mathbf{B}u, \tag{2.25a}$$

$$y = \mathbf{C}\boldsymbol{x} + \mathbf{D}u. \tag{2.25b}$$

Here $\boldsymbol{x}$ is the state vector with length d, a representation of the system's internal dynamics, and $\mathbf{A}$, $\mathbf{B}$, $\mathbf{C}$, and $\mathbf{D}$ are constant matrices with appropriate dimensions. The four matrices constitute the state-space system; d is called the order or the dimension of the system.

The state-space system (2.25) can be converted to the frequency-domain representation (2.24) by means of the Laplace transform, which yields

$$F(\omega) = \mathbf{C}(\mathrm{i}\omega\mathbf{I} - \mathbf{A})^{-1}\mathbf{B} + \mathbf{D}. \tag{2.26}$$

Hence, F is a rational function of $\mathrm{i}\omega$. Moreover, if the inverse in (2.26) is written in terms of the determinant and the adjugate, then it is apparent that the number of poles (the zeros of the denominator polynomial of this rational form) is equal to the order of the state-space system. Also, the state-space representation (2.25) is not unique. A similarity transform can be applied to $\mathbf{A}$, $\mathbf{B}$, and $\mathbf{C}$, which leaves the transfer function (2.26) unaltered. Therefore, (2.25) is also referred to as a state-space *realization*.

Transfer functions characterizing acoustic systems are often found to be of non-rational form. Consider, for example, the impedance of a closed-end duct, which can be written as $\mathcal{Z}(\omega) = -\mathrm{i}\cot(kL)$. Evidently, this transfer function has an infinite number of poles and, therefore, represents an infinite-dimensional system. A corresponding time-domain model would need to have an infinite number of states. Typically, infinite-dimensional systems arise whenever the input–output relation originates from a partial differential equation, whereas finite-dimensional representations result from systems of ordinary differential equations (which is what (2.25) is). Converting a non-rational transfer function to the time-domain form (2.25) is then only approximately possible by truncating it to a finite-dimensional state space. This can be done, for example, by using a Padé approximant (a rational approximation) of F around $\omega = 0$. Generally, this will be accurate only up to a certain frequency $\omega_{\max}$, but on the other hand, we are not interested in the high-frequency dynamics. In the following, we will denote the approximation of a non-rational

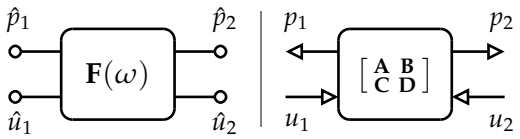

Figure 2.3: A 2×2 network element relating pressure and particle velocity on two sides of a subsystem. Frequency-domain transfer matrix (left) and time-domain state-space model (right).

transfer function by a finite-dimensional state-space system as

$$\left[\begin{smallmatrix}\mathbf{A} & \mathbf{B}\\ \mathbf{C} & \mathbf{D}\end{smallmatrix}\right] \overset{\mathrm{i}\omega}{\approx} F(\omega), \qquad \text{for } \omega < \omega_{\max}. \tag{2.27}$$

We will use this notation also for the identification of state-space models from frequency-response data, which is the topic of the next paragraph.

Identification

Submodels – network elements – of a thermoacoustic system are often not amenable to analytical modeling. In this case, there is no direct way of obtaining a transfer function or a state-space model. One possible remedy is to determine the frequency response of the element under investigation by experimental or numerical means. The subsystem is fed with an identification signal, containing the relevant frequencies, and subsequent spectral analysis of input and output signals then yields the frequency response. The latter is identical with the transfer function for a discrete set of real frequencies, but there is no direct possibility to infer the response at complex-valued frequencies or derive a time-domain representation. This is a system identification matter. There are various approaches to this task with numerous different algorithms (see, e.g., Ljung 1999). For our purpose, the identification of acoustic and thermoacoustic systems, we found the routine developed by Gustavsen & Semlyen (1999) to work quite well.

2.5.2 Network models

A low-order model of a thermoacoustic system is a collection – or a network – of submodels, each of which represents a different component of the entire configuration, with connections between geometrically adjacent entities. The individual submodels are mostly linear and represented in frequency domain by transfer matrices or in time domain by state-space systems. Such a submodel relates the system variables on different sides of the element. This technique is particularly efficient in purely plane-wave systems, where at an interface between two elements, only two acoustic variables, pressure and axial particle velocity, for instance, need to be coupled. Such an element is shown schematically in Fig. 2.3.

Combination of two submodels of this type that are represented by transfer matrices is a straightforward task. If $[\hat{p}_2\ \hat{u}_2]^T = \mathbf{F}\,[\hat{p}_1\ \hat{u}_1]^T$ and $[\hat{p}_3\ \hat{u}_3]^T = \mathbf{G}\,[\hat{p}_2\ \hat{u}_2]^T$, then it is easily inferred that $[\hat{p}_3\ \hat{u}_3]^T = \mathbf{GF}\,[\hat{p}_1\ \hat{u}_1]^T$. In the case of a time-domain representation of the elements, deriving the combined model is not as straightforward, but can be done by means of elementary matrix-algebraic operations on the state-space matrices of the individual submodels (see, e.g., Zhou et al. 1996). As Fig. 2.3 indicates, causality has to be taken into account when working in the time domain (see also discussions by Polifke & Gentemann 2003). This is not a problem for frequency-domain calculations, in which input and output variables can be interchanged as necessary.

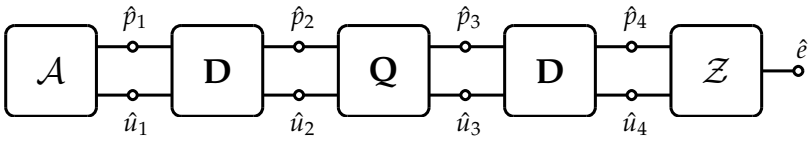

Figure 2.4: An example of a simple frequency-domain network with two boundary conditions, two ducts, one heat source, and an external input $\hat{e}$ at the downstream end

One powerful advantage of this approach is that the elements of a network model can be determined by different means. If the process inside the element is too difficult to model by theoretical means only, the transfer matrix can be considered as a black box fed with purely experimental or numerical data (Cremer 1971; Polifke et al. 2001*b*). A similar procedure is used extensively for muffler design (Munjal 1987); however, system instability is typically not an issue in this application.

An example of a simple network in frequency-domain representation is shown in Fig. 2.4. This system consists of two boundary conditions, two ducts, and a heat source. An external input, $\hat{e}$, is located at the downstream end. As mentioned above, it is possible to combine two or more elements into one. Combination of $\mathcal{A}$ and **D**, for instance, results in one scalar-valued transfer function that represents the boundary condition immediately upstream of the heat source **Q** by relating $\hat{u}_2$ to $\hat{p}_2$ or vice versa.

2.5.3 Linear stability

Coupling the transfer matrices of all elements in an appropriate way results in a representation for the complete system. If no external forcing is present, i.e., $\hat{e} = 0$, this representation takes the form of a homogeneous linear system

$$\boldsymbol{\mathcal{S}}(\omega)\hat{\boldsymbol{v}} = 0, \tag{2.28}$$

where $\boldsymbol{\mathcal{S}}$ is the system matrix, containing the transfer matrices of all the network elements and the boundary conditions, and $\hat{\boldsymbol{v}}$ is a vector of the acoustic variables at the element connections. For the network in Fig. 2.4, the system matrix takes the form

$$\boldsymbol{\mathcal{S}} = \begin{bmatrix} \mathcal{A} & -1 & 0 & 0 & 0 & 0 & 0 & 0 \\ D_{11} & D_{12} & -1 & 0 & 0 & 0 & 0 & 0 \\ D_{21} & D_{22} & 0 & -1 & 0 & 0 & 0 & 0 \\ 0 & 0 & Q_{11} & Q_{12} & -1 & 0 & 0 & 0 \\ 0 & 0 & Q_{21} & Q_{22} & 0 & -1 & 0 & 0 \\ 0 & 0 & 0 & 0 & D_{11} & D_{12} & -1 & 0 \\ 0 & 0 & 0 & 0 & D_{21} & D_{22} & 0 & -1 \\ 0 & 0 & 0 & 0 & 0 & 0 & -1 & \mathcal{Z} \end{bmatrix}, \tag{2.29}$$

and the associated vector of acoustic variables is given by

$$\hat{\boldsymbol{v}} = [\hat{p}_1 \;\; \hat{u}_1 \;\; \hat{p}_2 \;\; \hat{u}_2 \;\; \hat{p}_3 \;\; \hat{u}_3 \;\; \hat{p}_4 \;\; \hat{u}_4]^T. \tag{2.30}$$

It is important to note that (2.28) does not constitute a matrix eigenvalue problem. The *system eigenvalues* ω appear in possibly every element of $\boldsymbol{\mathcal{S}}$ in a complex algebraic way.

Non-trivial solutions of (2.28) require the dispersion relation

$$\det \boldsymbol{\mathcal{S}}(\omega) = 0 \tag{2.31}$$

to be satisfied. This equation determines the system eigenvalues. Since the transfer matrices of typical network elements have a non-trivial frequency dependence, Eq. (2.31) is, already for simple systems, a highly transcendental function in ω, which needs to be solved numerically. In general, the eigenfrequencies are complex, real and imaginary part corresponding to frequency of oscillation and to negative growth rate, respectively. Hence, linear stability of a system can be determined in this way.

Assessing linear stability from a state-space description of the individual elements (Eq. (2.25)) of a network can proceed in a similar manner. If the system is homogeneous and all elements are connected in an appropriate way, the state-space representation of the complete system will simply be of the form (Schuermans et al. 2003)

$$\dot{\boldsymbol{x}} = \mathbf{A}\boldsymbol{x}, \tag{2.32}$$

where $\mathbf{A}$ is a composition of the state-space matrices of the individual elements and $\boldsymbol{x}$ represents the internal dynamics of the system. Then stability is easily assessed on the basis of the eigenvalues of $\mathbf{A}$. As pointed out by Schuermans et al. (2003), computing linear stability from a state-space description is a straightforward task because even if the state dimension is high, (2.32) is only a matrix eigenvalue problem and can be solved with standard methods. In contrast, the solution of Eq. (2.31) is always an iterative procedure with the risk that not all eigenvalues are found. On the other hand, to arrive at (2.32), we already made the assumption that all elements in the network can be represented in a finite-dimensional state space. As mentioned above, this will, in general, not be true for acoustic systems and therefore requires artificial truncation to finite order. In this sense, the frequency-domain dispersion relation is exact, whereas (2.32) is only an approximation. However, in the low-frequency regime, in which we are interested, the difference of the results is often found to be numerically indistinguishable.

Merk (1957*a*) appears to have been the first to essentially apply a frequency-domain type of analysis to determine the stability of thermoacoustic systems (the classical Rijke tube, Merk 1957*b*, and a case with a laminar premixed flame, Merk 1958). The approach has been proven to be enormously useful to predict and analyze linear instability in thermoacoustic systems, evidence of which can be found in the numerous publications on the application of this method and variants of it (see, e.g., Bohn & Deuker 1993; Dowling 1995; Heckl 1988; Kopitz et al. 2005; Matveev & Culick 2003; Paschereit et al. 2001; Sattelmayer & Polifke 2003). Nowadays, network codes are a standard tool in most gas turbine companies (see, e.g., Krebs et al. 2005; Paschereit et al. 2005).

2.5.4 Forced response

A network model can also be used to compute the system response to external or internal forcing by sources which are independent of the system's acoustic variables. These sources can, for instance, correspond to acoustic excitation with loudspeakers or to the stochastic forcing through turbulent fluctuations in the flame. The source terms enter the network

model as inhomogeneous terms, and (2.28) takes the form

$$\boldsymbol{\mathcal{S}}(\omega)\hat{\boldsymbol{v}} = \hat{\boldsymbol{s}}, \tag{2.33}$$

where $\hat{\boldsymbol{s}}$ is the vector of source terms (which may be a function of frequency). Assuming that the element at the right end in Fig. 2.4 can be modeled as $\hat{p}_4 = \mathcal{Z}\hat{v}_4 + \mathcal{G}\hat{e}$, the corresponding source vector is $\hat{\boldsymbol{s}} = [0 \ \dots \ 0 \ \ -\mathcal{G}\hat{e}]^T$ with $\boldsymbol{\mathcal{S}}$ and $\hat{\boldsymbol{v}}$ unaltered.

The system response in terms of the acoustic variable $\hat{\boldsymbol{v}}$ to the forcing $\hat{\boldsymbol{s}}$ can then be obtained from (2.33) by inversion. This procedure is, however, only valid to compute the system's linear response to forcing in the stable case. If the system is unstable, the self-excited contribution will eventually overwhelm the response part and nonlinear effects render the linearized description invalid.

2.5.5 Limit cycle estimation

Although network models are primarily frequency-domain tools, the nonlinearity in the flame response can be incorporated in an approximate way. This procedure is based on the describing function of the flame, which essentially is an amplitude-dependent transfer function (Dowling 1997; Huang 2001; Noiray et al. 2008). It represents the (complex) fundamental harmonic gain of the heat release oscillation, $\mathcal{F}(\omega, a)$, when forced with a sinusoidal velocity disturbance of amplitude a. Using the describing function in combination with the linear acoustic representation in a network model then amounts to a first order harmonic balance analysis and yields, in analogy to (2.31), the amplitude-dependent dispersion relation

$$\det \boldsymbol{\mathcal{S}}(\omega, a) = 0. \tag{2.34}$$

From Eq. (2.34), the eigenvalues can be determined as a function of the oscillation amplitude. In case of a linearly unstable system, there is a positive growth rate for zero a. Due to the saturation character of the flame response, the growth rate decreases with increasing oscillation amplitude. For a certain amplitude, the growth rate vanishes, and this gives a good estimate of the actual limit cycle.

2.6 Feedback control

Feedback – or closed-loop – control is a tremendously large field, and we clearly do not attempt to give an adequate introduction to this topic. On the other hand, we apply feedback control at various instances in this thesis – an illustration of the basic principle, therefore, seems appropriate. Although not the only purpose of feedback control, we use it exclusively to stabilize a thermoacoustic system that, without the control action, exhibits high-amplitude oscillations.

Consider the schematic set-up in Fig. 2.5. The upper block represents the thermoacoustic system we intend to control. We assume that without control, the system is unstable so that essentially all system variables either tend to grow exponentially from the steady state or are already in a limit cycle. There is no access to complete information about the system state, but we measure one or more sensor signals p, which we assume to be, to some degree, representative of the system dynamics. In case of thermoacoustic instabilities, such a

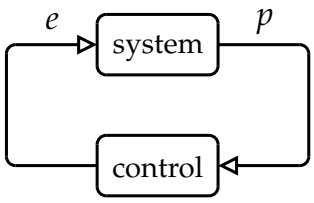

Figure 2.5: Schematic set-up of a feedback control scheme. p and e correspond to sensor and actuation signals, respectively.

signal could be the acoustic pressure or a surrogate measurement for the fluctuating heat release rate. The sensor signal p is passed to the controller which processes it in a suitable way to obtain one or more actuation commands e. These actuation commands are then fed back to the system by some actuation device(s). Typically, the actuators used for combustion instability control are loudspeakers or fuel valves. Given that the actuation mechanism has enough bandwidth and authority (which is often an issue), the objective of the control law is to map p to e such that the system is stabilized.

Applications of feedback control to systems exhibiting thermoacoustic instabilities are abundant. Reviews can be found in the work by Candel (2002, 1992), McManus et al. (1993), and Dowling & Morgans (2005); a comprehensive discussion of previous work is given in Chapter 9 of a recent compilation by Culick (2006). Despite the large number of applications on the laboratory and single-burner engine scale, active control for the suppression of combustion instabilities has not yet transitioned to industry practice. The only application in a full-scale engine over a considerable period of time (about three years) is summarized by Hermann & Hoffmann (2005). Passive approaches, based on the implementation of acoustic dampers or utilizing modifications of the burner and the fuel injector system, are still preferred by the industry, mainly because of their robustness.

In addition to permitting a combustor to operate at nominally unstable conditions, active control can also be used as a means to study the instability in a manner not possible without control. It allows to investigate the growth of thermoacoustic oscillations starting from the unstable steady state (Poinsot et al. 1989, 1992) so that, for example, the growth rates can be determined (Bothien et al. 2010; Culick 2006, Chapter 9).

As pointed out by Culick (2006, Chapter 9), it is also important to realize that the suppression of thermoacoustic oscillations by feedback control is fundamentally different from noise control by anti-sound (see, e.g., Ffowcs Williams 1984). In the latter, the sound emitted from a source (the primary field) is simply canceled by a secondary sound field, which is generated by the control action, so as to minimize the superposition of the two at a certain receiver location. However, since the source is independent of the acoustic field, there is no influence of the actuation on the source. This is in strong contrast to the control of combustion instabilities. Here, the control action affects the source of sound (the flame) such that it is eventually reduced to a minimum level. Accordingly, the highest actuation amplitudes are required to stabilize the system from the limit-cycle oscillation. Once this is achieved, comparatively small forcing amplitudes are sufficient to maintain stability.

Part I

Analysis, Modeling, and Control of Thermoacoustic Instabilities in a Model Combustor

We investigate different aspects of thermoacoustic instabilities and their control in an atmospheric combustor test-rig with a swirl-stabilized burner. After a brief description of the experimental arrangement (Chapter 3), including the basic measurement and actuation devices, we investigate the feasibility of multiple actuator control in Chapter 4. Although control of combustion instabilities was realized in a multitude of test-rig studies, application to full-scale configurations is extremely scarce. One major factor impeding the transition to industry has been identified as the lack of suitable actuators. We show that in combining different actuation mechanisms, higher flexibility and efficiency can be achieved. The control scheme we employ is an empirical, fixed-parameter controller that has to be tuned manually and only works at the design operating conditions. This drawback is removed in Chapter 5 by extending the controller with an adaptive loop. This scheme is shown to be capable of finding the optimal control parameters, corresponding to minimum pulsations, and track them during a transient variation of the operating conditions. Thermoacoustic oscillations are not necessarily a result of a linearly unstable steady state. So-called triggered – or subcritical – instabilities have been known for quite some time to frequently occur in rocket engines, but are less well investigated in gas turbine related combustors. In Chapter 6, we perform a detailed experimental study of subcritical thermoacoustic instabilities in the test-rig combustor, where we observe triggered oscillations and a hysteretic dependence of the pulsation amplitude on the operating parameters. Based on the experimentally determined combustor acoustics, we set up a low-order model that shows good agreement with the measurements.

Chapter 3

Test-rig Set-up and Measurement Equipment

3.1 Experimental facility

The experimental facility for the work presented in this part is an atmospheric combustor test-rig with a premixed swirl-stabilized burner. A schematic drawing of the arrangement is shown in Fig. 3.1. The actual test-rig is mounted vertically in the laboratory. Combustion air enters through an electrical preheater in order to generate higher inlet temperatures, which are more typical for gas turbine operation. The length of the upstream plenum is about 940 mm. This extent is necessary to allow for the installation of an acoustic excitation device and multiple axially distributed microphones.

The air is mixed with natural gas in the burner and generates an aerodynamically stabilized flame downstream of the dump plane. Diameters of the ducts up- and downstream of the burner are 110 and 200 mm, respectively. Based on these duct diameters (without accounting for the pilot lance, with a cross-sectional area of 11.34 cm^2), the area expansion ratio at the dump plane is 3.3. With respect to the free burner exit area, the expansion ratio is 5.8. The first 300 mm downstream of the dump plane are made of silica glass to allow for optical access to the complete reaction zone in the visible and the UV range. A 317 mm long radiation-cooled flame tube is attached to the silica cylinder. The set-up downstream of the flame tube is modular. In most cases, we use a measurement tube, equipped with axially distributed microphones, and an excitation segment with two speakers mounted perpendicularly to the main axis, as shown in Fig. 3.1. With this set-up, the complete length of the downstream part (from burner dump plane to exhaust outlet) is 1840 mm. This is quite long but has the advantage that there is enough space to accommodate a favorable spacing of the microphone array and the acoustic excitation. In addition to that, the quarter-wave mode associated with this length was found to couple with the unsteady heat release in the flame in large regions of the operating range, which is favorable for investigating thermoacoustic instabilities and their control.

Different orifice plates can be mounted at the exhaust exit plane to realize various degrees of reflectivity and thereby change the stability characteristics at fixed operating conditions. The two extreme cases for the exit boundary condition are (i) the open end with

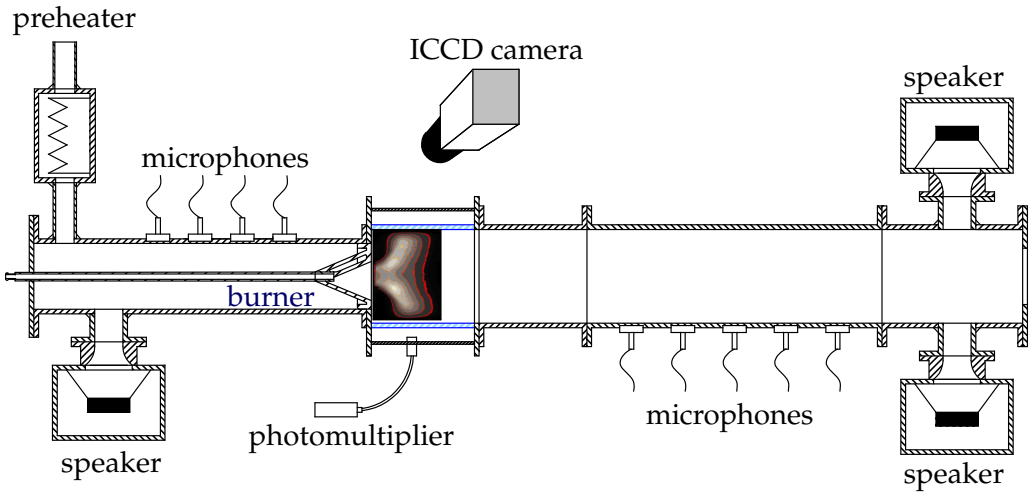

Figure 3.1: Combustor test-rig with basic measurement instrumentation. The airflow enters through the preheater; gas is injected inside the burner.

a reflection coefficient magnitude close to unity and (ii) an orifice with an area contraction designed to generate an anechoic termination as proposed by Bechert (1980).

The test-rig is equipped with a swirl-stabilized burner that is based on the EV-design by ABB (Döbbeling et al. 1994; Sattelmayer et al. 1992), developed for lean premixed operation.[1] The burner has a free exit area of 53.8 cm^2 and can be operated with thermal powers up to 250 kW. Figure 3.2 shows a detailed sketch of the burner. Two half-cones are shifted in such a way that the air is forced to enter the cone circumferentially through two slots. The resulting swirling airflow generates a recirculation zone along the centerline at the burner outlet associated with vortex breakdown (Leibovich 1978; Lucca-Negro & O'Doherty 2001). There is also an outer recirculation zone in the corner of the dump plane. The main fuel is injected through 64 small holes (0.7 mm diameter), which are distributed equidistantly along the two slots. Swirling air and main fuel are well but not perfectly mixed before reaching the flame. The fuel–air mixture is thus technically premixed, which means that the composition is premixed but cannot be considered homogeneous (in a spatial as well as in a temporal sense). For additional flame stabilization, pilot fuel can be injected at the cone apex. The pilot injector can also be used as an actuation port for control of combustion instabilities (Chapter 4). The flame is ignited with a high-voltage spark-electrode mounted in direction of the flow at the burner dump plane.

3.2 Measurement devices, sensors, and actuators

The combustor test-rig is equipped with measurement devices that allow for an extensive characterization of combustion instabilities associated with low frequency acoustic modes. In addition to several mean state indicators, such as Coriolis mass flow meters, thermocouples, and static pressure probes, a number of dynamic sensors can be used for time-resolved measurements. In particular, the test-rig was specifically designed to allow for a decomposition of the plane acoustic mode up- and downstream of burner and flame.

[1] The design of the EV-burner was a key step for the successful realization of lean premixed combustion technology and significant NOx reduction within ABB/ALSTOM (Döbbeling et al. 2007; Eroglu et al. 2009).

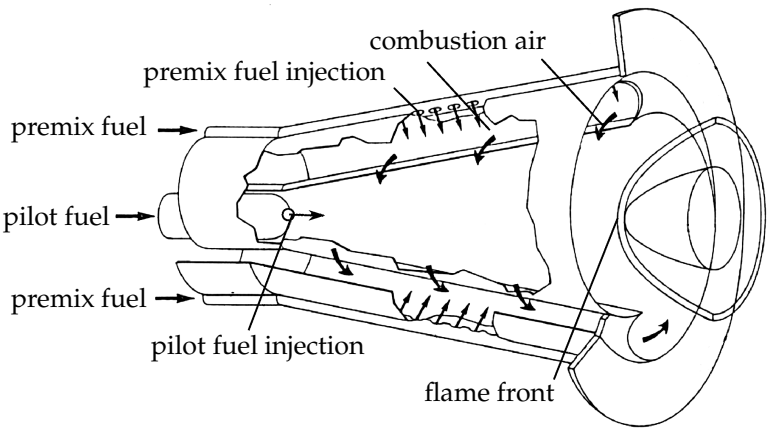

Figure 3.2: Schematic representation of the swirl-stabilized burner; adapted from Sattelmayer et al. (1992)

Multiple axially distributed microphone arrays are located in the up- and downstream ducts. We use G.R.A.S. type 40BP quarter-inch microphones that measure sound pressures up to 170 dB and have a flat response to about 10 kHz. The microphones are mounted to the duct walls in water-cooled probe holders. These impose a constant temperature of 60 °C to ensure proper working conditions. The microphones can be operated at up to 150 °C, but the preamplifiers (type 26AC) are restricted to below 60 °C and indeed fail to work properly at higher temperatures. Lower temperatures, on the other hand, cannot be used due to water condensation at the microphone membranes. Although carefully designed to minimize the impact on the signal frequency response, the probe holders have an effect on the measured pressure transfer function. Potentially, the deviation from the wall pressure is not identical for all probe holders, and that is why all microphones are calibrated in combination with their individual probe holders at operating temperature. The main purpose of the microphone arrays is the identification of the plane mode of the acoustic field (see Appendix A).

Photomultipliers (Hamamatsu H5784) with optical band-pass filters are used to characterize the unsteady heat release from the flame. A measure of this unsteady quantity is extremely important when investigating thermoacoustic processes because it carries crucial information about the interaction of the acoustic field with the flame. Measuring the unsteady heat release rate in a flame directly is hardly possible. Therefore, surrogate observables have to be used that can be related to the reaction source term. The chemiluminescence of excited intermediate reaction species, typically radicals, can be used as such a marker (Haber et al. 2000; Higgins et al. 2001; Najm et al. 1998). Candidates are the OH, CH, and C_2 radicals with peak wavelengths around 308, 431, and 512 nm, respectively. The photomultipliers with appropriate band-pass filters are connected to the test-rig via fiber optic probes (see Fig. 3.1) such that they collect light from almost the complete reaction zone. Accordingly, the photomultiplier signals are related to the integral heat release rate.

An intensified CCD camera with band-pass filters corresponding to light emission from excited OH-radicals is used to obtain information on the spatial distribution of the heat

release rate. The acquired images correspond to line-of-sight integrated intensity distributions of the flame's chemiluminescence. The camera has a sampling rate of only a few Hertz, so direct time-resolved measurements are not possible. Yet, by using a pressure or photomultiplier measurement as a reference signal, phase-averaged information can be obtained by means of a sorting algorithm in a post-processing step. The algorithm we use for this task is based on the instantaneous phase of the reference signal computed by means of the Hilbert transform (similar to that proposed by Güthe & Schuermans 2007).

Although the chemiluminescence intensity is related to the heat release rate, it is difficult to infer quantitative information from these measurements. The main problem is the dependence of the chemiluminescence intensity on other relevant and possibly non-homogeneous and unsteady properties, such as temperature, equivalence ratio, strain rate, turbulence intensity, mixture non-uniformity, etc. (Ayoola et al. 2006; Lauer & Sattelmayer 2010). These effects can be expected to be stronger in spatially resolved chemiluminescence measurements than for the integral assessment by means of a photomultiplier. However, in the following sections, we will frequently refer to the chemiluminescence signals as heat release rate, keeping in mind that this does not hold true in a perfectly quantitative sense.

A set of loudspeakers is mounted perpendicularly to the up- and downstream ducts (see Fig. 3.1). These allow for an excitation of the acoustic field necessary for the measurement of the up- and downstream traveling components of the plane acoustic mode. This is important, for instance, to determine the acoustic boundary conditions of the test-rig. In addition to that, the speakers are also used as actuators in a closed-loop mode in combination with a microphone signal and a controller to suppress thermoacoustic instabilities (Chapters 4 and 5). The speakers are flanged to the main ducts via water-cooled sidetubes. The speaker casings are additionally purged with air to prevent hot gas ingestion. This is also necessary on the upstream side because the air can be preheated up to 600 K.

As a second actuation mechanism, secondary fuel can be injected through the pilot lance. This is done either with proportional or on–off valves. Put simply, the secondary fuel generates a modulation of the heat release rate which can be used to cancel the effect of the primary interaction and thereby suppress the instability. The on–off valve, used in Chapter 4 for instability control, is a commercially available gaseous-fuel injector from the automotive industry.

A digital signal processing board DSP1103 (dSPACE) was used for all feedback control experiments. In principle, sound pressure as well as chemiluminescence measurements can be used as feedback signals. There are, however, two main disadvantages in using a photomultiplier signal: (i) compared to the microphones, the chemiluminescence measurement usually has a significantly higher broadband noise floor, and (ii) it contains strong frequency components at the harmonics of the fundamental oscillation (which do not need to be controlled). These two drawbacks can, in principle, be circumvented by using a narrow band-pass filter. On the other hand, this will introduce a steep phase-lag across the passband, which is undesirable in case the frequency of oscillation changes (Yu et al. 1998). Therefore, only microphones were used as feedback signals, rendering the use of a band-pass filter unnecessary.

Chapter 4

Feedback Control with Multiple Actuators

In this chapter, we apply feedback control to mitigate thermoacoustic instabilities in the combustor test-rig. Two actuation mechanisms will be used: pilot fuel injection and acoustic forcing. Modulated secondary fuel injection was recognized to be efficient in active control applications for the suppression of combustion instabilities (Hathout et al. 2002; Paschereit et al. 1999*b*). This is due to the high control authority that is provided by the chemical energy of the fuel. Adding small amounts of pilot fuel to a premixed flame strongly affects the combustion process. As pointed out by Hermann & Hoffmann (2005), modulated pilot fuel does not only represent an additional heat source, but it also affects the main premixed flame. Paschereit et al. (1999*b*) studied the influence of secondary fuel on premixed combustion with constant and modulated pilot fuel injection. This type of control is also applicable to full-scale engines (Seume et al. 1998). The effect of a modulation of the main premix fuel on instability suppression was investigated by McManus et al. (2004).

Besides secondary fuel injection, acoustic actuators have also proven their ability to control combustion instabilities effectively (Lang et al. 1987), while simultaneously reducing NOx emissions (Paschereit & Gutmark 2002). The advantage of acoustic actuators over a modulation of the fuel flow is their ability to generate high-bandwidth, proportional pressure signals in the combustion system with virtually no time lag. The main drawback, clearly, is their inapplicability at high power densities and elevated pressures.

Dowling & Morgans (2005) pointed out that one of the main issues in active control of combustion instabilities is to find suitable actuators. The implementation of loudspeakers, for example, is certainly not feasible for practical applications due to the relatively large amount of power needed to stabilize an unstable full-scale combustion system (Fung et al. 1991). According to Auer et al. (2005), the high variance of actuator control effectiveness reported in the literature can be partly traced back to the fact that the specific actuators do not supply the required modulation amplitudes. This underlines the difficulties in providing appropriate actuators. For this reason, a combination of secondary fuel injection and acoustic actuation is proposed here. The idea is to first control the unstable mode using modulated secondary fuel injection with its high control authority. After a stabilization has been achieved, acoustic actuation is employed to *maintain* stability. This approach

is possible because the highest actuation amplitudes are typically required only to stabilize the system from the limit-cycle oscillation. Once this is achieved, stability can be maintained with significantly smaller forcing amplitudes. The combination of different actuators could therefore result in a higher variety of applicable forcing mechanisms. Previous work utilizing multiple actuators for combustion instability control is scarce, but it is mentioned to be a possible way to increase control effectiveness in a recent review by Huang & Yang (2009).

In the following sections, experimental results from the test-rig described in the previous chapter are presented. The combustor is operated at an equivalence ratio of 0.56 and a thermal power of 90 kW with an air inlet temperature of 250 °C. A digital closed-loop control system is used to suppress the instabilities in the combustor. Unsteady combustor pressure and chemiluminescence data is recorded, and the pressure signal is used to drive the controllers. Control is achieved by means of two different mechanisms: secondary pilot fuel is injected through an on–off valve, and a loudspeaker, mounted upstream of the burner (Fig. 3.1), is used as an acoustic actuator. The speaker module for the downstream part was not mounted in this study. The two actuation methods are tested separately and simultaneously. The main control parameters investigated are (i) the time delay between the measured pressure signal and the control signal, (ii) the control gain in the case of acoustic actuation, and (iii) the secondary fuel mass flow when using the pilot valve.

In case of secondary fuel flow modulation, actuation at subharmonics of the main instability frequency is also applied. Subharmonic excitation reduces the need for high-frequency actuation and extends actuator lifetime. It was shown previously that subharmonic control of combustion oscillations can be effective. Jones et al. (1999) used subharmonic secondary fuel injection to suppress instabilities in a laboratory-scale dump combustor. They reported an attenuation of the noise level by 22 dB when modulating the secondary fuel with the fourth subharmonic of the dominant frequency of oscillation.

4.1 Uncontrolled instability

The operating conditions chosen for the investigations corresponded to a strong instability with high pulsation amplitudes. Although control efficiency at fixed operating conditions cannot be considered representative for all possible sets of parameter combinations, the conditions chosen here were the most demanding in terms of actuator authority.

Figure 4.1 displays spectra of normalized chemiluminescence and pressure signals acquired at unstable conditions. A PDF of the combustor pressure fluctuations for the unstable case is also shown. The strongest peaks in the pressure and chemiluminescence spectra, at 99 Hz, correspond to the quarter-wave mode in the combustion-chamber–exhaust-tube part. The pressure signal primarily consists of a single frequency component, whereas the heat release exhibits several harmonics, some of which have a magnitude close to that of the fundamental. This is consistent with the assumption that nonlinear acoustic effects are weak, even on the limit cycle, and the pulsation amplitude is determined by the nonlinear response of the flame (Dowling 1997).

Ensemble-averaged perturbation cycles of pressure and chemiluminescence, computed from 3200 realizations, are shown in Fig. 4.2. The pressure is essentially a pure harmonic,

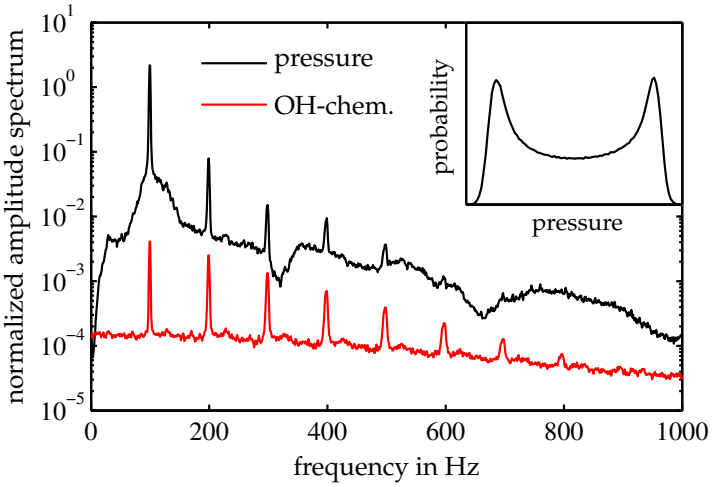

Figure 4.1: Normalized amplitude spectra of pressure and OH-chemiluminescence intensity fluctuations in the combustion chamber at unstable conditions. The inset shows a PDF of the measured pressure signal.

whereas the signal from the chemiluminescence intensity, representing the oscillations of the heat release rate, is strongly distorted by higher harmonic components. In particular, the maximum deviation from the mean is much larger than the minimum one. This is a typical characteristic of nonlinear heat release oscillations. One simple explanation for the lower bound of the fluctuations is that the total heat release rate obviously cannot become negative (Dowling 1997). Clearly, the Rayleigh index (product of unsteady pressure and heat release rate) is positive over the dominant part of the cycle, especially where the heat release peaks. This indicates a distinct net production of acoustic energy in the reaction zone (cf. Section 2.2.2).

It is important to note that the system is indeed in a limit-cycling state. In combustion systems operating closer to the stoichiometric case, high oscillation amplitudes may also be generated by a stable noise-driven system (Banaszuk et al. 1999*a*). Yet, the obvious nonlinearity in the heat release signal and the double-hump PDF of the pressure fluctuations (Fig. 4.1) are well-defined features of a limit-cycling system, as explained in Section 2.4.

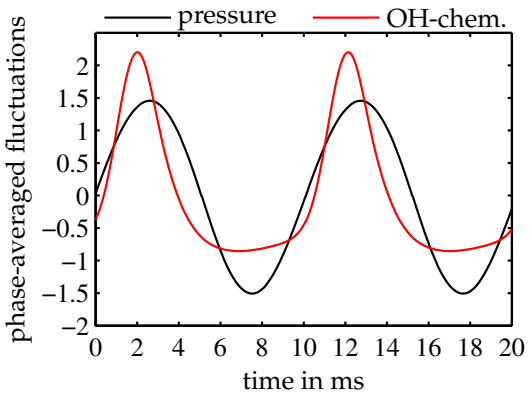

Figure 4.2: Ensemble averages of normalized pressure and OH-chemiluminescence intensity at unstable conditions. The Rayleigh criterion is clearly satisfied.

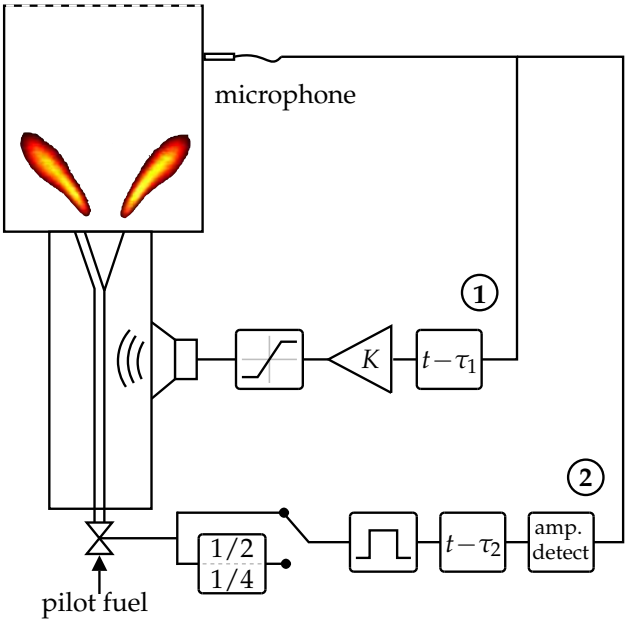

Figure 4.3: Schematic representation of the control set-up. The pressure is fed back to the loudspeaker via adjustable gain and delay. A static saturation in the speaker loop (①) is used in Section 4.2.3 to mimic insufficient actuation authority. The pilot-fuel loop (②) includes an additional amplitude detector and a trigger generater; the latter can also generate trigger signals at subharmonics.

4.2 Phase-shift control with actuators working in individual and combined mode

Figure 4.3 shows a schematic representation of the control set-up used for this investigation. The unsteady combustor pressure is fed back to generate the control command for the actuators. The microphone signal is phase-shifted and amplified in the first feedback loop. This signal is used to drive the upstream loudspeaker, which modulates the air mass flow into the burner and, in addition, directly excites sound waves. In the second loop, the control board generates a trigger pulse of the phase-shifted input signal. The triggered valve modulates the secondary pilot fuel, which results in a heat release rate fluctuation. Moreover, it is possible to set up a threshold value. If the pressure oscillations remain below this limit, the pilot valve does not open. This can save pilot fuel without adversely affecting the suppression of heavy oscillations (Jones et al. 1999).

The input signal to the controller was not band-pass filtered. Using a narrow band-pass filter on the input signal can help to track the dominant mode. However, such a filter generally induces a rapid phase change across the passband and adversely affects the control scheme if the frequency of oscillation is shifted by the controller, as mentioned in Section 3.2. This mechanism can cause an intermittent loss of control (Yu et al. 1998). As will be shown in Section 4.2.2, the dominant frequency was indeed affected by the phase-shift controller due to the so-called peak-splitting phenomenon (Banaszuk et al. 1999*a*; Hibshman et al. 1999). If noise levels are too high so that the unfiltered pressure is inadequate as a feedback signal, a Kalman filter, which identifies frequency, amplitude, and phase of the coherent oscillation, should be used (Gelb 1974). In the present work, the pressure oscillations provided a clear signal so that no further conditioning was necessary.

4.2.1 Pulsed pilot fuel

The influence of time delay and secondary fuel mass flow on the performance of the pilot fuel injector to suppress thermoacoustic instabilities was studied. The pilot actuator

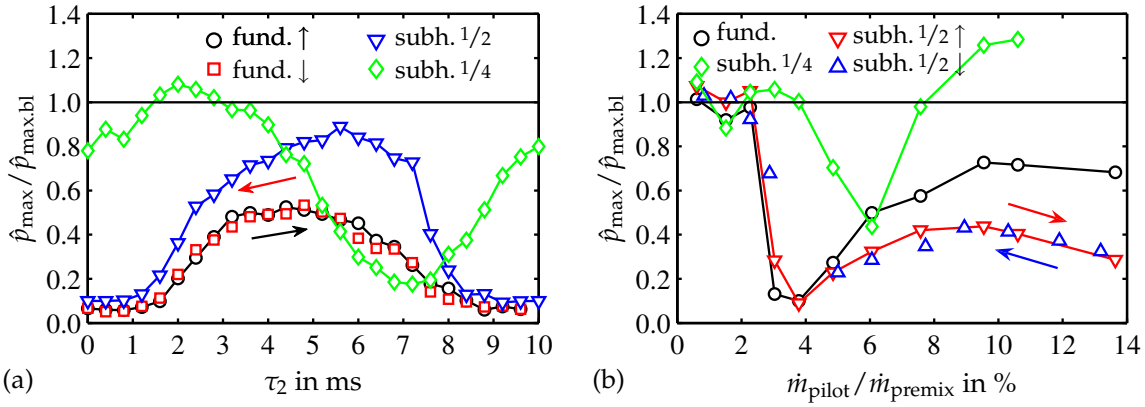

Figure 4.4: Spectral peak amplitudes of pressure oscillations vs. (a) time delay and (b) mean pilot-to-premix fuel mass flow ratio. Results are normalized to uncontrolled baseline conditions. Feedback at fundamental frequency (circles and squares), subharmonic of order 1/2 (triangles), and subharmonic of order 1/4 (diamonds). Additional labels ↑ and ↓ indicate increasing and decreasing control parameter, respectively.

was operated in three modes: generation of secondary fuel pulses at the frequency of the dominant mode and at the subharmonics of order 1/2 and 1/4. In case of actuation at the instability frequency, the valve command is a pulse train with its fundamental frequency equal to that of the measured pressure oscillation. For subharmonic control, the fundamental frequency of the pulse train is only one-half or one-quarter of that.

In Fig. 4.4(a), the normalized peak amplitude (with respect to baseline conditions) is plotted as a function of control time delay. The pilot-to-premix fuel mass flow ratio was held fixed at 3.5 %. This corresponds to the maximum suppression obtained from a pilot mass flow variation (see Fig. 4.4(b)). Maintaining a constant mean pilot mass flow had the effect of doubling and quadrupling the fuel pulse per stroke in case of control at the subharmonics of order 1/2 and 1/4, respectively. For all tests (modulation at fundamental and subharmonics), the time delay was first set to zero and then increased in steps of 0.4 ms to a maximum time delay of 10 ms. This maximum time delay corresponds to a phase shift of 360° with respect to the dominant oscillation frequency at baseline conditions. For fuel injection at the fundamental, the suppression performance was also investigated for decreasing time delay (from 10 ms to 0 ms) to check for hysteresis in the oscillation amplitude.

Regarding the influence of the time delay (Fig. 4.4(a)), a strong suppression of the oscillations is observed when operating at the fundamental of the instability frequency with a time delay of 0–1.2 ms or 8.8–10 ms. At $\tau_2 = 0.8$ ms, an attenuation of more than 20 dB in spectral peak amplitude is achieved. The minimum suppression was observed for a 4.4 ms time delay. However, the peak amplitude is still well below baseline conditions (6 dB). For fuel modulation at the subharmonic of order 1/2, the change of peak amplitude with time delay is similar to modulation at the fundamental. The suppression is slightly lower, achieving a maximum attenuation of 20 dB at a time delay of 9.2 ms. In the case of control at the subharmonic of order 1/4, the maximum attenuation is again lower than for that of order 1/2. However, the corresponding curve appears to be shifted by about −4 ms from the result we would expect when considering excitation at the fundamental and at the subharmonic of order 1/2. To rule out a measurement error, the corresponding

experiments were repeated; identical results were obtained. We also note that only for fuel modulation at the subharmonic of order 1/4, noise amplification is obtained in a narrow time-delay interval between 1.6 and 2.8 ms. Comparison of the data sets for increasing and decreasing control parameters shows no indication of hysteresis for the variation of the phase shift.

Feedback at the fundamental and at the subharmonic of order 1/2 results in smaller oscillations than in the baseline case for all phase shifts. Using the subharmonic of order 1/4 tends to amplify the instability slightly, but in a narrow phase interval only. Typically we would expect that generating additional heat release in phase with the pressure fluctuations should result in higher oscillation amplitudes. On the other hand, by pulsing the secondary fuel, we also introduce a mean pilot mass flow, which may already have a stabilizing effect (Paschereit et al. 1999*b*).

Figure 4.4(b) shows the normalized peak amplitude as a function of the pilot-to-premix fuel mass flow ratio at zero time delay. Generally, the mean fuel mass flow was increased during the measurements. Only for the second series, the mass flow was first set to its maximum and then reduced to check again for hysteresis. The data clearly shows that a threshold of the secondary fuel flow must be exceeded (here at least 3 % of the premix fuel mass flow) to achieve significant instability suppression. For all feedback modes, an optimal pilot-to-premix fuel ratio is found within the interval investigated. For control at the fundamental and at the subharmonic of order 1/2, the optimal pilot-to-premix mass flow ratio is 3.8 %; for the subharmonic of order 1/4, it is 6 %. As for the variation of the time delay, no hysteresis is found for the variation of the pilot fuel mass flow.

The fact that the optimal phase shift for modulation at the subharmonic of order 1/4 differs considerably from those found for modulation at the fundamental frequency and at the second subharmonic is not fully understood. We performed detailed investigations on the actuator response and found a rather complex behavior. From integral heat release measurements in the combustion chamber, it became evident that the fuel pulses strongly dispersed and partially overlapped. One reason for this is probably the relatively large distance between the valve and the fuel injection location (approximately 2 m). In addition to that, the fuel was not injected directly into the premixed flame but at the cone apex of the burner (see Fig. 3.2). Before reaching the flame, the fuel pulse was, thus, subject to extensive mixing due to the highly turbulent swirling flow.

It is generally undesirable to use a large amount of pilot fuel. Since the pilot flame burns in diffusion mode, it will increase NOx emissions due to locally higher temperatures. The advantage of high control authority associated with pilot fuel injection is accompanied by the drawback of increased NOx emissions. As Paschereit & Gutmark (2008) have shown, instability control with open-loop pilot fuel forcing can also lead to a reduction of NOx emissions for certain actuation amplitudes and frequencies. Minimizing the pressure oscillations in a technically premixed system improves mixture uniformity. Thus, controlling instabilities with pilot fuel can result in a net decrease in emissions. However, if stabilization can be achieved without or with less pilot fuel, we can expect the NOx emissions to be reduced even further. In the next sections, we therefore explore possibilities of minimizing the amount of pilot fuel necessary for control.

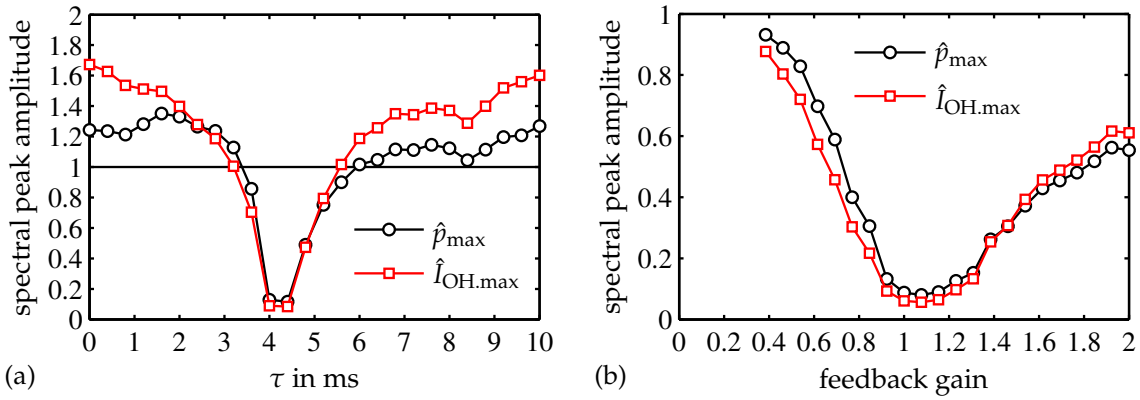

Figure 4.5: Peak amplitude of pressure and heat release perturbations vs. (a) control time delay and (b) feedback gain. Results are normalized to uncontrolled baseline conditions.

4.2.2 Acoustic excitation

Phase-shift control with proportional actuators has essentially two parameters: gain and time delay. These parameters can be tuned manually to yield an optimal suppression of the pressure oscillation amplitude or can be adjusted by an adaptive scheme, as will be done in Chapter 5 (see also, e.g., Schneider et al. 2000 or Murugappan et al. 2000). The latter has the advantage that the controller can compensate for a change in operating conditions. Since, in this study, the operating parameters were fixed, controller gain and delay were set manually. When searching for the best combination of parameters, we assumed that the optimal phase shift (the one that results in minimum peak amplitudes at the instability frequency) was independent of the feedback gain. The latter was then varied at the optimal phase shift to find the minimum pulsation amplitude. Hence, not the complete 2D parameter field was investigated, but only the variation of the time delay at one fixed gain and the variation of the gain for the optimal time delay.

Figure 4.5(a) shows the peak amplitudes of the fluctuating combustor pressure and of the heat release rate as a function of the control time delay. The gain was fixed to its optimal value. All results are normalized with their associated values at uncontrolled conditions. The time-delay interval shown corresponds to 360° in phase with respect to the main frequency of oscillation. Clearly, the range of time delays in which control is effective is rather narrow. The highest sound attenuation is obtained for a time delay of 4.6 ms, which corresponds to a phase shift of approximately 165°. Hence, the loudspeaker actuates in antiphase. Using the optimal phase shift, the amplitude of the dominant mode is reduced by about 20 dB. The overall sound pressure level decreases by only 14 dB (not shown) due to the broadband-noise components, which remain essentially unaffected by this type of control. For the larger part of possible phase shifts, the instability is, in fact, amplified.

The influence of the control gain on instability suppression is shown in Fig. 4.5(b). Here, values of the control gain have been normalized with the one yielding the largest suppression. The time delay was fixed to the optimum, i.e., 4.6 ms. Starting from small values, raising the gain has the effect to rapidly diminish the peak amplitude. After a minimum is attained at the optimal value, a further increase in the gain causes the amplitude of the

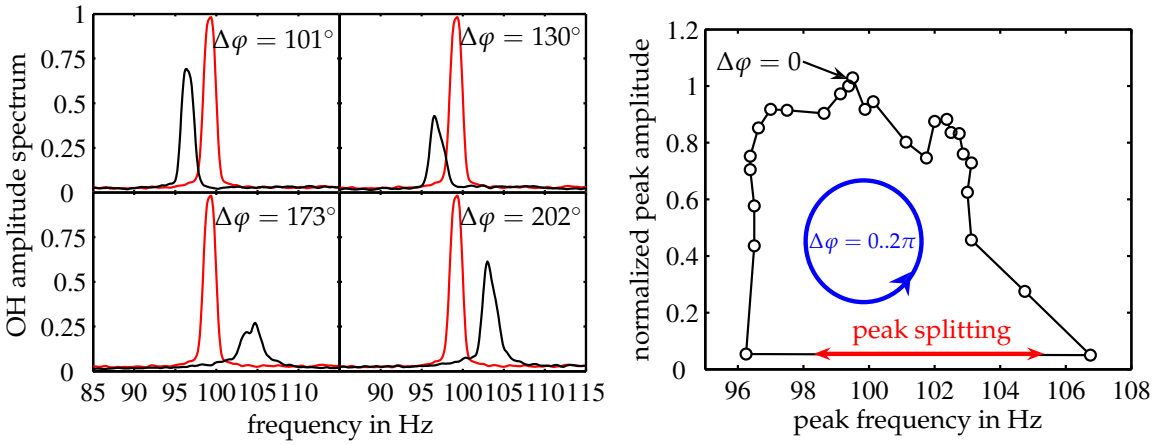

Figure 4.6: Left: OH spectra for different control phase shifts $\Delta\varphi$ (black line). The spectrum at uncontrolled conditions is plotted as reference (red line). Right: OH spectral peak amplitude vs. peak frequency for a full period of the control phase shift.

dominant mode to grow. However, for all values of the gain tested, the pulsations were attenuated compared to the uncontrolled case.

A typical phenomenon encountered when using phase-shift controllers to suppress combustion instabilities is the so-called peak splitting (Banaszuk et al. 1999*a*,*b*; Cohen & Banaszuk 2003; Hibshman et al. 1999). It is interpreted as a limit of achievable performance (Banaszuk et al. 2006). With the action of the phase-shift controller, the frequency of the dominant mode slightly changes. At the optimal phase shift, two peaks are present in the spectrum of the combustor pressure, one slightly shifted to the left and one slightly shifted to the right. Figure 4.6 (left) shows sections of the pressure spectrum for different control phase shifts. Increasing the phase shift from 0° has the effect of shifting the frequency of the dominant mode to lower values in addition to attenuating the amplitude. For phase shifts larger than the optimal value, the frequency of the dominant peak is shifted to the right with respect to the uncontrolled peak. The variation of the peak frequency over the full phase-shift interval is presented in Fig. 4.6 (right). At the lowest peak amplitude (the optimal phase shift), the peak frequency jumps from 96 Hz to 107 Hz. In fact, two peaks are present here: one that is decreasing and one that is increasing in amplitude. Both peaks are equally high at the optimal phase shift. The presence of two peaks in the combustor pressure spectrum is also apparent in Fig. 4.7 in the next section. In case of modulated pilot fuel control, this effect was also observed (not shown).

The peak-splitting phenomenon is not inherent to the controlled combustion process but rather a property of this type of control. Rowley et al. (2006), for example, observed this effect when using feedback control to suppress cavity flow oscillations. In fact, the results they obtained and those in Fig. 4.6 (left) look strikingly alike. As Rowley (2002) points out, cavity oscillations and combustion instabilities are very similar phenomena (limit-cycle oscillations, flow–acoustic interaction, time delay). An explanation for the peak-splitting phenomenon can be given based on the area rule and the sensitivity function of the feedback loop (Banaszuk et al. 1999*b*; Rowley & Williams 2006): for linear time-invariant systems with relative degree (number of transfer function poles minus number of zeros) of two or more, disturbance attenuation over some frequency range is necessarily accompanied by an amplification at other frequencies.

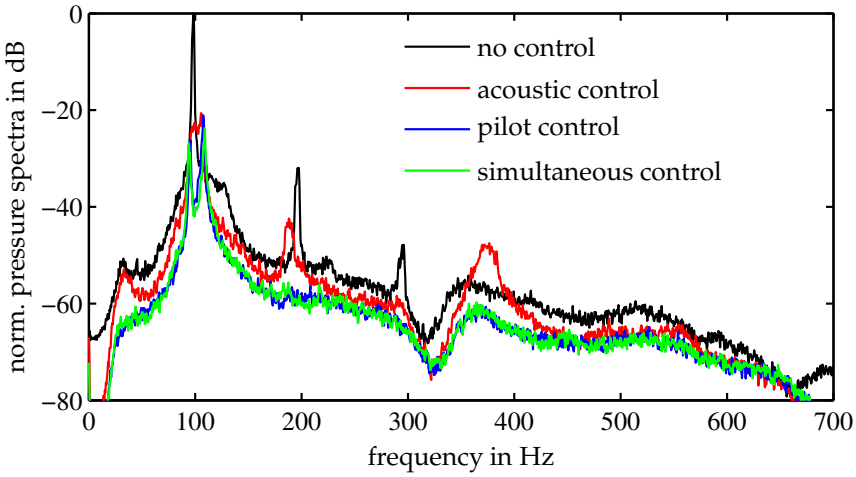

Figure 4.7: Combustor pressure spectra for the cases no control, pilot modulation, acoustic control, and simultaneous control with both actuators. All spectra are normalized with the maximum of the uncontrolled case.

4.2.3 Simultaneous pulsed pilot and acoustic control

As a first test for combined control, both actuators were used simultaneously. The control parameters were set to the optimal values determined in the experiments with only one actuator (Sections 4.2.1 and 4.2.2). Figure 4.7 shows combustor pressure spectra for the uncontrolled case, for control with pilot fuel modulation, for control with acoustic forcing, and for simultaneous control. Compared to the cases in which only one actuator was used to suppress the instability, a simultaneous operation of both actuators resulted in an additional attenuation of 3 dB; hence, a total reduction of 24 dB was achieved. These results were obtained without varying the control parameters in simultaneous mode. Since there are more parameters to tune when using both actuators at the same time, it can be expected that even better results could be obtained.

Purely acoustic forcing is unlikely to have the control authority necessary to suppress thermoacoustic instabilities in practical applications. On the other hand, far less power is required to *maintain* stability. In other words, an acoustic actuator might not have enough authority to suppress an instability initially, but might succeed in retaining the system in a controlled state. To investigate this case, we added artificial saturation to the acoustic control command in terms of a limiter (see Fig. 4.3). This essentially simulates a power limitation of the loudspeaker; the pressure sensor signal is not amplified proportionally but saturates at a predefined limit.

Figure 4.8 presents time traces of the unsteady combustor pressure, the pilot control command, and the acoustic control command. We consider the left frame first. At $t = 6\,\mathrm{s}$, acoustic control is activated, but due to its limited control authority, the pressure oscillations cannot be attenuated significantly. After 18 seconds, pilot control starts, and the pressure amplitude decreases almost immediately. Acoustic control is added again at $t = 23\,\mathrm{s}$, but now, after stopping pilot control, the loudspeaker is able to keep the pressure oscillations at a controlled level for 20 more seconds. However, once heavily perturbed from the controlled state, the acoustic actuator was not able to reattain control due to its limited authority. This process is shown in the right frame of Fig. 4.8. Initially, the system

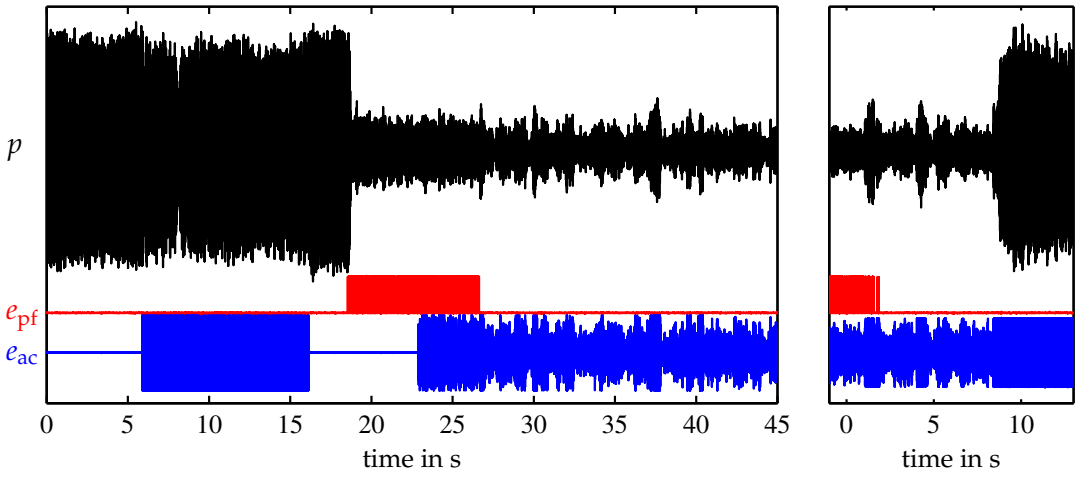

Figure 4.8: Time traces of unsteady combustor pressure p (top), pilot fuel control command e_{pf} (middle), and acoustic control command e_{ac} (bottom). Left: Purely acoustic control cannot suppress the instability but is able to maintain control. Right: Purely acoustic actuation is not able to maintain control.

is maintained in a controlled state using both actuators. After 3 seconds, pilot control is switched off. The acoustic actuator is able to maintain a low level of pressure fluctuations for a period of 9 seconds, but then abruptly loses control.

This drawback could be overcome by enabling the pilot actuator only to inject fuel if a predefined threshold value for the oscillation amplitude is exceeded. If the pressure pulsations fall again below this threshold, no additional pilot fuel is added, and control can be maintained only by actuating with the speaker. Figure 4.9 shows results for this type of control. An existing instability cannot be suppressed by purely acoustic control ($t = 8$–$15\,\mathrm{s}$). Therefore, pilot fuel is injected ($t = 16\,\mathrm{s}$). After eight injection pulses only, the oscillation amplitude decreases significantly, and pilot fuel injection is terminated. Every time the acoustic actuator starts to loose control and the pressure amplitude grows to the threshold value, secondary fuel injection is activated. To show that the loudspeaker is not able to keep the instability suppressed, the threshold is set to infinity at 42 seconds, i.e., no pilot fuel is added irrespective of the oscillation level. After 3 additional seconds, the loudspeaker loses control, and only after resetting the previous threshold (at $t = 48\,\mathrm{s}$), control is reattained. In comparison to the cases presented in Fig. 4.8, a lower saturation value for acoustic actuation was set (effectively putting tighter limits on control authority). Figure 4.9 (bottom curve) shows that this has the effect that the acoustic control is working at its limit most of the time.

4.2.4 Concluding discussion

We used different approaches for suppressing thermoacoustic instabilities based on phase-shifted pressure feedback. The pressure fluctuations in the combustion chamber were fed back to control the actuation mechanisms. Both secondary pilot fuel modulation by an on–off valve and acoustic control with a loudspeaker resulted in an attenuation of the pressure oscillation of approximately 20 dB. The control effectiveness exhibited a strong dependence on phase shift and gain. While the injection of secondary pilot fuel exhibited

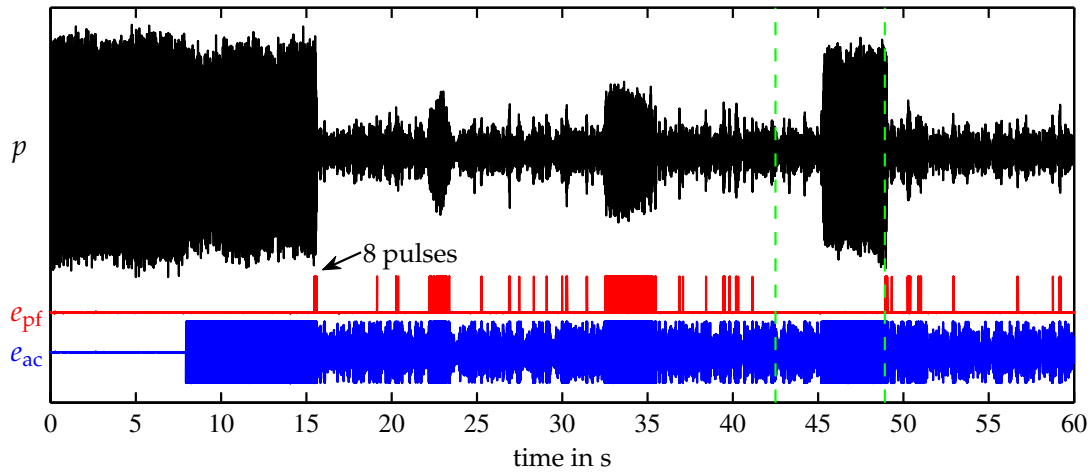

Figure 4.9: Instability control with combined acoustic actuation and pilot fuel injection. Pilot fuel is activated only when the pressure oscillation amplitude exceeds a threshold level. The dashed lines indicate an interval in which the threshold level is set to infinity.

a wide phase range in which the maximum attenuation of the instability was achieved, the best loudspeaker performance was found only in a narrow phase interval. Combining both actuators resulted in a total reduction of 24 dB in the spectral peak amplitude of the combustor pressure.

Contrary to pilot fuel modulation, a loudspeaker does not have the necessary control authority to suppress an instability in practical applications. The favorable performance of pilot fuel modulation, on the other hand, is accompanied by the drawback of increased NOx emissions. Therefore, we investigated a new scheme in which both actuators mutually support each other. In case of limited loudspeaker control authority, an instability could not be suppressed initially by pure acoustic forcing, but a controlled state could be maintained. Heavy perturbations exceeding a critical threshold value were additionally suppressed with secondary fuel injection. This strategy resulted in sufficient suppression of the instability, while consuming a minimum amount of pilot fuel. Finding suitable actuators is one of the major issues still impeding the practical application of combustion instability control (Dowling & Morgans 2005). Combining different actuators with their particular advantages and drawbacks, as introduced in this chapter, allows for more flexible control solutions. Yet, an adverse effect is the increased complexity of the hardware.

Chapter 5

Adaptive Control

As shown in the last chapter, simple empirical controllers can achieve a strong suppression of thermoacoustic instabilities. On the other hand, the control parameters have to be tuned manually, and the optimal values will generally only guarantee stabilization at fixed operating conditions. If the controller is required to handle several operating conditions and even transients, an adaptive algorithm is necessary (Seume et al. 1998). In principle, model-based control techniques allow to design a controller which stabilizes the system without any experimental testing. However, these techniques require a decent model, which accurately captures all of the essential mechanisms participating in the instability – in a quantitative manner. From the results in the preceding chapter, we note that the level of sound attenuation is very sensitive to the control parameters, in particular the control phase (Fig. 4.5(a)). In fact, there may be only a small phase interval in which the oscillation amplitude is decreased and not enhanced. A priori estimation of the optimal control phase needs knowledge on actuator and transport delays, which is hard to obtain with sufficient accuracy for practical configurations (Banaszuk et al. 2000; Johnson et al. 2000). If control is to be applied at varying process conditions, the system model has to capture these effects as well. Apart from very simple configurations, accurately capturing all essential thermoacoustic interaction mechanisms under varying operating conditions lies beyond current modeling capabilities. This suggests the application of an adaptive control scheme that is able to (i) find the pulsation minima in parameter space online and (ii) adapt to changing operating conditions. This type of control scheme is particularly attractive for combustion instabilities because it does not require any modeling effort.

In the last chapter, we already identified a suitable two-parameter control law, which achieved a significant reduction of the pulsation amplitudes. We will now endow this controller with an additional adaptive outer loop that optimizes the parameters according to a suitable cost functional representing control effectiveness. The optimization scheme we chose is called *extremum seeking* (Ariyur & Krstić 2003). It is an adaptive, closed-loop control scheme with the purpose to find an extremum in an unknown field of parameters, possibly changing in time. A major advantage of this type of scheme is that no plant model is required for controller synthesis. The algorithm guarantees closed-loop stability if designed properly (Ariyur & Krstić 2003; Krstić & Wang 2000).

Extremum-seeking control (ESC) has been used earlier for the suppression of combustion instabilities, mainly for phase tuning. Banaszuk et al. (2000, 2004) applied an extremum-seeking scheme to control combustion oscillations in a full-scale liquid-fueled

single-nozzle configuration. They used an extended Kalman filter in combination with a phase-shift controller actuating the main fuel with a proportional valve and an amplitude of about 10 % of the net fuel rate. The control phase was tuned by extremum seeking. It was noted that for the application of the extremum-seeking scheme during varying operating conditions, an adaptive gain would be required. This extension is realized in the present work.

Suppression of combustion oscillations in a swirl-stabilized spray combustor using an extremum-seeking scheme to tune the delay of a phase-shift controller was also investigated by Murugappan et al. (2000). They studied the effect of the extremum-seeking loop parameters on control efficiency and reported a reduction of the pressure oscillations by about 50 % at different operating conditions. Johnson et al. (2000) applied a real-time observer based on a pressure signal to identify the unstable mode in a liquid-fuel combustor. An adaptive scheme, which seems to be quite similar to extremum seeking (Johnson 2006), tuned the control phase based on the observer output. Actuation was achieved via modulated fuel injection. The control scheme attenuated the root-mean-square (RMS) pressure by up to 40 % and tracked the optimal control phase during transients. However, no gain adaptation was implemented in the controller.

Due to the advantage that the extremum-seeking scheme does not need a plant model, this adaptive algorithm was also used for other flow control problems with complex system behavior. Applications include compressor instability control (Ariyur & Krstić 2002; Wang et al. 2000), separation control on a high-lift configuration with pulsed jets (Becker et al. 2007), suppression of cavity oscillations (Kim et al. 2009), and separation control with plasma actuators (Benard et al. 2010).

Other adaptive control schemes for the suppression of combustion instabilities were successfully applied in test-rig experiments by Schuermans (2003), employing a genetic algorithm, and Riley et al. (2004), using a self-tuning regulator.

5.1 Feedback control by extremum seeking

The basic principles of ESC are shortly explained in Section 5.1.1 on the basis of the output minimization of a single-input–single-output system. The extension to a dual-input–single-output plant, as necessary to adapt gain and delay of a phase-shift scheme, and the application to control of thermoacoustic instabilities is described in Section 5.1.2.

5.1.1 Single-input–single-output system

We consider a plant represented by a static nonlinear input–output-map $y = F(v)$ (which is unknown), as shown in Fig. 5.1. In order to find the control input $v^\star$ corresponding to the minimum steady-state system-output $y^\star$, a gradient-based online optimization is performed. The steady-state input–output map $F(v)$ and especially its extremum $y^\star = \min_v y = F(v^\star)$ are unknown and/or changing in time due to variations in the operating conditions.

The initial control input v_0 is superimposed by a small amplitude dithering signal $a \sin \omega_\mathrm{p} t$. If the period of the harmonic perturbation is larger than the largest plant time

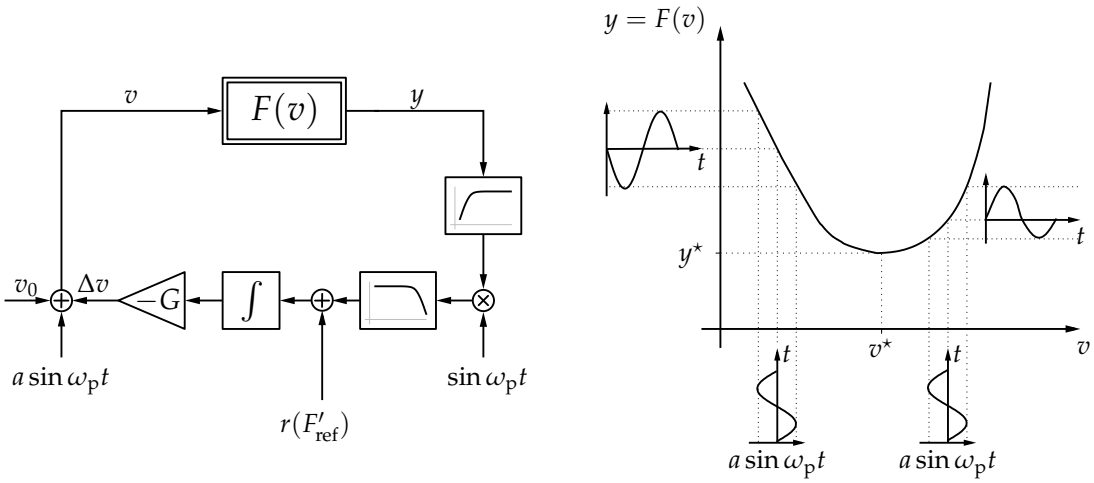

Figure 5.1: Single-input–single-output extremum-seeking feedback scheme for the minimization of the output y under a variation of the input v. Left: block diagram; right: static map $y = F(v)$

constant, an approximately sinusoidal output y will be obtained, initially oscillating around $y_0 = F(v_0)$. To achieve a gradient-based optimization, the output signal is passed through a high-pass filter, which removes the mean value but not the sinusoidal perturbation. Information on the slope of F is obtained by multiplying this zero-mean signal with a sine of the same perturbation frequency (ω_p). The product of the filtered output and the sine signal has a non-zero mean component as long as the minimum is not attained. If the plant is initially right of the minimum ($v > v^\star$), the input and output perturbations are in phase, and hence, the product will be positive. Conversely, an anti-phase relation, giving a negative product, will be an indication of being located to the left of the minimum. The subsequent low-pass filter smoothes the signal.

The term $r(F'_\mathrm{ref})$, that is added to the low-pass output before integration, is only relevant for the slope-seeking variant, which we will discuss in Section 5.2.3. In case of extremum seeking, this term is not necessary, and we set it to zero for the time being. The integrated signal is multiplied by an additional gain $-G$ to yield the parameter update Δv. As long as the output of the low-pass is negative, i.e., the system is located to the left of the minimum, Δv is positive, thus moving the control parameter v closer to the optimum $v^\star$. For a positive output of the low-pass, the opposite is true.

The choice of the design parameters depends on the dynamics of the plant. The overall feedback system has a fast, a medium, and a slow time scale corresponding to the plant dynamics, the periodic perturbation, and the filters in the extremum-seeking scheme, respectively. If the plant behavior varies due to uncertainties, the time scale of the perturbation signal needs to be larger than the slowest plant dynamics. Cut-off frequencies of the high-pass and the low-pass need to be lower than the frequency of the perturbation signal (ω_p). For these reasons, the speed of the algorithm is limited. The permanent harmonic input and output perturbations are another disadvantage. The numerical values of the control parameters, suitable for the control of thermoacoustic instabilities in the test-rig, are summarized in the next section.

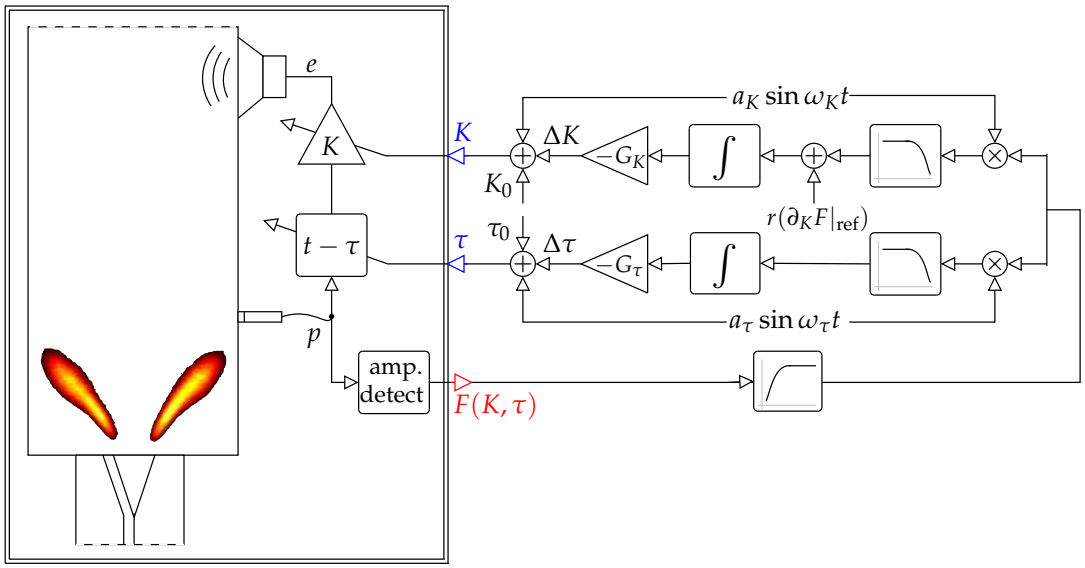

Figure 5.2: Block diagram of a dual-input–single-output extremum-seeking feedback scheme for the minimization of thermoacoustic oscillations. The plant $F(K,\tau)$ is boxed by the double frame. The extremum-seeking scheme optimizes K and τ such that F attains a minimum.

5.1.2 Dual-input–single-output system and application to control of combustion instabilities

In the present study, ESC is applied to find the optimal parameters of a phase-shift controller to suppress combustion instabilities in the test-rig. This type of controller is fed by a pressure signal measured in the combustion chamber (Fig. 5.2). The measured signal is sent through a variable gain and a time-delay block, and the generated command signal e is used to drive the actuator (in this case a woofer). The task of the underlying extremum-seeking scheme is to find the optimal gain $K^\star$ and time delay $\tau^\star$, such that the amplitude of the pressure oscillation is minimized. For the extremum-seeking scheme, the plant comprises the combustion test-rig, the phase-shift controller, and the amplitude detector (Fig. 5.2).

The amplitude detector, which generates the cost functional F from the unsteady pressure, is based on the scheme described by Wang & Krstić (2000), shortly summarized below. We assume the measured pressure signal has approximately the form of a harmonic oscillation $p = \hat{p}\cos(\omega t + \theta)$ with amplitude $\hat{p}$, frequency ω, and phase θ. This signal is squared, resulting in $\hat{p}^2/2\,[\cos(2\omega t + 2\theta) + 1]$ and subsequently low-pass filtered. The cut-off frequency needs to be chosen such that the component with twice the oscillation frequency is sufficiently attenuated, while the DC content, which is half the squared oscillation amplitude, remains unaffected. On the other hand, the cut-off frequency of the low-pass determines the speed of the plant and should, therefore, not be too small. For the extremum-seeking scheme, it is beneficial if the output responds as fast as possible to a variation in the input – ideally in phase. Since the squared pressure is oscillating with twice the instability frequency, the cut-off frequency of the low-pass filter was chosen to be one-tenth of that, which is a trade-off between plant speed and accurate amplitude detection.

Table 5.1: Parameters of the extremum-seeking scheme for control of thermoacoustic instabilities in the combustor test-rig. The perturbation and cut-off frequencies of the filters are given in terms of the reference instability frequency ω.

loop	ω_{lp}	a	ω_{p}	G	ω_{hp}
K	$\omega/200$	0.5	$\omega/20$	$a_K\omega_{\mathrm{p}.K}$	$\omega/2000$
τ	$\omega/2000$	0.5 ms	$\omega/200$	$a_\tau\omega_{\mathrm{p}.\tau}$	

The parameters used in the two-parameter extremum-seeking scheme to control combustion instabilities in the test-rig are summarized in Tab. 5.1. As mentioned in the preceding section, the largest time scale of the plant determines the highest possible perturbation frequency of the input variables. For a proper identification of the gradient, the system output must follow a perturbation at the inlet with a phase shift smaller than $\pi/2$. If the phase shift between input and output perturbation is larger than that, the ESC algorithm is bound to fail. Therefore, the perturbation frequency of the gain loop ($\omega_{\mathrm{p}.K}$) was chosen to be sufficiently smaller than the cut-off frequency of the low-pass filter in the amplitude detector. Since the algorithm must be able to distinguish whether a change in the amplitude $\hat{p}$ resulted from a perturbation in K or τ, the perturbation frequency of the delay loop was set to one-tenth of that of the gain loop. The cut-off frequencies of the low-pass filters in the two extremum-seeking loops were set to one-tenth of the respective perturbation frequency. The perturbation amplitudes a_K and a_τ of the gain and the delay loop were chosen to be 5 % of the whole parameter range of K and τ considered. Integrator gains G were set as functions of perturbation frequency and amplitude. Since the plant output, the pressure amplitude $\hat{p}$, is varying with the two perturbation frequencies, the cut-off frequency of the high-pass filter was chosen to be one-tenth of the lower one ($\omega_{\mathrm{p}.\tau}$). The term $r(\partial_K F|_{\mathrm{ref}})$ in the gain loop is set to zero for extremum seeking. It is only relevant if the cost functional is to attain a non-zero slope, which is discussed in Section 5.2.3.

5.1.3 Control simulation based on a simplified thermoacoustic model system

Before applying ESC based on phase-shift control to the combustor test-rig, the scheme was tested in a model simulation. The system we use is only a toy model and is not supposed to represent the actual test-rig dynamics. It was built just to include the basic features generating a thermoacoustic feedback loop, i.e., unsteady heat-release response to velocity perturbations and reflection of acoustic waves at the system boundaries.

Model set-up

The model system represents an elementary Rijke tube configuration consisting of a compact heat source in a duct with one closed and one open end (Fig. 5.3). The unsteady response of the heat source was described by an n–τ model in combination with a first order low-pass filter (with time constant t_0) as given, for example, by Dowling (1997). For the model simulation, the heat release response was supplemented by a static saturation nonlinearity $\mathcal{S}$ acting on the velocity perturbation to limit the growth of the unstable mode (see, e.g., Schuermans et al. 2003 or Pankiewitz & Sattelmayer 2003). The complete heat

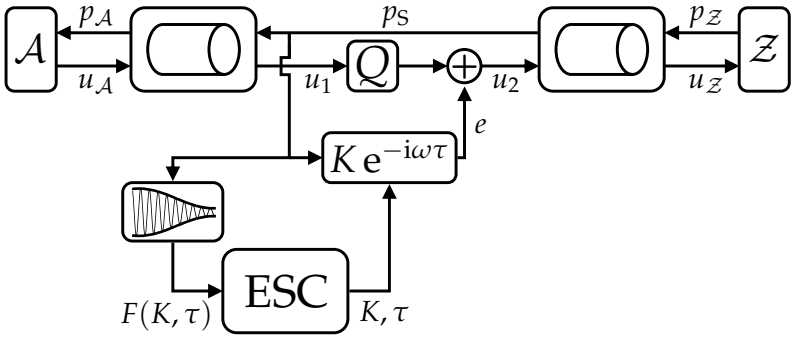

Figure 5.3: Schematic representation of the model for ESC simulation. A heat source Q is placed in a duct with boundary admittance and impedance $\mathcal{A}$ and $\mathcal{Z}$. The pressure at the heat source, p_{s}, is measured and serves as input signal for the amplitude detector and as feedback signal for the phase-shift controller. The extremum-seeking scheme minimizes the amplitude of oscillation by varying the phase-shift control parameters K and τ. Actuation is represented by an additional expansion downstream of the heat source.

release model reads

$$t_0 \frac{\mathrm{d}Q}{\mathrm{d}t} + Q = \mathcal{S}[u_1(t-\tau_{\mathrm{s}})], \tag{5.1}$$

where Q represents the global unsteady heat release, u_1 denotes the velocity perturbation upstream of the heat source, τ_{s} is the source time lag, and the saturation nonlinearity is given by $\mathcal{S}[\cdot] = \tanh[\cdot]$. The velocity perturbation downstream of the heat source, u_2, is obtained by invoking the jump conditions (2.16) across a compact heat source in a simplified form as $u_2 = u_1 + Q$. Since this is only a toy model, based on which we test our two-parameter extremum-seeking scheme, we assume that all dependent variables are non-dimensional.

Time-domain representations for the duct acoustics are set up based on state-space realizations of Padé approximants for the time delays associated with the wave propagation. The input–output models obtained in this way relate the amplitudes of the up- and downstream traveling waves. However, a conversion to acoustic pressure and velocity can be realized by means of elementary state-space algebra (see, e.g., Zhou et al. 1996). For the upstream boundary, a time-domain admittance $\mathcal{A}$, corresponding to a partially reflecting boundary of closed-end type, with a reflection coefficient magnitude of 0.8, is chosen. The downstream impedance $\mathcal{Z}$ is modeled as an unflanged open pipe using Eq. (2.10). The duct lengths and temperatures and the time lag in the heat release model are chosen such that the unstable $\lambda/4$-mode has a frequency close to the one observed in the experimental test-rig ($\approx 90\,\mathrm{Hz}$). The model is supplemented with a phase-shift controller actuating the unsteady heat release. In addition to that, two extremum-seeking loops (labeled ESC in Fig. 5.3) for the control parameters K and τ are added. The instantaneous value of the cost functional $F(K,\tau)$ is proportional to the amplitude of the pressure oscillation at the heat source (p_{s}) and is obtained by using the amplitude detector described in Section 5.1.2.

Control simulation

Simulation results for the suppression of the unstable quarter-wave mode in the model by extremum seeking are shown in Fig. 5.4. After the controller is activated at $t = 0.8\,\mathrm{s}$,

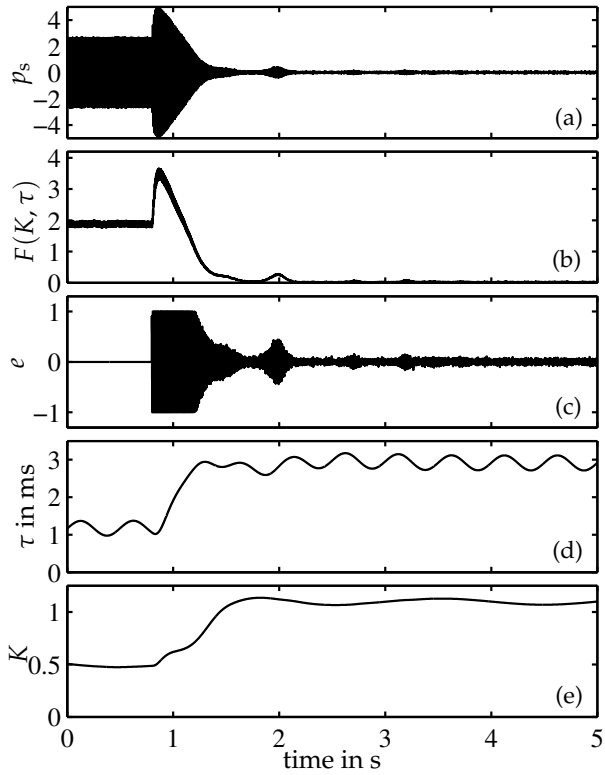

Figure 5.4: Simulation results for two-parameter extremum seeking to stabilize a thermoacoustic model system; (a) pressure at source position, (b) cost functional, (c) control command, (d) control delay, (e) control gain

the pressure amplitude actually increases due to unfavorable initial values of the control parameters (Fig. 5.4 (b)). A few seconds later, the extremum-seeking algorithm has adapted control delay and gain (τ and K in Fig. 5.4 (d) and (e)) such that the pressure oscillation amplitude attains a minimum. The output of the amplitude detector is shown in Fig. 5.4 (b). Essentially, it is an envelope of the unsteady pressure and represents the output of the nonlinear plant in the extremum-seeking loop (see Fig. 5.1). Since control in the model simulation is less demanding in terms of noise and system complexity, less conservative loop parameters were used than those given in Tab. 5.1, which allowed for faster adaptation of control gain and delay.

Control of a transient

The model simulations were further used to study the ability of the extremum-seeking scheme to maintain thermoacoustic stability of the closed-loop system during a change in the operating conditions. Changing the equivalence ratio or the preheat temperature typically results in a variation of the time-lag characterizing the flame response (Lohrmann & Büchner 2004), τ_s in Eq. (5.1). For this case, the simulation was run with control until the optimal control parameters were found by the extremum-seeking scheme. The time delay in the heat release model was then increased from 4 to 8 ms, representing a change in the operating conditions (Fig. 5.5). First, the system is in a controlled state. The control parameters have converged to the values corresponding to maximum suppression of the pressure oscillations. At $t = 2\,\mathrm{s}$, the time lag of the flame model (Eq. (5.1)) is increased

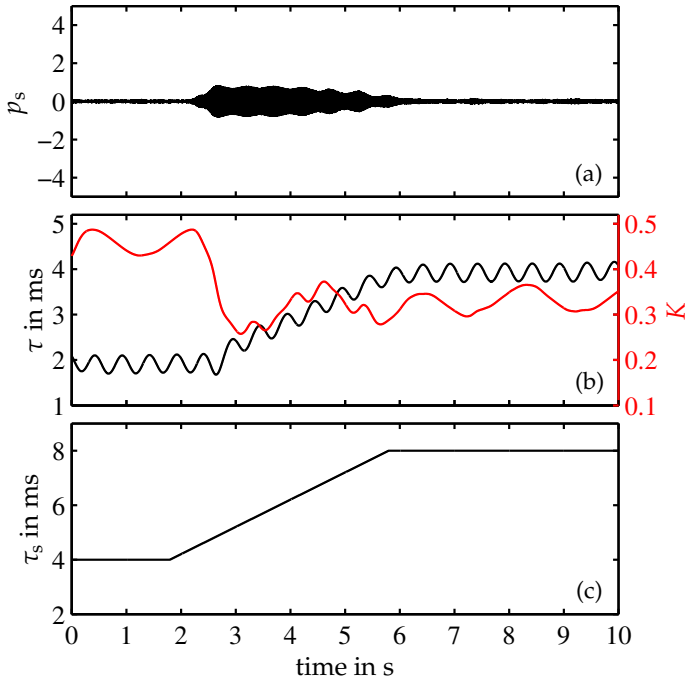

Figure 5.5: ESC simulation during a transient variation of the operating conditions, modeled by a variation of the flame time lag; (a) pressure at source position, (b) control parameters, (c) flame time lag

linearly at a rate of 1 ms/s, rendering the system with the current values of the control parameters unstable. The pressure oscillations increase, but after a few seconds, gain and delay of the phase-shift controller have been adapted so as to successfully suppress the instability for the new flame time lag.

5.2 Experimental application of extremum-seeking control to stabilize thermoacoustic oscillations

5.2.1 System response to phase-shifted acoustic feedback

To assess the efficiency of the extremum-seeking controller in the test-rig, the effect of phase-shifted acoustic feedback on the pressure oscillation amplitude was studied first in an open-loop mode. The parameters of the phase-shift controller were not adapted by the extremum-seeking scheme but were varied manually for the whole relevant range in gain–delay parameter space. The equivalence ratio was set to 0.63 at a thermal power of 105 kW. At these operating conditions, the system exhibited a strong instability at a frequency of 85 Hz, corresponding to a quarter-wave mode in the combustion chamber. In contrast to the test-rig set-up that we used in Chapter 4, the downstream speaker module (see Fig. 3.1) was also mounted for the adaptive control experiments.

A microphone signal in the combustor downstream of the flame was used as the input to the extremum-seeking controller. The effect of phase-shift control on the pressure oscillation for all relevant combinations of gain and delay was investigated by using the

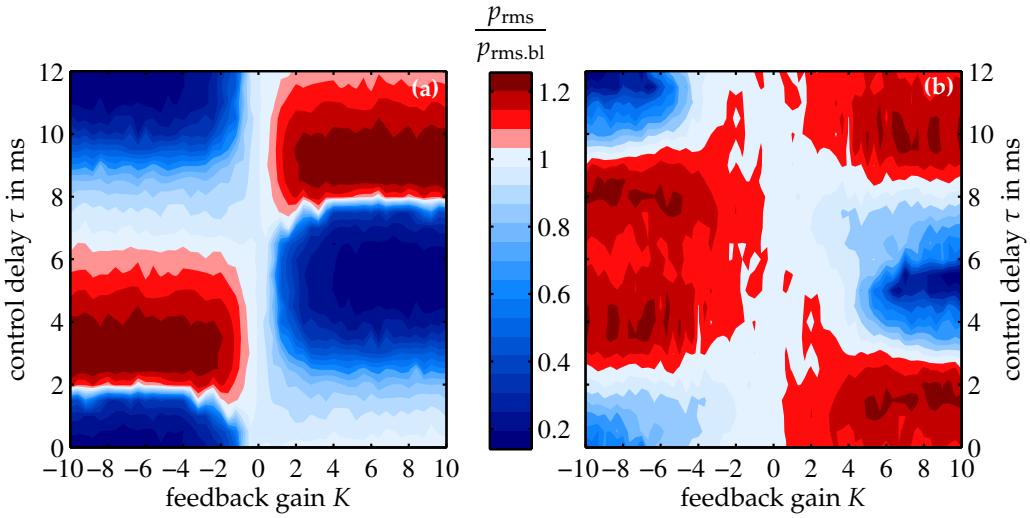

Figure 5.6: Root-mean-square of the acoustic pressure normalized with the uncontrolled case as a function of feedback gain and control delay for (a) downstream actuation and (b) upstream actuation. Blue and red regions correspond to damping and amplification, respectively.

following procedure: at a fixed gain, the control delay was varied from 0 to 12 ms (corresponding to roughly 2π in phase with respect to the oscillation frequency) in steps of 0.5 ms, where for each phase, the pressure response was measured for 2 seconds; the gain was then increased and the delay was repeatedly varied.

Figure 5.6 shows the scaled RMS value of the acoustic pressure, p_{rms}, as a function of feedback gain and control time delay. The RMS values for all K and τ have been normalized with p_{rms} for the baseline case (i.e., without control). Left and right frames in Fig. 5.6 correspond to downstream and upstream acoustic excitation, respectively. The results presented are not identical to the equilibrium map $F(K,\tau)$. The amplitude detector used to extract F from the pressure signal focuses on the main oscillation frequency, whereas p_{rms} takes the whole spectrum into account. Yet, since the pressure spectrum is dominated by the quarter-wave-mode component, the RMS value distribution shown in Fig. 5.6 can be considered to be representative of the static map $F(K,\tau)$.

In the identification of the maps, only positive gains were realized. The RMS values for negative gains are equivalent to those at positive gains with the phase shifted by π (corresponding to a change in control delay of 6 ms). Therefore, the results for negative gains presented in Fig. 5.6 were obtained by mirroring the results for positive gains at the delay axis and shifting them by a delay corresponding to a phase of π.

For both up- and downstream actuation, distinct regions of high and low pressure oscillations exist. In case of downstream actuation (Fig. 5.6 (a)), the minimum pressure fluctuations are obtained for relatively broad delay and gain intervals. For gains larger than 4 and delays between 4.5 and 6 ms, the sound pressure level reduces to only 15 % of the uncontrolled case. This corresponds to an attenuation of 16.5 dB compared to the uncontrolled case. High levels of attenuation also occur for delays close to the optimal values. Maximum amplification of the pressure oscillations is obtained for high gains and a delay ranging from 8.5 to 9.5 ms. At these control parameters, p_{rms} increases by a factor of 1.3. Values of the control delay corresponding to highest attenuation and amplification

are in very close proximity in case of downstream excitation. In fact, there is a rapid transition (at $\tau = 8\,\text{ms}$) from low to high RMS pressures with only small changes in τ. Due to this observation, the possibility of a hysteretic dependence of the oscillation amplitude on the control delay was also considered. Two successive measurements with increasing and decreasing delay for a fixed gain were made. Both results showed exactly the same dependence of the oscillation amplitude on the control delay so that hysteresis could be excluded.

With actuation upstream (Fig. 5.6 (b)), the highest levels of attenuation are obtained only for a very distinct delay of 5.5 ms and a high gain. Here, the RMS pressure is reduced to 30 % of the baseline case. This corresponds to a reduction of 10.5 dB in sound pressure level. In contrast to downstream actuation, two maxima can be observed, one at a time delay around 1.5 ms, the other one at 10 ms. Maximum amplification by a factor of 1.2 is obtained for both maxima with gains larger than 5. For gains smaller than 4, hardly any change in the RMS value can be observed. Hence, an extremum-seeking scheme will not perform well in this region because the driving gradient is absent. Another drawback of using upstream excitation is the local minimum generated by the "valley" between the two domains with maximum amplification. Starting the controller with initial conditions in the valley will not give satisfactory results because the global minimum in sound pressure level cannot be found by this type of gradient-based optimization.

Comparing both excitation cases, we observe that downstream actuation is more effective. There are two resons for this behavior: (i) two woofers are mounted downstream, while there is only one upstream; this obviously results in lower control authority for upstream actuation; (ii) the heat release couples to the $\lambda/4$-mode of the combustor–exhaust-tube combination, and the pressure oscillations are much stronger downstream of burner and flame than upstream; therefore, actuation downstream has a stronger effect on the system dynamics. We also note in Fig. 5.6 that there is more tolerance in setting the control parameters to achieve stabilization when using downstream actuation. These characteristics are specific to the test-rig used in this study and should not be directly translated to other configurations.

At different operating conditions, even higher attenuation or amplification of the oscillation amplitudes could be obtained for the same parameter ranges of control gain and phase. The location of minima and maxima of p_{rms} in control parameter space was also different; however, the qualitative dependence of the oscillation amplitude on the control parameters was always similar.

A meaningful choice for the cost functional $F(G, \tau)$ does not necessarily need to be solely based on the pressure. As an alternative, the chemiluminescence signal could be used as the input to the amplitude detector. Another possibility would be to use the product of pressure and heat release to minimize the (period-averaged, or low-pass filtered) Rayleigh index. To assess whether the chemiluminescence signal or the product of the pressure and the chemiluminescence signals should also be tested in the extremum-seeking scheme, the equilibrium maps corresponding to those shown in Fig. 5.6 were computed for $I_{\text{OH.rms}}$ and the low-pass filtered product of the pressure and the chemiluminescence signals. Since both were qualitatively similar to the p_{rms} map, it was concluded that there would be no significant difference in the performance of the extremum-seeking

scheme in case of the alternative cost functionals. Hence, only the pressure input to the amplitude detector was used.

5.2.2 Combustion instability control by extremum seeking

In this section, we present results from the application of the extremum-seeking scheme based on phase-shifted pressure feedback to the combustor test-rig. The parameters in the extremum-seeking scheme were set as given in Tab. 5.1 with a reference instability frequency of 100 Hz. Actuation was achieved by using the speakers mounted up- or downstream of the flame. The extremum-seeking scheme could be successfully applied in both cases. However, when using upstream excitation, the performance of the scheme was strongly dependent on the initial values of the control parameters due to the unfavorable topology of the equilibrium map $F(K, \tau)$, as shown in Section 5.2.1 (Fig. 5.6 (b)). Since the results obtained were otherwise similar, only the case with downstream actuation is discussed in the following.

Gain–delay trajectories for three different pairs of initial values are presented in Fig. 5.7. With the given initial values of the control parameters, the system state is characterized by high-amplitude pressure pulsations. The controller locates the region with the highest attenuation equally well for all initial control parameters. For certain initial values of K and τ, the algorithm converges to the second minimum, located at a delay around 11 ms and a gain between -5 and -10. Evidently, the two regions characterized by minimum pressure fluctuations have their respective basins of attraction. For clarity, the gain–delay trajectories were low-pass filtered to remove the dithering components.

The variation of the combustor pressure, the control parameters, and the cost functional F with time, during application of the extremum-seeking scheme to suppress an instability is shown in Fig. 5.8. Control is started shortly before $t = 20$ s. Immediately after the control scheme is activated, the oscillation amplitude increases slightly due to unfavorable initial values of the control parameters. Only a few seconds later, the scheme has adapted gain and delay such that the pressure fluctuations decrease below the uncontrolled level. The control delay has not fully converged to a distinct value after 80 s. This is because in case of downstream actuation, the delay interval in which stabilization is achieved is rather broad (see Fig. 5.6 (a)). In this region, $\partial F/\partial \tau$, which drives the variation of τ, is almost zero. In the case of upstream actuation, in which the range of a favorable control delay is much more narrow (Fig. 5.6 (b)), this slow drift was not observed.

Spectra of the acoustic pressure in the combustion chamber for the uncontrolled and the controlled case at two different preheat temperatures are shown in Fig. 5.9. For the non-preheated, uncontrolled case (Fig. 5.9 (a)), there is a distinct peak at 85 Hz, indicating a thermoacoustic instability coupled to the quarter-wave mode of the combustor. At higher preheat temperature (Fig. 5.9 (b)), a qualitatively similar spectrum is obtained, except that the peak frequency is now at 98 Hz, due to the increased speed of sound, and the noise level is slightly higher. Regarding the peak reduction at the instability frequency, a decrease of 26.5 dB is achieved for the non-preheated case. At higher preheat temperature (200 °C), the amplitude of the dominant mode is reduced by almost 40 dB. In Fig. 5.9 (a), the peak-splitting phenomenon, discussed in Section 4.2.2, can be clearly observed in the case of control at non-preheated conditions. This also underlines that the controller has

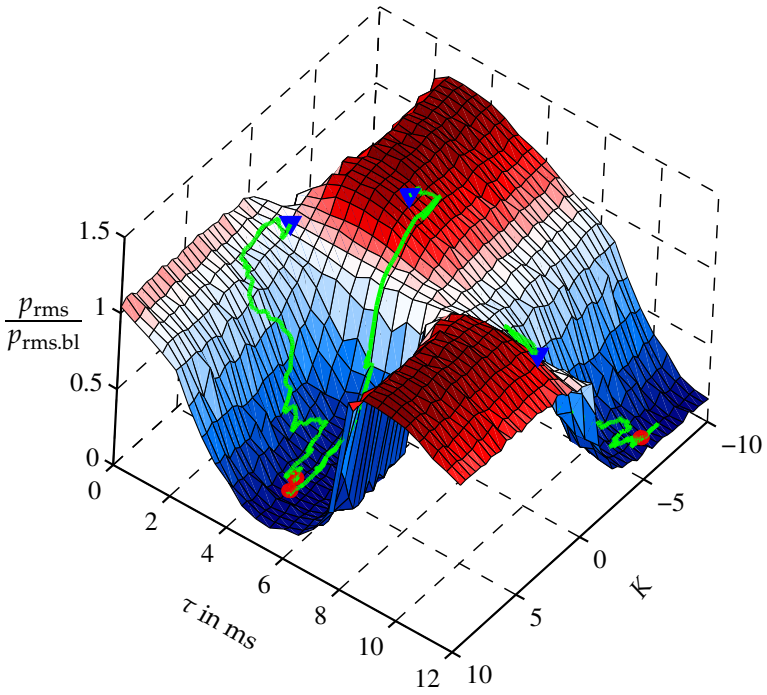

Figure 5.7: Scaled RMS value of the unsteady combustor pressure in gain–delay parameter space. Blue and red areas correspond to attenuation and amplification of the pressure oscillations, respectively. The green curves represent trajectories of the control parameters as set by the extremum-seeking scheme to find the pressure oscillation minimum.

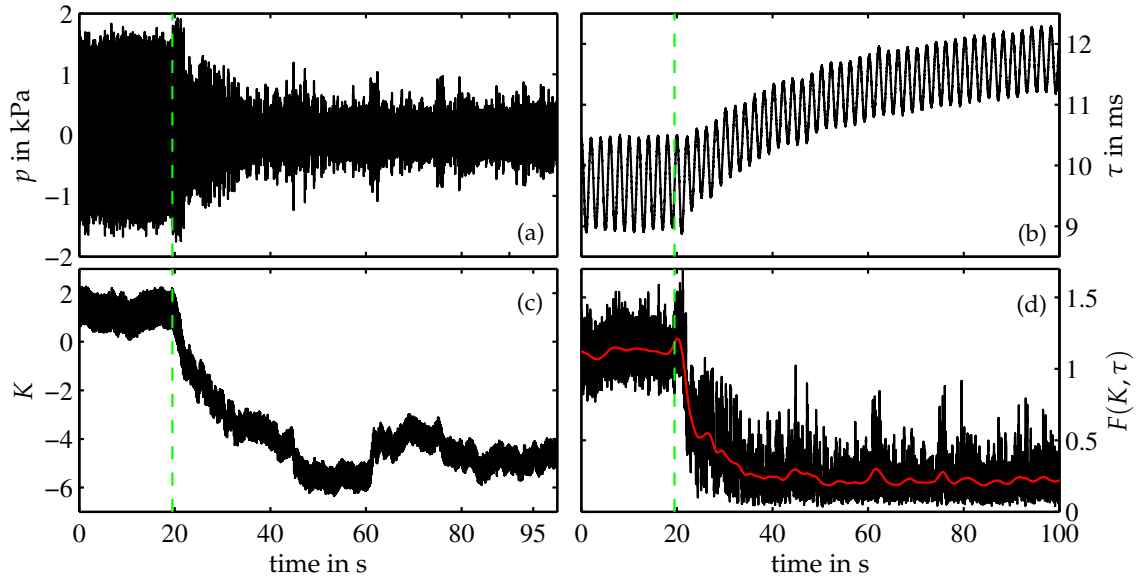

Figure 5.8: Time traces of (a) acoustic pressure, (b) control delay, (c) control gain, and (d) cost functional during extremum-seeking control of a combustion instability. Frame (d) shows in addition a low-pass filtered version of the cost functional. The dashed line marks the activation of control.

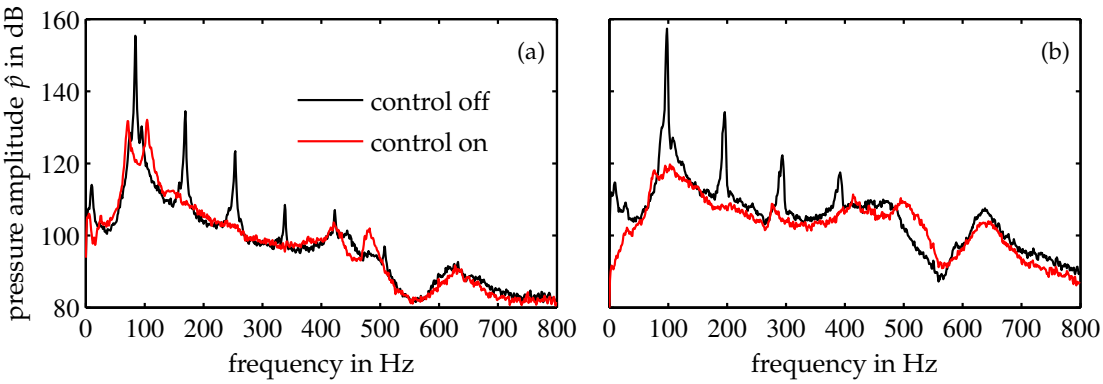

Figure 5.9: Spectra of acoustic pressure for the uncontrolled and the controlled case; (a) preheat temperature 25 °C, (b) preheat temperature 200 °C

indeed converged to the optimal control parameters because the two peaks are of exactly the same height (Fig. 5.9 (a)). Improper phase tuning would result in one of the peaks having a higher magnitude, as shown in Section 4.2.2. In case of a preheat temperature of 200 °C (Fig. 5.9 (b)), no peak splitting can be observed. Also, for both cases, there is a noticeable reduction in low-frequency oscillations around 10 Hz if control is activated. It is interesting to note that, although this low-frequency component is rather small in amplitude, a nonlinear interaction with the main oscillation is visible at the sum of the two frequencies (in the uncontrolled cases).

Control during a transient variation of the preheat temperature

One clear disadvantage of a fixed-parameter control scheme is that its effectiveness is guaranteed only in a narrow neighborhood of its design operating conditions. A properly designed adaptive controller, in contrast, is capable of tracking the optimal control parameters as a function of the operating conditions. Figure 5.10 shows results from the application of the extremum-seeking scheme during a variation of the preheat temperature. The time trace starts with the combustor being in a controlled state at an air inlet temperature of 25 °C. Increasing the preheat temperature to 200 °C makes a change in control delay necessary to maintain system stability. This is successfully tracked by the extremum-seeking scheme. During the transient, a few spikes in the pressure history can be observed, but no instability develops. With the variation in the preheat temperature, the main frequency of oscillation changes by about 20 %.

As can be noted in Fig. 5.10, the control delay has not fully converged to a distinct value, although the preheat temperature is approximately constant after 100 seconds. Again, the reason is that the delay interval in which control is effective is rather broad (see Fig. 5.6).

An interpretation of the effect of downstream control

To gain more insight into the stabilizing effect of phase-shift control with actuation downstream of the flame, and to understand why minimum pressure oscillations correspond to certain values of K and τ, the downstream end (including control) is regarded as an acoustic boundary condition which is affected by the feeback scheme. With sensor and actuator located downstream of the flame, the complete action of a (linear) feedback controller can be interpreted as a change in the effective acoustic boundary condition (Bothien et al.

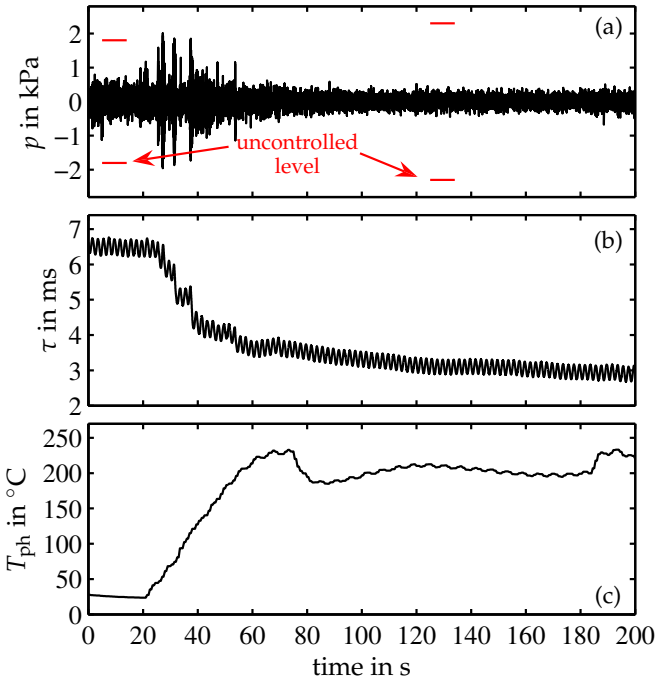

Figure 5.10: Application of ESC during a transient variation of the preheat temperature; (a) combustor pressure, (b) control delay, (c) preheat temperature. The red bars represent the oscillation level for the respective preheat temperature without control.

2008). Consider the downstream speaker module in Fig. 3.1. In terms of the plane-wave response, this part can be modeled as (Bothien et al. 2007)[1]

$$\hat{p} = Z\hat{u} + \mathcal{G}\hat{e}, \tag{5.2}$$

where Z corresponds to the uncontrolled end impedance with reference location at the microphone position, p and u are acoustic pressure and velocity at that position, $\mathcal{G}$ can be interpreted as an actuator transfer function, and e is the control command. Introducing now feedback via the control transfer function $\mathcal{K}(\omega)$ as $\hat{e} = \mathcal{K}\hat{p}$, (5.2) takes the form

$$\hat{p} = Z\hat{u} + \mathcal{G}\mathcal{K}\hat{p}, \tag{5.3}$$

from which we conclude that the control action effectively changes the boundary condition to $Z_{\text{eff}} = Z/(1 - \mathcal{G}\mathcal{K})$. If the uncontrolled impedance and the actuator transfer function are known, the controlled boundary condition Z_{eff} can be calculated as a function of the phase-shift control parameters K and τ (which determine the transfer function $\mathcal{K}$). We shall content ourselves at this point with a direct measurement of the uncontrolled and the controlled boundary conditions. Instead of the impedance we consider the reflection coefficient $\mathcal{R}$, defined as the ratio of the complex amplitudes uniquely associated with the reflected and the incident components of the plane acoustic wave (cf. Section 2.1). The complex wave amplitudes are determined from correlated pressure spectra at four different axial positions, as explained in Appendix A. The reflection coefficient was measured for three cases: (i) no control, preheater off (ii) ESC, preheater off, and (iii) ESC, preheat temperature set to 200 °C.

[1] Bothien et al. (2007) modeled the response of an actuated end element in terms of the Riemann invariants, but an equivalent representation can be given based on the primitive variables p and u.

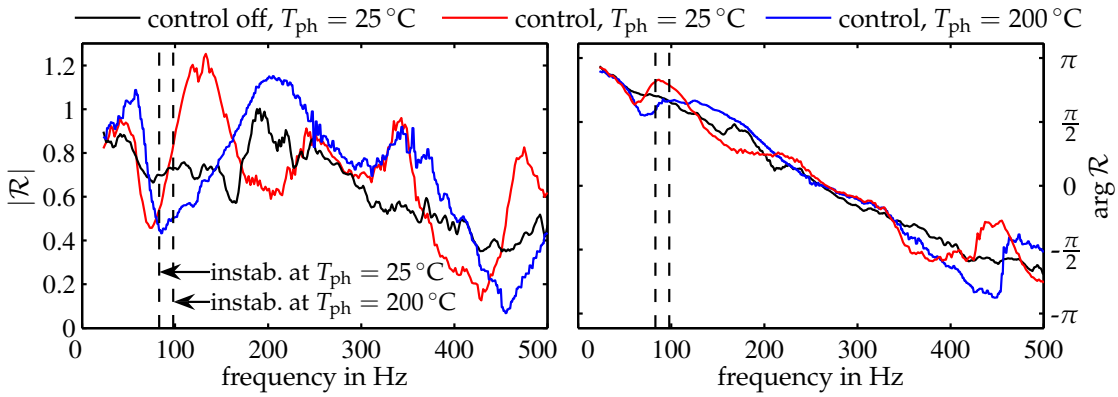

Figure 5.11: Effect of control on the downstream reflection coefficient. The frequency of the unstable mode at the respective preheat temperature T_{ph} is indicated by a dashed vertical line.

The reflection coefficients for the three cases are shown in Fig. 5.11. Additionally, the frequencies of the unstable mode for the cases with and without preheating are indicated by vertical dashed lines. The control scheme reduces the magnitude of the reflection coefficient around the frequency of the unstable quarter-wave mode. In the uncontrolled case, with the preheater turned off, the reflection coefficient has a magnitude of about 0.7 at the unstable frequency. With ESC, this value is reduced by 20 %. This has the effect that more acoustic energy is lost at the system boundary, and the system is stabilized. The impact of control on the reflection coefficient phase, on the other hand, is not significant. We also note that in the controlled cases, the magnitude of $\mathcal{R}$ achieves values larger than unity in certain frequency intervals. This is potentially destabilizing because acoustic waves are amplified at these frequencies; however, in the present case, no resonance condition is met at these frequencies.

5.2.3 Extension to slope seeking

The minimum pressure fluctuations are attained in relatively large gain and delay intervals (Figs. 5.6 and 5.7). Furthermore, no clear minimum in gain dependence can be observed. The larger the gain, the more actuator power is needed. This is certainly not a problem running a laboratory-scale combustor; the loudspeakers have enough authority to stabilize the system. In industrial applications, however, systems with higher thermal power are used. Also, the actuator power should be on the lowest limit necessary for stabilizing the system in order to reduce energy costs and increase actuator lifetime. When using pilot fuel for control, the adverse effect on emissions is another reason for keeping the actuation amplitudes as low as possible. In our control scheme, there are two possible means to reduce the forcing amplitudes: (i) modifying the cost functional F to include a penalty for high actuation amplitudes so that a distinct minimum in gain dependence exists, or (ii) extend the extremum-seeking scheme to slope seeking. The slope-seeking scheme is able to drive the plant output $F(K, \tau)$ to certain target values of the gradient of F, not necessarily zero (Ariyur & Krstić 2003). As shown by Becker et al. (2007), this method can be used to prevent the controller from setting higher forcing amplitudes than necessary to achieve optimal performance.

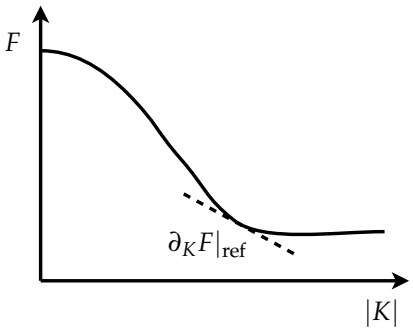

Figure 5.12: Qualitative dependence of the cost functional on the control gain magnitude with reference slope indicated. If K is positive (negative), then $\partial_K F|_{\mathrm{ref}}$ is negative (positive).

We consider again Figs. 5.1 and 5.2 and shortly discuss the role of $r(\partial_K F|_{\mathrm{ref}})$. In the extremum-seeking scheme, this term is zero, but it is essential in case of slope seeking. The desired reference slope, i.e., the one the plant output will be driven to by the algorithm, is related to r by

$$r(F'_{\mathrm{ref}}) = -\frac{a\,\partial_K F|_{\mathrm{ref}}}{2}\,\mathrm{Re}\left(\frac{\mathrm{i}\omega_{\mathrm{p}}}{\mathrm{i}\omega_{\mathrm{p}}+\omega_{\mathrm{hp}}}\right), \tag{5.4}$$

where ω_{hp} is the corner frequency of the high-pass filter in the scheme (see Ariyur & Krstić 2003 for details). In other words, we add the negative target slope to the detected gradient so as to generate an apparent extremum at the desired value. The slope-seeking algorithm is beneficial if no clear extremum is present in the equilibrium map (King et al. 2006) as evident in Fig. 5.7.

One particular problem we are facing here is that the desired target slope does not have a unique sign. For a fixed control delay, 5 ms say, a suitable target slope (with small value) occurs twice – close to the minimum and at amplified oscillation levels (Fig. 5.7). Since the extremum-seeking scheme is designed to find a minimum in the equilibrium map (due to the negative integrator gain $-G$, Fig. 5.2), the slope-seeking extension will cause convergence to the reference slope with the condition that $\partial^2 F/\partial K^2 > 0$. Hence, there is no danger that the control scheme will move towards higher-than-baseline pulsation levels. Yet, the two regions of low oscillation amplitudes (Fig. 5.7) correspond to different signs in the target slope. For $\tau = 5$ ms, the optimal slope, corresponding to low pulsation levels at the lowest gain possible, would be some small negative value. Conversely, at $\tau = 0$ or 11 ms, the optimal slope would be positive. As a result, the desired target slope depends on the initial control parameters and the domains of attraction of the pulsation minima. The details of the equilibrium map have to be considered unknown, but quite generally, we can assume that for some favorable control time delay, the gain dependence qualitatively takes the form shown in Fig. 5.12. Therefore, if K is positive, we need to set a negative target slope to achieve low oscillation amplitudes with minimum control gain. On the other hand, if K is negative, the target slope has to be positive. This can be realized by simply choosing $\partial_K F|_{\mathrm{ref}} = \varepsilon \operatorname{sgn} K$, where ε is some small value.

A comparison from the experimental application of extremum and slope seeking in the combustor test-rig in terms of the low-pass filtered cost functional and control gain is shown in Fig. 5.13. In case of slope seeking, the reference slope has been set to a small positive value so that the scheme converges to the RMS pressure minimum with $K < 0$. This successfully prevents the control scheme from setting control gains much larger than necessary with only a minor loss in control effectiveness.

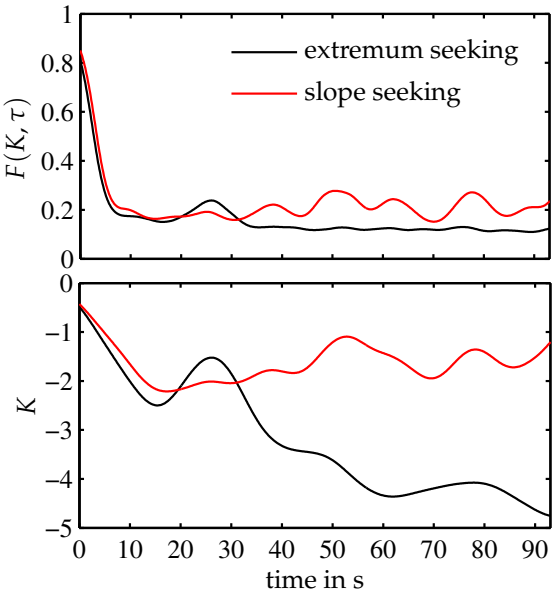

Figure 5.13: Low-pass filtered cost functional (top) and gain for extremum seeking and slope seeking. The extremum-seeking scheme drifts to unnecessarily large gains due to the small gradient at large values of $|K|$, see Fig. 5.7.

5.2.4 Summary

We successfully applied a two-parameter extremum-seeking scheme to control combustion instabilities in a combustor test-rig. Acoustic excitation downstream of the flame was used to suppress a quarter-wave-mode instability at frequencies ranging from 85 to 100 Hz for different preheat temperatures. The reduction of sound pressure levels and peak amplitudes was dependent on the operating conditions and could be as high as a 40 dB reduction in oscillation amplitude. The adaptive scheme was shown to be capable of locating the pulsation minima in control parameter space. We further demonstrated that the extremum-seeking scheme is able to maintain control during a variation of the operating conditions by tracking the optimal control parameters. Acoustic actuation downstream of the flame was interpreted as a change in the effective boundary condition. To prevent the controller from setting unnecessarily high actuation amplitudes, the extremum-seeking scheme was extended to slope seeking.

Chapter 6

Subcritical Thermoacoustic Instabilities

As described in Section 2.5, linear low-order models of thermoacoustic systems have been widely used to predict and analyze system stability. The linear representation suffers from two major drawbacks. The first one is well recognized: the oscillation amplitudes of an unstable system cannot be predicted based on a linear model (Bellows et al. 2007*b*). This may be acceptable if unstable operating regimes are strictly avoided. However, in a number of experimental studies, it has been found that lean premixed combustion systems may also feature subcritical instabilities (e.g., Lieuwen 2002). In this case, two stable equilibrium states exist at fixed operating conditions – one with (low-level) broadband noise and one with high-amplitude, coherent oscillations. From a dynamical systems point of view, the former corresponds to a stable fixed point, the latter to a limit cycle. In this set-up, the linearized system is stable with respect to infinitesimal disturbances, but a transition to the limit-cycling state can be triggered by perturbations of finite amplitude. The existence of two stable equilibrium states may then give rise to hysteresis phenomena when system parameters are varied[1].

Hysteresis related to thermoacoustic instabilities was observed by, e.g., Knoop et al. (1997), Lieuwen (2002), Matveev & Culick (2003), Lepers et al. (2005), and Noiray et al. (2008). In the works cited, fundamentally different experimental configurations were investigated. Lieuwen (2002) used a premixed swirl-stabilized combustor, which is closest to the configuration considered in the present work. He observed a hysteretic dependence of the oscillation amplitude on the combustor inlet velocity. Matveev & Culick (2003) studied thermoacoustic oscillations in a Rijke tube with an electrically heated grid. They found hysteresis over a considerable range of the heater power. Subcritical instabilities in a premixed dump combustor were investigated by Knoop et al. (1997) and Isella et al. (1997). Hysteresis was observed with respect to the equivalence ratio. In the hysteresis region, two stable combustion states were identified, one with a turbulent boundary layer

[1]Subcritical instabilities in liquid- and solid-propellant rocket engines have been known for a long time (see, e.g., Zinn 1970*b*). Combustion instabilities in rocket combustion chambers, however, differ markedly from those encountered in gas turbines when considering the fully nonlinear oscillations. In the former, the fluctuation amplitudes are significantly higher with clear shifts in the mean pressure. As a result, the nonlinearity cannot solely be attributed to the heat release but has to be taken into account in the gas dynamics (i.e., in the acoustic field), too. Yet, it was noted by authors working in this field that the acoustic nonlinearity alone cannot explain the appearance of triggered instabilities (Ananthkrishnan et al. 2005; Wicker et al. 1996).

downstream of the backward facing step, corresponding to weak oscillations, and one showing distinct vortex shedding and high-amplitude pressure pulsations. Moreover, it was demonstrated that a transition from the upper branch (the limit-cycling state) to the lower branch (the fixed point) could be invoked through active control, in this case, short pulses of secondary fuel injected near the dump plane or nitrogen injection in the recirculation zone (see Isella et al. 1997, for the latter).

Most notably, Lepers et al. (2005) found a hysteretic dependence of the oscillation amplitude of an azimuthal mode on the fuel–air mixture ratio in a full-scale annular combustion chamber. This demonstrates that subcritical instabilities cannot be considered to be merely peculiar phenomena observed in single-burner laboratory model combustors under special conditions but can potentially occur in realistic full-scale applications. Noiray et al. (2008) investigated nonlinear thermoacoustic oscillations in an unconfined configuration featuring a collection of laminar Bunsen-type flames anchored on a perforated plate. The plenum length could be varied. By a rigorous nonlinear analysis based on measured flame describing functions, while keeping the acoustic model linear, they were able to explain the mode triggering and hysteresis effects that were observed in the experiment. Bellows & Lieuwen (2004) investigated high-amplitude forcing of a nominally stable premixed swirl-stabilized combustion system. They found a hysteretic dependence of the oscillation amplitude on the excitation amplitude and frequency. The relation between velocity and heat release oscillations was, however, single-valued, supporting the assumption that subcritical phenomena appear as a result of the acoustic feedback and that the flame transfer function itself is continuous.

As a matter of fact, linear stability analysis does not tell the full truth in case of subcritical instabilities. Since the noise level generally has to be considered high in industrial turbulent premixed combustion systems, triggering of limit-cycle oscillations by stochastic system perturbations may occur. Hence, relying solely on linear stability analyses in the design process is precarious. High-amplitude self-sustained oscillations may emerge although the combustion system is linearly stable.

Studying subcritical instabilities is particularly important in the light of recent investigations on non-normal growth in thermoacoustic systems (Balasubramanian & Sujith 2008*a*,*b*). The discovery of non-normal – or non-modal – growth in hydrodynamic stability some 20 years ago (see, e.g., Schmid 2007) led to a major change in the understanding of turbulence transition. Non-normal growth is a consequence of the spectral properties of the linearized operator that describes the evolution of the system state in time. The eigenfunctions of a non-normal operator are in general not orthogonal. As a consequence, linear combinations of the eigenfunctions may grow over a finite period of time, even though all eigenvalues of the operator are stable. This so-called transient growth can be quite large – orders of magnitude, in fact – so that the assumption of small disturbance amplitudes, typical for linear stability analyses, is distinctly violated. Consequently, small initial perturbations may grow to large magnitudes and trigger nonlinear effects, which are not captured by the linearized representation. These nonlinear effects may then promote the disturbance growth. In essence, non-modal growth offers a route to trigger subcritical instabilities although the initial perturbations are small.

6.1 Energy gain–loss balance for super- and subcritical instabilities

The dominant nonlinearity in premixed combustion systems, which determines the high-amplitude behavior of thermoacoustic oscillations, is usually attributed to nonlinear mechanisms in the response of the flame to oscillations in velocity, as explained in Sections 2.3.3 and 2.4. Predicting subcritical phenomena, such as triggering of instabilities and hysteresis in parameter variations, therefore, requires knowledge of the nonlinear flame response. Experimental investigations have shown that the response of lean premixed flames to velocity fluctuations generally tends to saturate at high amplitudes (Balachandran et al. 2005; Bellows et al. 2007*a*; Noiray et al. 2009), but more complex behavior with a non-monotonic decrease in response was also observed (Thumuluru & Lieuwen 2009).

Subcritical instabilities may appear if the dependence of the energy gain due to thermoacoustic processes on the oscillation amplitude is such that the slope varies non-monotonically (Zinn & Lieuwen 2005). In the following, we will assume that the mechanisms responsible for the damping of acoustic energy are completely linear. This will hold only approximately at high oscillation amplitudes, in particular, when the velocity perturbations are of the order of the mean flow and whenever sharp corners, such as area contractions and expansions, are involved (see the discussion in Section 7.4.2). The dominant nonlinearity, causing a saturation in the oscillation amplitude, is however, typically assumed to be solely associated with the heat release response (Dowling 1999; Heckl 1990). For a qualitative discussion, the assumption of linear acoustic processes is, therefore, appropriate.

We consider the case of a supercritical instability first. If the damping is assumed to be linear, the gain/loss–amplitude relationship can be sketched as shown in Fig. 6.1(a). Intersections of the gain and damping curves mark equilibrium solutions. At zero oscillation amplitude, the gain curve has a larger slope than the damping curve; the system is linearly unstable. The fluctuation energy increases, exponentially in the linear regime, until the gain decreases. This is a result of the saturation in the heat release response. Since the increase in energy gain with oscillation amplitude is now smaller than that of the loss, there is an intersection of the two curves at finite amplitude, which represents an equilibrium solution – the limit cycle. Stability can be assessed by perturbing the solution to smaller and larger amplitudes. For lower amplitudes, the gain is larger than the loss so that the fluctuation energy increases again. Perturbations to larger amplitudes cause a higher loss and, therefore, a decrease in acoustic energy.

In case of a subcritical instability (Fig. 6.1(b)), the gain curve has a smaller slope than the damping curve at zero oscillation amplitude so that there is a stable fixed point. In practice, this state may still show well noticeable perturbations in the pressure and heat release fields due to the presence of noise, but no coherent oscillations would be observed. The next intersection of the gain and loss curves represents an unstable limit cycle. For oscillation amplitudes smaller than this, the system will return to the fixed point. However, if the system is perturbed beyond the amplitude of the unstable limit cycle, the next attracting equilibrium solution in state space is the stable limit cycle, the third intersection of the gain and loss curves. Once the system has entered this state, it will remain on it if no further action is taken. The two stable equilibrium states will be referred to as the

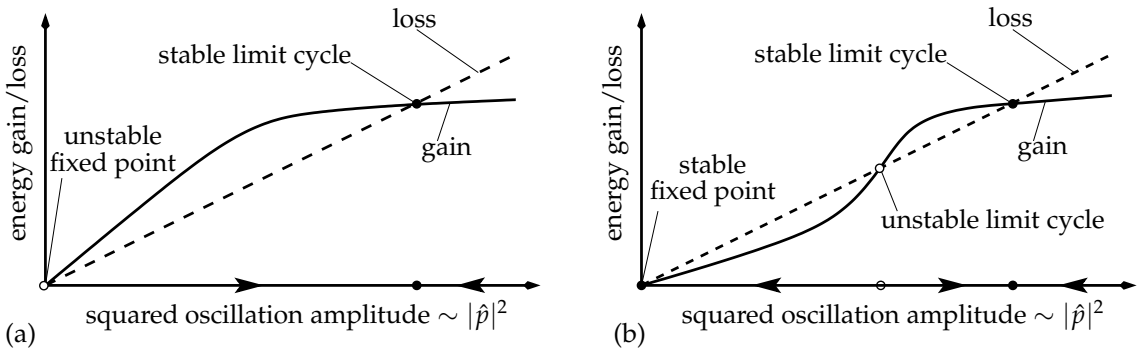

Figure 6.1: Acoustic energy gain–loss balance for (a) supercritical and (b) subcritical instability

lower and the upper branch in the following, with the bifurcation diagram in mind (Zinn & Lieuwen 2005 or Fig. 6.4).

6.2 Experimental observations of subcritical phenomena in the combustor test-rig

In this section, we present experimental results, which, based on the previous discussion, clearly demonstrate that subcritical phenomena are present. In particular, two stable equilibrium states at fixed operating conditions were observed, which differed by an order of magnitude in their oscillation amplitude. The two states were also associated with different flame anchoring positions resulting in an increased pressure loss. A change between these two states could be invoked by externally induced perturbations. Associated hysteresis phenomena were observed in the three major operating parameters.

6.2.1 Triggered instability

As mentioned at the beginning of this chapter, subcritical bifurcations give rise to triggered instabilities. If the system is initially in the non-oscillating state (the stable fixed point, see Fig. 6.1(b)), a perturbation with amplitude larger than that of the unstable limit cycle will cause the system to settle on the stable limit cycle. (Note here that we only consider the system dynamics in a strongly simplified way and do not adhere to any possible transient growth.) Exactly this behavior was observed in the test-rig. The time trace of the unsteady combustor pressure, at operating conditions corresponding to the subcritical case, is shown in Fig. 6.2. During the first 15 seconds, the pressure fluctuations consist of random noise components. The system is linearly stable. At $t = 15$ s, an external excitation is applied for one second via the speakers mounted downstream of the flame (see Fig. 3.1). The system immediately jumps on a high-amplitude limit-cycle oscillation and remains on it – even without external excitation. The oscillation is *self-sustaining* (in contrast to self-excited in the supercritical case).

This demonstrates that both equilibrium solutions, the fixed point with low level noise and the limit-cycle oscillation, are stable. On the limit cycle, the pressure signal is highly regular, as shown by the inset in Fig. 6.2. The spectra of the unsteady pressure upstream

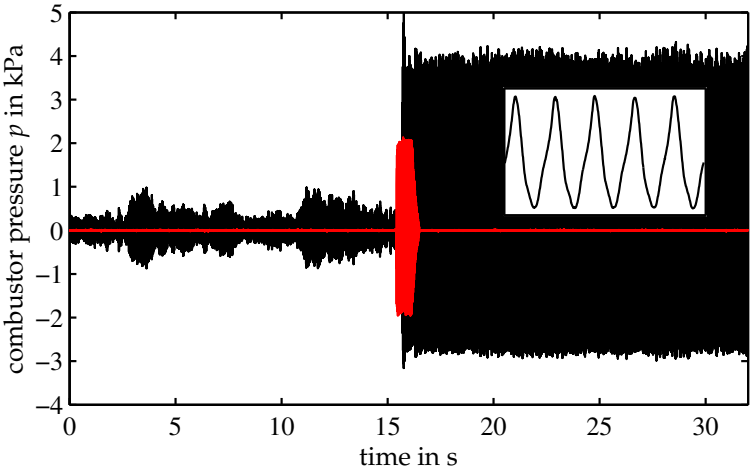

Figure 6.2: Combustor pressure (black) and excitation signal (red) histories for a triggered instability. The inset shows a close-up of the pressure oscillation pattern. The amplitude of the forcing signal has an arbitrary scale in this plot.

of the burner and the OH-chemiluminescence intensity in the limit-cycling state exhibit high-amplitude oscillations at 85 Hz (Fig. 6.3), the quarter-wave-mode frequency of the combustion chamber. Spectral peaks up to the ninth harmonic are clearly visible. It can also be noted in Fig. 6.3 that low-frequency oscillations around 20 Hz on the lower branch, which may be indicators for the flame being close to blow-off (Nair & Lieuwen 2005), are suppressed on the upper branch.

Without further action, the limit-cycling state would be sustained indefinitely. Through open-loop forcing with the speakers, a transition from the limit cycle to the fixed point could be invoked, using high amplitudes at frequencies sufficiently smaller or larger than that of the main oscillation. This is similar to the control investigations by Knoop et al. (1997). In the present case, however, it was also possible to cause a transition the other way round, in contrast to the work cited.

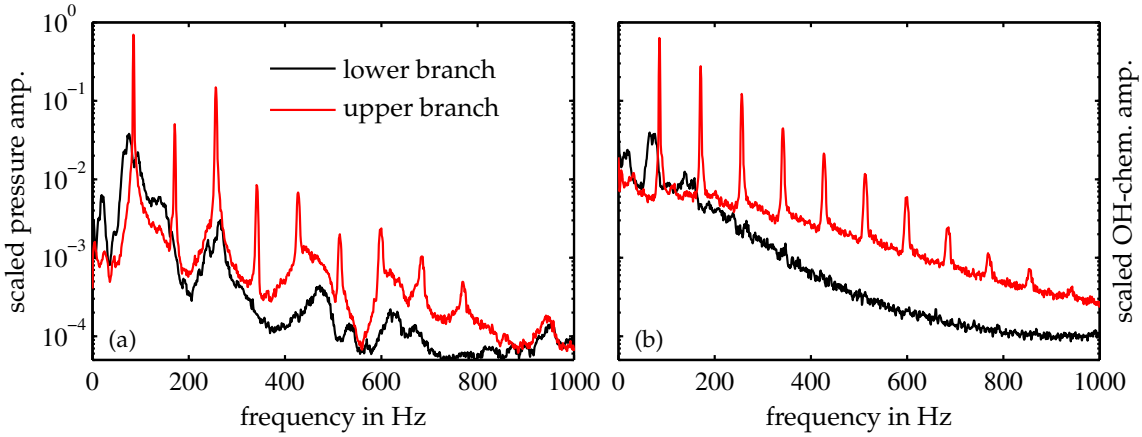

Figure 6.3: Spectra of (a) pressure and (b) OH-chemiluminescence. Data for the lower and the upper branch was taken at identical operating conditions and corresponds to the two stable equilibrium states.

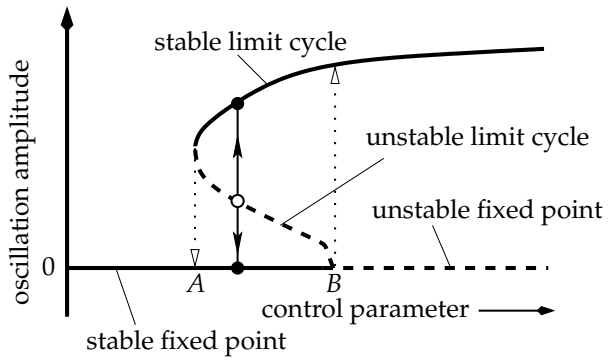

Figure 6.4: Principal bifurcation diagram showing hysteresis. Cyclic fold bifurcation at *A*; subcritical Hopf bifurcation at *B*

6.2.2 Hysteresis in parameter variations

A schematic of the principal bifurcation diagram for a subcritical case with hysteresis is shown in Fig. 6.4. For values of the control parameter smaller than A, only one equilibrium solution exists, a stable fixed point. No coherent oscillations will be observed, even if the system is perturbed by finite amplitude disturbances. At A, there is a cyclic fold bifurcation, a saddle–node bifurcation of periodic solutions (Nayfeh & Balachandran 1995), where two limit cycles, one being stable, the other unstable, are created. If the control parameter is increased beyond A but not beyond B, three equilibrium solutions coexist, the stable fixed point, the unstable, and the stable limit cycle. All perturbations from the stable fixed point with amplitude smaller than that of the unstable limit cycle will decay, and the system will eventually return to the fixed point. Disturbances with amplitudes higher than that of the unstable limit cycle will cause a transition to the upper branch, the stable limit cycle. For the control parameter equal to B, there is a subcritical Hopf bifurcation where the fixed point loses stability. For control parameters larger than B, even infinitesimal perturbations are amplified; the system is linearly unstable. The limit cycle is the only attracting solution, and only large amplitude oscillations would be observed in an experiment.

When increasing the control parameter starting from values smaller than A, the system will jump on the limit cycle as soon as B is crossed. In the presence of noise, an earlier transition to the upper branch may be caused. If the control parameter is now decreased, the system will remain on the upper branch until values smaller than A are attained. This is observed as hysteresis. For values of the control parameter between A and B, the system state depends on the history. This may be seen as a major simplification of the actual processes in the test-rig. The experimental observations, however, clearly demonstrate that the dominant dynamics follow this scheme.

A hysteretic dependence of the oscillation amplitude on the three essential operating parameters, the preheat temperature and the air and gas mass flows (which is equivalent to mixture ratio and power), was observed in the test-rig. The baseline operating conditions had a preheat temperature of 50 °C with a power of 97 kW at an equivalence ratio of 0.55. In the hysteresis experiments described below, two of the operating parameters were kept at their baseline values and the third was varied. The baseline case was in the

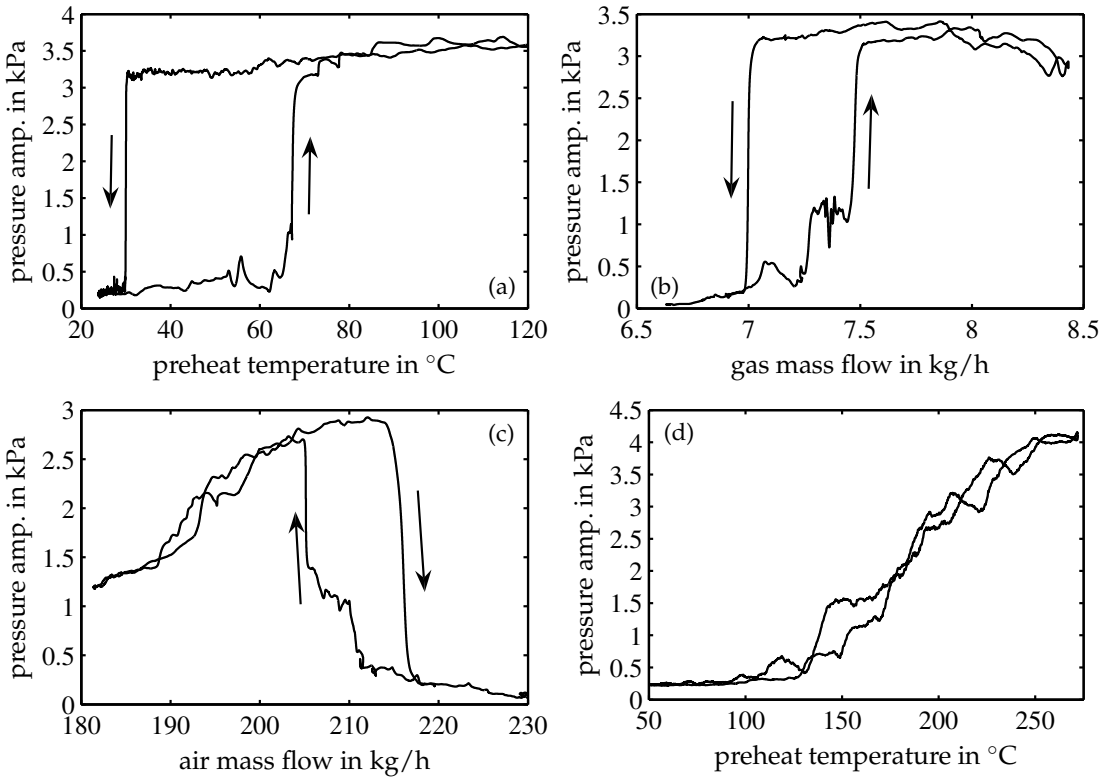

Figure 6.5: Instantaneous combustor pressure amplitude for increasing and decreasing control parameters. (a) Variation of preheat temperature, (b) variation of gas mass flow, (c) variation of air mass flow, (d) variation of preheat temperature, supercritical case

hysteresis region (control parameter between A and B, Fig. 6.4) for all three operating parameters.

The variation of the combustor pressure oscillation amplitude with increasing and decreasing preheat temperature is shown in Fig. 6.5 (a). The low-pass filtered magnitude of the analytic signal $p_a = p + i\mathcal{H}[p]$ ($\mathcal{H}$ denoting the Hilbert transform) is plotted versus the instantaneous value of the preheat temperature T_{ph}. For T_{ph} smaller than 30 °C, the system is globally stable. This was confirmed by introducing external perturbations at various frequencies and amplitudes. For preheat temperatures larger than 30 °C, a second equilibrium solution exists (point A in Fig. 6.4) – a limit cycle with oscillation amplitudes of more than 3 % of the mean combustor pressure. Increasing the preheat temperature further up to 65 °C, the amplitude of the lower branch slightly grows. At $T_{ph} = 65$ °C, the fixed point loses stability (point B in Fig. 6.4), and the only attracting solution in phase-space is now the upper branch, a limit-cycle oscillation. Once on the upper branch, the preheat temperature has to be decreased down below 30 °C to cause a switch to the non-oscillating solution.

At fixed preheat temperature, in the hysteresis region, a transition of the system state from the lower to the upper branch could be invoked, by acoustic forcing with the speakers at the limit cycle frequency at high amplitudes (as shown in Fig. 6.2). To cause a transition from the upper to the lower branch, i.e., to stabilize the system, strong forcing at frequencies sufficiently larger or smaller than that of the main oscillation was effective.

Hysteretic dependence of the pulsation amplitude on air and fuel mass flow was also observed. The corresponding bifurcation diagrams are shown in Figs. 6.5 (b) and 6.5 (c). The subcritical characteristics, similar to the variation in preheat temperature, are clearly visible. It can be noted here that the system is generally destabilized if the control parameters are varied such that the flame moves closer to the burner. As will be shown in the next section, the two coexisting equilibrium solutions in the hysteresis region are associated with two different flame anchoring positions – one outside and one inside of the burner.

The variation of the oscillation amplitude with preheat temperature for the supercritical case is shown in Fig. 6.5 (d). Here, the equivalence ratio was higher compared to the case shown in Fig. 6.5 (a). The oscillation amplitude increases continuously with preheat temperature, and there is a unique relation between the two.

Through the installation of an orifice with a moderate contraction and an additional extension of the combustion chamber length, it was possible to achieve a global stabilization of the system. For high forcing amplitudes at the limit cycle frequency of the original configuration (and frequencies close to that), high oscillations could be observed. When increasing and decreasing the forcing amplitude, hysteresis was observed in the system response with a distinct jump at a certain forcing strength (see also Section 6.3). There were, however, no oscillations without forcing, contrary to the self-sustained case in the original configuration. This behavior was also reported by Bellows et al. (2007*b*).

6.2.3 Oscillating and non-oscillating states associated with the flame anchoring position in the burner

Flame stabilization in combustion chambers with swirl burners usually relies on vortex breakdown at the burner dump plane (Escudier 1987; Lucca-Negro & O'Doherty 2001). In recent numerical (Biagioli 2006) and experimental (Güthe et al. 2006) investigations on the EV double-cone burner, it was found that for a certain equivalence ratio, there is a sudden transition of the flame anchoring position from outside to inside of the burner. The associated change in the burner flow field results in a significant increase in the pressure loss across the burner (henceforth denoted by Δp). Both flame anchoring positions were found to be stable over a range of equivalence ratios. It was further found that pressure pulsations due to thermoacoustic feedback were largest at those values of the equivalence ratio that correspond to the transition of the flame anchoring position (Biagioli et al. 2008; Güthe et al. 2006). With different flame imaging techniques, Güthe et al. demonstrated that during thermoacoustic pulsations, the flame moves between the two possible flame anchoring positions.

We also observed the two different flame anchoring positions in the experiments associated with the investigation of subcritical instabilities. Images of the line-of-sight integrated OH-chemiluminescence intensity of the flame were acquired with an intensified CCD camera. The results for a variation of the equivalence ratio around the baseline case are displayed in Fig. 6.6; the burner velocity was held constant. To suppress thermoacoustic oscillations, which would have been observed with the original set-up, we reduced the combustor length to approximately one third. With the shorter combustion chamber, no

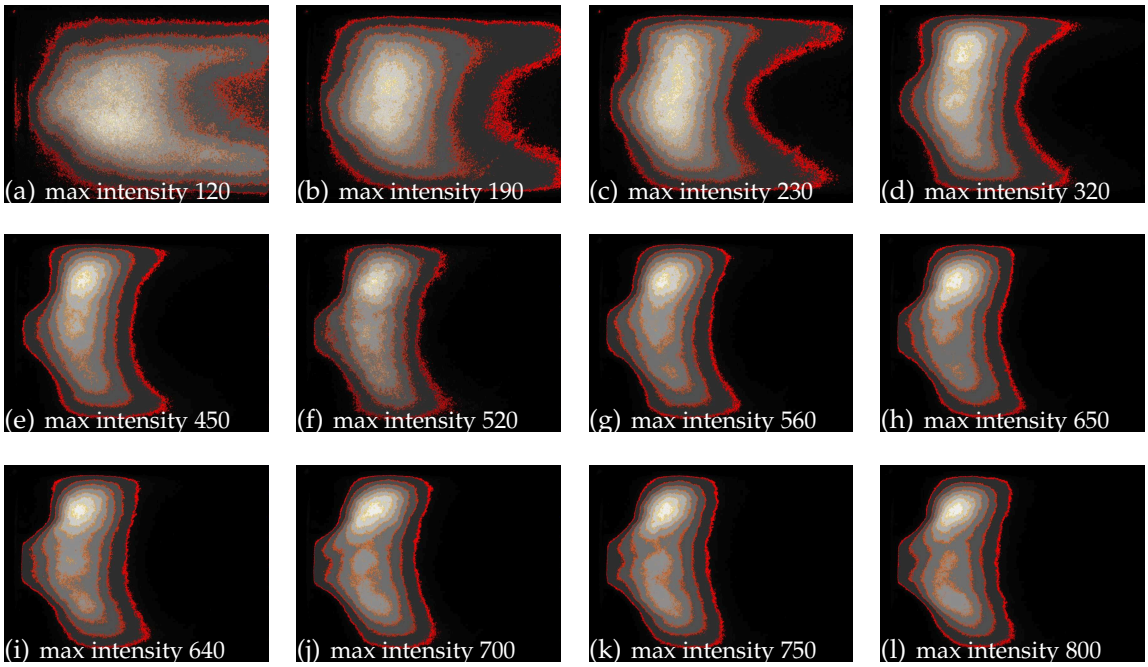

Figure 6.6: Line-of-sight integrated OH-chemiluminescence images of the flame for increasing equivalence ratio (constant burner velocity). Each image has been scaled with its maximum and represents the average of 500 pictures. Labels (a)–(l) correspond to equivalence ratio and pressure loss as indicated in Fig. 6.7.

significant pressure oscillations were present. Hence, the images in Fig. 6.6 correspond to the mean state with no oscillations.

For smaller equivalence ratios, the flame is completely located outside of the burner (Figs. 6.6(a)–6.6(c)). An increase in the fuel mass flow causes the flame to become more compact and to move closer to and eventually inside the burner. From Fig. 6.6(g) on, the flame is anchored deeply inside the burner and a further increase in the equivalence ratio does not lead to a noticeable change in the mean flame shape (Figs. 6.6(g)–6.6(l)).

The pressure loss associated with the equivalence ratio and the different flame shapes is shown in Fig. 6.7. A significant increase can be observed up to the point where the flame is completely anchored inside the burner. This is in agreement with the investigations of Biagioli (2006) and Güthe et al. (2006). From the point on where the flame does not change its shape significantly ((g)–(l)), the pressure loss remains approximately constant.

To understand which flame shape is associated with the oscillating and the non-oscillating state, mean images of the flame have been recorded for four more cases:

(i) strong forcing of the stabilized configuration (with orifice) on the lower branch, Fig. 6.8(a),

(ii) strong forcing of the stabilized system on the upper branch (same forcing amplitude as (i)), Fig. 6.8(b),

(iii) lower branch of the original configuration (low level noise), Fig. 6.8(c), and

(iv) upper branch of the original configuration (self-sustained oscillation), Fig. 6.8(d).

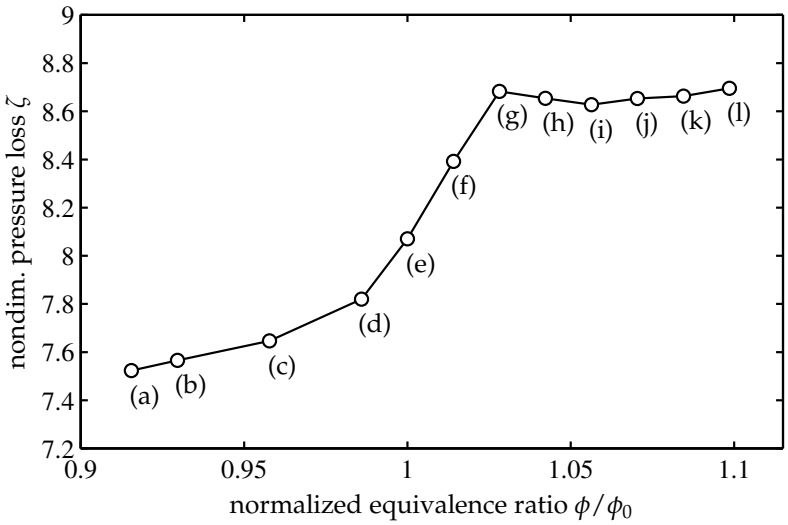

Figure 6.7: Non-dimensional pressure $\zeta = 2\Delta p/(\rho \bar{u}^2)$ loss as a function of the equivalence ratio at fixed burner velocity. Points (a) through (l) correspond to the chemiluminescence images of the flame in Fig. 6.6.

Upon comparison with Fig. 6.6, we note that the non-oscillating states (Figs. 6.8(a) and 6.8(c)) are associated with the flame being anchored outside the burner. For high-amplitude oscillations on the upper branch, driven (Fig. 6.8(b)) or self-sustained (Fig. 6.8(d)), the mean flame position is anchored deeply inside the burner. The OH-chemiluminescence intensity images in Fig. 6.8 are scaled with different maximum intensities to allow for a better comparison of the flame shapes. Although the mean heat release is identical for the four images, the equivalence ratio fluctuations for the oscillating cases 6.8(b) and 6.8(d) generate a significantly larger mean chemiluminescence intensity due to the exponential dependence on ϕ (Higgins et al. 2001).

The center of gravity along the streamwise coordinate as a function of the transverse coordinate, $C_x(y)$, was calculated for the four cases according to

$$C_x(y) = \frac{\int i(x,y)\, x \, \mathrm{d}x}{\int i(x,y) \, \mathrm{d}x}, \tag{6.1}$$

where $i(x,y)$ denotes the OH-chemiluminescence intensity distribution, x and y are streamwise and transverse coordinates, respectively, and the integration is performed over the

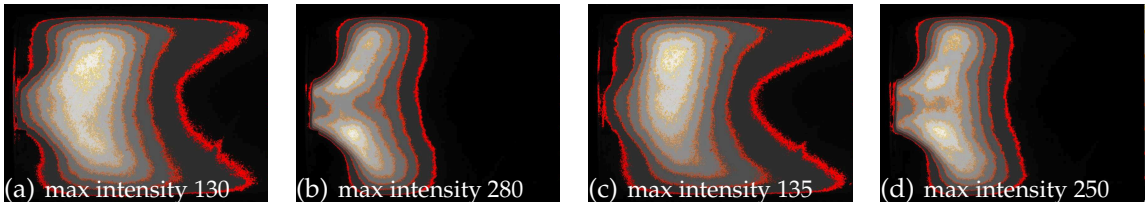

Figure 6.8: Line-of-sight integrated OH-chemiluminescence images of the flame on the upper and the lower branch with and without excitation; (a) stabilized configuration with forcing, lower branch, (b) stabilized configuration with forcing, upper branch, (c) original configuration, lower branch, (d) original configuration, upper branch

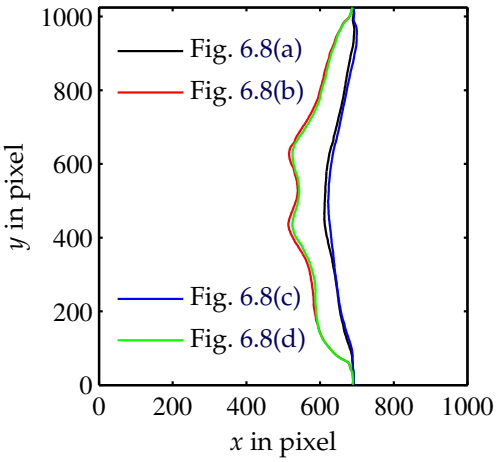

Figure 6.9: Centers of gravity $C_x(y)$ along the streamwise coordinate for the chemiluminescence images in Fig. 6.8. The burner exit plane is located at $x = 68$ pixel. The image resolution is 5 pixel/mm.

complete image length. The centers of gravity for the cases on the lower branch nearly coincide (Fig. 6.9). The same is true for the cases on the upper branch. Note again that cases (a) and (b) correspond to the same operating conditions, identical acoustic boundary conditions, and the same forcing amplitude. Likewise, cases (c) and (d) have identical parameters. A mean shift of the center of gravity of approximately 15 mm can be observed between the oscillating and the non-oscillating states. Resulting from this significant change in mean flame position and shape, a noticeable change in the flame response to velocity fluctuations for increasing amplitudes can be expected.

Since the pressure loss across the burner is inherently linked to the flame anchoring position (Biagioli 2006; Güthe et al. 2006, Figs. 6.6 and 6.7), hysteresis effects can be expected in the pressure loss, too. The oscillation amplitudes of the combustor pressure and the chemiluminescence intensity, the pressure loss coefficient ζ, and (the positive part of) the forcing signal, respectively the preheat temperature, are shown in Figs. 6.10 (a) and 6.10 (b). For the computation of the pressure loss coefficient, we used $\zeta = 2\Delta p/[\rho(\bar{u}^2 + \hat{u}^2/2)]$, where $\bar{u}$ represents the mean bulk velocity, and $\hat{u}$ is the amplitude of the velocity oscillations. The latter must be included to account for the DC shift in pressure loss generated by the quadratic nonlinearity in combination with the approximately harmonic oscillation. The acoustic velocity, necessary to determine $\hat{u}$, was reconstructed from the pressure measurements upstream of the burner by means of a time-domain realization of the Multi-Microphone-Method (Bothien et al. 2008; Moeck et al. 2007*a*).

The results shown in Fig. 6.10 (a) were obtained using the stabilized set-up (with orifice and chamber length extension). Forcing was applied at a frequency of 85 Hz, identical to the case with self-sustained oscillations. The pressure and heat release oscillation amplitudes as well as the pressure loss coefficient remain almost constant for forcing amplitudes smaller than a critical level. (Actually, the perturbations in heat release are apparently slightly stabilized by low level forcing.) As soon as the critical forcing level is exceeded, the oscillation amplitudes jump to significantly higher values. At the same time, the pressure loss coefficient increases by about 15 %, which corresponds to the same amount observed in non-oscillating conditions through an increase in equivalence ratio (Fig. 6.7). To reach the lower branch, the forcing amplitude has to be decreased down below the critical level. The oscillation amplitudes as well as the pressure loss coefficient drop to lower values simultaneously. Qualitatively similar characteristics with jumps to even higher oscillation

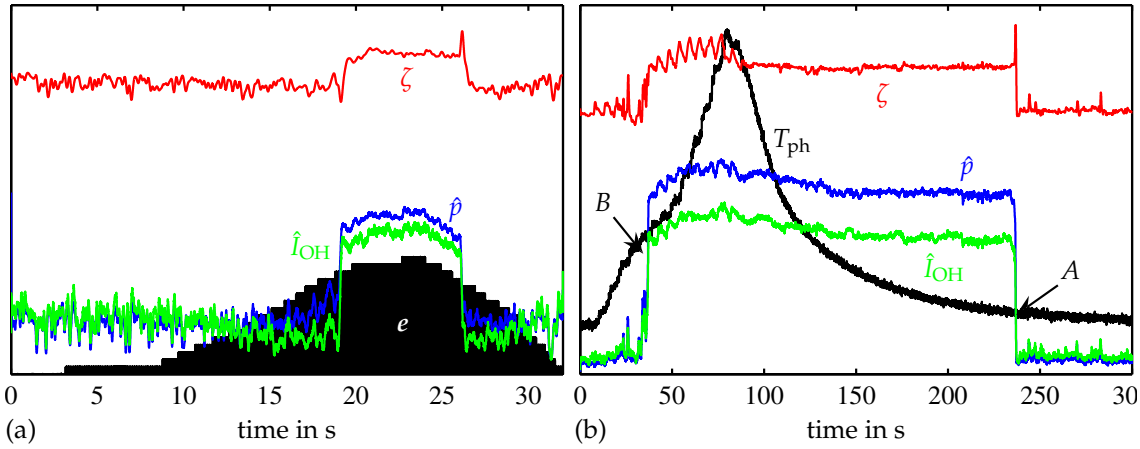

Figure 6.10: Time traces of normalized oscillation amplitudes of the combustor pressure $\hat{p}$ and the chemiluminescence intensity $\hat{I}_{OH}$, normalized pressure loss coefficient ζ, and (a) forcing signal e, (b) preheat temperature T_{ph}

amplitudes and a stronger increase in pressure loss were obtained when forcing at lower frequencies (80 Hz and 75 Hz). No transition could be caused, however, with forcing at higher frequencies (90 Hz and 95 Hz).

The variation of the oscillation amplitudes and the pressure loss for increasing and decreasing preheat temperature in the original set-up is shown in Fig. 6.10 (b). Up to a preheat temperature of 65 °C, the oscillations in pressure and heat release are small, and the pressure loss has approximately the baseline value. As the preheat temperature is increased beyond 65 °C, the oscillation amplitudes jump to high levels, and the pressure loss increases noticeably (point *B*). There is a somewhat irregular distribution of the pressure loss for preheat temperatures up to 120 °C. The oscillation amplitudes and the pressure loss remain on high levels until the preheat temperature is decreased down below 30 °C (point *A*). These results demonstrate that the pressure and heat release oscillations in the combustor are inherently linked to the static pressure loss at the burner and the associated change in the flame anchoring position.

6.3 Flame response to fluctuations in velocity

The crucial ingredient for the subcritical behavior is the nonlinear gain–amplitude relationship schematically shown in Fig. 6.1(b). As mentioned before, the damping processes are assumed to be linear since they are essentially acoustic phenomena.

The amplitude response of the normalized global OH-chemiluminescence intensity $I_{OH}/\bar{I}_{OH}$ to normalized velocity fluctuations $u/\bar{u}$ has been measured in the test-rig with the stabilized configuration for different excitation amplitudes at the frequency of the self-sustained oscillation observed in the original set-up (Fig. 6.11). Excitation was applied simultaneously with the upstream and the downstream speakers, the phase between them being shifted such that the maximum amplitude could be achieved. The global chemiluminescence intensity from the OH radical was collected with a photomultiplier equipped with a band-pass filter centered at 308 nm (see Fig. 3.1). Velocity fluctuations upstream of the burner were obtained from the Fourier transformed pressure signals by applying the

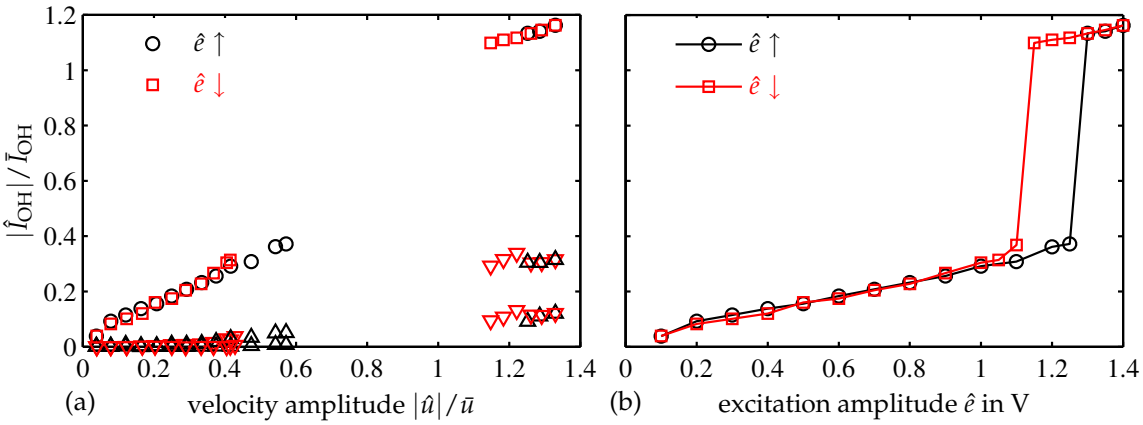

Figure 6.11: OH-chemiluminescence intensity fluctuation response as a function of (a) the velocity fluctuation amplitude and (b) the forcing level; data for increasing and decreasing excitation amplitude $\hat{e}$. In (a), the response at the first two harmonics is also shown (triangles).

Multi-Microphone-Method (Appendix A). The response at the fundamental frequency as well as at the first two harmonics is plotted in Fig. 6.11 (a). Due to the discontinuous dependence of the oscillation amplitude on the excitation level (see Fig. 6.10 (a)), an intermediate amplitude range could not be realized. Data for increasing as well as for decreasing excitation amplitude is plotted in Fig. 6.11. While the chemiluminescence fluctuation amplitude shows a hysteretic dependence on the excitation amplitude (Fig. 6.11 (b)), the $\hat{I}$ vs. $\hat{u}$ curve does not. The fact that the flame transfer function is continuous was also emphasized by Bellows & Lieuwen (2004). For smaller amplitudes (on the lower branch), the harmonic content in the chemiluminescence signal is hardly visible, but a significant harmonic response can be observed at higher amplitudes (on the upper branch).

We can already deduce from the available amplitude data in Fig. 6.11 (a) that there must be an inflexion point in the intermediate amplitude range if the flame transfer function is assumed to be continuous. To obtain more information on the q–u amplitude relation in the intermediate range, transient data with and without forcing at different amplitudes was recorded. In this way, several transitions from the upper to the lower branch and vice versa were captured. Figure 6.12 displays pairs of normalized global chemiluminescence intensity and normalized velocity fluctuation amplitude from the transient data. The I_{OH} and u time traces were zero-phase band-pass filtered around the fundamental frequency of oscillation to remove the higher-harmonic content. Application of the Hilbert transform then allowed to recover the instantaneous amplitude at the fundamental frequency. For comparison, the available data from constant amplitude forcing is also added. The dashed line represents a model for the nonlinear flame response, which is described in the next section.

Although there is large scatter, the transient data clearly shows a non-monotonic slope in the $\hat{I}$–$\hat{u}$ relation. Upon comparison with Fig. 6.1(b), this amplitude dependence can be assumed to be the reason for the subcritical phenomena observed. We also note that the inflexion point is quite accurately located at that oscillation amplitude at which backflow occurs. The large scatter in the data can be explained by the fact that in the transient case,

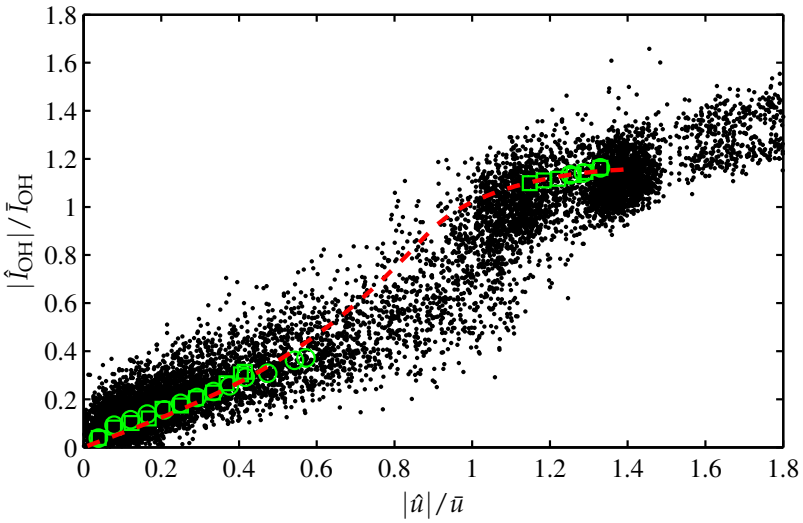

Figure 6.12: Instantaneous amplitude of OH-chemiluminescence intensity fluctuation vs. velocity fluctuation during a transient variation of the oscillation amplitude. The red dashed line represents a model for the nonlinear flame response, described in the next section. The symbols are values obtained from constant amplitude forcing (Fig. 6.11).

the $\hat{q}$–$\hat{u}$ relation is not unique but depends on the history. This is in particular true for a nonlinear system.

6.4 Nonlinear system model

In this section, we present a nonlinear model for a thermoacoustic system with a premixed flame coupled to a linear longitudinal acoustic field. The model is based on experimental data for the chamber acoustics to match the test-rig characteristics. The only mechanism of acoustic–flame interaction considered in the model is the generation of equivalence ratio perturbations by the oscillating air mass flow at the burner (cf. Section 2.3.1) and the associated fluctuations in the flame speed. Also, the generation and propagation of acoustic waves are treated in a completely linear fashion, assuming that the dominant nonlinearity is introduced through the interaction between the fluctuating air mass flow and the heat release in the flame, as detailed in Sections 2.3 and 2.5. Although this model is quite generic and ignores some physical mechanisms that may also be important (e.g., flame front kinematics, Thumuluru & Lieuwen 2009, or the negative pressure loss dependence on the burner velocity, Polifke et al. 2003), it bears qualitative and to a certain extent quantitative comparison with the experimental data from the test-rig.

6.4.1 Model set-up

Fluctuations in heat release induced by perturbations in equivalence ratio

Assuming a stiff fuel injection, perturbations in velocity at the burner generate fluctuations in equivalence ratio via (Peracchio & Proscia 1999)

$$\phi' = \bar{\phi}\left(\frac{1}{1+k_d u/\bar{u}} - 1\right), \tag{6.2}$$

where k_d is a model constant whose value will be discussed below. The propagation of the equivalence ratio perturbations (from fuel injection to flame front) is modeled as a one-dimensional convection–diffusion process so that the evolution of ϕ' is given by

$$\left(\partial_t + \bar{u}\partial_x - \Gamma\partial_x^2\right)\phi' = 0. \tag{6.3}$$

Here, Γ is an effective diffusion coefficient. For time-harmonic perturbations and the condition that $\phi' < \infty$ as $x \to \infty$, the transfer function between the fluctuating scalar at $x = L$ (which we take to be the flame position) and at $x = 0$ (the fuel injector) is given by

$$\mathcal{F}_\phi(\omega) = \frac{\hat{\phi}_L(\omega)}{\hat{\phi}_0(\omega)} = \exp\left[\frac{Pe}{2}\left(1 - \sqrt{1 + 4\mathrm{i}\omega\tau_c Pe^{-1}}\right)\right], \tag{6.4}$$

where $\tau_c = L/\bar{u}$ is a characteristic convection time and the Péclet number is defined as $Pe = \bar{u}L/\Gamma$. This model is similar to the one proposed by Schuermans et al. (2004*b*) for the linear flame transfer function of a turbulent premixed flame. In fact, the high Péclet number limit of Eq. (6.4) reads

$$\mathcal{F}_\phi(\omega) = \mathrm{e}^{-\mathrm{i}\omega\tau_c}\,\mathrm{e}^{-(\omega\tau_c)^2 Pe^{-1}}, \qquad \text{as } Pe \to \infty, \tag{6.5}$$

which corresponds to the successive application of a pure undamped time delay due to advection and a Gaussian low-pass with variance $Pe/(2\tau_c^2)$, and this is identical to the model given by Schuermans et al. The Péclet number and the convective delay were chosen to match with the low-pass and time-lag characteristics obtained from linear flame transfer function measurements.

To use $\mathcal{F}_\phi(\omega)$ as given in Eq. (6.4) in a time-domain simulation, a rational approximation is employed to set up a linear state-space model of the form (cf. Section 2.5.1)

$$\dot{\boldsymbol{x}} = \mathbf{A}\boldsymbol{x} + \mathbf{B}\phi_0', \tag{6.6a}$$
$$\phi_L' = \mathbf{C}\boldsymbol{x} + D\phi_0', \tag{6.6b}$$

with

$$\left[\begin{smallmatrix}\mathbf{A} & \mathbf{B}\\ \mathbf{C} & D\end{smallmatrix}\right] \overset{\mathrm{i}\omega}{\approx} \mathcal{F}_\phi(\omega). \tag{6.7}$$

The laminar flame speed s_l is computed from the equivalence ratio through the static relation given by Abu-Orf & Cant (1996)

$$s_l = a\phi^b\,\mathrm{e}^{-c(\phi-d)^2}. \tag{6.8}$$

Here, a, b, c, and d are empirical constants determined to match the available experimental data (Abu-Orf & Cant 1996). The influence of turbulence on the flame speed is modeled by the simple relation (see, e.g., Peters 1992, p. 227 or Lipatnikov & Chomiak 2002)

$$s_t = s_l\left[1 + C\left(\frac{v'}{s_l}\right)^n\right], \tag{6.9}$$

where C and n are model constants, and v' represents the turbulence intensity. We used the typical values $C = 1.25$ and $n = 0.7$. For the turbulence intensity, we chose $v' = 20\,\%$,

which is a representative value found in cold flow measurements (Lacarelle et al. 2010).

The total heat release associated with the unsteady flame is then obtained from

$$Q = \alpha \rho A_f s_t h_r. \tag{6.10}$$

Here, A_f represents the flame surface area, and the product αA_f is used as a tuning parameter to adapt the nonlinear flame response to the experimental data (see below). The specific heat of reaction, h_r, depends on the equivalence ratio and is (in case of methane) proportional to (Hubbard & Dowling 2001; Lieuwen 2003)

$$\frac{\min(\phi, 1)}{1 + 0.05825\,\phi}. \tag{6.11}$$

Combining all equations yields a nonlinear time-domain model for the heat release response to flow perturbations. The model constants k_d in Eq. (6.2) and the product αA_f in Eq. (6.10) have been determined so that the response at 85 Hz matches the amplitude dependence obtained from the experiments (see Fig. 6.12). There is good correspondence between the model and the experimental data at low and high amplitudes. In the intermediate amplitude range, the agreement is not as good. However, the stable equilibria in the experiments were located at low and high amplitudes so that the amplitude dependence in the intermediate range can be expected to mainly influence the transient characteristics (such as the critical triggering amplitude).

Chamber acoustics

Since we are dealing with a low-Mach-number flow, the pressure is continuous across the flame (Lieuwen 2003). The role of the plane acoustic field can then be lumped into a relation mapping the acoustic velocity downstream of the flame to that upstream. This is done by means of the specific admittance $\mathcal{A}$ and impedance $\mathcal{Z}$, which represent the plane wave acoustics up- and downstream of the flame in frequency domain, respectively (see Section 2.1). The admittance and impedance were obtained from experimental test-rig data as follows. To determine the upstream admittance, the reflection coefficient at the flame $\mathcal{R}_{\mathrm{us}}(\omega)$ was measured in cold flow conditions using sweep excitation with the downstream speakers and subsequent application of the Multi-Microphone-Method to the microphone array in the downstream duct (see Fig. 3.1). From the discrete frequency-domain data, we then identify a state-space realization (see Section 2.5.1)

$$\left[\begin{smallmatrix} \mathbf{A} & \mathbf{B} \\ \mathbf{C} & D \end{smallmatrix}\right] \overset{\mathrm{i}\omega}{\approx} \mathcal{R}_{\mathrm{us}}(\omega) \tag{6.12}$$

and obtain a time-domain admittance model by using

$$\mathcal{A} = \frac{1 - \mathcal{R}_{\mathrm{us}}}{1 + \mathcal{R}_{\mathrm{us}}}. \tag{6.13}$$

This operation can be performed on the state-space system representing the upstream reflection coefficient and results in a system of the same type for the admittance. The state-space matrices of the two systems are related by elementary matrix-algebraic operations.

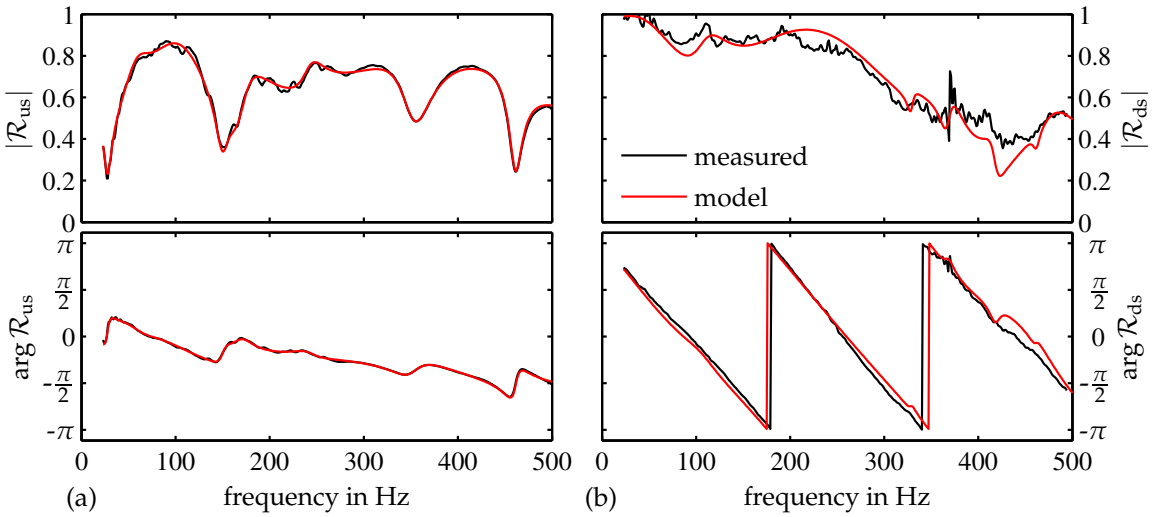

Figure 6.13: Measured and identified reflection coefficients (a) upstream and (b) downstream of the flame

The downstream reflection coefficient was determined by forcing the system with the upstream speakers in hot (reacting) conditions and applying the Multi-Microphone-Method again to the microphone array in the downstream duct. The same procedure as described above for the reflection coefficient on the upstream side then allows to obtain a time-domain model for the downstream admittance from

$$\mathcal{Z} = \frac{1 + \mathcal{R}_{\mathrm{ds}}}{1 - \mathcal{R}_{\mathrm{ds}}}. \tag{6.14}$$

The two measured reflection coefficients and the identified models are shown in Fig. 6.13. There is good agreement in the frequency range considered. The reference plane for the reflection coefficients is the average flame location, 105 mm downstream of the burner dump plane.

Since the pressure is assumed continuous, we can now construct a time-domain relation in state-space form which maps the velocity perturbation downstream of the flame to that upstream, viz.,

$$u_{\mathrm{us}} = \xi^{-1} \left[\begin{smallmatrix} \mathbf{A} & \mathbf{B} \\ \mathbf{C} & D \end{smallmatrix}\right] u_{\mathrm{ds}}, \quad \text{with} \quad \left[\begin{smallmatrix} \mathbf{A} & \mathbf{B} \\ \mathbf{C} & D \end{smallmatrix}\right] \overset{\mathrm{i}\omega}{\approx} (\mathcal{Z}\mathcal{A})(\omega), \tag{6.15}$$

where $\xi = (\rho c)_{\mathrm{us}}/(\rho c)_{\mathrm{ds}}$. This mapping is a representation of the whole chamber acoustics. The acoustic model is based on experimental data taken at the reference conditions at an equivalence ratio of $\phi = 0.55$. In Section 6.4.2, simulation results for a variation of the equivalence ratio are shown. The associated change in the temperature field and the impact on the acoustic wave propagation has not been taken into account in the model.

Coupling acoustic and flame models, noise source terms, and excitation

A representation for the complete thermoacoustic system, the nonlinear flame response coupled to a linear longitudinal acoustic field, is obtained by combining the acoustic model explained above with the nonlinear flame model. The relation between u_{us} and

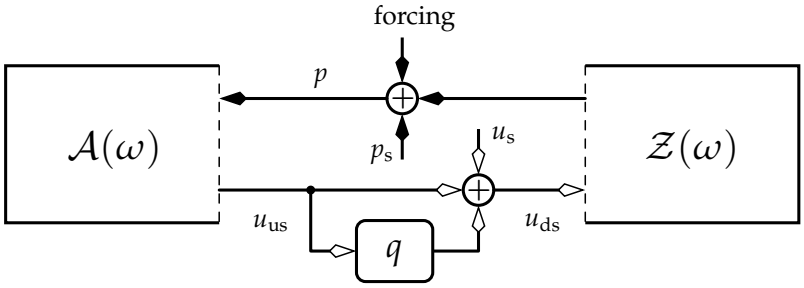

Figure 6.14: Schematic representation of the nonlinear system model. The acoustics up- and downstream of the flame are lumped into admittance $\mathcal{A}(\omega)$ and impedance $\mathcal{Z}(\omega)$; q denotes the nonlinear heat release model, and p_s and u_s represent the acoustic source terms of the flame. External forcing is modeled as an additional pressure source.

u_{ds} (Eq. (6.15)) is closed by invoking the jump conditions (2.16)[2] to calculate the jump in acoustic velocity across the flame front from the heat release perturbation. In the coupled model, an additional delay of 2.7 ms was added to the flame response to match the frequency of the self-sustained oscillation in the simulation with that observed in the experiments.

In the simulation, we add colored noise to the pressure at the flame and to the acoustic velocity downstream of the flame. A colored-noise sequence is generated by filtering white noise through experimentally determined source spectra (Paschereit et al. 2002; Schuermans et al. 2009) that were obtained in parallel with flame transfer matrix measurements for the same burner. For the simulation of triggered instabilities and the stabilization from the upper to the lower branch, we include harmonic forcing in terms of an additional pressure source at the flame in the model. This mimics the open-loop excitation by the speakers in the experiment. A block diagram of the simulation model, including all components described above, is shown in Fig. 6.14.

6.4.2 Simulation results

Time-domain simulations were performed in order to investigate if the model exhibits subcritical behavior. Figure 6.15 shows a triggered instability in the model simulation. Although noise is present, the pressure oscillations remain small in the beginning; the system is linearly stable. At $t = 1.5$ s an external perturbation in form of harmonic forcing at 85 Hz is introduced. After a few cycles, the combustor pressure oscillations grow to the upper branch, and even if the forcing is stopped, the system remains in a limit-cycling state – the oscillation is self-sustaining. This clearly demonstrates that subcritical behavior is present and two stable equilibria exist. Triggering was most effective when perturbing the system on the lower branch with frequencies equal or close to the limit cycle frequency (± 5 Hz). As in the experiment, a transition from the upper branch to the lower one could be forced by excitation at frequencies sufficiently larger or smaller than the frequency of the self-sustained oscillation. At $t = 3$ s, harmonic excitation at 60 Hz is applied, and a transition from the upper to the lower branch is induced; the system is stabilized (Fig. 6.15).

[2]The same strategy – setting up an acoustic mapping which relates the velocity fluctuations downstream of the flame to those upstream and then closing the system model with a heat release "module" – is used in Chapters 8 and 9. There, however, the heat release is computed by a detailed zero-Mach reacting-flow solver.

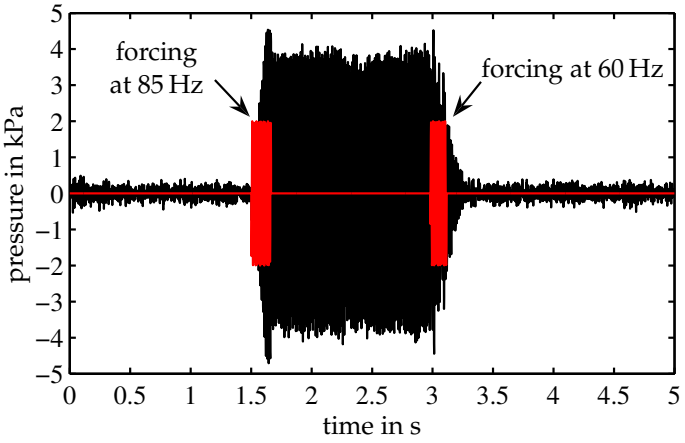

Figure 6.15: Triggered instability and stabilization in the model simulation. Combustor pressure (black) and excitation signal (red). The amplitude of the forcing signal has an arbitrary scale in this plot.

To test the model for hysteresis, the equivalence ratio was decreased below the point where no limit-cycle oscillations could be triggered. The equivalence ratio was then increased beyond the point where the fixed point loses stability and a self-excited oscillation appears. The variation of the pressure oscillation amplitude for increasing and decreasing equivalence ratio is shown in Fig. 6.16. Results for two different noise levels are plotted. A broad region of hysteresis can be noted between $\bar{\phi} = 0.53$ and $\bar{\phi} = 0.65$ for the lower noise level (solid line). However, the parameter range in which hysteresis can be observed depends on the noise level introduced in the simulation. Increasing the noise level resulted in a narrower hysteresis region (dashed line in Fig. 6.16). This is because when approaching the critical parameter values (bifurcation points A and B in Fig. 6.4), the domains of attraction of the respective equilibrium solutions shrink and larger noise components may cause an earlier transition to the other branch.

6.4.3 Nonlinear energy gain and describing function associated with the flame model

The energy gain in the acoustic field is proportional to the heat release–pressure correlation integrated over one cycle of the fundamental oscillation (see Section 2.2.2)

$$E_{\text{gain}} \sim \int_0^T Qp \, \mathrm{d}t. \tag{6.16}$$

If attention is restricted to the fundamental component, we can write

$$E_{\text{gain}} \sim |\hat{Q}_\text{f}||\hat{p}_\text{f}| \cos\left(\angle(\hat{Q}_\text{f}, \hat{p}_\text{f})\right), \tag{6.17}$$

where the subscript 'f' denotes the Fourier component at the fundamental frequency. Since the flame model does not include an amplitude dependence of the phase, the phase angle between $\hat{Q}_\text{f}$ and $\hat{p}_\text{f}$ is constant for all oscillation levels. Also, the acoustic field is treated linear, and therefore, the relation between $\hat{p}_\text{f}$ and $\hat{u}_\text{f}$ is also independent of the amplitude. Hence, the energy gain is proportional to the product of the amplitudes of the fundamental

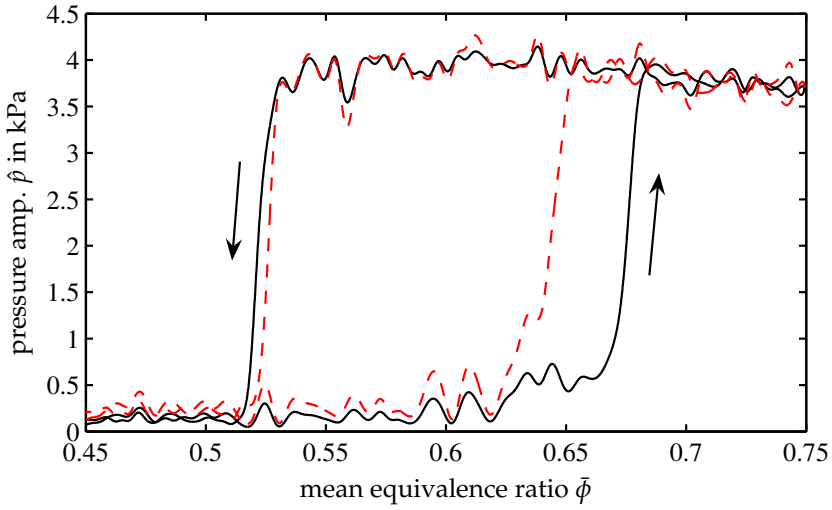

Figure 6.16: Low-pass filtered instantaneous amplitude of pressure oscillations vs. mean equivalence ratio, simulation results. The red dashed line corresponds to an increased noise level.

components of the heat release and velocity fluctuations

$$E_{\text{gain}} \sim |\hat{Q}_{\text{f}}||\hat{u}_{\text{f}}|. \tag{6.18}$$

We used the nonlinear flame model (Section 6.4.1) to compute the fundamental component of the heat release response to a velocity forcing and determined $|\hat{Q}_{\text{f}}(\hat{u}_{\text{f}})|\,|\hat{u}_{\text{f}}|/(\bar{Q}\bar{u})$ at the main frequency of oscillation for the two critical and one intermediate equivalence ratio (inferred from Fig. 6.16). This term is proportional to the energy gain, as explained above, and is displayed as a function of $(|\hat{u}|/\bar{u})^2$ in Fig. 6.17 (a). The loss curve plotted over the squared oscillation amplitude is a straight line due to the linearity of the acoustic field. The slope matches that of the gain curve for $\bar{\phi} = 0.65$ at low amplitudes because, at this point, the system loses linear stability (point B in Fig. 6.4). With decreasing equivalence ratio, the gain is reduced. For equivalence ratios smaller than 0.53, the gain does not exceed the losses for any oscillation amplitude. Hence, the system is globally stable because the fluctuation energy always decreases. For an intermediate equivalence ratio, in the hysteresis region ($\bar{\phi} = 0.58$), the gain and loss curves have two intersections at finite oscillation levels. The one at higher amplitudes corresponds to the stable limit cycle, the upper branch in the bifurcation diagram (Fig. 6.4).

We obtain equivalent results by considering the amplitude dependence of the transfer function gain (the describing function) of the heat release model evaluated at the oscillation frequency, which we compute as the fundamental response to harmonic forcing divided by the amplitude of the input signal, viz.,

$$N(a) = \frac{\hat{Q}_{\text{f}}[a\sin(\omega_{\text{f}}t)]}{a}, \tag{6.19}$$

where a corresponds to $|\hat{u}|/\bar{u}$. The transfer function gain as a function of the velocity perturbation amplitude at 85 Hz is shown in Fig. 6.17 (b) for the three equivalence ratios as in Fig. 6.17 (a). The critical gain, above which the growth rates are positive, is marked by

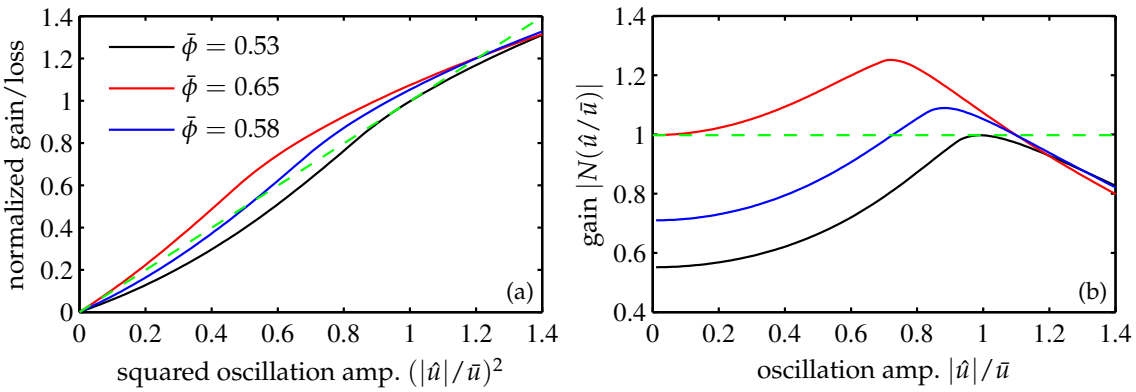

Figure 6.17: (a) Gain and loss curves for critical and intermediate equivalence ratios at an oscillation frequency of 85 Hz. The green dashed line represents the linear acoustic losses. (b) Describing function gain at 85 Hz for critical and intermediate equivalence ratios. The green dashed line represents the critical gain.

the dashed line. It coincides with the transfer function gain for $\bar{\phi} = 0.65$ at low amplitudes. The next intersection at $\hat{u}/\bar{u} = 1.1$ represents the amplitude of the limit-cycle oscillation. For an equivalence ratio of $\bar{\phi} = 0.58$, the gain is smaller than the critical gain for low amplitudes so that the growth rate is negative. There are two oscillation amplitudes at which the growth rate of the 85 Hz mode is zero, $\hat{u}/\bar{u} = 0.72$ and 1.1. The first corresponds to the unstable, the latter to the stable limit cycle. For equivalence ratios below $\bar{\phi} = 0.53$, the critical gain is not attained for any oscillation amplitude, and therefore, the system is globally stable.

6.5 Discussion

We investigated subcritical thermoacoustic instabilities in the combustor test-rig. For certain operating conditions, a linearly stable system, initially exhibiting only low level noise, could be triggered to high-amplitude self-sustained oscillations. This phenomenon is particularly dangerous because it cannot be predicted by linear stability analysis. In fact, for the case at hand, a linear analysis would predict the system to be stable for operating parameters corresponding to the hysteresis region.

Associated with the subcritical character of the system, we observed a hysteretic dependence of the oscillation amplitude on the three major operating parameters. The sudden increase in pulsation amplitude, when the system jumped from the lower to the upper branch, was always accompanied by a noticeable increase in the pressure loss across the burner. OH-chemiluminescence images of the flame revealed that the two stable equilibrium solutions in the hysteresis region, the fixed point and the limit-cycle oscillation, were associated with different mean flame anchoring locations.

The response of the heat release rate to fluctuations in velocity was determined at the instability frequency for a range of amplitudes up to those of the self-sustained oscillation. We found that the flame response exhibits a non-trivial, not purely saturating amplitude dependence, which explains the appearance of subcritical instabilities.

A nonlinear thermoacoustic model based on flame speed fluctuations induced by perturbations in equivalence ratio was presented. The model was capable of simulating

subcritical phenomena such as triggering self-sustained limit-cycle oscillations and a hysteretic dependence of the oscillation amplitude on the equivalence ratio. A transition between stable and unstable branch could be induced by open-loop harmonic forcing. From a dynamical systems point of view, it is easy to see why open-loop forcing is able to trigger a transition between the two equilibrium states. Both have their domains of attraction in phase space, and the forcing offers a way to transit from one to the other.

It is often implicitly assumed that strong pressure oscillations observed in an experiment are the result of linear instability, the overall impression being that subcritical instabilities are less common than supercritical instabilities. However, in many studies, it is not really clear whether an experimentally or numerically investigated instability is actually sub- or supercritical. This question can be thoroughly answered only if the actual growth phase can be clearly identified to be exponential or if some control technique is used to suppress the oscillation and it is then assessed if growth sets in immediately after control is ceased.

Part II

A Hydrodynamic–Acoustic Two-way Coupling for Modeling Thermoacoustic Instabilities

Thermoacoustic phenomena comprise a multitude of time and length scales. Therefore, numerical simulations of combustion instabilities and their control is conceptually challenging. For low-frequency instabilities, one of the clearest discrepancies in scales is that of the acoustic wavelength and the longitudinal extent of the reaction zone. Tackling this problem with a compressible reacting-flow solver is inherently inefficient for two reasons: (i) detailed numerical resolution is required only in a fraction of the relevant domain and (ii) time step constraints associated with the speed of sound and with the mean flow velocity differ by a factor of the Mach number. In the following chapters, we propose a method to deal with this problem. The method is based on an explicit decomposition of the actual domain into an acoustic and a hydrodynamic zone. After the methodology is explained in detail (Chapter 7), it is applied to three different configurations. The first is a simple model problem (Section 7.5) based on which the procedure is demonstrated to deliver meaningful results. The second configuration has an experimental counterpart to validate the method (Chapter 8). Finally, the two-way coupling approach is applied to a numerical configuration based on the test-rig acoustics, where two control schemes are used to suppress combustion oscillations (Chapter 9).

Chapter 7

Formulation of the Approach and Application to an Elementary Model Problem

7.1 Motivation for a hydrodynamic–acoustic coupling

Computational modeling of thermoacoustic processes in combustion chambers in order to predict unstable operating regimes and to develop and test control methods is highly desirable because this would reduce the need for expensive experimental investigations. As shown recently, fully compressible reacting-flow computations based on large eddy simulations manage to accurately capture the essential thermoacoustic interaction mechanisms in realistic configurations and bear quantitative comparison with experimental data (Schmitt et al. 2007). The computational effort is, however, still exceedingly high. One reason for this is that, in the compressible case, the time step restriction has to be based on the speed of sound as opposed to a characteristic advection velocity in incompressible simulations. In gas turbine applications, the Mach number is typically of the order of 0.1 or less so that the time step in a compressible simulation has to be smaller by more than an order of magnitude compared to the incompressible case. In addition to that, it is far from trivial to impose the proper acoustic boundary conditions, represented by frequency-dependent impedances or reflection coefficients, in a compressible CFD simulation (Huber et al. 2008; Widenhorn et al. 2008). This is a major restriction because the acoustic boundary conditions have a strong influence on stability, frequency, and amplitude of thermoacoustic oscillations (Bothien et al. 2008).

Various modeling approaches of lower complexity (and therefore less computational demand) have been proposed in the literature. Network models, as introduced in Section 2.5, divide the thermoacoustic system under investigation in several elements, each being represented by acoustic frequency response functions for plane-wave (and possibly azimuthal) modes. The coupling of the acoustic field with the flame is incorporated by means of a flame transfer function/matrix. Such models have been shown to agree reasonably well with measured instability regimes and oscillation frequencies (see references in Section 2.5). The major weakness of the network approach is that the flame dynamics still need to be determined by experiment or by CFD (see, e.g., Paschereit et al.

2002; Polifke et al. 2001*b*). Also, taking into account nonlinearities in the flame response is not straightforward. Information on the transfer function of turbulent premixed flames at high forcing amplitudes is not easily obtained from experiments because this requires strong excitation over a broad frequency range. Accordingly, the prediction of the oscillation amplitude under unstable conditions or capturing inherently nonlinear phenomena, for example, a hysteretic dependence of the pulsation amplitude on system parameters, as shown in Chapter 6, is difficult.

For these reasons, we consider a hydrodynamic–acoustic coupling, in which the incompressible flame dynamics are coupled to a representation of the acoustic field, as a valuable tool, trading-off accuracy and efficiency in an ideal way. The principal idea of coupling different models for thermoacoustic phenomena is not new. A brief overview of previous work in this field is given in the next section.

7.2 Previous work

One possibility of reducing the computational effort is to use different models for the computation of the reacting flow and the acoustic field. The comprehensive form of such a coupling requires a mutual exchange of the two models, in the sense that the action of the heat release influences the acoustic field and vice versa. For obvious reasons, this is referred to as a two-way coupling. In the last ten years, various authors have used this strategy with different approaches.

Dowling (1999) used a *G*-equation model of a premixed bluff-body-stabilized flame combined with a wave-amplitude-based representation of the plane mode acoustics for the computation of self-excited thermoacoustic oscillations. Fluctuations in heat release rate were obtained from the kinematic evolution of the flame surface area, while assuming a constant burning velocity. The model reproduced limit-cycle oscillations, observed in the experiments of Langhorne (1988), with reasonable agreement.

Schuermans et al. (2005*a*,*b*) proposed a coupling strategy in which the reacting flow is computed with compressible URANS (unsteady Reynolds-averaged Navier–Stokes) or LES (large eddy simulation) solvers, and the acoustic domain is represented in terms of equivalent boundary conditions. Based on a modal expansion of the Green's function for the geometry considered, an acoustic input–output map in the form of a linear time-invariant state-space model is set up. The latter is either of admittance or impedance type (i.e., maps pressure to velocity fluctuations or vice versa) and is applied directly to the boundaries of the CFD domain. The input signals to the acoustic state-space models are obtained from a plane-wave-based spatial filter of the compressible solution field. By applying the measured test-rig impedance to the unsteady CFD simulation, they were able to quantitatively reproduce the experimentally determined pressure spectrum.

A somewhat different approach, considering only linear stability characteristics, was proposed by Kopitz & Polifke (2008). The system is divided into a CFD and a network model domain. In a first step, the CFD domain is considered isolated. At the downstream end, a fully reflecting boundary condition (a pressure node) is specified. The upstream end is made non-reflective, and an additional identification signal is added, such as broadband noise. In this way, essentially, the reflection coefficient of the downstream part can be

computed from the time-domain solution data. In conjunction with the network representation of the upstream part, the stability of the entire system can be assessed. The method was validated with pure network model solutions of an elementary Rijke tube configuration with a heater grid. Kaess et al. (2008) applied the same strategy to the configuration investigated by Noiray et al. (2007, 2008), an unconfined collection of conical laminar premixed flames stabilized by a perforated plate and coupled to an upstream duct. A comparison with the experimental data showed good agreement in the mode frequencies, but the growth rates were overpredicted.

A coupled model based on separate representations for the combustion zone and the acoustics was also proposed by Tyagi et al. (2007). They considered a generic configuration with a ducted non-premixed flame described by a global one-step reaction as well as infinite-rate chemistry. A Galerkin method was used to model the one-dimensional acoustic field. Only fully reflecting boundary conditions were considered, which do not account for the loss of acoustic energy across the system boundaries. In the computations, no stable limit-cycle oscillation was obtained.

The approach proposed here is the application of a two-way coupling strategy for the simulation of thermoacoustic instabilities. The method takes advantage of the efficient acoustic modeling capabilities of the network approach, while on the other hand, incorporating the thermoacoustic (linear *and* nonlinear) flame response by means of a detailed numerical computation based on an incompressible scheme. Thus, this method will be able to capture the essential stages of thermoacoustic oscillations – linear instability and exponential growth, nonlinear saturation, and limit-cycle oscillation. Since the dominant nonlinearity is fully accounted for, no restriction is made to supercritical instabilities.

In the next section, the methodology of the coupled simulation is presented. An elementary model problem is considered in Section 7.5 – a one-dimensional flame burning freely in a closed–open duct. The interaction of the flame with the acoustic field is modeled through oscillations in equivalence ratio. An actual test case is considered in Chapter 8. To validate the approach, a flat flame Rijke-type set-up was built. The configuration shows strong thermoacoustic oscillations at a frequency of approximately 430 Hz, corresponding to the $5\lambda/4$-mode of the geometry. The coupled simulation was applied to this case. Control applications are considered in Chapter 9. Here, a two-dimensional flame is embedded into a real acoustic environment.

7.3 Theoretical basis for the coupled system representation

In the low-Mach-number, long-wave-length case, which is encountered in typical gas turbine combustors, acoustic perturbations act on a scale L much larger than the axial extent l of burner and flame (Fig. 7.1). Therefore, the effect of an acoustic wave on the burner flow reduces to a global acceleration of an incompressible medium in the limit of vanishing Mach number (Klein 1995). Conversely, the heat released by the flame acts as a point source on the large scale acoustic field, inducing a jump in the velocity fluctuation. Therefore, the general strategy is to decouple the small scale hydrodynamic and the large scale acoustic computation. Then a bilateral coupling can be achieved based on results from low Mach number asymptotics. It is important to note here that, in contrast to the work cited in the preceding section, where a compressible CFD solver has been used for

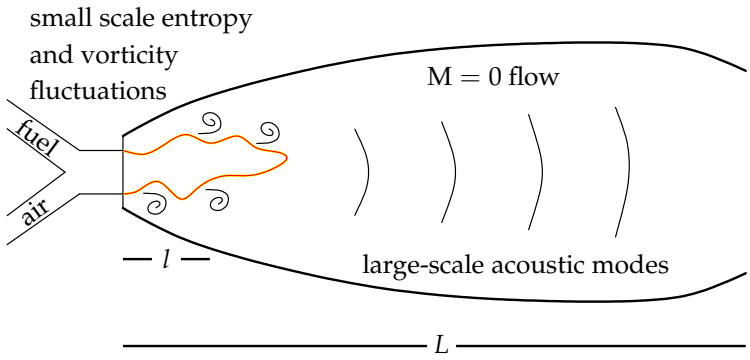

Figure 7.1: Scale separation between combustion/flow phenomena and long-wave acoustics

the combustion zone, we represent the hydrodynamic/combustion part by a zero Mach incompressible model.

The momentum balance for compressible flow is ill-conditioned for characteristic flow velocities much smaller than the speed of sound. This is revealed by the dimensionless form of the Euler equations

$$\partial_{\tilde{t}}(\tilde{\rho}\tilde{\boldsymbol{u}}) + \tilde{\nabla}\cdot(\rho\tilde{\boldsymbol{u}}\tilde{\boldsymbol{u}}) + \frac{1}{M^2}\tilde{\nabla}\tilde{P} = 0. \tag{7.1}$$

Here, $\tilde{(\cdot)}$ denotes a dimensionless quantity, and reference length and time scale are related by the characteristic flow velocity. We drop the tildes in the following discussion. The pressure gradient term becomes singular as $M \to 0$. To resolve this deficiency, Klein (1995) introduces a multiple scale ansatz, in which the solution vector $\boldsymbol{U}$ is expanded in powers of the Mach number M, viz.,

$$\boldsymbol{U}(\boldsymbol{x}, t; \mathrm{M}) = \sum_i \mathrm{M}^i \boldsymbol{U}^{(i)}(\boldsymbol{x}, \mathrm{M}\boldsymbol{x}, t). \tag{7.2}$$

Here, $\boldsymbol{x}$ resolves the short hydrodynamic length scale and $\boldsymbol{\xi} = \mathrm{M}\boldsymbol{x}$ the long acoustic scale. The consequences of this ansatz, relevant in the present case, can be summarized as follows:

(i) To second order in the Mach number, the expansion of the pressure takes the form

$$P(\boldsymbol{x}, t; \mathrm{M}) = P_0(t) + Mp^{(1)}(M\boldsymbol{x}, t) + M^2 p^{(2)}(\boldsymbol{x}, \mathrm{M}\boldsymbol{x}, t), \tag{7.3}$$

where each term represents a physically different part. The zeroth-order pressure is constant in space and corresponds to the thermodynamic background pressure. In principle, P_0 is a function of time, but in our applications of isobaric combustion, it will be simply a constant. The first-order pressure $p^{(1)}$ takes the role of the acoustic pressure and satisfies a wave equation (2.4) on $\boldsymbol{\xi}$. $p^{(1)}$ may vary on the long acoustic scale, but is spatially constant on the hydrodynamic scale $\boldsymbol{x}$. The second-order pressure $p^{(2)}$ is identified as the hydrodynamic part and is a function of the short as well as of the long scales.

(ii) The momentum equation at leading order reads

$$\partial_t(\rho \boldsymbol{u})^{(0)} + \nabla_{\boldsymbol{x}} \cdot (\rho \boldsymbol{u}\boldsymbol{u})^{(0)} + \nabla_{\boldsymbol{x}} p^{(2)} = -\nabla_{\boldsymbol{\xi}} p^{(1)}, \tag{7.4}$$

which reveals that, in addition to the hydrodynamic pressure $p^{(2)}$, the acoustic gradient on the long scale, $\nabla_{\boldsymbol{\xi}} p^{(1)}$, affects the flow field at leading order, acting essentially as a momentum source. This term pulls the flow on the hydrodynamic scale in the opposite direction of the acoustic pressure gradient and generates vorticity through baroclinic torque whenever the flame front normal is not aligned with $\nabla_{\boldsymbol{\xi}} p^{(1)}$.

(iii) The leading order energy equation implies a divergence constraint, which, in a simplified form, can be written as

$$\oint_{\partial V} \boldsymbol{u}^{(0)} \cdot \boldsymbol{n} \, \mathrm{d}A = \frac{\gamma - 1}{\gamma P_0} \int_V q \, \mathrm{d}V. \tag{7.5}$$

In the full form, the divergence constraint includes an additional term related to the temporal variation of the thermodynamic background pressure, which is important in the case of non-isobaric combustion (see, e.g., Oevermann et al. 2008). Also, for a clearer discussion, we neglected terms resulting from non-isomolar reactions, heat conduction, and diffusion, which can be taken into account, though.

The right hand side of (7.5) is of crucial importance for thermoacoustic systems. It is responsible for the flow divergence of the incompressible velocity field resulting from heat-release-induced density changes in the domain. This type of unsteady expansion is a source for the acoustic field, as was shown in Section 2.2. In fact, on comparing (7.5) with Eq. (2.15), the latter representing the effect of a compact heat source on the acoustic field, we observe that the two are identical. However, whereas (2.15) is related to the acoustic field, the divergence constraint (7.5) imposes the heat-release-associated divergence on the hydrodynamic flow. Accordingly, to be consistent in the limit of (i) vanishing Mach number and (ii) heat sources compact with respect to the acoustic wavelength, the hydrodynamic and the acoustic flow perturbations have to be identical. This applies, in particular, to the purely longitudinal case represented by Eq. (2.16).

Since Eq. (7.5) is linear in $\boldsymbol{u}$ as well as in q, we can apply it to deviations from a mean state without being restricted to small fluctuations. This point is important as, in general, relative fluctuations in the heat release rate will not be small in the case of finite-amplitude oscillations, which we want to include in our approach. In a quasi-one-dimensional setting, in which the velocity fluctuations are approximately plane at the inlet and the outlet of the hydrodynamic domain, (7.5) simplifies to

$$A \Delta u_{\mathrm{av}}^{(0)} = \frac{\gamma - 1}{\gamma P_0} Q, \tag{7.6}$$

where A is the cross-sectional area, the subscript 'av' denotes an area average, and Q is the global heat release.

The time-dependent acoustic pressure gradient $\nabla_{\xi} p^{(1)}$ is provided by the computation of the acoustic domain. However, in the quasi-one-dimensional applications considered in the following, this term will not have any effect on the reactive calculation but is important for studying instabilities associated with multi-dimensional effects. In the model

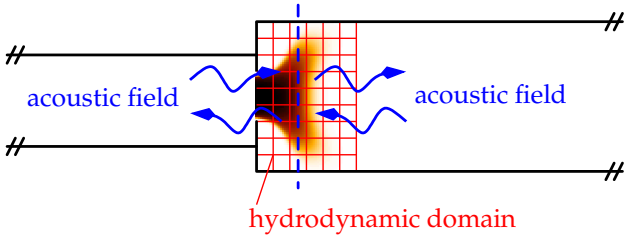

Figure 7.2: Schematic representation of the spatial decomposition into hydrodynamic and acoustic domains

problem considered in the next section, the acoustic field influences the hydrodynamics only via a model that relates the chemical composition at the inflow to the acoustic velocity (Section 7.5). The perforated-plate-stabilized flame configuration in Chapter 8, on the other hand, exhibits heat release fluctuations that result from the dependence of the burning velocity and the flame temperature on the approach flow. The response of the two-dimensional flame investigated in Chapter 9 is caused, in addition, by kinematic effects.

7.4 Coupling strategy

To make use of the proposed coupling strategy, we apply a subdivision of the total domain into hydrodynamic and acoustic parts. Consider the generic combustor set-up in Fig. 7.2, which corresponds to a typical single-burner test-rig. The actual reaction zone with the associated flow dynamics – the hydrodynamic domain – is short compared to the overall longitudinal dimension. This hydrodynamic domain is assumed compact with respect to the acoustic wavelengths relevant to the problem. For a configuration as in Fig. 7.2, the flow/flame–acoustic coupling can be considered as essentially one-dimensional: the acoustic velocity enforces an oscillation in the bulk velocity on the upstream side of the hydrodynamic zone, and the heat release acts as a volume source for the axial particle velocity.

Assuming the flame had no unsteady contribution, the acoustic variables on the up- and downstream side must be continuous (even in the presence of a temperature jump). With unsteady heat release in the hydrodynamic domain, the pressure remains continuous because the flame cannot sustain a pressure difference, but the particle velocity has a jump proportional to the amount of fluctuating heat release (Eq. (2.16)). If there are fluctuations in the velocity on the upstream side, u_{us}, the hydrodynamic domain entirely determines the unsteady flow divergence resulting from the associated perturbation in heat release.

In principle, the flow divergence over the hydrodynamic domain will be explicitly computed by a zero-Mach-type solver through the integration of the divergence constraint Eq. (7.5). However, using the jump conditions (2.16), the integrated heat release can also be used to deduce the velocity fluctuation on the downstream side, u_{ds}. Given now u_{ds}, there are associated pressure fluctuations at the same location that are only determined by the acoustic properties downstream of the flame. If the combustion chamber diameter is small compared to the acoustic wavelength, this relation can be simply expressed in

frequency domain by the impedance $\mathcal{Z}$ on the downstream side, viz.,

$$\hat{\wp} = \mathcal{Z}(\omega)\hat{u}_{\mathrm{ds}}, \tag{7.7}$$

where $\wp = p/(\rho c)$. Now, since the pressure is continuous across the flame (ρc is not), the same reasoning can be applied to the upstream side but vice versa. This gives a relation between the pressure and the velocity fluctuation upstream in terms of the admittance $\mathcal{A}$

$$\hat{u}_{\mathrm{us}} = \mathcal{A}(\omega)\hat{\wp}. \tag{7.8}$$

With Eqs. (7.7) and (7.8), the upstream velocity fluctuations can be directly related to those downstream as

$$\hat{u}_{\mathrm{us}} = \xi^{-1}\mathcal{A}\mathcal{Z}(\omega)\hat{u}_{\mathrm{ds}}, \tag{7.9}$$

where $\xi^{-1} = (\rho c)_{\mathrm{us}}/(\rho c)_{\mathrm{ds}}$, as before. This is the same strategy that we used in Section 6.4. The ratio of characteristic impedances appears only because we work with *specific* admittance and impedance, which are scaled with the product of density and speed of sound on either side of the flame.

The acoustic models are defined at the flame location (the maximum in mean heat release, say) and, accordingly, contain all factors affecting the plane-wave response upstream/downstream of the hydrodynamic zone. As such, complete information on the acoustic field without unsteady heat release is contained in $\mathcal{A}$ and $\mathcal{Z}$. If u_{us} is connected straight to u_{ds}, with no unsteady heat release in between, the resulting homogeneous system represents the unforced acoustics of the entire system. Hence, the purely acoustic eigenfrequencies ω_k satisfy $\xi^{-1}\mathcal{A}\mathcal{Z}(\omega_k) = 1$.

Construction of the admittance and impedance models $\mathcal{A}(\omega)$ and $\mathcal{Z}(\omega)$ can proceed in a variety of ways – using network-type techniques, finite-element-based Helmholtz solvers, or experimental measurements (or combinations of all). This offers a superior flexibility in setting up the acoustic representation. Also, changing geometric parameters like duct lengths, for instance, is easily accomplished. All of the methods mentioned above will be used in the following sections for the application of the two-way coupling to different configurations. For the first case, which is an elementary model problem, we set up the acoustic model purely based on simple one-dimensional acoustic relations. More elaborate tools have to be used for the second case because this is an actual thermoacoustic system with an experimental counterpart. A combination of experimentally identified and FEM (finite element method)-calculated submodels is used. For the third problem, we employ a model exclusively based on experimental combustor test-rig data.

To use the acoustic mapping (7.9) in conjunction with a hydrodynamic solver, a time-domain version is required. In principle, Eq. (7.9) can be translated to time domain by means of a convolution integral. This is, however, neither feasible nor efficient. On the other hand, since the acoustic mapping represents a linear time-invariant system, it is possible to give a time-domain variant in terms of a standard state-space formulation

$$\dot{\boldsymbol{x}} = \mathbf{A}\boldsymbol{x} + \mathbf{B}u_{\mathrm{ds}}, \tag{7.10a}$$

$$u_{\mathrm{us}} = \mathbf{C}\boldsymbol{x} + Du_{\mathrm{ds}}. \tag{7.10b}$$

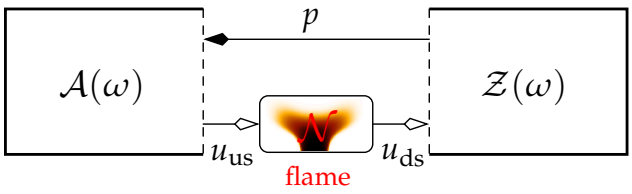

Figure 7.3: Illustration of the coupling strategy. The plane-wave acoustic field up- and downstream of the flame is represented by specific admittance and impedance $\mathcal{A}$ and $\mathcal{Z}$. The velocity divergence across the hydrodynamic domain is related to the upstream velocity fluctuation by the nonlinear operator $\mathcal{N}$. The pressure is assumed continuous on the up- and downstream sides.

The dimension of the state vector $\boldsymbol{x}$ is equal to the number of poles of $\mathcal{AZ}(\omega)$ (see Section 2.5.1). In general, this number will be infinite because the acoustic wave equation represents an infinite-dimensional system. This can be easily inferred from the presence of time delays associated with finite propagation speed. However, we are only interested in the low frequency regime, and therefore, a finite-dimensional truncation, approximating (7.9) in a certain frequency range, is sufficient. As introduced in Section 2.5.1, we write this as

$$\left[\begin{smallmatrix}\mathbf{A} & \mathbf{B}\\ \mathbf{C} & D\end{smallmatrix}\right] \overset{\mathrm{i}\omega}{\approx} \mathcal{AZ}(\omega), \qquad \text{for } \omega < \omega_{\max}. \tag{7.11}$$

Closure can now be achieved through the computation of the hydrodynamic zone with u_{us} as an unsteady boundary condition, with either the unsteady heat release or the downstream velocity fluctuation u_{ds} as the output. Naturally, this is not an instantaneous mapping, but we can write it symbolically as

$$u_{\mathrm{ds}} = \mathcal{N}[u_{\mathrm{us}}], \tag{7.12}$$

where $\mathcal{N}$ is a nonlinear operator given by a zero-Mach-type solver applied to the hydrodynamic zone. If the hydrodynamic solver does not deliver the velocity fluctuation on the downstream side, u_{ds}, we can alternatively use the integrated heat release and invoke the jump conditions (7.6) explicitly.

The coupled system now consists of (7.10), representing the acoustic field on the overall longitudinal scale, and (7.12), handling the complete hydrodynamic domain. A schematic illustration is shown in Fig. 7.3. By construction, this scheme treats the acoustic field as linear, but the nonlinearity of the flame response is fully accounted for in the hydrodynamic solver. (See also the discussion on the linearity assumption for the acoustics at the end of this section.)

We shall also remark that if the hydrodynamic solver runs with a constant time step, (7.10) can be replaced by an equivalent discrete time state-space model. The advantage is that numerical stability can be ascertained beforehand, and no additional time-integration scheme has to be implemented for the acoustic model.

In principle, a premixed flame may not only respond to acoustically induced velocity fluctuations, but also directly to perturbations in pressure (McIntosh 1991; Schmidt & Jiménez 2010; Wangher et al. 2008). This mechanism, resulting from the sensitivity of the chemical reaction rate to pressure, can indeed lead to instabilities (Clavin et al. 1990), in particular if additional coupling with a hydrodynamic instability is present (Pelcé &

Rochwerger 1992; Searby & Rochwerger 1991; Wu et al. 2003). We assume that in practical configurations, this effect will be inferior to velocity-fluctuation-induced heat release. Anyway, including a pressure coupling in the approach presented above is straightforward. Since the pressure perturbation at the heat source is known from the acoustic model, we can pass it as an additional input to the hydrodynamic solver. Then instead of (7.12), we simply have

$$u_{\mathrm{ds}} = \mathcal{N}[u_{\mathrm{us}}, p], \tag{7.13}$$

with the same coupling relations as before.

7.4.1 Linear stability

Our coupling approach is also easily extended to obtain information on linear stability of the system. Since the acoustic model is already linear, we only need a linearization of the hydrodynamic operator (7.12). An explicit linearization of a zero-Mach-type CFD solver is a rather non-trivial undertaking (but it is possible, van Kampen et al. 2007), and therefore, we will apply a linearization in a more pragmatic manner, as explained below.

Since the hydrodynamic operator is time-invariant, complete information on its linearized version is contained in the transfer function $\mathcal{N}_{\mathrm{lin}}(\omega) = \hat{u}_{\mathrm{ds}}/\hat{u}_{\mathrm{us}}$. The experimental measurement of flame transfer functions is an elaborate, time-consuming task and requires a dedicated experimental set-up (Paschereit et al. 2002). In the simulation, however, the determination of the flame response is not that involved. Since, in our case, the reaction zone can be computed free from acoustics, we do not have to take care of spurious signals due to wave reflections at the outlet, as would be the case when using a compressible solver. The linear response of the flame can be obtained from an isolated computation of the hydrodynamic domain with a suitable forcing signal at the inlet. For this purpose, different input signals, such as white noise, random binary sequences, multi-sines, pulses, or steps can be used (Huber & Polifke 2009; Polifke et al. 2001*b*; Zhu et al. 2005). However, two properties have to be ensured: (i) the forcing amplitude has to be sufficiently small so that the response lies entirely in the linear regime and (ii) the spectral content of the input signal must cover the relevant frequency range. As pointed out by Huber & Polifke, a random binary sequence is particularly favorable with respect to these requirements. From the forcing computation, we determine the discrete Fourier transforms of the input signal u_{us} and the output signal u_{ds}. Subsequent system identification (using the routine from Gustavsen & Semlyen 1999, for instance) then gives a linear model for the heat release response in time-domain form, viz.,

$$\dot{\boldsymbol{x}}_q = \mathbf{A}_q \boldsymbol{x}_q + \mathbf{B}_q u_{\mathrm{us}}, \tag{7.14a}$$

$$u_{\mathrm{ds}} = \mathbf{C}_q \boldsymbol{x}_q + D_q u_{\mathrm{us}}, \tag{7.14b}$$

where $\boldsymbol{x}_q$ is an auxiliary state vector.

Combining now Eqs. (7.10) and (7.14) results in a homogeneous linear system of the form $\dot{\boldsymbol{x}}_{\mathrm{c}} = \mathbf{A}_{\mathrm{c}} \boldsymbol{x}_{\mathrm{c}}$, where $\boldsymbol{x}_{\mathrm{c}}$ is the combined state vector of the two systems. $\mathbf{A}_{\mathrm{c}}$ is the dynamics matrix of the coupled system, which, using standard results from state-space algebra (Zhou et al. 1996), can be written in terms of the acoustic (no index) and flame

(index 'q') subsystems as

$$\mathbf{A}_\mathrm{c} = \begin{bmatrix} \mathbf{A} & \mathbf{B}\mathbf{C}_q \\ 0 & \mathbf{A}_q \end{bmatrix} + \frac{1}{1 - DD_q} \begin{bmatrix} \mathbf{B}D_q \\ \mathbf{B}_q \end{bmatrix} \begin{bmatrix} \mathbf{C} & D\mathbf{C}_q \end{bmatrix}. \tag{7.15}$$

The spectrum of $\mathbf{A}_\mathrm{c}$ determines stability for the combined system. If $\mathbf{A}_\mathrm{c}$ has at least one eigenvalue in the right half-plane, the linearized system is unstable and will exhibit exponential growth. Checking linear stability is particularly useful when running combined simulations with an expensive hydrodynamic solver, for then it can be checked beforehand whether any instabilities will be excited.

7.4.2 Discussion on the validity of linear acoustic models

Although the pulsations associated with thermoacoustic instabilities in gas turbine combustors may have significant amplitudes, the pressure variation compared to the mean pressure is still small, typically not more than 5 %. Therefore, a linear description of the acoustic field is commonly considered sufficient (Dowling 1997). In general, acoustic waves tend to steepen at high amplitudes due to the increase of the propagation velocity with pressure. However, in a recent assessment, Davies & Holland (2004) find that in practical cases, linear and nonlinear models for acoustic wave propagation in a duct show only negligible difference for amplitudes up to 10 % of the static pressure. This corresponds to a sound pressure level of 170 dB in the atmospheric case. Yet, this addresses only pure propagation issues. Strong geometrical non-uniformities, such as sharp corners at discontinuous area contractions or expansions, have to be considered as more critical to the assumption of linearity.

Area discontinuities provide the possibility of converting acoustic energy to fluctuating vorticity, which is then dissipated into heat (Bechert 1980; Bellucci et al. 2004; Zinn 1970*a*). This mechanism typically enters the nonlinear regime as the amplitude of the fluctuation velocity becomes comparable to the mean flow. For the no flow case, then obviously, there is no linear regime at all. Results in clear support of this can be found, for instance, in a recent paper by Rupp et al. (2010) on the investigation of an orifice subject to sound excitation with different amplitudes and mean flow conditions. The same applies to the acoustic boundary conditions, e.g., the termination impedance of an open-ended pipe (Heckl 1990; Skulina 2005).

Evidently, we have to expect localized nonlinear behavior in the acoustic field whenever the geometry changes abruptly. However, this phenomenon depends on the particular case considered and, thus, cannot be handled in a general fashion. We therefore continue to model the acoustics with linear theory, keeping in mind that for specific parts of the investigated configuration, nonlinear models may be required. Since our method works in time domain, this will generally not be difficult to implement.

7.5 Application to an elementary model problem

The simplest thermoacoustic system exhibiting self-excited oscillations, generated by the interaction of unsteady heat release with the acoustic field, is the well-known Rijke tube

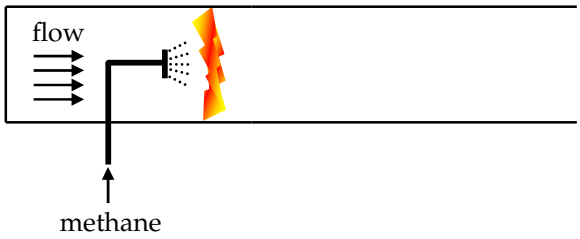

Figure 7.4: The considered model configuration. A laminar flame is stabilized in a tube with closed–open boundary conditions. Methane is injected with high pressure loss shortly upstream of the flame front so that perturbations in the upstream velocity induce fluctuations in equivalence ratio.

(Raun et al. 1993). This device consists of a tube, usually with open–open or closed–open boundaries, with a heat source concentrated at a certain axial position. Heat is transferred to the fluid either by an electrically heated gauze (Heckl 1990; Raun et al. 1993) or by a compact flame (e.g., Morgans & Dowling 2007).

The set-up we consider here for exemplary purposes is a one-dimensional closed–open Rijke tube with a flat laminar premixed flame. Different degrees of acoustic reflectivity (i.e., reflection coefficient magnitude) at the boundaries will be used for the coupled simulations. No specific flame stabilization mechanism is included. We consider the approach flow velocity to be equal to the flame speed, as e.g., in the experiments of Wangher et al. (2008). In this case, acoustically induced velocity fluctuations do not generate any unsteady heat release directly because the flame is merely displaced. A coupling from the acoustic field to the flame can be established if we account for fluctuations in equivalence ratio. These will generate perturbations in the burning velocity and thus generate unsteady heat release. In the model configuration, methane is injected with high pressure loss at a mean equivalence ratio of $\bar{\phi} = 0.7$ just upstream of the flame front (Fig. 7.4). In this case, acoustic velocity fluctuations induce perturbations in equivalence ratio via the relation proposed by Peracchio & Proscia (1999), which was already introduced in Chapter 6 (Eq. (6.2)). For the simulation of the Rijke tube, we set k_d to 0.5.

In the one-dimensional set-up considered here, the axial extent of the hydrodynamic domain, l, can be chosen so small as to merely accommodate the flame. Since the thickness of a lean, unstrained laminar premixed flame is of the order of 1 mm (Göttgens et al. 1992), the hydrodynamic domain length was chosen to be 5 mm with the flame front being located at a distance of 1.5 mm (in the mean) from the upstream boundary. The total up- and downstream duct lengths, denoted by L_{us} and L_{ds}, were chosen such that $L_{\mathrm{ds}}c_{\mathrm{us}}/(L_{\mathrm{us}}c_{\mathrm{ds}}) = 3/2$, and the total length was set to 2.8 m.

7.5.1 Hydrodynamic domain

The flame dynamics on the hydrodynamic scale are represented by a one-dimensional zero-Mach solver on a uniform grid.[1] The appropriate balance equations for species mass fractions and temperature and the divergence constraint, that are used for the computation, as well as the numerical details are given in the paper by Moeck et al. (2009).

[1] The computations of the hydrodynamic domain with the zero-Mach reacting-flow solver were made by Prof. Dr.-Ing. Heiko Schmidt, BTU Cottbus.

Methane–air combustion was represented by a skeletal mechanism consisting of 16 species and 25 elementary reactions (Peters 1992, p. 41). The velocity at the inflow boundary is set equal to the time-dependent flame speed to prevent the flame from moving out of the domain (see previous section). Air and methane mass fractions are set according to the mean equivalence ratio and the perturbations induced by the acoustic field according to Eq. (6.2). Integration of the divergence constraint (7.5) over the hydrodynamic domain yields the velocity outflow condition. The unsteady component of the outflow velocity is then passed to the acoustic model and serves as input to (7.10).

7.5.2 Representation of the acoustic field

For ease of notation, we work with the scaled acoustic pressure $\wp = p/(\rho c)$ in the following. With reference to Section 7.4, the objective of the acoustic model is to deliver a time-domain relation which maps the velocity fluctuations downstream of the flame to those upstream. We split this task into two parts, a lumped impedance downstream of the flame and a lumped admittance upstream. Eventually, these relations will take the form of finite-dimensional, linear time-invariant systems, mapping u_{ds} to $\wp$ and $\wp$ to u_{us}, which can be combined to give the desired acoustic model (7.10).

When dealing with purely acoustic systems, a more intuitive approach is to model the input–output behavior of the plane wave mode in terms of the amplitudes of the up- and downstream traveling waves g and f (cf. Section 2.1.1). Then, for the downstream part with constant cross-sectional area and uniform temperature, we have

$$\hat{g}_{\mathrm{ds}}/\hat{f}_{\mathrm{ds}} = -|\mathcal{R}_{\mathrm{ds}}|\,\mathrm{e}^{-\mathrm{i}\omega\tau_{\mathrm{ds}}}, \tag{7.16}$$

where the propagation time is given by $\tau_{\mathrm{ds}} = 2L_{\mathrm{ds}}/c_{\mathrm{ds}}$, and $|\mathcal{R}_{\mathrm{ds}}|$ is the reflectivity (which we will specify). Due to the time delay involved, the transfer function (7.16) represents an infinite-dimensional system and cannot be converted to a state-space representation in an exact manner. However, truncation to a finite-dimensional state space is accomplished by making use of a Padé approximant of the time delay. Following this procedure yields a state-space description of the reflection coefficient on the downstream side of the form

$$\dot{\boldsymbol{x}} = \mathbf{A}\boldsymbol{x} + \mathbf{B}f_{\mathrm{ds}}, \tag{7.17a}$$

$$g_{\mathrm{ds}} = \mathbf{C}\boldsymbol{x} + Df_{\mathrm{ds}}, \tag{7.17b}$$

with

$$\left[\begin{smallmatrix}\mathbf{A} & \mathbf{B}\\ \mathbf{C} & D\end{smallmatrix}\right] \overset{\mathrm{i}\omega}{\approx} \mathcal{R}_{\mathrm{ds}}. \tag{7.18}$$

The dimension of the linear system (7.17) is equal to the order of the Padé approximant.

The state-space representation of the impedance on the downstream side, mapping u_{ds} to $\wp_{\mathrm{ds}}$, is then written analogously as

$$\dot{\boldsymbol{x}} = \tilde{\mathbf{A}}\boldsymbol{x} + \tilde{\mathbf{B}}u_{\mathrm{ds}}, \tag{7.19a}$$

$$\wp_{\mathrm{ds}} = \tilde{\mathbf{C}}\boldsymbol{x} + \tilde{D}_{\mathrm{ds}}u_{\mathrm{ds}}. \tag{7.19b}$$

Using now the elementary plane wave relations $\wp = f + g$ and $u = f - g$, it is found that the state-space matrices in (7.19) are related to those in (7.17) by the transformation

$$\tilde{\mathbf{A}} = \mathbf{A} + \beta \mathbf{B}\mathbf{C}, \quad \tilde{\mathbf{B}} = \beta \mathbf{B}, \tag{7.20a}$$

$$\tilde{\mathbf{C}} = 2\beta \mathbf{C}, \quad \tilde{D} = \beta(1 + D), \tag{7.20b}$$

with $\beta = 1/(1 - D)$. Apparently, this transformation is only possible whenever $D \neq 1$. This makes sense because a unit feedthrough in (7.17) corresponds to a velocity node (+ something dynamic) which has an infinite impedance. Note, however, that D will be zero, typically, as the wave incident to the downstream part, f_{ds}, will have no direct feedthrough to the reflected wave g_{ds}.

The same strategy can be used to construct a state-space model for the admittance on the upstream side, which has a structure analogous to (7.19) but with $\wp$ as input and u_{us} as output. The time-domain impedance and admittance systems can then be combined to yield the relation (7.10), mapping u_{ds} to u_{us}, for the particular case considered here.

In the simple case of a duct with constant cross section and uniform temperatures up- and downstream of the flame, which we consider in this model problem, the exact frequency domain relation (7.9) takes the form

$$\hat{u}_{\mathrm{us}} = -\xi^{-1} \frac{1 + \mathrm{i}\mathcal{Z}_{\mathrm{us}} \tan(k_{\mathrm{us}} L_{\mathrm{us}})}{\mathcal{Z}_{\mathrm{us}} + \mathrm{i} \tan(k_{\mathrm{us}} L_{\mathrm{us}})} \frac{\mathcal{Z}_{\mathrm{ds}} + \mathrm{i} \tan(k_{\mathrm{ds}} L_{\mathrm{ds}})}{\mathrm{i}\mathcal{Z}_{\mathrm{ds}} \tan(k_{\mathrm{ds}} L_{\mathrm{ds}}) + 1} \hat{u}_{\mathrm{ds}}, \tag{7.21}$$

which is based on elementary plane wave calculations. $\mathcal{Z}_{\mathrm{us}}$ and $\mathcal{Z}_{\mathrm{ds}}$ are the specific boundary impedances at the upstream and the downstream end of the acoustic domain. The frequency response of the state-space model (Eq. (7.10)), as it is used in the coupled simulation for the present case, was set up with a state dimension of 26 and is plotted in Fig. 7.5 with a boundary reflectivity of 0.8 (at the inlet and at the outlet). The analytic relation (Eq. (7.21)) is added for comparison. Up to 600 Hz, the agreement is excellent. Deviations at higher frequencies are due to the limited order of the Padé approximants used to represent the time delays in finite-dimensional state space. The accuracy could be easily increased by using higher-order Padé approximants. However, since we consider only the long-wave case, this representation was regarded as being sufficient.

7.5.3 Simulation results

Coupled simulations were run with different degrees of reflectivity at the boundaries. The state vector $\boldsymbol{x}$ in Eq. (7.10) was initialized with an array of uniformly distributed random numbers with small magnitude to accelerate the growth of unstable modes.

Figure 7.6 shows the temporal evolution of the laminar burning velocity s_l and the equivalence ratio at the inlet of the hydrodynamic domain. Initially, the reflection coefficient magnitude at the up- and downstream ends is set to 0.8. The system is unstable, and the quarter-wave mode starts to grow exponentially in time until it settles on a finite-amplitude limit-cycle oscillation with a frequency of 45 Hz. At $t = 0.32$ s, the reflectivity $|\mathcal{R}|$ of both boundary conditions is decreased to 0.7. This results in a lower oscillation amplitude; however, the system is not stabilized.

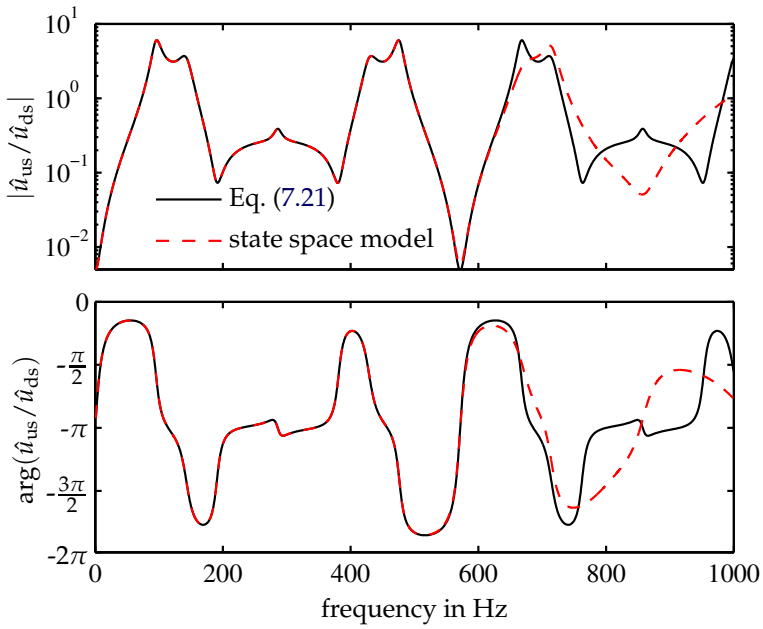

Figure 7.5: Transfer function relating velocity fluctuations downstream of the flame to those upstream. The analytic solution (Eq. (7.21)) is compared with a state-space model based on Padé approximants for the time delays associated with the acoustic wave propagation.

The same computation was repeated, except that now the reflectivity is decreased from 0.8 to 0.6 (Fig. 7.7). This results in a stabilized system, and the oscillations in equivalence ratio and burning velocity slowly decrease and settle to zero. Simulations were also performed with reducing the reflectivity even further to 0.2. In this case, the system is stabilized almost immediately (not shown) because virtually all fluctuation energy that is generated by the flame is transported out of the system at the boundaries. Similar results were obtained by Giauque et al. (2007) and Martin et al. (2006) with compressible solvers and a change in the relaxation coefficient of the characteristic boundary condition (which changes the reflectivity).

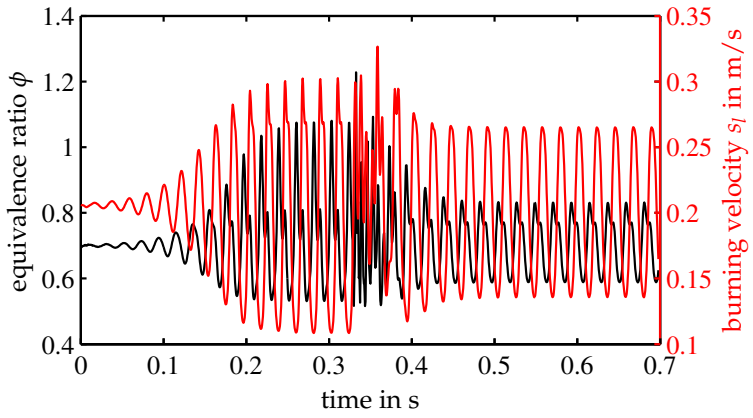

Figure 7.6: Time traces of equivalence ratio and laminar burning velocity. A finite-amplitude limit-cycle oscillation at 45 Hz is established. The reflection coefficient magnitude is decreased from 0.8 to 0.7 at $t = 0.32$ s.

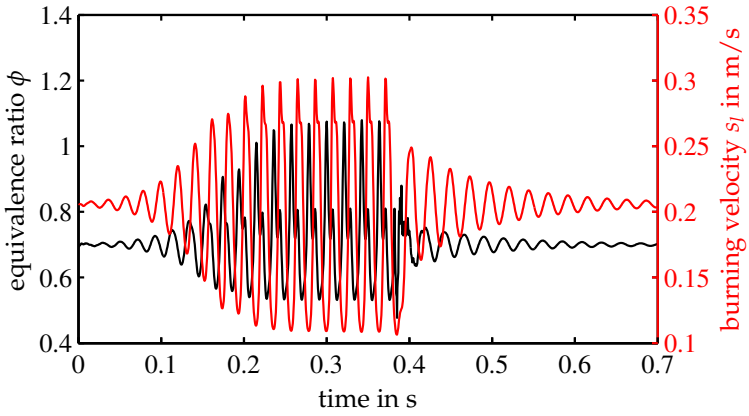

Figure 7.7: Time traces of equivalence ratio and laminar burning velocity. A finite-amplitude limit-cycle oscillation at 45 Hz is established. The reflection coefficient magnitude is decreased from 0.8 to 0.6 at $t = 0.39$ s.

Normalized amplitude spectra of the fluctuations in equivalence ratio and the flame speed are shown in Fig. 7.8 for a boundary reflectivity of $|\mathcal{R}| = 0.7$. Nonlinear distortion is more apparent in the ϕ oscillations, but on the other hand, these are also damped by diffusion before reaching the flame front. Since the convection speed is equal to the burning velocity (≈ 0.2 m/s) in the current set-up, the wavelength of the equivalence ratio perturbations, traveling from the inlet of the hydrodynamic domain to the flame front, is rather small. The higher harmonic components are therefore strongly damped by diffusion even though the ϕ wave travels less than 2 mm from the inlet to the reaction zone.

To assess the complexity of the unsteady response of the flame, we consider the trajectory of the limit-cycle oscillation in equivalence-ratio–burning-velocity phase space (Fig. 7.9). This is a suitable representation of the flame dynamics for this case because the ϕ perturbations are imposed by the acoustic field, and the unsteady heat release is a direct result of the burning velocity oscillation. For comparison, the static correlation of Abu-Orf & Cant (1996) is added in the plot. The trajectory corresponding to lower reflectivity remains close to the equilibrium parametrization throughout the whole oscillation cycle. In

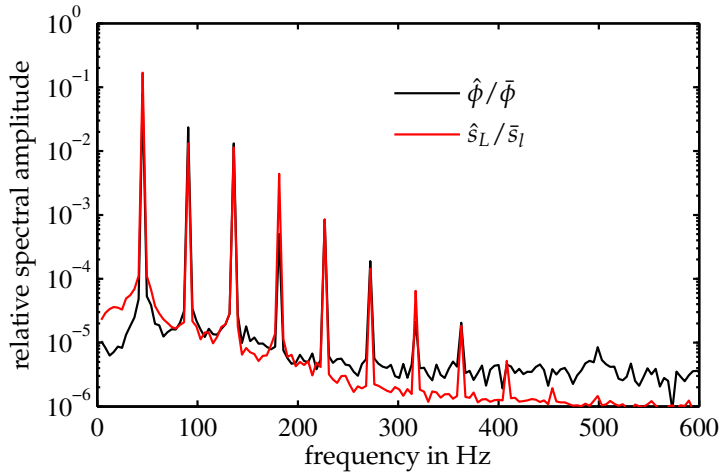

Figure 7.8: Amplitude spectra of equivalence ratio and burning velocity fluctuations (normalized with the mean values) for a reflection coefficient magnitude of $|\mathcal{R}| = 0.7$

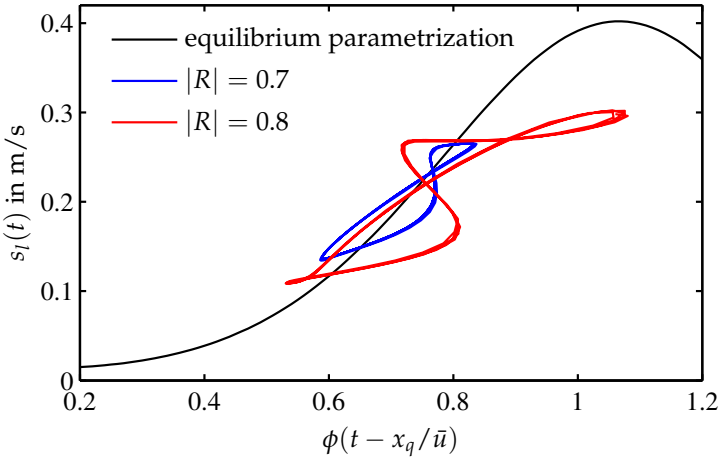

Figure 7.9: Limit cycle in equivalence-ratio–burning-velocity phase space for reflection coefficient magnitudes $|\mathcal{R}| = 0.7, 0.8$. The time lag from the inlet of the hydrodynamic domain to the flame front (at x_q) has been accounted for. The equilibrium parametrization for $s_l(\phi)$ as given by Abu-Orf & Cant (1996) is added for comparison.

this case, the flame dynamics are not unduly complex and could have been modeled by a static relation and a time lag with reasonable accuracy. With stronger reflection, the instability grows to higher amplitudes and larger deviations from the static ϕ–s_l correlation can be observed.

7.5.4 Discussion

The hybrid method, a combination of an incompressible reacting-flow simulation and a time-domain realization of an acoustic network, was shown to be capable of delivering meaningful results for an elementary model configuration. Linear instability and nonlinear saturation could both be captured by the coupled method. A change in the acoustic boundary conditions had the expected effect in the coupled simulation. Although the acoustic model in this example was of the most simple form, there is no restriction in using more complex networks. The approach is applied to a flat flame Rijke tube in the next chapter, in order to validate the method with experimental data. Control applications are considered in Chapter 9.

Chapter 8

Validation of the Coupling Approach on the Basis of an Experimental Flat Flame Rijke Tube

To validate the two-way coupling approach for modeling thermoacoustic instabilities, which was presented in the previous chapter, we consider a generic combustor set-up specifically built for this purpose. This set-up is similar to the model configuration investigated before, but more complexities are involved, typical for a real system. The set-up is essentially of Rijke tube type, but up- and downstream ducts have different cross-sectional areas. Also, as we will see below, considerable more effort has to be made in modeling the temperature field and the acoustic boundary conditions. The flame, which is still flat in the operating regime considered, is stabilized downstream of a perforated plate. Accordingly, the same zero-Mach solver as in the previous chapter can be used with only slight modifications. The linear transfer function of this type of burner-stabilized premixed flame has been studied extensively in the literature. Experimental investigations were made by Schreel et al. (2002) and analytical and numerical studies by Rook et al. (2002). However, so far no attempt has been made to model finite-amplitude limit-cycle oscillations for this kind of set-up numerically.

8.1 Experimental set-up

A schematic of the experimental arrangement is shown in Fig. 8.1. Natural gas and air are mixed upstream of the plenum duct in feed line tubes of 4.7 mm diameter. The water-cooled plenum duct has a diameter of $D_{\mathrm{us}} = 105\,\mathrm{mm}$, a length of $L_{\mathrm{us}} = 725\,\mathrm{mm}$ and is made of steel. A perforated brass plate of 2 mm thickness, mounted between the upstream and the downstream duct, is used to anchor a planar flame. The holes of the perforation have a diameter of 0.5 mm with a pitch of 0.7 mm and are assembled in a hexagonal pattern. For this kind of burner, the stabilization of the flame is mainly heat loss controlled (de Goey et al. 1993).

The downstream duct has a diameter of $D_{\mathrm{ds}} = 51\,\mathrm{mm}$, a length of $L_{\mathrm{ds}} = 505\,\mathrm{mm}$ and is made of aluminum; the base is air-cooled. Four 1/4″ condenser microphones (G.R.A.S. 40BP) are mounted in the upstream part, three in the upper half, at $x = -168.5$,

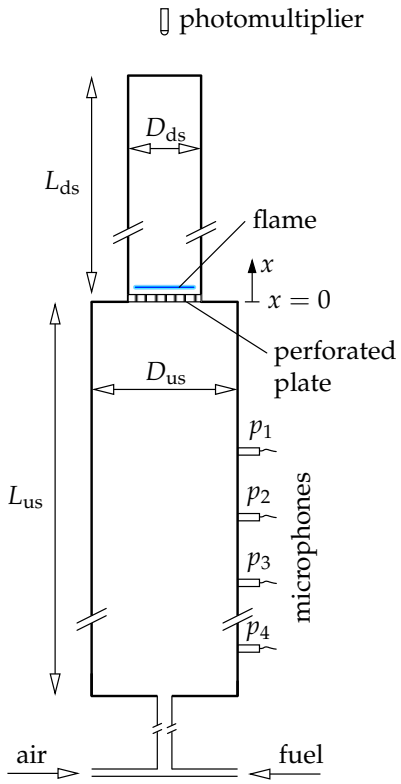

Figure 8.1: Experimental set-up of the flat flame Rijke tube. The air–natural-gas mixture enters the plenum duct from the bottom. A laminar flat flame stabilizes downstream of the perforated plate in a duct of smaller diameter. The acoustic field in the plenum duct can be accessed with four microphones. Chemiluminescence of OH-radicals is monitored with a photomultiplier.

-257.5 ,-346.5 mm, and one close to the bottom at $x = -648$ mm. A photomultiplier (Hamamatsu H5784-04), equipped with a UV-filter (Edmund Optics U-340, passband 295–385 nm) and a collimator (Glen Spectra LC-4U), is set up to detect the chemiluminescence intensity from OH-radicals. A thermocouple with a 0.3 mm bead is attached inside one of the holes of the perforation. Air and gas mass flows are monitored with Coriolis flow meters (Endress & Hauser).

8.2 Coupled model for the flat flame Rijke tube

8.2.1 Hydrodynamic domain

The flame in our set-up is nominally flat. At low equivalence ratios, a cellular instability was observed (see Section 8.3.2), but these conditions are not considered for the coupled simulation. Therefore, we can represent the flame still in a one-dimensional setting. In contrast to the configuration considered in the previous section, the flame is stabilized downstream of a perforated plate. For this case, the same zero-Mach solver with the identical chemical scheme was used.[1] The hydrodynamic field through the perforated plate was not modeled in detail. Flame stabilization is achieved by taking into account the heat loss to the burner plate (Rook 2001, see below). The total length of the hydrodynamic domain is 7 mm. This amounts to approximately 0.5 % of the total domain length.

The first 2 mm in the numerical model for the hydrodynamic domain represent the burner. We assume the burner has a constant temperature (infinite heat capacity, Rook

[1] The computations of the hydrodynamic domain with the zero-Mach reacting-flow solver were made by Prof. Dr.-Ing Heiko Schmidt, BTU Cottbus.

2001) and that there is perfect heat transfer to the fluid. The plate temperature was set to 500 K, close to the temperature measured at the plate in the experimental set-up. At the inflow boundary, the velocity is set equal to the mean velocity plus a fluctuation. The latter is obtained from the acoustic model in the coupled simulation.

8.2.2 Acoustic model

In the upstream duct, the cut-on frequency for the first azimuthal mode is approximately 2 kHz (at room temperature). For the downstream part, the plane-wave regime extends to even higher frequencies, in particular for the case with combustion. We can therefore model the major part of this set-up with plane-wave assumptions. The mean flow can be safely neglected in the acoustic model, the Mach number being of the order of 10^{-3}.

As in the preceding chapter, we will set up the acoustic model in two parts, handling the up- and downstream plane-wave response individually. In principle, we could resort to purely analytical techniques in a network-type fashion. For the set-up considered here, however, we choose to employ a finite element computation based on the Helmholtz equation (2.5) to derive a low-order acoustic model. We use the commercial multi-purpose finite element solver Comsol Multiphysics[2] (Version 3.3).

The reason for not using simplified network techniques is twofold: (i) the perforated plate is located immediately downstream of an area contraction (see Fig. 8.1); the acoustic near-fields of the two elements thus interfere, which is difficult to account for in a network model; (ii) the temperature distribution in the downstream tube is far from being homogeneous, in axial as well as in radial direction, due to heat losses at the duct walls.

The finite element model was set up as follows. The geometry of the Rijke tube, as described in Section 8.1, was represented in an axisymmetric manner. The perforated plate was modeled as a sequence of rings with the same integral porosity as that of the original perforation. In general, there will be some dissipation inside the holes of the perforation associated with the acoustic boundary layer (Melling 1973; Noiray et al. 2007). Since the plate thickness was only 2 mm, we neglected this effect. Another potential source for acoustic losses is the mean flow through the perforated plate. Due to the small Mach number, we consider this effect to be negligible, too. The temperature distribution in the duct downstream of the flame was calculated by assuming laminar flow inside the tube and natural convection and radiation to the ambient outside of the tube. The acoustic boundary condition at the tube exit was specified according to an unflanged open pipe (Eq. (2.10)).

The upstream boundary condition is close to being sound hard. Due to the mixture feed line, which acts similar to a $\lambda/4$-resonator, the magnitude of the reflection coefficient was noticeably decreased at distinct frequencies. Therefore, we measured the upstream reflection coefficient using the Multi-Microphone-Method (Appendix A). The downstream tube was removed and exchanged for a speaker to facilitate this measurement. A sweep signal was used to excite the acoustic field over a broad frequency range. The four microphones were used to decompose the acoustic field into incident and reflected components, from which the reflection coefficient was calculated. The measured reflection coefficient is then used as a boundary condition for the upstream end in the finite element model.

[2] http://www.comsol.com

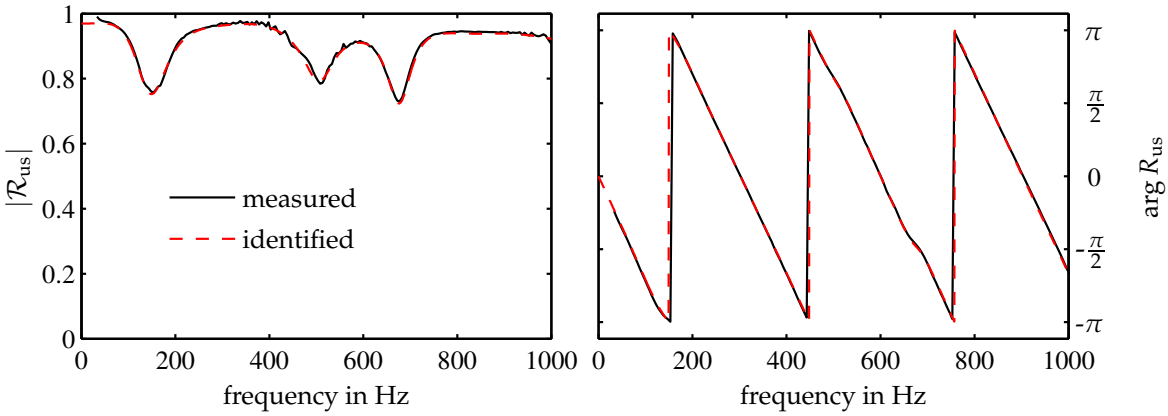

Figure 8.2: Upstream reflection coefficient. Measured results and identified model used in the finite element computation. The phase reference is at the microphone closest to the burner plate.

Figure 8.2 shows the measured reflection coefficient and an identified rational approximation. Reduced reflectivity at frequencies around 150, 500, and 670 Hz can be observed, which underlines the need to take into account accurate boundary conditions. The phase reference for the reflection coefficient shown in Fig. 8.2 is at the topmost microphone. In the finite element model, the phase was corrected to the actual upstream boundary.

The lumped impedance/admittance shown in Fig. 7.3 contain all components affecting the plane-wave response downstream/upstream of the flame. They can be obtained from the finite element model by cutting the geometry in two halves at the flame location and computing the response for the individual parts. In other words, to compute the downstream impedance, only the upper half of the geometry is considered. At the flame location, a velocity boundary condition $\hat{\boldsymbol{u}}\cdot\boldsymbol{n} = 1$ ($\boldsymbol{n}$ denoting the unit normal pointing inside) is applied at all frequencies of interest. The impedance is then calculated from the solution as $\mathcal{Z} = \hat{\wp}$, where $\hat{\wp}$ is the scaled pressure at the boundary. An analogous procedure applied to the upstream part gives the admittance $\mathcal{A}$.

The transfer function relating the velocity perturbation downstream of the flame to that upstream is simply the product of impedance and admittance, as explained in Section 7.4, viz., $\hat{u}_{us} = \xi^{-1}\mathcal{Z}\mathcal{A}(\omega)\hat{u}_{ds}$. The transfer function $\hat{u}_{us}/\hat{u}_{ds}$, as obtained from the finite element model, is shown in Fig. 8.3. The frequencies of the resonant modes of the purely acoustic system can be estimated from this plot by noting that $\hat{u}_{us}(\omega) = \hat{u}_{ds}(\omega)$ holds, whenever ω is an eigenvalue. Since, in our case, the boundary conditions are not fully reflecting, the eigenvalues are all located in the upper half of the ω-plane, i.e., they are damped. However, we can recover the approximate mode frequencies by requiring that the transfer function $\hat{u}_{us}/\hat{u}_{ds}$ is close to 1. The first six mode frequencies, which are all members of the $\lambda/4$-family of the entire geometry (up- and downstream ducts), are plotted as dashed lines in Fig. 8.3.

From the finite element computation, the transfer function $\mathcal{Z}\mathcal{A}(\omega)$ is only available at discrete real frequencies. A time-domain relation $u_{ds} \rightarrow u_{us}$ in form of a finite-dimensional state-space realization (Eq. (7.10)) is obtained from subsequent system identification using

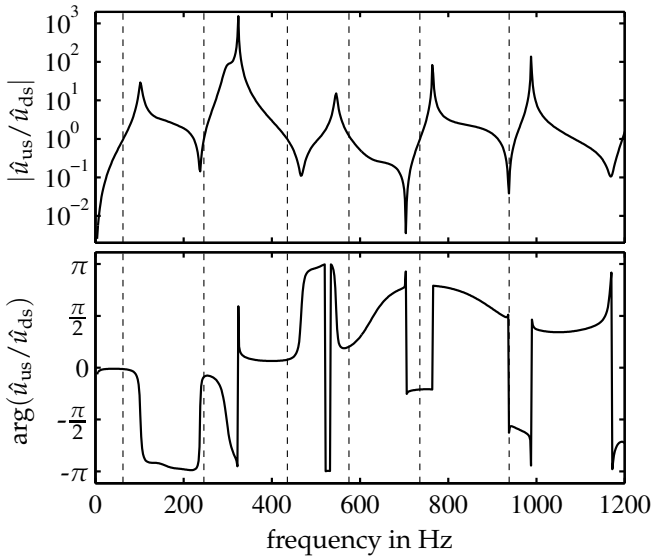

Figure 8.3: Transfer function relating perturbations in velocity downstream of the flame to those upstream. Dashed vertical lines denote acoustic resonant modes, from left to right: $\lambda/4$ at 63 Hz, $3\lambda/4$ at 246 Hz, $5\lambda/4$ at 435 Hz, $7\lambda/4$ at 575 Hz, $9\lambda/4$ at 736 Hz, $11\lambda/4$ at 938 Hz.

the routine of Gustavsen & Semlyen (1999), as described in Section 2.5. To cover a frequency range of 0–1200 Hz, a state dimension of 24 was found to be sufficient. The absolute error of the transfer function computed with the Helmholtz solver and that of the identified state-space realization was smaller than 10^{-4} in the frequency range mentioned above.

8.3 Results and discussion

We begin with a discussion of the flame's response to forcing at the frequency of the $5\lambda/4$-mode, which was found unstable in the experiment. Subsequently, we shortly summarize the stability characteristics as observed in the experiment and give a detailed comparison of the finite-amplitude oscillations computed with the coupled model and obtained from the measurements.

8.3.1 Flame response to fluctuations in velocity at the $5\lambda/4$-mode frequency

Results for an open-loop forcing of the flame (without acoustic feedback) are shown in Fig. 8.4. In the experiment, the duct downstream of the flame was removed, and an additional forcing segment with two compression drivers was installed in the upstream part. With this set-up, no self-excited oscillations were observed, and the flame response to fluctuations in velocity could be visualized. A mean image of the side-view of the flame is shown in Fig. 8.4 (a). The horizontal extent corresponds to roughly half of the burner plate. Based on the maximum intensity along every image column, the flame can be considered as flat. The intensity has a larger vertical extent in the middle resulting from the circular shape of the flame and the associated intensity projection detected by the camera. Figure 8.4 (b) represents phase-averaged intensity distributions for a forcing frequency of

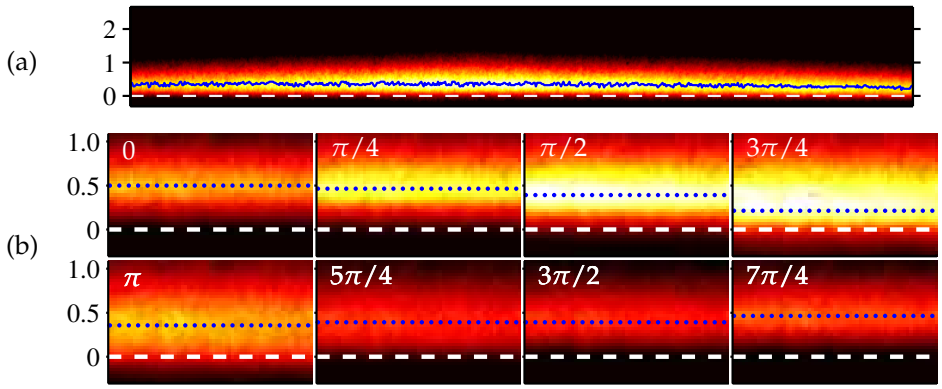

Figure 8.4: (a) Mean image of the flame. The black solid line represents the maximum intensity along the vertical direction. The dashed line marks the location of the perforated plate. The vertical scale is in millimeters (true aspect ratio). (b) Phase-averaged images of the center part of the flame submitted to harmonic forcing. The dotted lines denote the vertical location of the maximum intensity integrated along the horizontal direction.

431 Hz and a velocity fluctuation amplitude of 0.5 m/s. Corresponding numerical results in terms of the H-radical mass fraction distributions over the forcing cycle are shown in Fig. 8.5.

The phase-averaged images (Fig. 8.4 (b)) show that the flame acquires its maximum intensity while moving upstream to the burner. At the minimum stand-off distance, the intensity drops and remains on a low level while the flame moves back downstream. The same characteristic is reflected in the H-radical mass fraction distributions for one forcing cycle from the numerical computation (Fig. 8.5). The absolute movement of the Y_H-maximum is about 0.4 mm and agrees reasonably well with a displacement of the image intensity maximum of 0.3 mm in the experiment.

8.3.2 Summary of the stability characteristics of the Rijke tube

Self-excited oscillations were observed in the experiment for equivalence ratios ranging from 0.65–0.75 (depending on mass flow) up to 1.2–1.3 (Fig. 8.6). Thermoacoustic stabilization, as the equivalence ratio was decreased, was accompanied by the onset of a cellular flame front instability (Matalon 2007). The boundary between flat and cellular flames is also shown in Fig. 8.6. It is interesting to note here that the boundaries for thermoacoustic and cellular flame front stability almost coincide. The data for the onset of the cellular

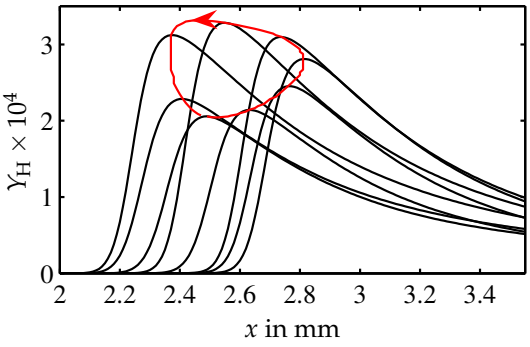

Figure 8.5: H-radical mass fraction distributions from the numerical computation for the same forcing conditions as in Fig. 8.4. x represents the coordinate in the hydrodynamic domain; the trailing edge of the the perforated plate is located at 2 mm.

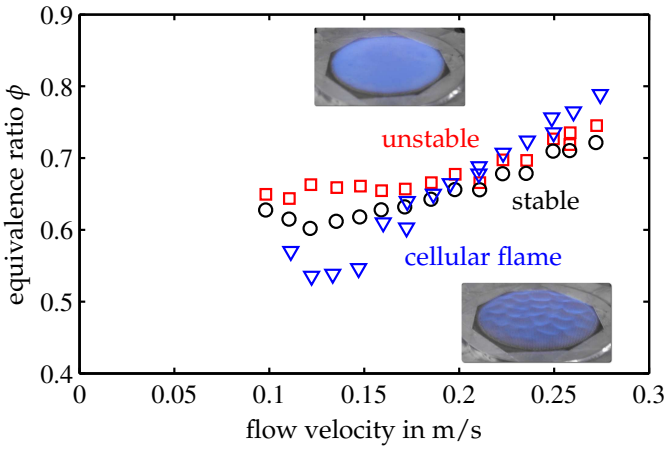

Figure 8.6: Stability map for the experimental configuration. Squares mark conditions at which thermoacoustic oscillations were observed, circles those for which this was not the case. For conditions leaner than the triangles, a cellular flame front instability was evidenced for the case without downstream tube. The flow velocity is given as a bulk value with respect to the downstream area.

flame front was, however, acquired with the downsteam tube removed so that, in this case, the flame is unconfined. This uncertainty could have been removed by using a Pyrex tube. In this way, it would have been possible to assess whether thermoacoustic stabilization is indeed accompanied by the onset of a cellular flame front instability. Since this was not the focus of this investigation, we simply note that there is an intriguing coincidence of thermoacoustic and hydrodynamic stability borders.

A general trend was that increasing the equivalence ratio from the lean stability border resulted in higher oscillation amplitudes. The instability was always associated with the $5\lambda/4$-mode of the geometry. With shorter downstream tube ($L_{\mathrm{ds}} = 300\,\mathrm{mm}$), unstable $3\lambda/4$- and $7\lambda/4$-modes were also observed.

8.3.3 Comparison of coupled simulation and experiment

The results of the coupled simulation are compared to those from the experiment at an equivalence ratio of 0.85 and a total mass flow of $0.61\,\mathrm{g/s}$, corresponding to a thermal power of 1.36 kW. These operating conditions were chosen based on the following considerations. Close to the stability border, multi-dimensional effects were expected to be significant, due to the onset of a cellular flame front instability (see Section 8.3.2). In the coupled model, the combustion zone is treated only one-dimensional, and therefore, the equivalence ratio had to be chosen sufficiently far away from the stability border. Linear stability analysis (see below) was used to assess whether the experimentally observed oscillation mode was indeed linearly unstable in the coupled model.

Linear stability

The linear stability analysis was based on the acoustic model mapping u_{ds} to u_{us} (Eq. (7.10), see also Section 8.2.2), combined with a numerically determined flame transfer function, as explained in Section 7.4.1. The latter was obtained from impulse response computations

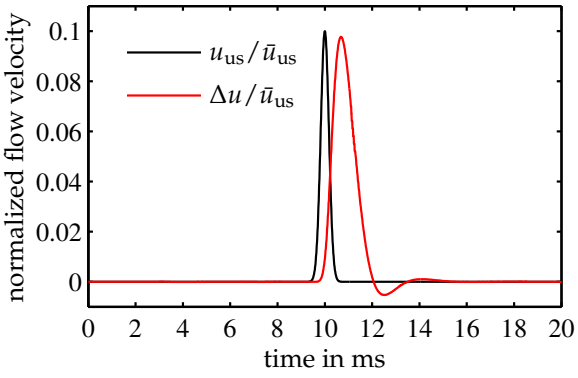

Figure 8.7: Response of the unsteady expansion across the flame, Δu, to an impulse excitation in the approach flow velocity. Normalized unsteady components of the expansion and the approach flow velocity are shown.

of the flame with the zero-Mach solver. The numerically computed impulse response is shown in Fig. 8.7. The inflow velocity was perturbed with a Gaussian pulse with an amplitude of 10 % of the mean and a standard deviation of $\sigma = 0.173$ ms. The corresponding standard deviation in frequency domain is about 1 kHz so that the input signal has sufficient spectral content up to that frequency. In general, a pulse is not the optimal excitation signal for the numerical calculation of a transfer function because the maximum amplitude is large compared to its spectral content. This can be an issue in the presence of significant noise (Zhu et al. 2005); however, in the present case, the flame is laminar, and input and output signals were found to be well correlated. A test for the linearity of the response was conducted by computing a second case with a negative (but otherwise identical) inflow perturbation. This resulted in a negligible difference in the negative output signal, $-\Delta u$, compared to the first simulation. The computed flame response shows typical effects, such as time-lag and low-pass characteristics (Fig. 8.7).

The dominant eigenvalues of the dynamics matrix of the combined acoustics–flame system (see Section 7.4.1) are plotted in Fig. 8.8. For a better comparison with the acoustic convention $\sim e^{i\omega t}$, the eigenvalues have been multiplied by $-i$ so that the lower half-plane corresponds to instability. The family of $\lambda/4$-modes can be clearly identified without combustion (squares). Since the acoustic boundary conditions are partially absorbing, all the eigenvalues are in the upper half-plane. Through the interaction with the flame (triangles), the $5\lambda/4$- and the $7\lambda/4$-modes are destabilized significantly. The unstable $5\lambda/4$-mode, which exhibits the larger growth rate, has a frequency of 446 Hz. This is close to the oscillation frequency observed in the experiment and in the coupled simulation (see below).

Pressure histories and spectra for self-excited oscillations

Sample time traces of the pressure at the microphone positions (see Fig. 8.1) from the coupled simulation and from the experiment are compared in Fig. 8.9. The pressures at the microphone positions are not explicit variables in the coupled simulation, but they can be recovered from the velocity fluctuation u_{us} in a post-processing step. Based on the finite element model for the combustor acoustics, transfer functions relating $\hat{u}_{us}$ to the pressures at the microphone locations can be determined. Time-domain realizations of these transfer functions are then used to compute the acoustic pressures corresponding to the velocity fluctuation u_{us} that is obtained from the coupled simulation.

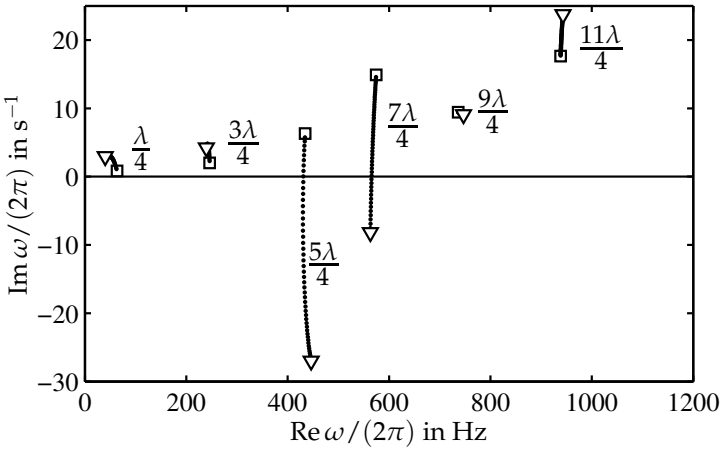

Figure 8.8: Eigenvalues from linear analysis. Squares: eigenvalues of the purely acoustic system with $u_{\mathrm{us}} = u_{\mathrm{ds}}$; triangles: eigenvalues with flame; dots: loci for zero to full flame model amplitude.

The pressure signals exhibit strong oscillations at the $5\lambda/4$-mode frequency, as predicted by linear stability analysis (see Fig. 8.8). The maximum measured sound pressure level was 137 dB. Significant subharmonic components can also be observed, most clearly at the location of microphone 4 (see Fig. 8.1). The amplitude of microphone 1 is smallest because its location is close to a pressure node of the $5\lambda/4$-mode. Although the amplitude of the fundamental oscillation is slightly larger in the experimental pressure signals, good agreement is found compared to the computation. In particular, the amplitude and phase relationships between the four signals are clearly preserved in the simulation.

Corresponding amplitude spectra of the acoustic pressure at the microphone locations are shown in Fig. 8.10. Results from the experiment and from the coupled simulation are shown. The highest spectral peak (*d*) stems from the unstable $5\lambda/4$-mode. The main frequencies of oscillation as obtained from the experiment (427 Hz) and from the simulation (432 Hz) differ by less than 2 %. Close agreement is found for the amplitudes, too. Both results also reveal a strong subharmonic component of order 1/2 (*b*). As a result of the nonlinear interaction, spectral peaks are also found at frequencies corresponding to the sum of the fundamental frequency and its subharmonic (*e*), the 2nd harmonic of the fundamental frequency (*g*), and the sum of the 2nd harmonic and the subharmonic (*i*). The features labeled *a*, *c*, *f* and *h* correspond to damped resonances associated with the stable $\lambda/4$-, $3\lambda/4$-, $9\lambda/4$- and $11\lambda/4$-modes (cf. Fig. 8.8), respectively.

Comparing numerical and experimental results, good quantitative agreement is found for the dominant features, i.e., the spectral peaks at the fundamental frequency and at the subharmonic. With respect to the minor spectral features, there is qualitative correspondence between experiment and simulation, but the associated amplitudes are quite different. In essence, the peaks belonging to the harmonics and nonlinear combinations with the subharmonic are more distinct in the experimental results. On the other hand, the resonances associated with the stable acoustic modes are more pronounced in the simulation, in particular, the $\lambda/4$-mode. Also, the noise floor is higher in the numerical results.

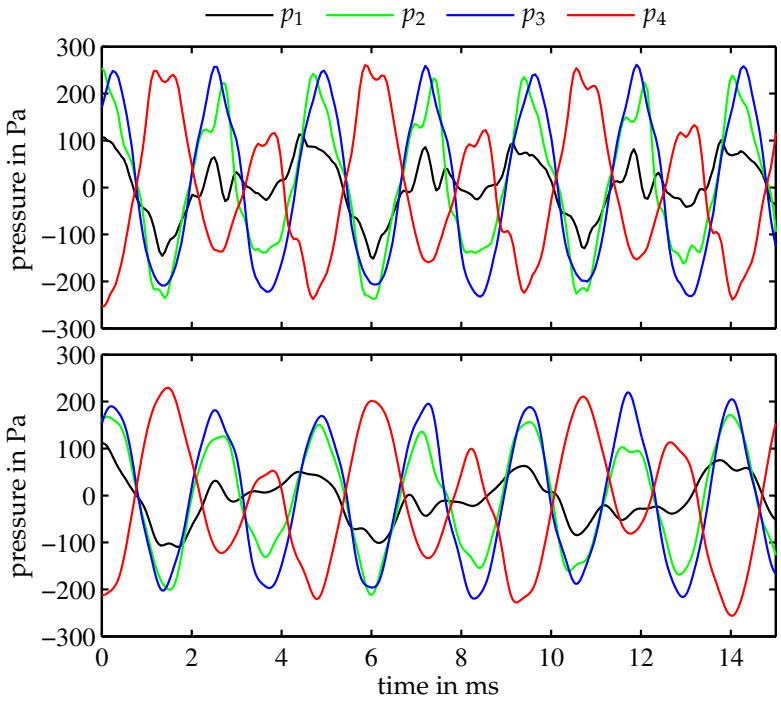

Figure 8.9: Sample time traces of acoustic pressure at microphone locations. Top: experiment; bottom: coupled simulation

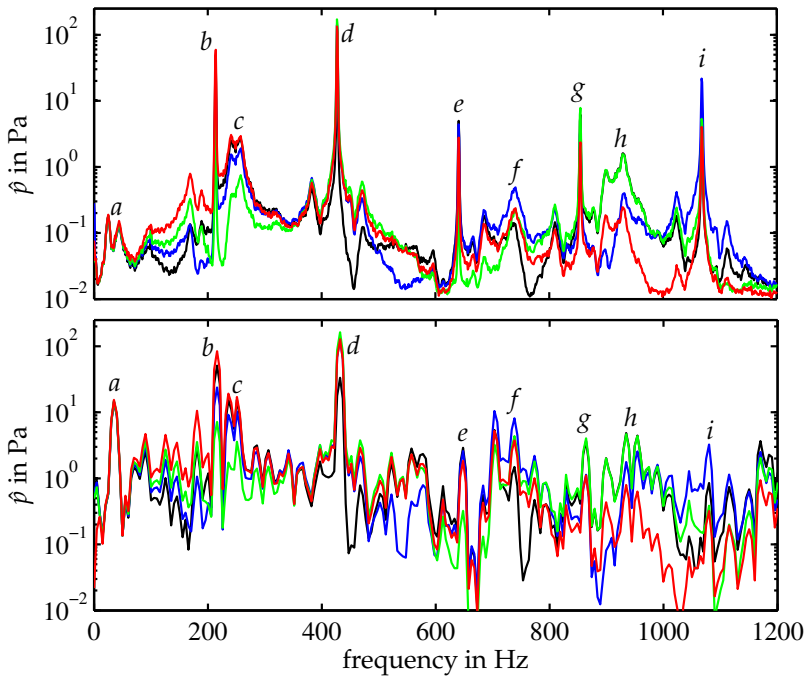

Figure 8.10: Amplitude spectra of the acoustic pressure (line colors as in Fig. 8.9). Top: experiment; bottom: coupled simulation. *a*: $\lambda/4$-mode, *b*: subharmonic of fundamental oscillation, *c*: $3\lambda/4$-mode, *d*: $5\lambda/4$-mode (fundamental oscillation), *e*: fundamental + subharmonic, *f*: $9\lambda/4$-mode, *g*: harmonic of fundamental oscillation, *h*: $11\lambda/4$-mode, *i*: harmonic + subharmonic

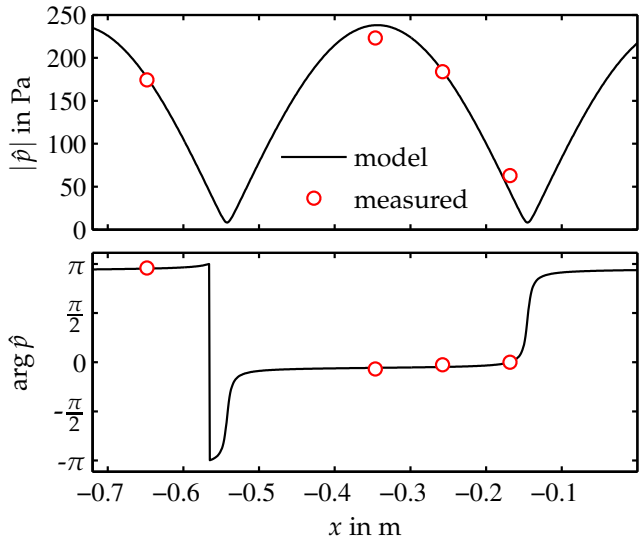

Figure 8.11: Modeled and measured pressure distribution upstream of the flame for the unstable $5\lambda/4$-mode. The coordinate origin is as shown in Fig. 8.1.

It should be noted here, however, that the experimental spectra were obtained from pressure time traces of 32 seconds in length, whereas the total simulation time was only 0.2 seconds. To accelerate the growth to the limit cycle amplitude in the coupled simulation, the state vector for the representation of the acoustic field (Eq. (7.10)) was initialized with uniformly distributed random numbers corresponding to moderate amplitudes. Accordingly, all modes are excited at the beginning of the simulation. Due to relatively small damping rates (Fig. 8.8), the stable modes might thus have had a stronger contribution in the computation.

We consider the pressure distribution of the unstable $5\lambda/4$-mode in the plenum next. According to our model, the complex mode shape upstream of the flame can be written as

$$\hat{p}(x) = \hat{g}\left(\mathcal{R}_{\mathrm{us}}(\omega_{\mathrm{osc}})\,\mathrm{e}^{-\mathrm{i}\omega_{\mathrm{osc}}x/c} + \mathrm{e}^{\mathrm{i}\omega_{\mathrm{osc}}x/c}\right), \tag{8.1}$$

where $\mathcal{R}_{\mathrm{us}}$ denotes the upstream reflection coefficient (see Fig. 8.2) with reference at $x = 0$ and ω_{osc} corresponds to the oscillation frequency of the $5\lambda/4$-mode. In principle, $\hat{g}$ represents the upstream traveling wave, but it can be considered an undetermined factor because (8.1) has arbitrary amplitude and phase reference (being an eigenfunction). Amplitude and phase of the modeled pressure distribution compare well with the measured results (Fig. 8.11).

Recalling the result from the linear stability analysis (Fig. 8.8), the role of the $7\lambda/4$-mode needs to be discussed. Clearly, the mode is linearly unstable, but a corresponding spectral marker cannot be found in Fig. 8.10. The first thing to mention here is the essential difficulty of predicting the linear growth rates *quantitatively* correct from a model. In fact, Bothien et al. (2010) used linear models directly identified from experimental data to compute growth rates of an unstable premixed combustor and found that – even with essentially no modeling assumptions – a decent quantitative agreement with the measured

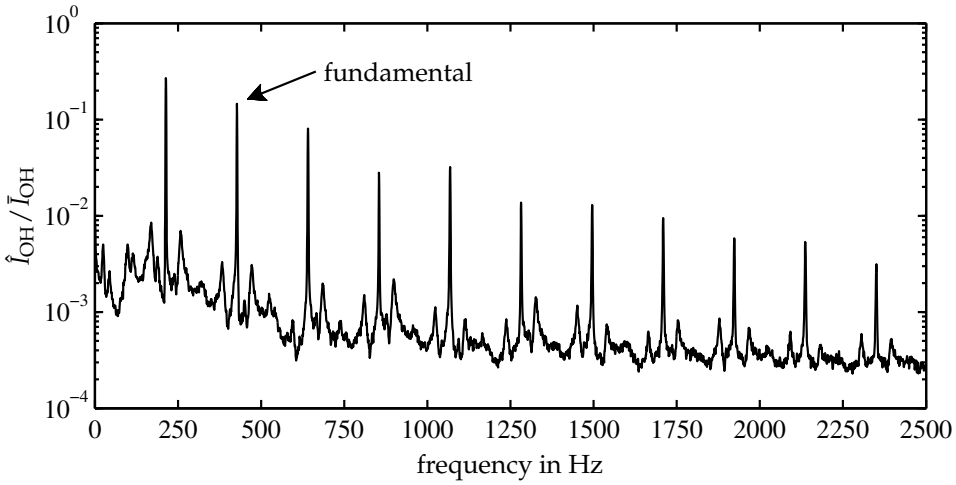

Figure 8.12: Normalized amplitude spectrum of global OH-chemiluminescence measured at unstable conditions

growth rates could not be obtained. Second, the growth rate of the $7\lambda/4$-mode is significantly weaker than that of the $5\lambda/4$-mode. Although it cannot be generally assumed that the most linearly unstable mode dominates the limit-cycle oscillation, the significant difference in the growth rates makes it plausible in the present case.

Subharmonic response of the flame

A striking characteristic in the pressure spectra (Fig. 8.10) are the strong subharmonic components, that were observed in the experimental and in the numerical results. In fact, the measured OH spectrum (Fig. 8.12) exhibits higher amplitudes at the subharmonic than at the fundamental frequency of oscillation.

To see whether this phenomenon is a result of the interaction between the acoustic field and the combustion zone, or solely a property of the flame, simulations with an open-loop excitation of the flame (no feedback through the acoustic field) at high forcing amplitudes were run. Figure 8.13 (top frame) displays the inflow velocity perturbation (dashed line) and the fluctuation of the OH-radical mass fraction normalized with the mean. The excitation amplitude of the upstream velocity was set to 1 m/s, which was close to the self-excited case. The frequency was set to 431 Hz, corresponding to the unstable $5\lambda/4$-mode. A strong subharmonic response with respect to the excitation frequency can be clearly identified. Hence, the spectral peaks at the subharmonic frequency of the fundamental oscillation in the pressure spectra (Fig. 8.10) are not a result of the acoustic feedback but rather a natural property of the flame submitted to strong acoustic forcing. The flame–acoustic coupling at the subharmonic is, therefore, dominantly unilateral – the pressure field simply responds to the heat release forcing at that frequency.

A sample time trace of the normalized fluctuation of the OH-chemiluminescence intensity, as acquired with the photomultiplier during self-excited oscillations in the experiment, is shown in the lower frame of Fig. 8.13. There is good qualitative correspondence between the two waveforms from the simulation and the experiment. The normalized fluctuation amplitude is clearly higher in the experimental results, but in that case, there is also some additional driving through the acoustic field directly at the subharmonic

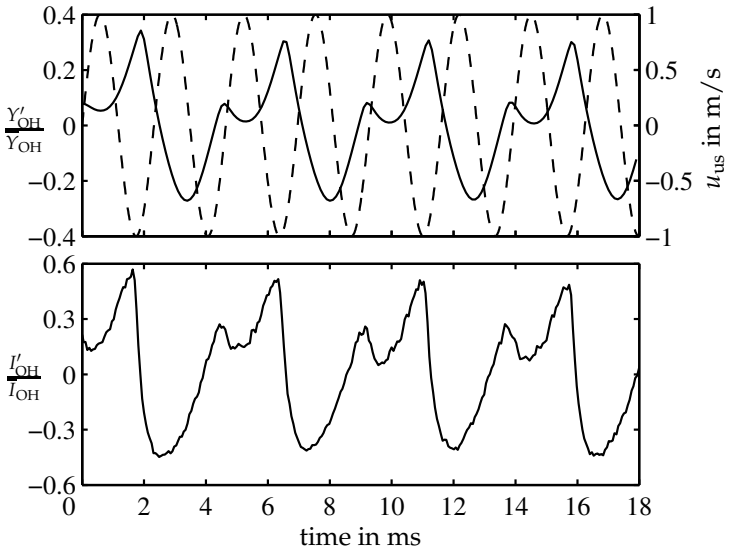

Figure 8.13: Subharmonic response of the flame. Top: simulation results for high-amplitude flame forcing at the unstable $5\lambda/4$-mode frequency. Inflow velocity perturbation (dashed) and normalized OH-radical mass fraction response (solid). Bottom: Normalized perturbation of OH-chemiluminescence intensity during thermoacoustic oscillation in the Rijke tube (experiment).

(cf. Fig. 8.10). Also note that the numerical result corresponds to the actual OH concentration whereas the OH-chemiluminescence intensity is – at best – proportional to the concentration of OH molecules in the excited state.

H-radical mass fraction distributions for *two* periods of the forcing cycle are plotted in Fig. 8.14. The locus of the maxima is a closed curve with a repetition rate of half the forcing frequency. Clear differences in height and burner distance of the concentration maximum can be observed between two successive periods of the forcing cycle. This subharmonic pattern was qualitatively similar for most of the species in the reaction scheme.

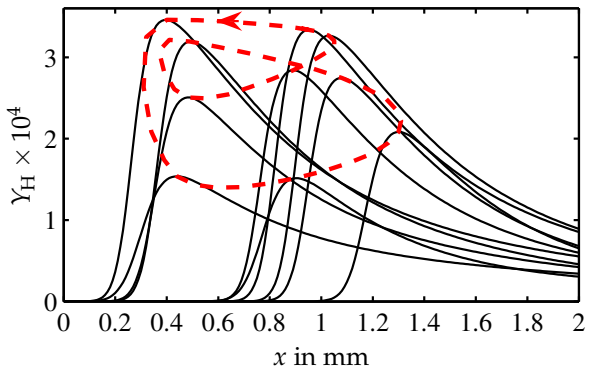

Figure 8.14: H-radical mass fraction distributions for the subharmonic oscillation. The dashed line marks the location of the maxima, the arrow the direction of orientation within the forcing cycle.

8.3.4 Discussion of the results

The results obtained with the coupled model bear qualitative and, to a certain extent, quantitative comparison with the experimental data. Thermoacoustically induced self-excited oscillations could be captured with favorable agreement in the frequency and amplitude of the fundamental mode. Higher-order frequency content of the pressure signals was also found to be in line, and the strong subharmonic component in the flame response was confirmed. It remains to demonstrate that the two-way coupling approach can be used with multi-dimensional flames in the same manner and that the procedure is well suited for control applications. This is the subject of the next chapter.

Chapter 9

Modeling and Control of a Two-dimensional Flame in the Acoustic Test-rig Environment

In this chapter, we apply the coupled method to a configuration with a two-dimensional flame. The acoustic environment in which the flame is placed is that of the combustor test-rig, which was investigated in Part I. The combustor acoustics are modeled on the basis of measured impedance and admittance, as we did in Section 6.4 to set up the non-linear system model for the investigation of subcritical instabilities. In the present case, the flame is represented by a zero-Mach solver, which is shortly described below. Also, as an extension to the preceding applications of the coupled method, we introduce active control in the simulation to suppress thermoacoustic oscillations. We consider the linear dynamics of the system first and then proceed to self-excited oscillations and their control.

The numerical solutions for the hydrodynamic domain in this chapter were computed at the Freie Universität Berlin[1] with a CFD solver called MOLOCH (Münch 2008). The governing equations that are implemented in this solver are:

- the zero-Mach equations,
- the standard k–ε equation to account for turbulence,
- an additional advection–diffusion equation for a turbulent reaction progress variable, and
- an additional advection–diffusion equation for the unburnt equivalence ratio ϕ.

Combustion is represented by a modified Eddy-Breakup model based on the work of Lindstedt & Váos (1999). More details on the numerical solution process can be found in the paper by Moeck et al. (2010). The particular flame considered here is a two-dimensional lean premixed methane–air flame with a mean equivalence ratio of 0.64 and an approach flow temperature of 300 K.

[1] The CFD computations were made by Dipl.-Ing. Carsten Scharfenberg, Freie Universität Berlin.

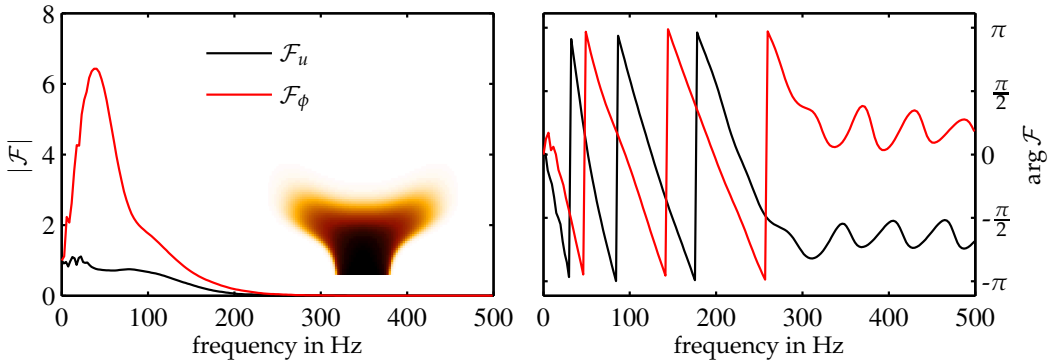

Figure 9.1: Transfer functions relating linear fluctuations in heat release to those in approach flow velocity and equivalence ratio as defined in Eq. (9.1). A picture of the mean flame shape in terms of the progress variable distribution is shown in addition.

9.1 Linear and nonlinear flame response

To determine the linear response of the flame, we follow the procedure described in Section 7.4.1. For the identification signal, we used a Gaussian pulse with an amplitude of 10 % of the mean value, which already proved to work well for the laminar flat flame in the previous chapter (see Section 8.3.3).

Equivalence ratio fluctuations are not considered in the flame–acoustic interaction here; the reactants are assumed to be perfectly mixed. However, equivalence ratio modulation will be used as one means to control the instability. To design the controller, it is therefore necessary to assess the response of the heat release rate to perturbations in the equivalence ratio, too. The same method as for the heat release response to fluctuations in approach flow velocity is used, with an analogous identification signal. The heat release transfer functions with respect to u_{us} and ϕ perturbations are shown in Fig. 9.1 in terms of a normalized response, defined as

$$\mathcal{F}_u(\omega) = \frac{\hat{Q}}{\hat{u}_{\mathrm{us}}} \frac{\bar{u}_{\mathrm{us}}}{\bar{Q}}, \quad \mathcal{F}_\phi(\omega) = \frac{\hat{Q}}{\hat{\phi}} \frac{\bar{\phi}}{\bar{Q}}. \tag{9.1}$$

Both transfer functions show low-pass character with distinct time delay, which is typical for a flame response (Lieuwen 2003). The transfer function with respect to equivalence ratio perturbations has a significantly higher gain compared to that with respect to fluctuations in approach flow velocity. This shows that the flame is highly susceptible to fluctuations in equivalence ratio – an asset for an efficient actuation mechanism. Above 300 Hz, the phase response saturates at a constant level, but this might not be accurate because the gain is virtually zero.

The transfer function $\mathcal{F}_u$ only characterizes the flame response to small perturbations. This is sufficient to determine linear system stability and design a control method that stabilizes the fixed point. However, the linear flame response cannot be used to calculate the limit-cycle oscillation amplitude because it contains no information on the saturation characteristics. To determine the level of the pressure oscillation, we need a flame describing function, as described in Sections 2.5.5 and 6.4.3, which in addition to the linear response, also holds information on the amplitude dependence. Furthermore, knowledge on the

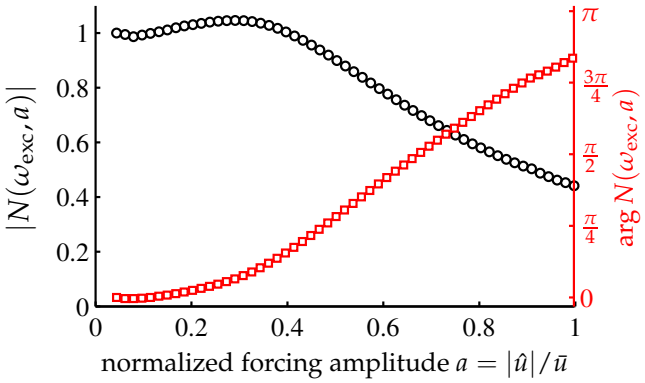

Figure 9.2: Amplitude dependence of the flame response at a forcing frequency of 100 Hz. The complex gain is normalized with the linearized response.

linear flame transfer function is generally not sufficient to guarantee that self-excited oscillations can be suppressed. A controller based on the linear model only stabilizes the steady state but might not be able to suppress limit-cycle oscillations if the flame response shows significant amplitude dependence (Dowling 1997).

To determine the nonlinear response of the flame, simulations with the zero-Mach solver, in which the inlet velocity was forced sinusoidally with varying amplitude, were evaluated. The maximum fluctuation amplitude considered was more than 100 % of the mean. Although saturation set in clearly before, the flame showed no signs of blow-off. Figure 9.2 displays the amplitude dependence of the flame response at a frequency of 100 Hz. (This is close to the frequency of the instability, as we will see below.) The amplitude dependence is represented in normalized form as

$$N(\omega_{exc}, a) = \frac{\mathcal{F}_u(\omega_{exc}, a)}{\mathcal{F}_u(\omega_{exc}, 0)}, \tag{9.2}$$

where $a = |\hat{u}|/\bar{u}$ denotes the normalized oscillation level, and $\omega_{exc} = 2\pi \times 100\,\text{Hz}$. The gain dependence clearly exhibits saturation characteristics agreeing qualitatively well with nonlinear flame response measurements (Noiray et al. 2008; Schimek et al. 2010). While approximately constant for small amplitudes, the gain decreases monotonically starting at relative velocity perturbations of about 40 %. A striking fact is that the phase response also shows considerable variation. In the amplitude range considered, the phase lag changes almost by π. The decrease in phase lag for high forcing amplitudes can be partially attributed to a shift in mean flame position to the inlet so that the convective time delay decreases. As a result, a controller solely designed on the basis of a linearized system model might not be able to stabilize the oscillations at high amplitudes.

9.2 Acoustic model

In the present work, the primary purpose of the network model is not to represent the complete system, but this will be done in the next section to assess linear stability and estimate the limit-cycle amplitude. For the coupled simulation, we use a network-type model only to represent the acoustic environment of the flame. To use a real acoustic environment, we follow the procedure in Section 6.4 and use acoustic boundary conditions which were measured in the combustion test-rig (Section 3.1) to set up the acoustic model.

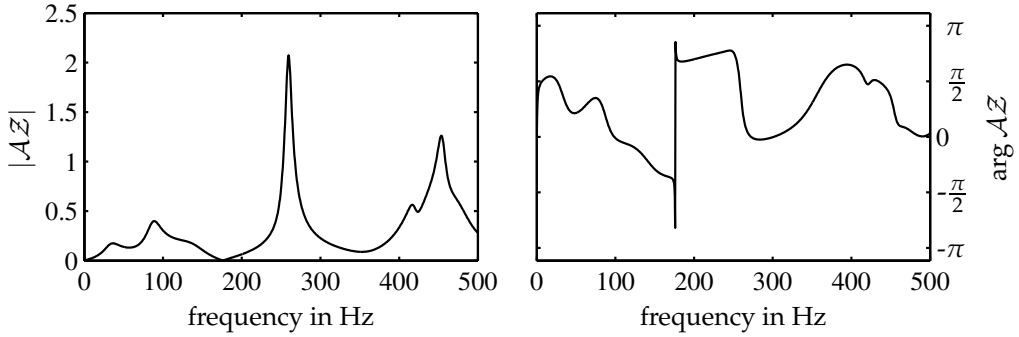

Figure 9.3: Frequency response of the experimentally identified acoustic system $\mathcal{AZ}(\omega)$

In Section 6.4, we combined the acoustic model based on measured test-rig data with an analytical nonlinear heat-release model for the simulation of subcritical instabilities and associated hysteresis phenomena. Here, the flame is represented by the zero-Mach solver introduced at the beginning of this chapter. As in Section 6.4, we use the impedance and admittance subsystems identified from the measurements to set up a state-space model that maps the velocity fluctuations downstream of the flame to those upstream (Eq. (7.10)). The impedance and admittance models can be directly deduced from the associated reflection coefficients shown in Fig. 6.13. The transfer function mapping u_{ds} to u_{us}, $\mathcal{AZ}(\omega)$, as identified from the experimental data, is displayed in Fig. 9.3. The resonant $\lambda/4$-mode of the combustion chamber has a frequency of slightly below 100 Hz, approximately where the phase response has the first zero-crossing.

In the coupled model, the upstream velocity fluctuations u_{us}, as obtained from (7.10), are prescribed as a time-varying boundary condition at the inlet of the hydrodynamic zone (which is computed by the flow solver). The induced heat release fluctuations are used in conjunction with the jump conditions (2.18) to obtain the velocity perturbations on the hot side. The two-way coupling is then achieved as explained in Section 7.4.

9.3 Linear stability and limit cycle amplitude

Based on the acoustic model and the flame transfer function, linear stability of the coupled system can be determined as explained in Section 7.4.1. However, to have a clearer connection to the describing function analysis, which we consider subsequently, we develop the frequency-domain dispersion relation as well. In frequency domain, the acoustic mapping (7.10) is simply $\zeta^{-1}(\mathcal{ZA})(\omega)$. Combining this with the jump conditions (2.18) and using the flame transfer function to express the heat release in terms of the velocity perturbation upstream, the dispersion relation takes the form

$$1 = \zeta^{-1}(\mathcal{AZ})(\omega)\left[1 + (T_{\mathrm{ds}}/T_{\mathrm{us}} - 1)\mathcal{F}_u(\omega)\right]. \tag{9.3}$$

The eigenvalues for the linearized system, calculated from Eq. (9.3), are shown in Fig. 9.4. The two lower frequencies correspond to a plenum resonance at 36 Hz and a quarter-wave mode in the combustion chamber at 88 Hz. These two modes are significantly destabilized through the interaction with the heat release. However, only the

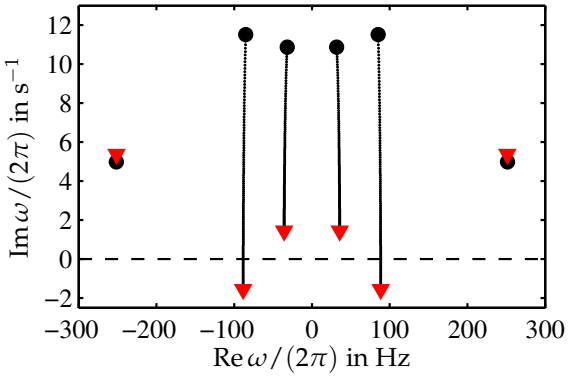

Figure 9.4: Eigenvalues of the linearized system model. Circles represent purely acoustic eigenvalues, triangles those including heat release feedback.

quarter-wave mode is linearly unstable. The 3/4-wave mode at 250 Hz is essentially unaffected, a result of the strong low-pass character of the flame (see Fig. 9.1). Computed growth rate and frequency of the unstable mode are consistent with the experimental data of Bothien et al. (2010), which was obtained in the same acoustic environment, but with a different flame. We find identical frequencies and similar growth rates. (Note that the growth rates in the reference above are not divided by 2π.)

With the results in Fig. 9.4, linear instability of the coupled model has been established. However, the final oscillation amplitude cannot be assessed from the linearized model because it predicts exponential growth for all times. To determine the amplitude of the limit-cycle oscillation – at least in an approximate way – we make use of the describing function technique as introduced in Section 2.5.5 (see also Dowling 1997, 1999 and Noiray et al. 2008). Since the flame response is the sole source of nonlinearity in the system, it is sufficient to only take into account the fundamental component of the output. In other words, we consider the flame transfer function to have amplitude-dependent gain and phase and compute the growth rates as a function of the oscillation level. With the nonlinear flame response determined in Section 9.1, the dispersion relation can be written as

$$1 = \xi^{-1}(\mathcal{A}\mathcal{Z})(\omega)\left[1 + N(\omega, a)(T_{\mathrm{ds}}/T_{\mathrm{us}} - 1)\mathcal{F}_u(\omega)\right]. \tag{9.4}$$

Since only information on the amplitude dependence at a frequency of 100 Hz was available from the nonlinear flame response computations (Section 9.1), $N(\omega, a)$ is approximated with the values at that forcing frequency. We conjecture that this will be reasonably accurate as long as only this particular mode is considered.

The solution pair (ω, a) of (9.4) with $\mathrm{Im}\,\omega = 0$ corresponds to amplitude and frequency of the limit-cycle oscillation. Figure 9.5 presents the complex eigenfrequencies as a function of the pulsation level. The intersection of the growth rate $-\mathrm{Im}\,\omega$ with the x-axis marks the oscillation amplitude, which is determined as $|\hat{u}|/\bar{u} = 0.48$. The associated combustor pressure can then be simply calculated from the experimentally identified admittance model $\mathcal{A}(\omega)$ at the oscillation frequency; this yields a pressure amplitude of 1018 Pa. We also note that the oscillation frequency increases by about 7 Hz from the unstable steady state to the limit cycle.

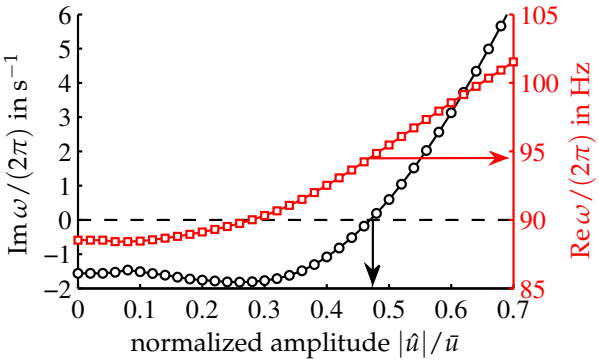

Figure 9.5: Solutions of the nonlinear dispersion relation (9.4). Vertical and horizontal arrows mark limit cycle amplitude and frequency, respectively.

9.4 Coupled simulation and control

We first show some results of the uncontrolled instability and compare them with the predictions based on the describing function in the preceding section. Then we apply two types of control, that were found to be effective in related experiments, to mitigate the oscillations.

9.4.1 Uncontrolled instability

As an initial perturbation for the coupled simulation, the state vector of the acoustic model (Eq. (7.10)) was set to uniformly distributed random numbers of small magnitude. Figure 9.6 shows the temporal evolution of the acoustic pressure at the flame and the normalized heat release rate fluctuation from the coupled simulation. In agreement with the linear stability analysis in Section 9.3, the steady state of the coupled system is unstable with respect to small perturbations. Amplitudes of pressure and heat release grow, exponentially in the linear regime, and then settle on a constant level after passing through a small overshoot. The close-up in the right frame of Fig. 9.6 shows that Rayleigh's criterion is satisfied. Pressure and heat release oscillations are not completely in phase, but the correlation is certainly positive so that the instability can be sustained. The nonlinearity in the flame response distorts the heat release perturbations from a harmonic form to one that peaks to higher positive than negative values. This is a common characteristic of nonlinear heat release oscillations (see, e.g., Fig. 4.2).

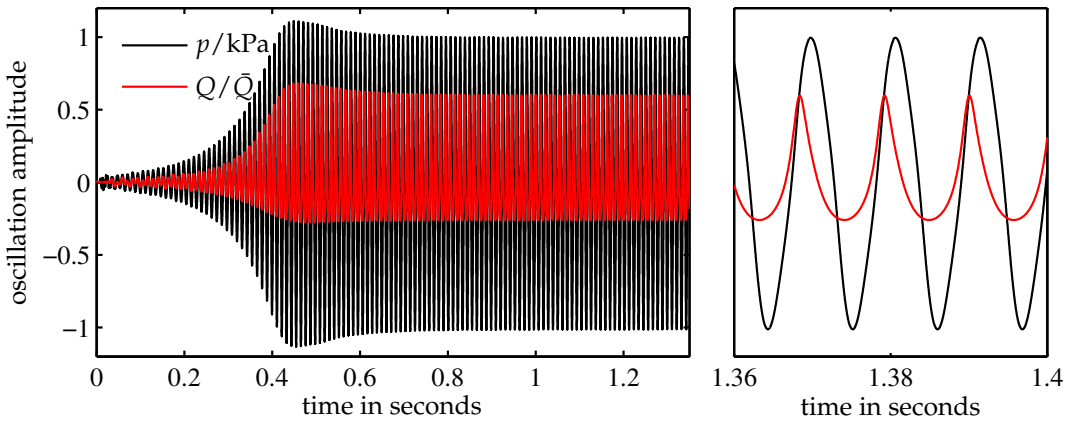

Figure 9.6: Time-domain evolution of the instability. The close-up evidences positive heat-release–acoustic correlation.

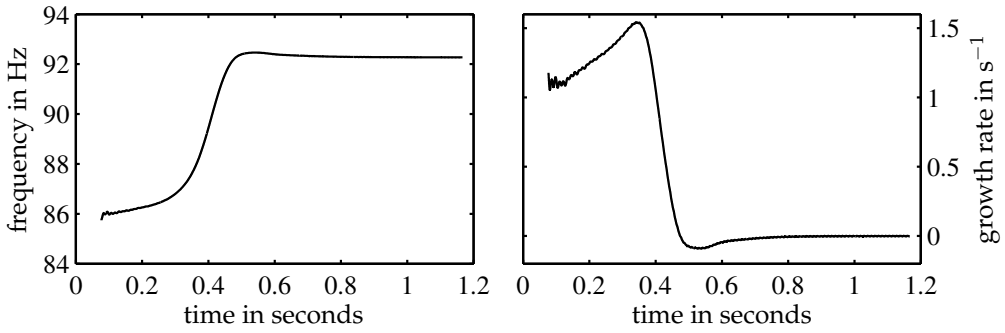

Figure 9.7: Instantaneous frequency (left) and growth rate (right) of the pressure signal in Fig. 9.6

The describing function analysis in Section 9.3 predicted a frequency shift during the growth of the unstable mode (Fig. 9.5). To see whether this characteristic is present in the coupled simulation, we compute the instantaneous oscillation frequency of the pressure signal. From the properties of the Hilbert transform, we can determine the instantaneous frequency of a narrow-band signal[2] as $\mathrm{d}/\mathrm{d}t(\arg p_\mathrm{a})/(2\pi)$, where $p_\mathrm{a} = (1 + \mathrm{i}\mathcal{H})[p]$ is the analytic signal of p, and $\mathcal{H}$ denotes the Hilbert transform. Moreover, since we have the instantaneous amplitude available as $|p_\mathrm{a}|$, we can compute the associated exponential growth rate as $\mathrm{d}/\mathrm{d}t(\log|p_\mathrm{a}|)/(2\pi)$. Instantaneous frequency and growth rate are shown in Fig. 9.7. For small amplitudes, the instability has a frequency of 86 Hz, agreeing well with the results obtained from the linearized system model (Section 9.3). While the amplitude is growing, the instability frequency increases up to 92 Hz at the established limit-cycle oscillation. This is obviously a result of the amplitude dependence of the flame response (Fig. 9.2) and compares well with the analysis based on the describing function of the flame in the preceding section. Yet, we have to note that there is a slight deviation of about 3 Hz in the predicted frequency compared to the one computed from the coupled simulation data.

The instantaneous growth rate (Fig. 9.7, right) is somewhat smaller at low amplitudes compared to the linear stability analysis (Fig. 9.4). Between 0.2 and 0.4 seconds, the growth rate actually increases before saturation sets in. This feature can also be observed in Fig. 9.5. We may conjecture at this point that when increasing some linear damping mechanism continuously, we might find a range (albeit small) in which the system exhibits subcritical instabilities.

9.4.2 Control by equivalence ratio modulation

Control of combustion instabilities by equivalence ratio (or fuel flow) modulation was shown to be effective in Chapter 4. Other successful experimental applications were reported by Paschereit et al. (1999*b*), Hibshman et al. (1999), Campos-Delgado et al. (2003), Riley et al. (2004), and Guyot et al. (2007). In case of a technically premixed burner, a loudspeaker also introduces fluctuations in equivalence ratio (the details depending on the fuel-line impedance), but we do not consider this here.

[2] Due to the harmonics, the pressure signal is only reasonably narrow-band. Therefore, before applying the Hilbert transform, the pressure signal was low-pass filtered.

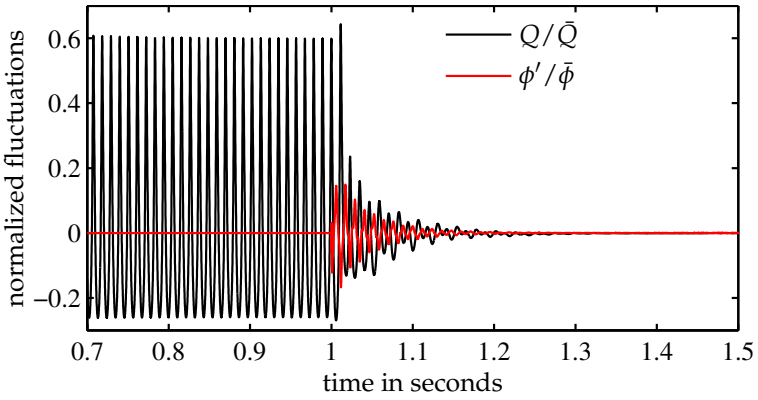

Figure 9.8: Control of combustion instability by equivalence ratio modulation

We use a direct actuation of the equivalence ratio in the coupled simulation to achieve a stabilization of the system. With reference to Fig. 9.1, it can be observed that, at the oscillation frequency, the heat release transfer functions $\mathcal{F}_u$ and $\mathcal{F}_\phi$ are almost in antiphase. Hence, a ϕ' feedback proportional to u can be expected to have a stabilizing effect. We have to consider, however, the amplitude dependence of the heat release response. As Dowling (1997) pointed out, a controller designed to stabilize the steady state is not necessarily capable of suppressing a fully established limit-cycle oscillation. If the heat release response is strictly of saturation type with no nonlinearity in the phase, a controller based on the linearized system model can be considered as conservative (Dowling 1997). In the present case, however, the phase response is strongly amplitude dependent so that the above argument does not hold. In the framework of the describing function analysis, stabilizing control for the whole amplitude range can be guaranteed if the growth rates are negative for all relevant $|\hat{u}|/\bar{u}$. Equivalence ratio feedback with a stabilizing effect over the whole amplitude range was achieved with an additional small time-lag in the form of a Padé approximant. The gain had to be chosen quite small so as not to destabilize the lower frequency mode (see Fig. 9.4).

Results from the application of the equivalence ratio controller are shown in Fig. 9.8. The control scheme is activated at $t = 1\,\mathrm{s}$. The heat release fluctuations are quickly diminished by the control action. Only slightly more than 10 % of the mean equivalence ratio is needed at most to suppress the instability. After 0.2 seconds, hardly any oscillations remain.

9.4.3 Control of the acoustic boundary conditions

Reflection of acoustic waves at the system boundaries is an essential part in the thermoacoustic feedback loop. For this reason, reducing the magnitude of the reflection coefficient, for instance at the combustor outlet, has a stabilizing effect. This was already demonstrated on the basis of the elementary model configuration in Section 7.5.3. Moreover, this effect is general because it does not depend on the particular characteristics of the flame or the burner. In addition to passive methods for the specific manipulation of combustor boundary conditions (Paschereit & Gutmark 2002; Paschereit et al. 1998, 2000; Tran et al. 2009), active methods based on feedback control have been developed (Bothien et al. 2008). While these active methods allow to prescribe a general desired impedance, reducing the

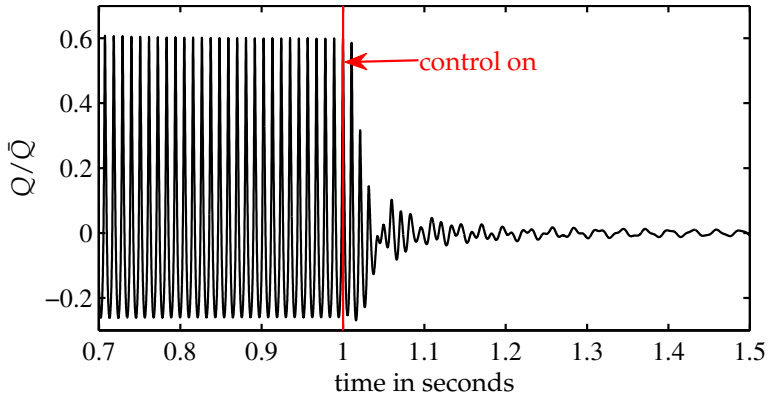

Figure 9.9: Control of combustion instability by tuning the downstream acoustic boundary condition

reflectivity was shown to have a stabilizing influence in several test-rig experiments (Bothien et al. 2008, 2010). In these cases, it was sufficient to reduce the magnitude of the reflection coefficient only in a narrow interval around the main frequency of oscillation.

Implementing the control strategy described above in the coupled simulation is straightforward because, effectively, the control action simply modifies the impedance of the acoustic model. Hence, instead of the nominal acoustic model (7.10), representing a time-domain realization of the transfer function $\mathcal{AZ}(\omega)$, we have one that corresponds to lower reflection at the downstream side. As in the work of Bothien et al. (2010), we restrict the control scheme to lower the wave reflection only in a narrow band around the oscillation frequency.

Results from the coupled simulation for the acoustic boundary control are presented in Fig. 9.9. To realize this type of control in the coupled simulation, the downstream impedance model $\mathcal{Z}(\omega)$ was adapted to mimic the controlled reflection coefficient as determined in test-rig experiments by Bothien et al. (2010). Control is activated at $t = 1\,\mathrm{s}$. The heat release oscillations quickly decrease, and the system is stabilized. In contrast to control by equivalence ratio modulation, a low-frequency oscillation, corresponding to the lower acoustic mode (see Fig. 9.4), diminishes only slowly. In principle, this mode could be also stabilized by the control scheme, but in a practical situation, very low frequencies are difficult to actuate with acoustic drivers.

9.5 Summary

In this chapter, we applied the coupled method to a two-dimensional flame embedded in a real acoustic test-rig environment. Based on linear and nonlinear flame response calculations, linear stability characteristics as well as the limit cycle amplitude and a nonlinear frequency shift could be predicted. The limit-cycle oscillation observed in the coupled simulation had a frequency close to those seen in the test-rig. Active control with two types of actuation was applied: manipulation of the acoustic boundary conditions and feedback through equivalence ratio modulation. Both control methods successfully mitigated the instability.

Part III

An Annular Thermoacoustic Surrogate System: Modeling and Control of Azimuthal Instabilities in an Annular Rijke Tube

The vast majority of experimental and numerical investigations of thermoacoustic instabilities focuses on single-burner configurations, in which the heat release couples only to longitudinal acoustic modes, and the interaction is essentially one-dimensional. However, modern gas turbines are equipped with annular combustion chambers featuring a large number of burners around the circumference. Azimuthal modes, for which the dominant pressure variation occurs in angular direction, are often observed in full-scale engines. Since a complete annular combustor with a multitude of flames is an exceedingly complex system, the knowledge on thermoacoustic instabilities coupled to azimuthal acoustic modes is distinctly less developed compared to the longitudinal case. Here, we therefore introduce a thermoacoustic surrogate system – an *annular Rijke tube* – which, albeit its simplicity, possesses the basic mechanisms to feature unstable azimuthal modes. A review of previous work on annular thermoacoustic systems and details on the configuration considered are given in Chapter 10. Chapter 11 introduces modeling tools generally applicable to annular configurations and particularly useful for the annular Rijke tube. We set up a frequency-domain network-type model that is capable of predicting the unstable modes in this configuration and permits to study the impact of asymmetry. Experimental results and active control of azimuthal instabilities are presented in Chapter 12. The structure of the unstable modes is investigated, and the effect of an asymmetric power distribution is assessed. Based on the frequency-domain model, a control scheme is developed, which is able to achieve a complete stabilization, but can also target individual modes only.

Chapter 10

Instabilities in Annular Domains and the Rationale for Studying a Surrogate System

For reasons of compactness and of having a uniform temperature distribution at the turbine inlet, most modern gas turbine combustion chambers have an annular shape with multiple circumferentially arranged burners. Apart from the fact that, in this set-up, multiple heat sources interact with the unsteady pressure simultaneously, the acoustic modes in an annular geometry are quite different from the purely longitudinal case. An annular chamber hosts azimuthal acoustic modes, which may become unstable under certain conditions. As in the purely longitudinal case, the heat release provided by the flame responds dynamically to acoustic perturbations so that energy can be added to the acoustic field, and pressure fluctuations grow until limited by nonlinear effects. Although investigations on annular thermoacoustic systems are significantly more complex than in the purely longitudinal single-burner case, a number of experimental, numerical, and modeling studies focusing on azimuthal modes have been performed over the last decade. We give a brief overview in the following.

10.1 A review of previous work on instabilities in annular combustor configurations

Thermoacoustic instabilities in annular combustion chambers are often associated with azimuthal acoustic modes, where both rotating and standing wave patterns have been observed. The first Siemens gas turbine featuring an annular combustion chamber, the V84.3A with 24 burners and a base load power of 170 MW, exhibited strong instabilities coupled to 2nd and 4th order circumferential modes at 217 and 433 Hz. Seume et al. (1998) applied a feedback control scheme using modulated pilot fuel to suppress these instabilities. Due to this success, the control scheme was also implemented in the larger V94.3A engine (Hermann & Hoffmann 2005).

The unstable acoustic modes in the Siemens Vx4.3A combustors have been further analyzed by Krebs et al. (1999, 2001, 2002), Berenbrink & Hoffmann (2000), and Krüger et al.

(2001) based on test-rig measurements and low-order Galerkin and network-type models. From the experimental data, first-, second-, and fourth-order azimuthal modes, dominantly standing as well as rotating, were identified from the magnitude and phase patterns of the acoustic pressure along the circumference of the annular combustion chamber. Introducing an azimuthal asymmetry by means of a cylindrical burner outlet applied to part of the burners was found to have a stabilizing influence.

Evesque & Polifke (2002) and Evesque et al. (2003) developed a low-order network model for annular combustion chambers allowing for asymmetries introduced by the burner transfer matrices. They considered an annular model combustion chamber geometry and compared eigenvalue computations with a Helmholtz solver; good agreement was found. Since no flame model was implemented, stability calculations were not performed. Evesque et al. (2003) defined a method for characterizing the rotating or standing nature of azimuthal modes, the spin ratio. A similar modeling approach was used by Kopitz et al. (2005) to model longitudinal and circumferential instabilities that were observed in an annular model combustion chamber. Flame transfer functions measured at stable operating conditions were extrapolated in thermal power and equivalence ratio (Lohrmann & Büchner 2004) to compare the model results to the measured instabilities. Partial success was achieved – the stability of the longitudinal mode was predicted correctly but not so for the azimuthal mode. In the latter case, the extrapolation of the flame transfer function was judged to be more critical.

Pankiewitz & Sattelmayer (2003) used an FEM solver for time-domain simulations of thermoacoustic instabilities in an annular model configuration based on the wave equation with nonlinear flame model. In cases where the axial mean flow was neglected, they only found rotating modes in the limit cycle solutions. When taking the axial mean flow into account, only azimuthally standing waves appeared in the oscillations. The conclusion that the mean flow promotes standing waves was, however, revised by Evesque et al. (2003) who found that there was no influence on the occurrence of standing or rotating modes.

A model of a symmetric annular combustor was investigated by Schuermans et al. (2003) with a time-domain network model. The acoustic response of the annular chamber was modeled using a modal expansion of the Green's function of the Helmholtz equation. On the basis of a linear analysis, two unstable modes were found. Time-domain simulations with a limiter to saturate the heat release response showed only one mode oscillating in a limit cycle. When suppressing this mode by active control, the second unstable mode started to grow and settled on a finite-amplitude oscillation. In subsequent work based on a similar configuration, Schuermans et al. (2006) observed that, while growing, the unstable mode was of standing type (resulting from axisymmetric white noise excitation). However, the long-time periodic solution was always of dominantly rotating type, with no preference of either spinning direction. It was shown that the saturation nonlinearity in the flame destabilizes the standing wave mode at finite amplitude and therefore promotes the traveling wave solution. For a simpler model system consisting of only two first order azimuthal wave components, this mechanism was investigated in more detail. Depending on the initial conditions the growing wave could be arbitrarily made up of azimuthally traveling or standing components, but the final periodic solution was again

always of rotating type. It was shown that there exist two types of equilibrium solutions at finite amplitude in wave amplitude phase-space, one with equal clockwise and counter-clockwise traveling wave components and the other purely spinning. The former, corresponding to a standing wave, was associated with a saddle and therefore unstable. The two purely rotating solutions were found to be stable fixed points.

The Rolls-Royce/Cambridge network code LOTAN (low order thermoacoustic network model) was used in a number of modeling and control studies considering annular combustor configurations (Morgans & Stow 2007; Stow & Dowling 2004, 2003, 2009). Stow & Dowling (2003) implemented the effect of Helmholtz resonators attached to the circumference of the combustion chamber and studied the associated modal coupling. Optimal resonator placement for maximum damping of unstable azimuthal modes was deduced. The same authors extended the approach to account for nonlinearities in the flame model (Stow & Dowling 2004). By using describing function techniques, the limit cycle amplitude of thermoacoustic oscillations in an annular configuration could be calculated. Stow & Dowling (2009) extended the approach to time-domain simulations based on the impulse response of heat release perturbations to those in approach flow velocity and a nonlinear flame model. The final limit cycle solutions of unstable azimuthal modes were always of rotating type, in accordance with the theoretical considerations of Schuermans et al. (2006). Morgans & Stow (2007) and Illingworth & Morgans (2008) used the same network code to develop model-based and adaptive control strategies for thermoacoustic instabilities in an annular model combustor. Based on the simulations, they were able to suppress decoupled azimuthal modes in a rotationally symmetric set-up but also coupled modes resulting from non-identical burners.

Tiribuzi (2006) used a URANS computation on an extremely coarse grid of a full annular combustion chamber with 24 burners. He found unstable 2nd- and 3rd-order azimuthal modes, depending on the parameters of the combustion model. More surprisingly, for fixed conditions (and model parameters), dominantly standing as well as rotating modes were found, depending on the initial conditions. Using the same approach, Tiribuzi (2007) investigated the effect of four angular subdivisioning walls in the annular plenum. He found that an asymmetric pattern could significantly reduce thermoacoustic oscillations associated with the second azimuthal mode. The symmetric configuration, with subdivisioning walls at equidistant angles, forced a standing mode, but did not have a strong impact on the pulsation strength.

Subcritical instabilities of a circumferential mode in a full annular combustor test-rig with 24 burners were investigated by Lepers et al. (2005). They found a pronounced hysteretic dependence of the pulsation amplitude on the equivalence ratio. Application of two different sets of 14 Helmholtz resonators resulted in a shift of only the Hopf point (see Fig. 6.4) or a complete movement of the hysteresis region to fuel richer conditions. In the latter case, the operating conditions subcritically unstable in the baseline case were globally stabilized. Accompanying calculations with a network model gave consistent results.

Richards et al. (2007) applied open-loop control to a Solar Turbines full-scale engine with 12 burners. The control scheme was based on periodic modulation of the equivalence ratio using solenoid valves at each of the 12 injectors. Six pressure transducers were installed to measure the acoustic pressure along the circumference. In the uncontrolled case, a self-excited oscillation at 288 Hz was observed. Unfortunately, no information on the

type of acoustic mode is given, but a standing wave is mentioned. When modulating the fuel injectors in two groups, each with six burners (odd and even), the RMS pressure could be reduced to one-third of the baseline conditions. Different forcing frequencies were used but showed similar reduction in the pressure oscillations. As a side-effect, NOx emissions were slightly decreased (in contrast to tests in a single-burner rig), but CO emissions increased significantly. A steady increase of the equivalence ratio at every second injector did not stabilize the system. Since the azimuthal order of the unstable mode is not stated, these results are difficult to interpret.

Finite element computations of annular configurations based on the Helmholtz equation with feedback from the heat release and non-trivial boundary conditions were discussed by Nicoud et al. (2007) and Sensiau et al. (2008). It was shown by Sensiau et al. (2009) that an asymmetry in the heat release response can amplify the eigensolution associated with a certain spinning direction whereas the other is damped.

Staffelbach et al. (2009) performed an LES of a full annular helicopter combustion chamber. They observed a dominantly rotating first order azimuthal wave at 740 Hz with a clockwise-to-counter-clockwise amplitude ratio of 3. Due to the common rotation sense of all (15) swirlers, an azimuthal mean flow is established in the annular combustion chamber. Yet, since the mean flow component was of essentially negligible Mach number, it was unclear whether this mechanism promotes the appearance of spinning waves. The dominant effect of the acoustic waves on the heat release rate was found to result from a modulation of the axial mass flow through the burners.

10.2 Generic system set-up and the rationale for studying an annular Rijke tube

Studying thermoacoustic instabilities and their control in annular combustion chambers is a complex task, from an experimental as well as from a computational point of view. As a result, in contrast to thermoacoustic instabilities in purely longitudinal geometries, less information regarding azimuthally unstable modes is available. We therefore propose to study a surrogate system – an annular Rijke tube – which, albeit its simplicity, possesses the basic mechanisms to feature unstable azimuthal modes. This system, having all essential ingredients to generate this phenomenon, narrows the gap between elementary model studies in longitudinal configurations and full-scale applications in annular geometries.

The generic system set-up we consider is as follows. N straight tubes (the "burners") are connected to an annular duct (the "combustion chamber") with their downstream end. In each tube, there is an element that provides a mean heat release and responds dynamically to fluctuations in axial velocity. The source of unsteady heat release in the original Rijke tube is a grid of heated wires. It is the simplicity of this source that makes it attractive for fundamental studies of thermoacoustic instabilities, and this is the reason why we use it in our annular model system as well. Obviously, a heating grid is much simpler than a premixed flame; however, both have a qualitatively similar frequency response to axial flow perturbations – low-pass characteristics with an associated phase-lag.

A principal difference to an annular combustion chamber in a gas turbine is that, in the set-up proposed here, the sources of heat release do not respond to azimuthal velocity

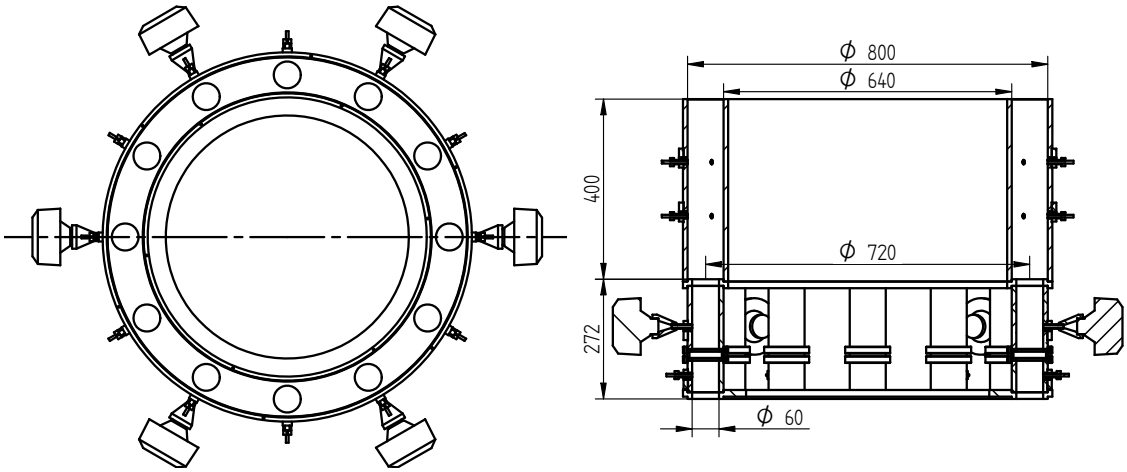

Figure 10.1: Schematic representation of the annular Rijke tube with basic dimensions. Left: top view; right: vertical cut-plane; dimensions in mm.

fluctuations in the downstream annulus but only to an axial perturbation in the tubes. We assume the latter effect to be dominant, as was found by Staffelbach et al. (2009).

To avoid confusion in this chapter, we refer to the N objects in which the heat sources are located exclusively as *tubes*; the term *duct* is reserved for the annular component.

10.3 Experimental arrangement

The annular Rijke tube has 12 tubes connected to an annular duct at their downstream end. Figure 10.1 shows a schematic of the set-up with the basic geometrical dimensions; a photograph of the experimental arrangement is presented in Fig. 10.2. The tubes have an inner diameter of 60 mm with an associated cut-on frequency for the first azimuthal mode beyond 3 kHz at room temperature. The annular duct is 400 mm in length and has a mean diameter of 720 mm with a "hub–tip ratio" of 0.8; the downstream end is simply open. All parts are made of aluminum with a wall thickness of 10 mm. Although coincidental, we note that the cross-sectional set-up is quite similar to Solar Turbines' Centaur engine (see, e.g., Smith & Blust 2005).

As in a conventional Rijke tube (e.g., Heckl 1990 or Raun et al. 1993), the sources of mean and unsteady heat release are electrically driven heating grids. The axial center of the grids is located 100.5 mm downstream of the tube inlets. The axial extent of the grid modules is 15 mm, thus clearly complying with the assumption of a compact heat source. Three independent DC sources (EA-PS 9080-50), each with a maximum output of 1.5 kW, are used to power the grids. In the nominal set-up, 4 heating grids are connected in parallel. The chosen DC sources have a power stage providing the maximum output power for voltages and currents up to 80 V and 50 A, respectively. Thus, the heating grid resistance does not need to have one specific value to obtain the maximum power output but can lie in a certain range. The admissible values of the heating grid resistance, allowing for a maximum power output, based on the power staging of the DC supplies, is illustrated in Fig. 10.3(a). If four heating grids are connected in parallel to one power supply, minimum and maximum grid resistance are given by $R_{\min} = 4P_{\max}/I_{\max}^2$ and $R_{\max} = 4U_{\max}^2/P_{\max}$,

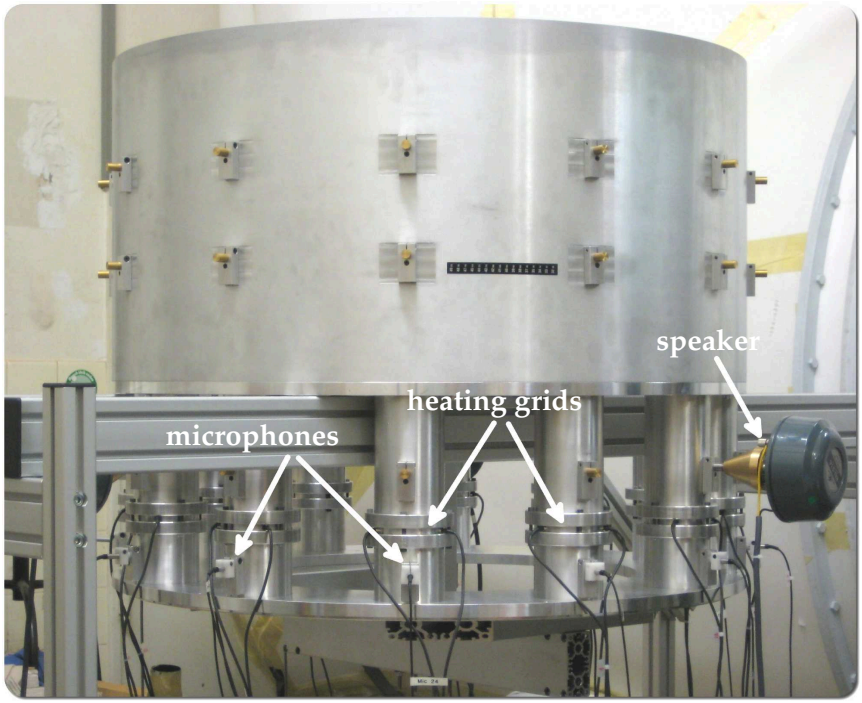

Figure 10.2: Photograph of the annular Rijke tube. Only three of the six loudspeakers are mounted.

respectively, where maximum power, current, and voltage are $P_{\max} = 1500\,\mathrm{W}$, $I_{\max} = 50\,\mathrm{A}$, and $U_{\max} = 80\,\mathrm{V}$ for the specific power supply used. Based on these constraints, the heating grids were manufactured to have a cold resistance of $13\,\Omega$ (Fig. 10.3(a)).

Special care was taken that all heating grids are identical so that the nominal system would be as symmetric as possible. The relative difference in the cold electrical resistance of the 12 heating grids was less than 0.5 %. Unless mentioned otherwise, all heating grids are supplied with equal electrical power. A photograph of one of the heating grids is shown in Fig. 10.3(b). The grids have a meandering pattern in two layers and are made from flat wire with a rectangular $0.18\,\mathrm{mm} \times 0.58\,\mathrm{mm}$ cross section.

The heating grids are driven by a constant voltage. If the fluid velocity at the grid oscillates, the heat transfer coefficient is modulated, and as a result, the heat released to the fluid fluctuates, too. In principle, this may have two effects which are difficult to account for in a model: (i) the temperature of the wire does not remain constant and (ii) as a result of (i), the resistance of the wire also changes, which would lead to an unsteady electric power supplied to the grid. However, an estimate of the thermal inertia of the wire, as done by Kopitz (2007), shows that the grid temperature can be clearly considered as constant for frequencies down to 100 Hz.

No external source is used to drive a mean flow. As in the original Rijke tube, the mean flow is solely convection induced. This restricts the parameter space (power input and mean flow velocity cannot be varied independently) but allows for essentially noise-free measurements. Moreover, the acoustic boundary conditions, which have a significant effect on stability and oscillation amplitudes (Bothien et al. 2008), are well defined.

Microphones, thermocouples, and speakers can be mounted to the annular Rijke tube via 48 ports in total, 24 each at the tubes and at the annular duct. We use 12 microphones,

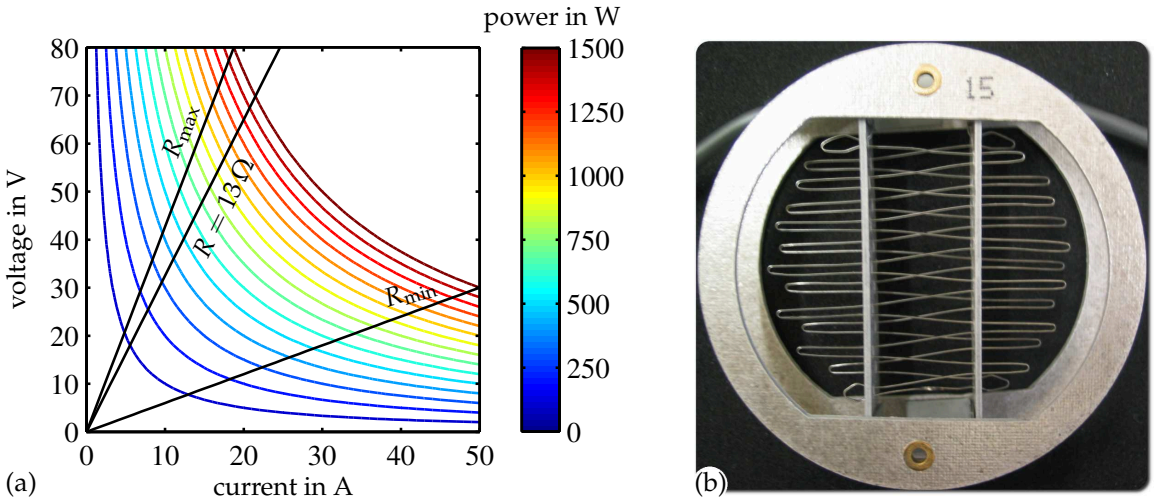

Figure 10.3: (a) Operating chart for one of the power supplies. Black lines correspond to the electrical resistance of one heating grid, with four grids connected in parallel to the power source. (b) Photograph of a heating grid (top view).

mounted in the tubes, upstream of the heating grids. In this way, we do not have to monitor the temperature at the microphones, and the information on the circumferential structure of the pressure field is identical to what would be inferred from measurements in the annular duct. For the application of feedback control, six speakers were used in total, one attached to every second tube, downstream of the heat sources (see Fig. 10.1). The distance between the axial center of the heating grid and the microphone is 47 mm in each tube; between heating grid and speaker, the distance is 65 mm.

Chapter 11

Modeling Annular Thermoacoustic Systems

Modeling thermoacoustic systems is markedly different when considering annular configurations as opposed to geometries with mainly longitudinal extent. In addition to multiple sources of unsteady heat release, there is now also a three-dimensional acoustic field, which is difficult to represent by lumped parameter models in an accurate way. While complete numerical approaches, representing essentially all the physics involved (see references in Section 10.1), are possible, this remains a costly task and does not permit to vary system parameters extensively. Accordingly, acoustic-based models, taking into account the interaction with the heat release by transfer functions, are still attractive. We will follow this modeling route for the investigation of our surrogate system.

11.1 The acoustic field in an annular domain

We consider an annular duct as shown in Fig. 11.1. L denotes the axial length and R and hR the radii of the outer and inner cylinder, respectively (h is the hub–tip ratio).

For vanishing mean flow Mach number and a homogeneous temperature, the acoustic pressure field is a solution of the Helmholtz equation

$$\nabla^2 \hat{p} + k^2 \hat{p} = 0, \tag{11.1}$$

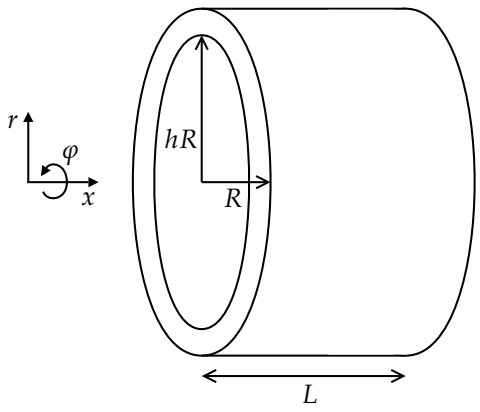

Figure 11.1: An annular duct with associated coordinate system and outer and inner radii R and hR, where h is the hub–tip ratio.

where p is the acoustic pressure, $\hat{(\cdot)}$ denotes a Fourier transformed variable, and $k = \omega/c$ is the wavenumber, as before. The solution to Eq. (11.1) can be written as an infinite superposition of modes (Rienstra & Hirschberg 2006)

$$\hat{p} = \sum_{m=-\infty}^{\infty} \sum_{n=0}^{\infty} \left(A_{mn}\, \mathrm{e}^{-\mathrm{i}k_{mn}x} + B_{mn}\, \mathrm{e}^{\mathrm{i}k_{mn}x} \right) \mathrm{e}^{\mathrm{i}m\varphi}\, p_{mn}(\kappa_{mn} r). \tag{11.2}$$

Here, m and n are azimuthal and radial mode orders, k_{mn} is the axial wavenumber, p_{mn} is the radial eigenfunction of order (m, n), κ_{mn} is the radial eigenvalue, and A_{mn} and B_{mn} are complex coefficients (the modal amplitudes). The compatibility condition, induced by the separation ansatz which leads to (11.2), requires $k_{mn}^2 = k^2 - \kappa_{mn}^2$. With a suitable definition of the square root, involved in evaluating k_{mn}, the part of the pressure field associated with A_{mn} corresponds to a downstream traveling wave and that associated with B_{mn} with an upstream traveling one. Since the pressure field must be 2π-periodic in the angular coordinate, we can only have azimuthal eigenvalues $m = 0, \pm 1, \pm 2, \ldots$ Instead of the complex exponential $\mathrm{e}^{\mathrm{i}m\varphi}$, the angular dependence of the pressure field can be represented by $\cos m\varphi$ and $\sin m\varphi$ with $m \geq 0$ only. We will use both types of angular basis functions, depending on which form is more convenient. The reason for this freedom of choice is the degeneracy of the circumferential eigenfunctions. This topic is discussed in detail in Section 11.2.

The radial eigenfunctions p_{mn} are solutions of Bessel's equation satisfying homogeneous Neumann conditions at hR and R. Hence, they are given by

$$p_{mn}(\kappa_{mn} r) = \mathrm{J}_m(\kappa_{mn} r) + C_{mn}\, \mathrm{Y}_m(\kappa_{mn} r), \tag{11.3}$$

where J_m and Y_m are Bessel functions of the first and second kind of order m, and C_{mn} and κ_{mn} can be determined from the radial boundary conditions. In particular, upon introducing the scaled radial eigenvalue $\sigma_{mn} = \kappa_{mn} R$, the eigenvalue condition can be written as

$$\mathrm{Y}'_m(h\sigma_{mn})\, \mathrm{J}'_m(\sigma_{mn}) - \mathrm{Y}'_m(\sigma_{mn})\, \mathrm{J}'_m(h\sigma_{mn}) = 0, \tag{11.4}$$

where $(\cdot)'$ denotes a derivative with respect to r, and the radial order n is defined such that $\sigma_{m(n+1)} > \sigma_{mn}$. For small $1 - h$ (a "thin" gap), the lower eigenvalues can be approximated as (Stow et al. 2002)

$$\sigma_{m0} = \frac{2m}{1+h}\,, \tag{11.5a}$$

$$\sigma_{mn} = \frac{n\pi}{1-h}, \quad \text{for } n \geq 1. \tag{11.5b}$$

The first few eigenvalues for radial mode orders 0 and 1 (computed numerically from Eq. (11.4)) and the small gap approximations (11.5) are shown in Fig. 11.2.[1] Apparently, there is sufficient accuracy for the eigenvalues shown for hub–tip ratios larger than 0.7. For the cases we are interested in, radial modes (i.e., $n > 0$) are typically highly cut-off.

The complex coefficients A_{mn} and B_{mn} are determined by the axial boundary conditions at the inlet and the outlet of the annular duct. For a closed outlet (at $x = L$), e.g., we have

[1] The approximation (11.5a) simply means that $\kappa_{m0} = m/\bar{R}$, where $\bar{R}$ is the mean radius of the annular duct.

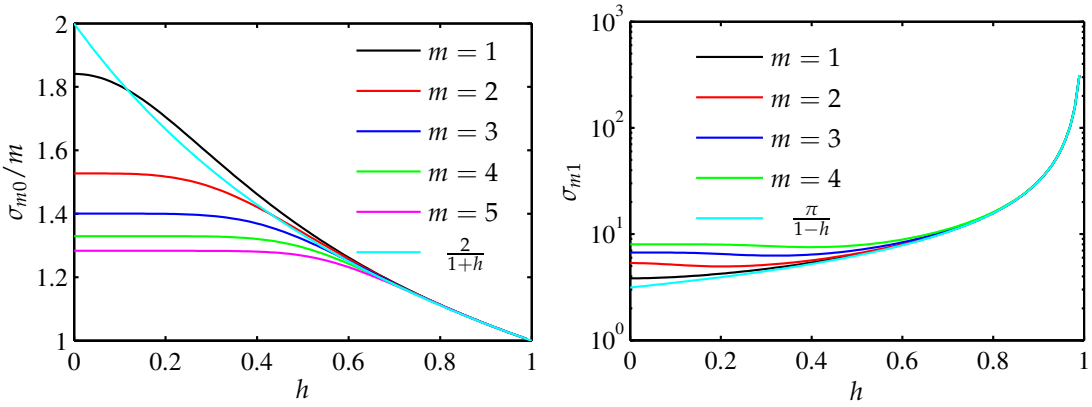

Figure 11.2: Radial eigenvalues as a function of the hub–tip ratio h; numerical solutions of Eq. (11.4) and small gap approximation (11.5). m denotes the azimuthal mode order.

$\partial_x \hat{p} = 0$ (for all r and φ) and, therefore, $B_{mn} = \mathrm{e}^{-2\mathrm{i}k_{mn}L} A_{mn}$. A_{mn} can then be determined from the boundary data at the duct inlet. If both axial boundary conditions are homogeneous, a non-trivial pressure field only exists for special choices of the axial wavenumbers k_{mn} and, hence, only for global eigenvalues k. More general boundary conditions can be given in terms of modal reflection coefficients $\mathcal{R}_{mn} = B_{mn}/A_{mn}$ which relate the reflected modal amplitudes to those incident. If the axial boundaries are such that they break the symmetry of the annulus, there may generally be modal coupling, and the amplitudes of the reflected and incident waves corresponding to different cross-sectional modal orders mix.

Taking into account the effect of a constant axial mean flow in the solution of the Helmholtz equation (11.1) is straightforward (Rienstra & Hirschberg 2006, p. 212). Since the mean flow Mach number in the application considered here is of the order of 10^{-3} (see Section 12.2), there is, however, no reason to include this additional complexity.

11.2 Symmetry and azimuthal mode degeneracy

Since the radial eigenfunctions J_m and Y_m are symmetric with respect to their order m, it follows from (11.4) that for an annular duct, the eigenvalues corresponding to m and to $-m$ are identical. The angular eigenfunctions for positive and negative m, $\mathrm{e}^{\mathrm{i}m\varphi}$ and $\mathrm{e}^{-\mathrm{i}m\varphi}$, are linearly independent, and hence, there is a two-dimensional eigenspace. This is a manifestation of eigenvalue degeneracy. For an axisymmetric configuration this degeneracy persists for all azimuthal mode orders m.

Mode degeneracy can – in most cases – be attributed to the presence of symmetries in the eigenvalue problem[2] (Hamermesh 1989). The group theoretical explanation is that if the eigenvalue operator is equivariant under the action of a symmetry group (i.e., it commutes with the group), then every admissible symmetry operation transforms an eigenfunction associated with a certain eigenvalue into an(other) eigenfunction with the same eigenvalue. If the group operations generate linearly independent eigenfunctions, this

[2] An exception are so-called accidental degeneracies. These dynamical peculiarities are, however, considered to be rare in occurrence (Perrin & Charnley 1973).

particular eigenvalue is degenerate. In this case, the eigenfunctions form a vector space which is invariant under the action of the symmetry group. Since a certain system symmetry is the reason for some eigenvalue to be degenerate, removing that symmetry will, consequently, split the degenerate mode into two distinct ones.

Loosely speaking, an eigenfunction can be suspected to be a member of a degenerate set if it has a lower symmetry than that of the eigenvalue problem.[3] Since complete axisymmetry is an infinite-order rotational symmetry, all eigenvalues with $m \neq 0$ are degenerate in case of an annular duct. As the eigenspace of the degenerate modes is two-dimensional, we need not stick to the exponential-type azimuthal eigenfunctions, but can use any linear combination as basis, such as $\sin m\varphi$ and $\cos m\varphi$. In this case, using positive m only is sufficient.

Annular combustion chambers, as well as our surrogate model system, feature only a discrete rotational symmetry because the configuration is not invariant with respect to rotations by arbitrary angles. In the simplest case, the order of rotational symmetry is equal to the number of burners. (A counterexample is ALSTOM's GT13E2, which has two circumferentially arranged burner rows, with each burner pair being shifted radially with respect to its neighbors.) The annular Rijke tube has nominally a rotational symmetry of order 12 and, in addition to that, 12 reflection symmetries at planes which contain the symmetry axis and pass through angles with multiples of $\pi/24$ (see Fig. 10.1). Here, we consider only the unforced system so that the 6 speakers, mounted in every second tube, do not reduce the symmetry order. Since the symmetry is only discrete, modes with certain circumferential orders are distinct. Based on group-theoretical arguments, Perrin (1977) has shown that this is true for azimuthal orders which are a half-integer multiple of the order of the associated symmetry group. In the following, we will denote the group of Nth order rotational symmetry, including the N additional reflection symmetries, by C_N.[4]

Assuming a uniform temperature field, the Helmholtz operator has no explicit coordinate dependence, and the relevant symmetry group is essentially determined by the geometry and the boundary conditions. We denote geometrical transformations which leave the problem unchanged by O_R. These are the actions of the associated symmetry group, in our case, rotations by specific angles and reflections with respect to the given planes of symmetry. Applying one of these symmetry transformations to the Helmholtz equation (11.1), we obtain

$$O_R(\nabla^2\hat{p}) + O_R(k^2\hat{p}) = 0. \tag{11.6}$$

Since the Laplacian is equivariant with respect to O_R, the two operations commute, and we have $O_R(\nabla^2\hat{p}) = \nabla^2(O_R\hat{p})$. Furthermore, the eigenvalue is only a scalar number, and hence, (11.6) is equivalent to

$$\nabla^2(O_R\hat{p}) + k^2(O_R\hat{p}) = 0. \tag{11.7}$$

[3] Eigenvalue problem refers to differential equation, boundary conditions, and geometrical configuration.

[4] According to the Schönflies notation (Hamermesh 1989), this group is labeled with C_{Nv} to indicate the additional reflection symmetries. In contrast to the order of rotational symmetry, we cannot change the reflection symmetries in our set-up. Therefore, we omit the index 'v' for convenience and understand the reflection symmetries to be included when referring to C_N.

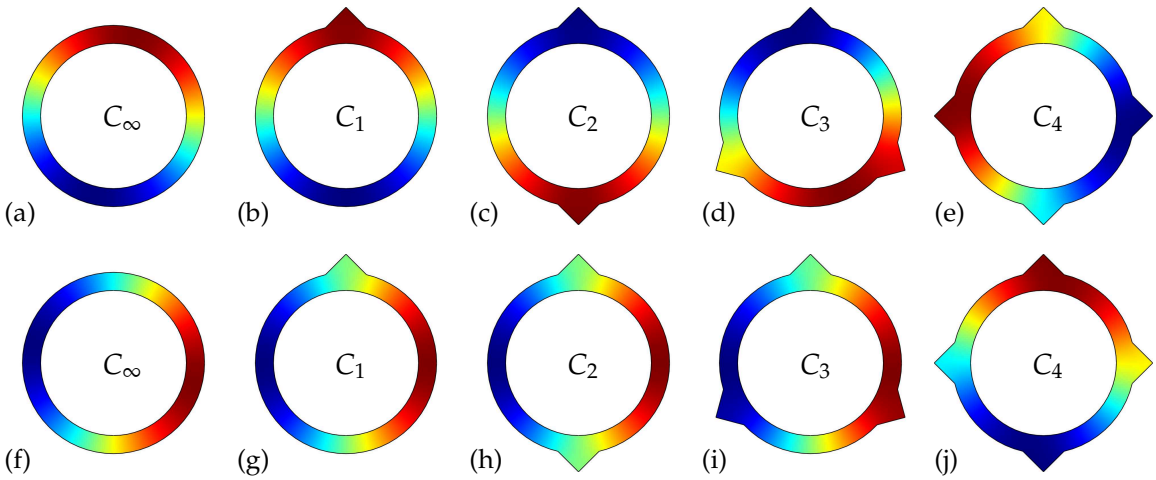

Figure 11.3: Pressure patterns of the first azimuthal mode for different degrees of rotational symmetry. Top and bottom rows correspond to two orthogonal eigenfunctions which may or may not share the same eigenvalue, depending on the degree of symmetry. The $m = 1$ mode is degenerate for the C_∞, C_3, and C_4 configurations.

But this means that if $\hat{p}$ is an eigenfunction with eigenvalue k^2, then so is $O_R\hat{p}$ – with the same eigenvalue. Now if $O_R\hat{p}$ and $\hat{p}$ are linearly independent, then it follows immediately that the eigenvalue is degenerate because the associated eigenspace is (at least) two-dimensional.

This somewhat abstract concept can be made more instructive by studying the set of examples in Fig. 11.3. We consider the first circumferential eigensolutions of the Helmholtz equation (11.1). The geometrical configurations exhibit symmetries of different order. From the left to the right column, the associated symmetry groups are C_∞, C_1, C_2, C_3, and C_4.[5] The configuration in the left column exhibits C_∞ symmetry; it is invariant with respect to rotations by an arbitrary angle and reflections with respect to any plane containing the axis of symmetry. Because of this property, the eigenfunction shown in the top row can be rotated by an arbitrary angle and is still an eigenfunction associated with the same eigenvalue. Clearly, we will manage to find some rotations for which the transformed pressure pattern is linearly independent from the initial one. A possible choice is shown in the lower row. These two pressure patterns form a basis of the eigenspace corresponding to the degenerate first azimuthal eigenvalue. It is easy to see that we can apply this argument to modes of arbitrary azimuthal order. Therefore, all eigenvalues with $m \neq 0$ are degenerate. Eigenfunctions with $m = 0$ are still mapped to eigenfunctions by the O_R, but since they are axisymmetric, the symmetry transformations do not generate linearly independent members, and the corresponding eigenvalues are distinct.

We consider now the configuration in the second column in Fig. 11.3. There is a small triangular perturbation from the axisymmetric ring shape. The specific form of this geometrical perturbation is not important. We can also assume it to be a Helmholtz resonator, for instance. However small, this geometrical imperfection breaks the axisymmetry. As a

[5] Thinking in three dimensions, the proper symmetry group associated with the patterns in Fig. 11.3 is the dihedral group D, which includes reflections with respect to the paper plane. As these additional symmetries are obviously irrelevant for thermoacoustic problems in annular domains (because that additional symmetry is not present), we will only consider the rotational group C.

result, there remain only two admissible symmetry transformations which leave the problem invariant: a rotation by 2π (the identity, in fact) and a mirror symmetry with respect to a line which passes through the centerpoint of the ring and the apex of the triangular perturbation. If there is a line of symmetry, all eigenvalues have eigenfunctions which are either symmetric or skew-symmetric with respect to that line (Trefethen & Betcke 2006). For distinct circumferential eigenvalues corresponding to one azimuthal order, then simply, one eigenfunction is symmetric and the other is skew-symmetric. In case of a degenerate eigenvalue, the basis of the degenerate eigenspace can be chosen such that these properties apply. For $m = 1$ modes, this means that either the node or the anti-node is located at the circumferential position of the triangular shape. However, since rotations by $\pi/2$ do not belong to the admissible symmetry transformations for this case, $m = 1$ modes are not degenerate, and the eigenvalues associated with the two pressure patterns in the second column in Fig. 11.3 are different. (The eigenvalue associated with the upper frame is smaller than that for the lower one.) For this simple case, this makes sense: if the triangular shape were a Helmholtz resonator, then the upper pressure pattern would be strongly damped and the lower not. The same reasoning applies to all circumferential modes, and therefore, they are all distinct.

The first azimuthal mode in case of a C_2 symmetry is shown in the middle column in Fig. 11.3. There are two additional symmetries compared to the C_1 case: a rotation by π and a mirror symmetry along a horizontal line passing through the midpoint of the ring. Again, we cannot generate linearly independent eigenfunctions by the admissible symmetry transformations. Consider modes of first azimuthal order. Rotations by π merely map them onto their negative images; in fact, this is true for all odd m. More generally, we have for rotations by π, $O_R\hat{p} = (-1)^m\hat{p}$. Therefore, also in the case of a C_2 symmetry, all azimuthal modes are distinct.

Next consider the fourth column in Fig. 11.3, which shows a configuration with C_3 symmetry. At first azimuthal order, there has to be an eigenfunction which has its nodal line passing through the triangular shape at 12 o'clock, say. Due to the C_3 symmetry of the system, we may rotate this eigenfunction by $2\pi/3$ without altering its associated eigenvalue. In contrast to the C_1 and C_2 patterns considered before, the eigenfunction generated by this transformation is linearly independent from the original one. This is immediately clear by looking at the movement of the nodal line: the rotated eigenfunction is non-zero at the circumferential position where the original eigenfunction has its node, and clearly, the two cannot be related by a constant factor. Therefore, the first azimuthal eigenvalue is degenerate. The same holds for $m = 2$ because the symmetry transformation again generates a linearly independent pressure pattern. In case of the third azimuthal mode, rotations by $2\pi/3$ and $4\pi/3$ map the eigenfunctions onto themselves. Hence, there are two distinct eigenvalues for $m = 3$. We can apply these arguments for all values of m and find, for this specific case, that only the eigenvalues with azimuthal orders being a multiple of 3 are distinct.

In case of the C_4 symmetry, shown in the fifth column in Fig. 11.3, the 1st-order azimuthal mode is again degenerate because now we may apply rotations by multiples of $\pi/2$ without changing the eigenvalue. As in the case of the C_3 symmetry, this produces a linearly independent eigenfunction. For $m = 2$, however, this is not the case. Rotations by multiples of $\pi/2$ map the 2nd-order azimuthal mode onto itself or its negative image.

Hence, in case of the C_4 symmetry, the $m = 2$ mode is distinct, as well as modes with azimuthal orders being multiples of 2.

The annular Rijke tube has nominally a 12-fold rotational symmetry with 12 additional reflection symmetries; its associated symmetry group is C_{12}. From the explanation above, we conclude that all azimuthal modes except for those with circumferential order equal to 0 or multiples of 6 will be degenerate. As in an annular combustion chamber, there are various additional ways in which the nominal symmetry of the system can be reduced. This will be the case if any of the following conditions is violated:

(i) the tubes are all geometrically equivalent;
(ii) the azimuthal spacing between the tubes is identical;
(iii) the heat sources are all located at the same axial position in the tubes;
(iv) the heat sources in the tubes are all identical and driven by the same electric power;[6]
(v) there is no azimuthal mean flow in the annular duct; and
(vi) the acoustic boundary condition at the outlet of the annular duct preserves the symmetry.[7]

Conditions (i)–(iii) and (vi) are related to purely geometrical properties. They can be changed but only discontinuously and by demounting the set-up. Condition (v) can, in principle, be violated by generating an azimuthal mean flow artificially, but this is not a straightforward procedure either. One convenient way to introduce an asymmetry is a circumferential modulation – or staging – of the power distributed to the heating grids (condition (iv)). It will be shown in later sections that this leads indeed to a splitting of nominally degenerate modes.

11.3 A frequency-domain network-type model for the annular Rijke tube

In this section, a theoretical system model for the annular Rijke tube is presented. The model is based on a frequency-domain representation of the acoustic field coupled to the heat release transfer functions of the unsteady heat sources. Although the heat sources considered in this work are electrically driven heating grids, the principal methodology can be applied to annular combustors as well.

The basic strategy in setting up the system model will be to represent the acoustic response up- and downstream of the elements of heat release separately and then combine the two by making use of the appropriate coupling relations across the heat sources. Figure 11.4 displays the notation that will be used for the acoustic pressures and velocities

[6] This ensures that the dynamic response in each tube is identical and that the mean temperature field preserves the C_{12} symmetry. It would be possible to have non-identical dynamic responses in the tubes without breaking the symmetry of the mean temperature field by using different heating grids (with different wire diameters, for example) but with the same electric power.

[7] This condition is trivially satisfied in case of a completely open or completely closed end, the former being what we have in the experimental set-up. However, if the downstream end of the annulus is not fully closed or open, then, to preserve the full order of symmetry, the outlet area would have to adhere to certain geometrical properties. We could use, for instance, a plate with N holes coaxially arranged with the tubes or located halfway between two tubes.

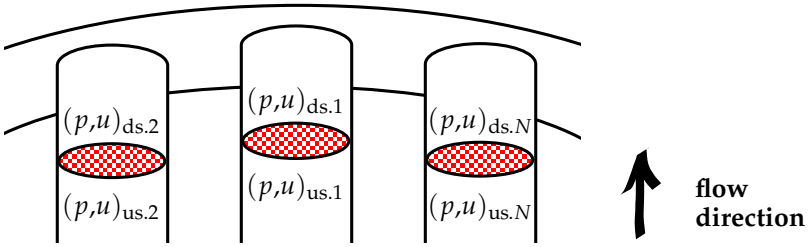

Figure 11.4: Notation for acoustic pressure and axial particle velocity up- and downstream of the heat sources

immediately up- and downstream of the heat sources. $p_{\mathrm{us/ds}.n}$ and $u_{\mathrm{us/ds}.n}$ denote acoustic pressure and axial particle velocity up-/downstream of the heat source in tube n. The tubes are counted in anti-clockwise direction when looking downstream. In setting up the model, it will be convenient to work with the acoustic pressure scaled by the (local) characteristic impedance ρc, which we denote by $\wp = p/(\rho c)$. The axial extent of the elements of heat release as well as the diameters of the tubes are much shorter than the relevant acoustic wavelengths. Therefore, we can consider the zone of heat release as compact, and the acoustic field in the tubes can be treated as one-dimensional.

The model is completely linear. Accordingly, we only intend to identify unstable modes and do not attempt to quantify the limit cycle amplitude. For the latter, detailed knowledge on the nonlinear response of the heat sources would be required (see Section 2.5.5), which is not available.

11.3.1 Up- and downstream acoustic response

To model the acoustics up- and downstream of the heat sources, we first consider each part separately. Since we assume plane wave propagation in the tubes, the whole action of the acoustic field downstream of all heat sources can be represented as a generalized impedance in the sense that it maps the velocity fluctuations downstream of the heat sources to the pressures, viz.,

$$\hat{\wp}_{\mathrm{ds}} = \boldsymbol{\mathcal{Z}}\hat{\boldsymbol{u}}_{\mathrm{ds}}, \tag{11.8}$$

where $\boldsymbol{\mathcal{Z}}$ is an impedance matrix such that element (i,j) is the pressure response downstream of the heat source in tube i to a unit excitation in acoustic velocity in tube j, while all other acoustic velocities are set to zero. Hence, the elements of $\boldsymbol{\mathcal{Z}}$ are given by $\mathcal{Z}_{ij} = \hat{\wp}_{\mathrm{ds}.i}/\hat{u}_{\mathrm{ds}.j}$, with $\hat{u}_{\mathrm{ds}.k} = 0$ for all $k \neq j$.

Although the acoustic field in the tubes upstream of the heat sources are not directly connected, we construct the model to allow for such a coupling, too (in the presence of a plenum, for instance). Analogous to the downstream part, we define an admittance matrix $\boldsymbol{\mathcal{A}}$, which relates the acoustic velocities upstream of the heat sources to the pressures by

$$\hat{\boldsymbol{u}}_{\mathrm{us}} = \boldsymbol{\mathcal{A}}\hat{\wp}_{\mathrm{us}}. \tag{11.9}$$

11.3.2 Heat release dynamics

In each tube, the relations between the up- and downstream acoustic variables are determined by the dynamic response of the heat source (in that tube). In a general linear framework, this relation can be expressed by a 2×2 transfer matrix in frequency domain

$$\begin{bmatrix} \hat{\wp}_{\mathrm{ds}.n} \\ \hat{u}_{\mathrm{ds}.n} \end{bmatrix} = \mathbf{T}_n \begin{bmatrix} \hat{\wp}_{\mathrm{us}.n} \\ \hat{u}_{\mathrm{us}.n} \end{bmatrix}. \tag{11.10}$$

For the type of compact heat source we consider here, and for a vanishing mean flow Mach number, the pressure loss is negligible, and the change in acoustic velocity due to the heat release fluctuations is given by the jump conditions (2.16).

We introduce heat release transfer functions $F_n(\omega)$ that relate the normalized heat release response in tube n to the normalized perturbation in the upstream velocity (in tube n) via

$$F_n = \frac{\hat{Q}_n}{\hat{u}_{\mathrm{us}.n}} \frac{\bar{u}_{\mathrm{us}.n}}{\bar{Q}_n}. \tag{11.11}$$

Then the transfer matrix of the heat source in tube n can be written as

$$\mathbf{T}_n = \begin{bmatrix} \xi_n & 0 \\ 0 & 1 + \left(\frac{T_{\mathrm{ds}.n}}{T_{\mathrm{us}.n}} - 1\right) F_n \end{bmatrix}, \tag{11.12}$$

where $\xi_n = \sqrt{T_{\mathrm{ds}.n}/T_{\mathrm{us}.n}}$ is the ratio of characteristic impedances up- and downstream of heating element n. As proposed by Lighthill (1954) for the case of small wire Strouhal numbers, we model the heat release transfer function as a first order low-pass

$$F_n = \frac{c_k}{1 + \mathrm{i}\omega c_{\tau.n}}, \tag{11.13}$$

with gain and phase parameters c_k and $c_{\tau.n}$. We explicitly allow for different temperature jumps and heat release transfer functions in each tube so that we can study the effect of an asymmetry in the heat release feedback. For later use, we define diagonal matrices $\mathbf{X}$ and $\boldsymbol{\mathcal{F}}$ with elements $\mathrm{X}_{ij} = \xi_i\delta_{ij}$ and $\mathcal{F}_{ij} = (T_{\mathrm{ds}.i}/T_{\mathrm{us}.i} - 1)F_i\delta_{ij}$ (δ_{ij} is the Kronecker delta) and scalar tube transfer functions

$$\mathcal{F}_n = (T_{\mathrm{d}.n}/T_{\mathrm{u}.n} - 1)F_n. \tag{11.14}$$

Note here that the definition of $\mathcal{F}$ is different from that in Parts I and II. In the present case, the normalized temperature ratio is included, as this will be more convenient in the following.

11.3.3 Submodel coupling and dispersion relation

The model for the entire system can be built as indicated in Fig. 11.5. To couple the acoustic models of the up- and downstream parts, we use the dynamic heat release characteristics given by Eq. (11.12). Hence, we have $\hat{\boldsymbol{\wp}}_{\mathrm{ds}} = \mathbf{X}\hat{\boldsymbol{\wp}}_{\mathrm{us}}$, i.e., the pressure is continuous across

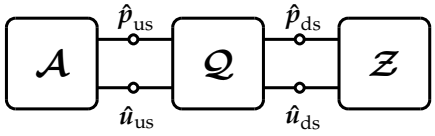

Figure 11.5: Network model representation of the annular Rijke tube. $\mathcal{Q}$ maps upstream to downstream pressures and velocities via $\mathbf{X}$ and $\mathbf{I}+\mathcal{F}$, respectively.

the heat source, and the jump in acoustic velocity is given by

$$\hat{\boldsymbol{u}}_{\mathrm{ds}} = \big(\mathbf{I}+\mathcal{F}\big)\hat{\boldsymbol{u}}_{\mathrm{us}}. \tag{11.15}$$

Combining Eqs. (11.8), (11.9), (11.15), and the pressure continuity condition, and dropping the subscript 'us' of the vector of pressures upstream of the heat source, we obtain

$$\mathbf{X}\hat{\wp} = \mathcal{Z}\big(\mathbf{I}+\mathcal{F}\big)\mathcal{A}\hat{\wp}. \tag{11.16}$$

From Eq. (11.16), it follows that for non-trivial solutions to exist, the dispersion relation

$$\det \mathcal{S} = 0 \tag{11.17}$$

must be satisfied, where the system matrix $\mathcal{S}$ is given by

$$\mathcal{S} = \mathcal{Z}\big(\mathbf{I}+\mathcal{F}\big)\mathcal{A} - \mathbf{X}. \tag{11.18}$$

Solutions ω_k of the dispersion relation are the system eigenfrequencies, $\operatorname{Re}\omega_k$ representing the (angular) oscillation frequency and $-\operatorname{Im}\omega_k$ the growth rate. The purely acoustic eigenfrequencies can be obtained for the case with no dynamic heat release as the solutions of $\det|\mathcal{Z}\mathcal{A}-\mathbf{X}| = 0$. In case of the full nominal discrete symmetry, the system matrix $\mathcal{S}$ has some special properties, which are discussed in Section 11.3.7.

It is interesting to note that (11.17) with $\mathcal{S}$ given in (11.18) is a generalization of the simple one-dimensional case of a single Rijke tube. In this case, the impedance and admittance are scalar functions which relate acoustic velocity to pressure and vice versa. The dispersion relation for this configuration can be written as $\mathcal{Z}(1+\mathcal{F})\mathcal{A} - \xi = 0$ (Schuermans 2003), where $\mathcal{A}$ and $\mathcal{Z}$ are admittance and impedance immediately up- and downstream of the source of heat release.

If an eigenvalue ω_k of (11.17) has been obtained, the corresponding pressure pattern in the N tubes, at the heat source positions, can be computed as the null space of the system matrix evaluated at ω_k

$$\hat{\wp}_k = \ker \mathcal{S}(\omega_k). \tag{11.19}$$

The multiplicity of the eigenvalue, hence its degeneracy, can be determined from the dimension of the null space of $\mathcal{S}$. For a distinct eigenvalue, we have $\dim\ker\mathcal{S}(\omega_k) = 1$, whereas for a degenerate one, such as in the case of a fully symmetric configuration, where two mode shapes share one characteristic value, the eigenspace is two-dimensional.

The modal content $\hat{a}_m$ of the eigenfunction in the tubes can be determined by means of a discrete projection on a basis of angular Fourier modes $b_m^{c,s}(\varphi)$, viz.,

$$\hat{a}_m^{c,s} = \sum_{n=1}^{N} \hat{\wp}_{k.n} b_m^{c,s}(\varphi_n). \tag{11.20}$$

In our case of even N, we use

$$b_m^c = w_m \cos m\varphi, \quad m = 0 \ldots N/2, \tag{11.21a}$$

$$b_m^s = w_m \sin m\varphi, \quad m = 1 \ldots (N/2 - 1), \tag{11.21b}$$

were the coefficients w_m are chosen as $w_0 = w_{N/2} = N^{-1/2}$ and $w_1, \ldots, w_{N/2-1} = (N/2)^{-1/2}$. Then the N vectors with elements $b_m^{c,s}(\varphi_n)$ form an orthonormal basis in N-dimensional Euclidean space. Naturally, using the N pressures in the tubes only, we cannot resolve modes with azimuthal order higher than $N/2$. In the case of N even, only the cosine part of an $m = N/2$ mode can be detected. However, as will be seen in Section 11.5, all eigenfunctions associated with frequencies below 1000 Hz lie within the subspace spanned by the basis (11.21).

11.3.4 Upstream response matrix $\mathcal{A}$

Now, as mentioned above, in the present case considered, the upstream ends of the tubes are not connected to each other so that $\mathcal{A}$ is a diagonal matrix. (This holds true only approximately, see below.) Moreover, since the tubes are all of the same length, the diagonal entries are all identical and simply correspond to the admittance of a tube with an unflanged open end. Hence, we have

$$\mathcal{A}_{ij} = -\frac{1 - \mathrm{i}\,\mathcal{Z}_{\mathrm{LS}} \tan kL_{\mathrm{us}}}{\mathcal{Z}_{\mathrm{LS}} - \mathrm{i} \tan kL_{\mathrm{us}}} \delta_{ij}, \tag{11.22}$$

where $\mathcal{Z}_{\mathrm{LS}}$ is the small-Helmholtz-number approximation of the end impedance of an open, unflanged tube (Eq. (2.10)); L_{us} denotes the length upstream of the heat source. In principle, L_{us} could be different in each tube, which corresponds to the case where the heating grids are at different axial locations. Then $\mathcal{A}$ would still be diagonal but not isotropic.

Modeling the upstream admittance matrix by Eq. (11.22) is only an approximation for two reasons. First, the upstream ends of the tubes are not ideally unflanged due to a supporting ring (see Fig. 10.2). Second, since there is some sound radiation out of the tube inlets, $\mathcal{A}$ is not strictly diagonal. The sound radiated out of tube inlet is reflected from the laboratory walls and eventually impinges on all others (and also on itself). Modeling these effects is difficult. The supporting ring is a non-standard geometry and no correlations exist for this case. Likewise, taking into account the sound waves reflected from the laboratory walls is rather cumbersome. We assume, however, that these effects are not dominant for small tube Helmholtz numbers.

11.3.5 The acoustic response matrix of an annular duct

To represent the impedance matrix of an annular duct, we use the approach proposed by Schuermans, which is based on an eigenfunction expansion of the Green's function for the Helmholtz equation. Since the eigenfunctions for an annular duct are known analytically, this method is flexible and fast. The procedure was described in detail by Schuermans et al. (2003) and Schuermans (2003); we only reproduce the essentials below.

In terms of the eigenfunctions of the Helmholtz equation, the pressure response to a velocity excitation on a surface S at the boundary can be written as

$$\hat{\wp}(\boldsymbol{x}) = -\mathrm{i}k \sum_{\alpha} \frac{\psi_\alpha(\boldsymbol{x})}{k^2 - k_\alpha^2} \int_S \psi_\alpha^*(\boldsymbol{x}_0) \hat{u}_\nu(\boldsymbol{x}_0) \mathrm{d}A_0, \tag{11.23}$$

where $\alpha = \{l, m, n\}$ is a multiindex ordered such that $\mathrm{Re}\, k_\alpha \leq \mathrm{Re}\, k_{\alpha+1}$, l, m, and n are longitudinal, azimuthal, and radial mode indices, respectively, and ψ_α is the eigenfunction associated with the eigenvalue k_α; $\hat{u}_\nu$ is the particle velocity normal to the boundary. The eigenfunctions are assumed to form an orthonormal set with respect to the inner product $\langle a, b \rangle = \int_V ab^* \mathrm{d}V$ so that $\langle \psi_\alpha, \psi_\beta \rangle = \delta_{\alpha\beta}$. This will be possible if the homogeneous problem has only Dirichlet or Neumann conditions at the boundaries (Nicoud et al. 2007).

Considering now an annular geometry enclosed by rigid cylinders, the transversal dependence of the eigenfunctions is the same as that in (11.2). The axial variation of the eigenfunctions follows from the boundary conditions at the inlet and outlet. In our modeling approach, we need the response of the annular duct to axial velocity fluctuations at the tube connections. Therefore, we have to consider a hard-walled boundary condition at the inlet. Since the outlet represents an open end, the axial variation of the eigenfunctions is simply given by $\cos(k_l x)$ with $k_l L = (l + 1/2)\pi$, $l = 0, 1, \ldots$ (L being the axial extent of the annular duct). Hence, the set of eigenfunctions and eigenvalues for this case is

$$\psi_{lmn} = \Lambda_{lmn}^{-1} \cos(k_l x) p_{mn}(\kappa_{mn} r)\, \mathrm{e}^{\mathrm{i}m\varphi}, \tag{11.24a}$$

$$k_{lmn} = \sqrt{\kappa_{mn}^2 + [(l + 1/2)\pi L^{-1}]^2}, \tag{11.24b}$$

where the scaling constant Λ_{lmn} is introduced so that the norm of all eigenfunctions is unity, and the radial variation p_{mn} is as given in (11.3).

With a constant forcing amplitude at the inlet section on an area corresponding to one of the tubes, the impedance matrix can be computed from (11.23), when the series is truncated at sufficiently large values of α. Since the annular Rijke tube has a hub–tip ratio close to unity (as is the case for most gas turbine combustion chambers), we do not include any radial modes when computing the response. We simply use the mean radius for the eigenvalues, which is a good approximation for hub–tip ratios close to unity (see Section 11.1). For acoustic wavelengths distinctly larger than the tube diameter, we can further approximate the circumferential variation of the eigenfunctions over the tube surface with their value at the center of the tube. Then the integral in (11.23) can be simply replaced with a multiplication by the cross-sectional tube area A. Evaluating (11.23) at the tube–annular-duct transition at φ_i with forcing at φ_j then gives

$$\hat{\wp}(\varphi_i) = \mathrm{i}kA \sum_{\alpha} \frac{\psi_\alpha(\varphi_i)\psi_\alpha^*(\varphi_j)}{k^2 - \mathrm{i}\zeta_\alpha k - k_\alpha^2}\, \hat{u}_\nu(\varphi_j), \tag{11.25}$$

where we added a modal damping term ζ_α, representing visco-thermal effects, and assumed that the cross-sectional areas of all tubes are identical. Viscous damping typically increases with frequency, and therefore we assume the relation $\zeta_\alpha = \zeta k_\alpha$, where ζ is a small constant. We set this constant to 0.025 and keep this value throughout this work. This value is actually somewhat large to merely represent visco-thermal damping, but we

use it concurrently to account for acoustic power losses by radiation from the open end of the annular duct. This effect is not modeled by the eigenfunction expansion, in which we used an ideally reflecting pressure-node boundary condition. In Section 12.3, we measure the modal open-loop response to speaker excitation and compare it with the model results. The width of the resonance peak, which is a measure for the modal damping, agrees quite well. Thus, we assume that this damping model can be considered as reasonably accurate.

Equation (11.25) represents the impedance matrix of an annular duct with elements $\mathcal{Z}_{0.ij} = \hat{\wp}(\varphi_i)/\hat{u}_\nu(\varphi_j)$, where ψ_α and k_α are as given in (11.24) evaluated at $x = 0$. However, this is not the impedance matrix in Eq. (11.8) because that one is defined with respect to the location at the heat sources. To keep track of this distinction, we denote the impedance matrix defined through (11.25), i.e., with reference location at the tube–annular-duct transition, by $\boldsymbol{\mathcal{Z}}_0$.

The method outlined above is not restricted to configurations with analytically available eigenfunctions. For more complex geometries with possibly non-uniform temperature distributions, numerically calculated eigenfunctions can be used (Schuermans 2003) in Eq. (11.25).

There are also alternative methods to represent the acoustic response matrix $\boldsymbol{\mathcal{Z}}$ of an annular duct. One possibility is to compute it directly by using a numerical Helmholtz solver. The advantage of this method is that the computation can be evaluated precisely at the desired location, i.e., the position of the heat sources. In addition to that, it is possible to specify arbitrary frequency-dependent boundary conditions at the outlet plane of the annular duct. Computing the response matrices numerically is straightforward. We specify a velocity excitation as boundary condition on the coupling surface of one of the tubes. The acoustic velocity on the coupling surfaces of all other tubes are set to zero. As part of the solution, we obtain the pressures in all N tubes and can thus evaluate one column of $\boldsymbol{\mathcal{Z}}$. Depending on the degree of symmetry, it may be necessary to do more than one computation (per frequency).

Determination of the impedance matrix in an experiment is also possible. In principle, this can be accomplished as in the numerical case. The application of the correct boundary conditions is obviously more difficult. Assuming that the system can be splitted into an upstream and a downstream part, at the location of the heat source, a sound hard boundary condition can be realized by simply closing the tubes with a stiff plate. One tube has to remain open so that excitation with a speaker can be applied. Then, the acoustic velocity has to be determined in the tube in which the excitation is applied, at the reference plane, and the pressure in all tubes. This can be realized by using the Multi-Microphone-Method, but if the tubes are short, this might be difficult to accomplish. Also, by closing the tubes at the inlet, it is only possible to measure the impedance matrix in the cold case.

However, the numerical solution as well as the measurements provide only discrete data at real frequencies. In the general case, the stability analysis based on Eq. (11.17) requires evaluation of the impedance matrix $\boldsymbol{\mathcal{Z}}$ at complex frequencies, due to damping, non-ideal boundary conditions, and acoustically active elements (dynamic heat release). We would then need to resort to system identification techniques in addition, which is non-trivial in this case due to the multi-input–multi-output character of the system.

Comparing the three methods for the determination of the impedance matrix outlined above, we find the eigenfunction expansion to be the most suitable. Therefore, it is our method of choice for modeling the annular duct acoustics of the annular Rijke tube.

Symmetry of the annular duct response matrix

If the annular duct exhibits the maximum order of discrete rotational symmetry (this must also hold for the temperature field), the associated acoustic response matrix $\boldsymbol{\mathcal{Z}}_0$ has only very few distinct elements. For even and odd N, the number of distinct elements is $N/2+1$ and $(N+1)/2$, respectively. This is because only the relative locations of excitation ($u_{\mathrm{ds}.j}$) and response ($\wp_{\mathrm{ds}.i}$) are of relevance. Excitation at 12 o'clock, for example, results in identical responses at 10 and 2 o'clock. Moreover, this response is identical to that at 1 and 5 o'clock, when forcing at 3 o'clock. Note, however, that this holds only if the additional reflection symmetries are present. Otherwise, $\boldsymbol{\mathcal{Z}}_0$ has N distinct elements. In any case, the second column of $\boldsymbol{\mathcal{Z}}_0$, which represents the pressure responses to a velocity excitation at the coupling area to the second tube, can be obtained from the first column by shifting all elements down by one. If we denote the first column of $\boldsymbol{\mathcal{Z}}_0$ by $\boldsymbol{z}$, we have

$$\mathcal{Z}_{0.ij} = z_{1+(i-j) \bmod N}. \tag{11.26}$$

This is precisely the definition of a circulant matrix (Gray 2006). Besides significantly simplifying the numerical or experimental determination of the impedance matrix, this property also carries over to the system matrix $\boldsymbol{\mathcal{S}}$ defined in (11.18) if the entire system exhibits the maximum degree of symmetry. This will be further discussed in Section 11.3.7.

11.3.6 Prolongation of the annular duct response along an array of straight tubes

The acoustic response matrix $\boldsymbol{\mathcal{Z}}$ needs to be known at the reference locations immediately downstream of the heat source. The eigenfunction expansion presented above, however, only allows to calculate $\boldsymbol{\mathcal{Z}}_0$, which is defined directly at the tube–annular-duct transition. A transformation of the reference locations along an array of straight tubes (which do not necessarily need to have identical lengths), such as in Fig. 11.4, can be achieved in the following way.

Consider the impedance matrix of an annular duct (no tubes attached). We denote the up- and downstream traveling plane wave components at coupling area i as $\hat{g}_{0.i}$ and $\hat{f}_{0.i}$. Then the elements $\mathcal{R}_{0.ij}$ of the reflection coefficient matrix $\boldsymbol{\mathcal{R}}_0$ can be defined as $\mathcal{R}_{0.ij} = \hat{g}_{0.i}/\hat{f}_{0.j}$, with $\hat{f}_{0.k} = 0$ if $k \neq j$. Since, for plane waves, we have $\hat{\wp}_{0.i} = \hat{f}_{0.i} + \hat{g}_{0.i}$ and $\hat{u}_{0.i} = \hat{f}_{0.i} - \hat{g}_{0.i}$, the impedance matrix relates incident and reflected plane wave components according to $\hat{\boldsymbol{f}}_0 + \hat{\boldsymbol{g}}_0 = \boldsymbol{\mathcal{Z}}_0(\hat{\boldsymbol{f}}_0 - \hat{\boldsymbol{g}}_0)$. Hence, the reflection coefficient matrix can be computed from the impedance matrix via

$$\boldsymbol{\mathcal{R}}_0 = (\boldsymbol{\mathcal{Z}}_0 + \mathbf{I})^{-1}(\boldsymbol{\mathcal{Z}}_0 - \mathbf{I}), \tag{11.27}$$

where $\mathbf{I}$ is the $N \times N$ identity matrix. This is again a generalization of the case of a plane wave in a single tube, for which the reflection coefficient and the impedance are scalar functions, related by $\mathcal{R} = (\mathcal{Z}-1)/(\mathcal{Z}+1)$.

Denoting the length of the tubes as Δx_i, the up- and downstream traveling waves at the tube entrances (the heat source locations), $\hat{g}_i$ and $\hat{f}_i$, can be related to those at the inlet of the annular duct as $\hat{g}_i = \mathrm{e}^{-\mathrm{i}k\Delta x_i}\,\hat{g}_{0.i}$ and $\hat{f}_i = \mathrm{e}^{\mathrm{i}k\Delta x_i}\,\hat{f}_{0.i}$. Accordingly, we have for the reflection coefficient matrix with reference planes at the heat sources

$$\mathcal{R}_{ij} = \mathrm{e}^{-\mathrm{i}k(\Delta x_i + \Delta x_j)}\,\mathcal{R}_{0.ij}. \tag{11.28}$$

Finally, the impedance matrix at the desired reference location, $\boldsymbol{\mathcal{Z}}$, can be calculated using the equivalent of (11.27)

$$\boldsymbol{\mathcal{Z}} = (\mathbf{I} - \boldsymbol{\mathcal{R}})^{-1}(\mathbf{I} + \boldsymbol{\mathcal{R}}). \tag{11.29}$$

With (11.28) and (11.29), Eq. (11.27) can be reformulated to directly relate the impedance matrix at the heat sources to that at the inlet of the annular duct, viz.,

$$\boldsymbol{\mathcal{Z}} = \left[(\boldsymbol{\mathcal{Z}}_0 + \mathbf{I})\mathbf{D}^{-1} - (\boldsymbol{\mathcal{Z}}_0 - \mathbf{I})\mathbf{D}\right]^{-1}\left[(\boldsymbol{\mathcal{Z}}_0 + \mathbf{I})\mathbf{D}^{-1} + (\boldsymbol{\mathcal{Z}}_0 - \mathbf{I})\mathbf{D}\right]. \tag{11.30}$$

In (11.30), the matrix $\mathbf{D}$ has elements $\mathrm{D}_{ij} = \mathrm{e}^{-\mathrm{i}k\Delta x_i}\,\delta_{ij}$.

In the preceding section, we established that the impedance matrix of an axisymmetric annular duct, $\boldsymbol{\mathcal{Z}}_0$, is circulant. If the heat source positions are all identical, the matrix $\mathbf{D}$ in Eq. (11.30) is a multiple of the identity and therefore also circulant. Since inverses, products, and sums of circulant matrices are again circulant (Gray 2006), it is evident from (11.30) that the impedance matrix $\boldsymbol{\mathcal{Z}}$, with reference location at the heat sources, is circulant, too.

11.3.7 Special properties of the system matrix $\boldsymbol{\mathcal{S}}$

As we found in Sections 11.3.5 and 11.3.6, if the annular duct, the mean temperature field, and the heat source locations exhibit the maximum degree of discrete rotational symmetry (i.e., of order N), the impedance matrix $\boldsymbol{\mathcal{Z}}$ is circulant. We now assess whether this property also holds for the system matrix $\boldsymbol{\mathcal{S}}$ defined in Eq. (11.18). We first note that in case of identical heat release transfer functions, the matrix $\boldsymbol{\mathcal{F}}$ is a (frequency-dependent) multiple of the identity. Such a matrix is obviously also circulant. Second, for identical tubes and mean temperature increase across the grids, the admittance matrix $\boldsymbol{\mathcal{A}}$ and the matrix of characteristic impedance ratios $\mathbf{X}$ are also multiples of $\mathbf{I}$. Since the sum and the product of two circulant matrices is again circulant (Gray 2006), we find from (11.18) that for a completely symmetric system set-up, the system matrix $\boldsymbol{\mathcal{S}}$ is also circulant.

Having established that $\boldsymbol{\mathcal{S}}$ is a circulant matrix, we list a few special properties as given, for example, by Gray (2006). We denote the first column of $\boldsymbol{\mathcal{S}}$ by $\boldsymbol{\varsigma}$ and call it the generating vector. Most of the special properties of a circulant matrix can all be readily derived from the sole fact that it has the spectral decomposition

$$\boldsymbol{\mathcal{S}} = \mathbf{W}\boldsymbol{\Theta}\mathbf{W}^{\dagger}, \tag{11.31}$$

where $(\cdot)^{\dagger}$ denotes the Hermitian transpose, and $\mathbf{W}$ is the unitary discrete Fourier transform matrix of size N with elements

$$W_{ij} = N^{-1/2}\exp\left(2\pi\mathrm{i}(i-1)(j-1)/N\right), \tag{11.32}$$

and $\boldsymbol{\Theta} = \operatorname{diag} \boldsymbol{\vartheta}$ with the vector of eigenvalues given by $\boldsymbol{\vartheta} = N^{1/2}\,\mathbf{W}\boldsymbol{\varsigma}$. In other words, the eigenvectors of $\boldsymbol{\mathcal{S}}$ (in fact, of every circulant matrix) are given by a discrete Fourier basis, and the eigenvalues are the discrete Fourier transform of the generating vector $\boldsymbol{\varsigma}$. However, we are not interested in the eigenvalues of $\boldsymbol{\mathcal{S}}$ in general, but only if there is one which is zero. For then $\boldsymbol{\mathcal{S}}$ has a non-empty null space, and the dispersion relation (11.17) is satisfied. In terms of the generating vector $\boldsymbol{\varsigma}$, the dispersion relation can be written as

$$\det \boldsymbol{\mathcal{S}} = N^{N/2} \operatorname{prod}(\mathbf{W}\boldsymbol{\varsigma}) = 0, \tag{11.33}$$

where $\operatorname{prod}(\cdot)$ represents the product of all elements of vector $(\cdot)$. Hence, the dispersion relation is equivalent to the requirement that the generating vector $\boldsymbol{\varsigma}$ has at least one vanishing Fourier component (which corresponds to the azimuthal order of the corresponding eigenfunction). Then evaluating the dispersion relation becomes particularly simple because we only have to check for zero components of the discrete Fourier transform of the first row of the system matrix.

11.4 Perturbation of acoustic modes

The frequency-domain system model presented in Section 11.3 is essentially a low-order method to find solutions to the fundamental thermoacoustic equation (2.13), which is repeated here for convenience:

$$\nabla \cdot \left(c^2 \nabla \hat{p}\right) + \omega^2 \hat{p} = -\mathrm{i}\omega(\gamma - 1)\hat{q}. \tag{2.13}$$

In the case of thermoacoustic instabilities, the source term on the right hand side of (2.13) is a linear homogeneous function of the acoustic field at some reference location (typically with quite localized support) that can be expressed in terms of a transfer function. The heat release transfer function is generally a transcendental function of ω so that (2.13) constitutes a nonlinear eigenvalue problem (nonlinear in the eigenvalue parameter). It is possible to solve this equation with numerical tools iteratively, but this is time consuming and may hide some essential insight, which is only accessible by an analytical technique.

The low-order method presented in Section 11.3, on the other hand, rests on the simplicity of the geometrical set-up and additional assumptions, such as uniform temperature fields up- and downstream of the heating grids and a concentrated acoustic source with δ-support. More complex geometries and non-uniform temperature fields could actually be taken into account by either computing the acoustic response matrices or the eigenfunctions for the modal expansion with a numerical Helmholtz solver. Yet, it would be desirable to tackle Eq. (2.13) directly, with all complexities involved (in the case of combustion chambers, in particular, multi-dimensional distributed heat release–acoustic interaction). For these reasons, we consider an alternative method based on perturbations of the acoustic modes without heat release interaction. A similar approach was presented by Benoit & Nicoud (2005) and Nicoud et al. (2007). However, they did not address degenerate modes, which are of major importance for annular systems.

The acoustic source resulting from a normalized heat release perturbation is proportional to the normalized temperature increase $T_{\mathrm{ds}}/T_{\mathrm{us}} - 1$ (see Eq. (2.18)). In case of a

heating grid, this quantity is quite small. We can therefore think of a particular eigensolution of (2.13) as a perturbation of one without feedback from the heat release (i.e., with zero right hand side). The advantage is that without heat release, Eq. (2.13) is just an elementary Helmholtz equation which can be solved with standard tools.

We start by abbreviating the right hand side of Eq. (2.13) as $\theta = \theta(\boldsymbol{x}, \omega, \hat{p}, \nabla\hat{p})$. As proposed by Benoit & Nicoud (2005) and Nicoud et al. (2007), we expand the eigenfunction $\hat{p}$, the eigenvalue ω, and the source term θ in a power series in ε,[8] viz.,

$$[\hat{p}, \omega, \theta] \sim \sum_{n=0}^{\infty} [\hat{p}_n, \omega_n, \theta_n]\varepsilon^n, \qquad \text{as } \varepsilon \to 0. \tag{11.34}$$

The assumption that the interaction from the heat release, i.e., the right hand side of (2.13), is small enters the analysis by imposing $\theta_0 = 0$ and $\theta_1 = \partial_\varepsilon\theta|_{\varepsilon=0} = -\mathrm{i}\rho\omega_0(\gamma-1)\hat{q}_0$ with $\hat{q}_0 = \hat{q}(\boldsymbol{x}, \omega_0, \hat{p}_0, \nabla\hat{p}_0)$. Introducing the ansatz (11.34) into Eq. (2.13) and collecting terms with like powers of ε, we obtain at leading and first order

$$\varepsilon^0: \qquad \nabla\cdot\left(c^2\nabla\hat{p}_0\right) + \omega_0^2\hat{p}_0 = 0, \tag{11.35}$$

$$\varepsilon^1: \qquad \nabla\cdot\left(c^2\nabla\hat{p}_1\right) + \omega_0^2\hat{p}_1 = \theta_1 - 2\omega_0\omega_1^q\hat{p}_0, \tag{11.36}$$

where we added a superscript q to ω_1 to indicate that this eigenvalue correction results from taking into account heat release feedback. At leading order, we recover the Helmholtz eigenproblem with no heat release. We assume that this unperturbed problem satisfies homogeneous Dirichlet and/or Neumann conditions at the boundaries. This is a crucial restriction, but slight deviations from these ideal boundary conditions can be taken into account, as we will show later. The leading-order problem (11.35) with these ideal boundary conditions is just a standard Helmholtz problem that can be solved (numerically if necessary) without too much effort.

At first order in ε, we obtain an inhomogeneous Helmholtz equation for the correction of the eigenfunction, $\hat{p}_1$. The forcing terms on the right hand side contain the unperturbed eigenfunction and the correction of the eigenvalue. The latter, ω_1^q, can be determined by invoking a solvability condition for the correction of the eigenfunction. Since the operator acting on $\hat{p}_1$ in Eq. (11.36) is the same as that in (11.35), which is a homogeneous problem, the first-order equation cannot be solved for arbitrary forcing terms (the Fredholm alternative). Because the null space of the operator is non-empty, we have to require that the right hand side of (11.36) lies completely in the complement of the kernel of the adjoint operator (see, e.g., Miller 2006). Since the unperturbed problem (with homogeneous Neumann and Dirichlet conditions) is self-adjoint, we simply need the right hand side of (11.36) to be orthogonal to a basis of the eigenspace of the unperturbed problem. As we will see below, this holds only in the case of a non-degenerate eigenvalue or if the perturbation preserves the degeneracy. If the perturbation breaks the symmetry associated with the degenerate eigenvalue, the solvability condition needs to be considered more carefully.

[8] We do not associate ε with any particular parameter in (2.13). We assume that it is small and later set it to unity.

11.4.1 Non-degenerate eigenvalues and degeneracy-preserving perturbations

We consider first the case for which the unperturbed eigenvalue is non-degenerate. The kernel of the Helmholtz operator in (11.35) and (11.36) is then one-dimensional, and we only have to require that the right hand side of (11.36) be orthogonal to the unperturbed eigenfunction $\hat{p}_0$. By using the standard inner product $\langle a, b\rangle = \int_V ab^* \mathrm{d}V$, the solvability condition can be written as

$$\langle \theta_1, \hat{p}_0\rangle = 2\omega_0\omega_1^q ||\hat{p}_0||_2^2, \tag{11.37}$$

where $||\cdot||_2^2 = \langle\cdot,\cdot\rangle$ denotes the square of the L^2-norm. Since θ_1 only depends on the solution of the leading-order problem, we can compute the eigenvalue correction as

$$\omega_1^q = \frac{1}{\omega_0}\frac{\langle \theta_1, \hat{p}_0\rangle}{2||\hat{p}_0||_2^2}. \tag{11.38}$$

It is interesting to note that (11.38) is yet another representation of Rayleigh's criterion. The first-order correction of the eigenvalue has a destabilizing effect if ω_1^q has a negative imaginary part, in other words if $-\pi < \arg\omega_1^q < 0$. Since we have $\arg\theta_1 = \arg\hat{q}_0 - \pi/2$ and we can assume $\hat{p}_0$ to be real due to the Hermitian nature of the unperturbed problem, this condition translates to $-\pi/2 < \arg\langle\hat{q}_0, \hat{p}_0\rangle < \pi/2$. But this simply means that ω_1^q is destabilizing whenever the integral correlation of heat release and pressure has a non-vanishing in-phase component (which is essentially Rayleigh's criterion).

Once ω_1^q has been determined, the first-order correction of the eigenfunction can be computed from (11.36). However, the solution $\hat{p}_1$ is not unique. Since the operator on the left hand side annihilates the unperturbed eigenfunction, $\hat{p}_1$ is only determined up to an additional multiple of $\hat{p}_0$. The solution can be made unique by requiring that the correction is orthogonal to the leading-order solution.[9] Suppose a particular correction $\hat{p}_1$ has been computed from (11.36). Then we can determine one that is orthogonal to $\hat{p}_0$ through a projection on the complement space

$$\tilde{\hat{p}}_1 = \hat{p}_1 - \frac{\langle\hat{p}_1, \hat{p}_0\rangle}{||\hat{p}_0||_2^2}\hat{p}_0, \tag{11.39}$$

which can be easily verified to satisfy $\langle\tilde{\hat{p}}_1, \hat{p}_0\rangle = 0$.

We assumed that the unperturbed eigenvalue is distinct. However, as we will see in the next section, the procedure described above is also valid if the unperturbed eigenvalue is degenerate and the perturbation preserves the degeneracy. This will, for instance, be the case whenever the perturbation does not reduce the symmetry order. For the annular Rijke tube, this means that a fully symmetric heat release feedback $\hat{q}$, i.e., one which is identical in every tube, can be treated with this approach.

11.4.2 Degeneracy-unfolding perturbations

As we have already seen in the preceding sections, degenerate modes are quite common in annular systems due to the (in general discrete) rotational symmetry. However, applying the perturbation scheme in case of a degenerate eigenvalue is slightly more complex

[9] If the unperturbed operator was not self-adjoint, the additional constraint would be that the correction is orthogonal to the adjoint eigenfunction.

because the null space of the operator is two-dimensional. We closely follow classical Rayleigh–Schrödinger perturbation theory (see, e.g., Ballentine 1998).

In the degenerate case, the unperturbed problem yields two eigenfunctions, $\hat{p}_0^\eta$ and $\hat{p}_0^\mu$, say, corresponding to one ω_0. These two eigenfunctions are not unique since any pair of linearly independent basis functions of the null space of the unperturbed operator would be equally appropriate. Therefore, we use a general linear combination of $\hat{p}_0^\eta$ and $\hat{p}_0^\mu$ to represent the right hand side of (11.36). Since $\hat{q}$ is a linear homogeneous function of the pressure field, so is θ_1. Hence, we can explicitly split the contributions of the two eigenfunctions and write $\theta_1 = a_\eta \theta_1^\eta + a_\mu \theta_1^\mu$. (This separation could have been applied to the full right hand side disregardless of the perturbation.) For the general linear combination of the unperturbed eigenfunctions, Eq. (11.36) takes the form

$$\nabla\cdot\left(c^2\nabla\hat{p}_1\right) + \omega_0^2\hat{p}_1 = a_\eta\theta_1^\eta + a_\mu\theta_1^\mu - 2\omega_0\omega_1^q(a_\eta\hat{p}_0^\eta + a_\mu\hat{p}_0^\mu). \tag{11.40}$$

There are now two solvability conditions induced by the pair of eigenfunctions $\hat{p}_0^\eta$ and $\hat{p}_0^\mu$, viz.,

$$a_\eta\langle\theta_1^\eta, \hat{p}_0^\eta\rangle + a_\mu\langle\theta_1^\mu, \hat{p}_0^\eta\rangle = 2\omega_0\omega_1^q\left(a_\eta\langle\hat{p}_0^\eta, \hat{p}_0^\eta\rangle + a_\mu\langle\hat{p}_0^\mu, \hat{p}_0^\eta\rangle\right), \tag{11.41a}$$

$$a_\eta\langle\theta_1^\eta, \hat{p}_0^\mu\rangle + a_\mu\langle\theta_1^\mu, \hat{p}_0^\mu\rangle = 2\omega_0\omega_1^q\left(a_\eta\langle\hat{p}_0^\eta, \hat{p}_0^\mu\rangle + a_\mu\langle\hat{p}_0^\mu, \hat{p}_0^\mu\rangle\right). \tag{11.41b}$$

This is a linear homogeneous system for the two eigenfunction coordinates a_η and a_μ, which can be rearranged to yield

$$\frac{1}{2\omega_0}\begin{bmatrix}\langle\theta_1^\eta, \hat{p}_0^\eta\rangle & \langle\theta_1^\mu, \hat{p}_0^\eta\rangle\\ \langle\theta_1^\eta, \hat{p}_0^\mu\rangle & \langle\theta_1^\mu, \hat{p}_0^\mu\rangle\end{bmatrix}\begin{bmatrix}a_\eta\\ a_\mu\end{bmatrix} = \omega_1^q\begin{bmatrix}\langle\hat{p}_0^\eta, \hat{p}_0^\eta\rangle & \langle\hat{p}_0^\mu, \hat{p}_0^\eta\rangle\\ \langle\hat{p}_0^\eta, \hat{p}_0^\mu\rangle & \langle\hat{p}_0^\mu, \hat{p}_0^\mu\rangle\end{bmatrix}\begin{bmatrix}a_\eta\\ a_\mu\end{bmatrix}. \tag{11.42}$$

This is another (generalized algebraic) eigenvalue problem for the eigenvalue correction and the eigenfunction coordinates.[10] In general, the solvability conditions cannot be satisfied by arbitrary combinations of the two chosen basis functions of the unperturbed eigenspace but only for some special choice. The reason for this will become clearer when we discuss the two types of possible solutions of (11.42).

Suppose (11.42) admits a double eigenvalue (with geometric multiplicity two). In this case, the perturbation does not unfold the degeneracy of the leading-order eigenvalue; to first order, the eigenspace is still two-dimensional. Assuming that the basis of the unperturbed eigenspace is chosen such that it is orthonormal, the matrix on the left hand side of (11.42) is a multiple of the identity. (It could be upper or lower diagonal and still have a double eigenvalue, but then the geometric multiplicity would be only one.) Then it is clear that the eigenvalue correction is identical to that given in (11.38). Corrections to the eigenspace can be computed from Eq. (11.36) by substituting two basis functions $\hat{p}_0 = a_\eta\hat{p}_0^\eta + a_\mu\hat{p}_0^\mu$ with arbitrary but linearly independent combinations of a_η and a_μ.

On the other hand, if Eq. (11.42) has two distinct eigenvalues, the perturbation breaks the degeneracy of the leading-order solution. The unperturbed eigenfunctions then cannot be chosen arbitrarily because the corrections "spin off" of certain directions in the

[10] The two degenerate eigenfunctions $\hat{p}_0^\eta$ and $\hat{p}_0^\mu$ can be made orthonormal. In this case, the matrix on the right hand side of (11.42) is the identity and can hence be omitted. This is also possible if the unperturbed operator is not self-adjoint.

eigenspace. In other words, letting $\varepsilon \to 0$, the perturbed eigenfunctions approach two distinct elements in the unperturbed eigenspace. Those are precisely the ones we have to add the first-order correction to. These two eigenfunctions form a basis in the degenerate subspace that diagonalizes the matrix on the left hand side of (11.42).

Until now, we have not made any specific assumptions about the particular configuration. Therefore, the perturbation formulas are valid for a general annular thermoacoustic system which can be modeled by Eq. (2.13). The specification to the annular Rijke tube allows some significant simplifications. This is discussed in the next section.

11.4.3 Application to the annular Rijke tube

To assess the usefulness of the perturbation scheme, we apply it to the annular Rijke tube and compare the results with those obtained from the network model. The first-order contribution of the right hand side of (2.13) can be written as

$$\theta_1 = -\mathrm{i}\omega_0(\gamma - 1)\hat{q}(\boldsymbol{x}, \hat{p}_0, \nabla\hat{p}_0, \omega_0). \tag{11.43}$$

The volumetric heat release in tube n, $\hat{q}_n$, can be related to the heat release transfer function (11.11) by writing it in terms of the integral heat release as

$$\hat{q}_n = \hat{Q}_n A^{-1}\delta(x - x_{q.n}), \tag{11.44}$$

where we used the compactness of the heat source (assuming also that $\hat{q}$ is constant over the cross section), and A and $x_{q.n}$ denote the tube cross-sectional area and the axial location of the heat source, respectively. We allow for different heat source locations in each tube, but assume equal cross-sectional areas. Variations in the latter could be easily included, though. Substituting now the heat release transfer function for $\hat{Q}_n$, we have

$$\hat{q}_n = F_n(\omega_0)A^{-1}\delta(x - x_{q.n})\bar{Q}_n\hat{u}_{0x.n}/\bar{u}_{\mathrm{us}.n}. \tag{11.45}$$

Note here that all of the variables in (11.45) are potentially different in each tube, in other words, they are functions of space.

Using now the steady-state energy balance in tube n

$$\bar{Q}_n = \rho_{\mathrm{us}.n}\bar{u}_{\mathrm{us}.n}Ac_p(T_{\mathrm{ds}.n} - T_{\mathrm{us}.n}), \tag{11.46}$$

(11.43) takes the form

$$\theta_1 = -\mathrm{i}\omega_0\gamma P_0\mathcal{F}_n(\omega_0)\hat{u}_{0x.n}\delta(x - x_{q.n}), \tag{11.47}$$

where $\mathcal{F}_n = F_n(T_{\mathrm{ds}.n}/T_{\mathrm{us}.n} - 1)$, as before. With the above representation for θ_1, the inner product for the eigenvalue correction reads

$$\langle\theta_1, \hat{p}_0\rangle = -\mathrm{i}\omega_0\gamma P_0\langle\mathcal{F}_n\hat{u}_{0x.n}\delta(x - x_{q.n}), \hat{p}_0\rangle. \tag{11.48}$$

Evaluating the integration associated with the inner product and replacing the particle velocity with the pressure gradient by means of the linearized momentum balance (2.1b),

we have

$$\langle \theta_1, \hat{p}_0 \rangle = \gamma P_0 \sum_{n=1}^{N} \left\{ \mathcal{F}_n(\omega_0) \int_{A_n} \left[\tfrac{1}{\rho_n} \partial_x \hat{p}_{0.n} \hat{p}^*_{0.n} \right]_{x_{q.n}} \mathrm{d}A \right\}, \tag{11.49}$$

where the square brackets with the subscript $x_{q.n}$ denote evaluation at x_q (in tube n). As explained earlier, the acoustic field in the tubes is planar for the relevant modes, and the integration can therefore be replaced by a multiplication with the tube cross-sectional area. Also note that the pressure gradient is not continuous at the heat source location in our model because the temperature increases discontinuously. The quantity $\rho^{-1}\partial_x \hat{p}_0$, however, is continuous, and hence there is no ambiguity in evaluating the term in the square brackets in (11.49). This is so only for the zeroth-order pressure field. Since the heat release induces a jump in the acoustic velocity, the higher-order velocity eigenfunctions contain a jump at x_q. The ambiguity would then be resolved by the fact that the $\hat{q}$-response is defined with respect to the upstream velocity so that the higher-order equivalent to the term in the square brackets should then be evaluated at $x \uparrow x_q$.

Non-degenerate eigenvalues and degeneracy-preserving perturbations

For the non-degenerate case or if the perturbation does not break the degeneracy, substituting the inner product (11.49) in the first-order correction of the eigenvalue (Eq. (11.38)) yields

$$\omega_1^q = \frac{\gamma P_0 A}{2||\hat{p}_0||_2^2 \, \omega_0} \sum_{n=1}^{N} \left\{ \mathcal{F}_n(\omega_0) \left[\tfrac{1}{\rho_n} \partial_x \hat{p}_{0.n} \hat{p}^*_{0.n} \right]_{x_q.n} \right\}, \tag{11.50}$$

where we assumed identical cross-sectional areas for all tubes. This is not strictly necessary; for asymmetric cross-sectional areas, A_n would need to stay inside the curly brackets.

Consider a fully symmetric system first, in which $\mathcal{F}_n$ and $x_{q.n}$ are identical in each tube. The only term left in the sum in (11.50) is then the one in the square brackets. This term can be assumed to be positive for all relevant modes for the following reason. Since the up- and downstream ends of the annular Rijke tube are both open, the modes with the lowest eigenfrequencies have an axial structure corresponding to a half-wave. All modes with a three-half-wave or higher axial structure are associated with eigenfrequencies with too large damping to be unstable, as will be seen in Section 11.5. Since the heat source is located much closer to the upstream end (see Figs. 10.1 and 10.2), the pressure and its axial gradient are in phase for axial half-waves. The unperturbed eigenvalue problem (11.35) is self-adjoint, and hence, the eigenfunction $\hat{p}_0$ can be assumed to be real. Then clearly, as stated above, the term in the square brackets in (11.50) is positive for every n. As a result, for ω_1^q to have a negative imaginary part, i.e., for the perturbation to be destabilizing, we need $\mathrm{Im}\, \mathcal{F}(\omega) < 0$. This is analogous to the case of a single Rijke tube.

Degeneracy-unfolding perturbations

To treat perturbations which break the degeneracy of a mode, we need to solve the algebraic eigenvalue problem (11.42) using a basis of the unperturbed degenerate eigenspace. The inner products of the type $\langle \theta_1^{\eta/\mu}, \hat{p}_0^{\eta/\mu} \rangle$ can be evaluated based on (11.49).

It may happen that we do not know if a given perturbation unfolds the degeneracy of a certain mode. In this case, we have to solve the algebraic eigenvalue problem and check whether the degeneracy persists.

Accounting for volume damping

We shall later compare the results obtained from the network-type model described in Section 11.3 and from the perturbation method. However, there are two effects in the network model which we have not yet accounted for. The first effect is the modal damping in the expression for the impedance matrix of the annular duct (Eq. (11.25)). We can incorporate this term in the perturbation method by realizing that this mechanism represents volume damping and modifies the Helmholtz equation according to

$$\nabla\cdot\left(c^2\nabla\hat{p}\right) - \mathrm{i}\zeta\omega_0\omega\hat{p} + \omega^2\hat{p} = 0, \tag{11.51}$$

where, as we assumed in Section 11.3, ζ is frequency independent. Note, however, that ζ is not constant in space because we applied it only in the annulus, in part to account for open-end radiation. Therefore, to be consistent with the network model, we use

$$\zeta(\boldsymbol{x}) = \begin{cases} 0.025, & \text{if } \boldsymbol{x} \text{ in annulus,} \\ 0, & \text{else.} \end{cases} \tag{11.52}$$

Assuming now that the damping term is small, we can copy the procedure from Section 11.4.1 to obtain an expression for the eigenvalue correction due to damping as

$$\omega_1^{\mathrm{vd}} = \frac{\mathrm{i}}{2}\frac{\int_V \zeta||\hat{p}||_2^2\mathrm{d}V}{||\hat{p}||_2^2}. \tag{11.53}$$

If ζ was constant throughout the whole annular Rijke tube, then this would be ordinary oscillator damping. We do not have to consider degeneracy unfolding perturbations because the damping is constant in the angular direction.

Accounting for radiation from the tube inlets

The second effect we have yet to take into account in the perturbation method is the radiation of acoustic energy from the upstream ends of the tubes. We modeled this effect explicitly in the network model by using the open-end impedance (2.10). Since this boundary condition deviates only slightly from the idealized pressure-node condition for small tube Helmholtz numbers $\omega R/c$, we can consider this again as a perturbation from the ideal case with homogeneous Dirichlet conditions. For this purpose, we express the impedance at the tube inlets as

$$\mathcal{Z}(\omega) = \mathcal{Z}_0 + \varepsilon\mathcal{Z}_1(\omega) + O(\varepsilon^2), \qquad \text{as } \varepsilon \to 0, \tag{11.54}$$

with $\mathcal{Z}_0 = 0$ and $\mathcal{Z}_1(\omega) = (kR)^2/4 + \mathrm{i}\,0.61\,kR$. Here, $k = \omega/c$, and R denotes the tube radius, as before. Again, we use ε simply as an order parameter and eventually set it to unity.

The boundary conditions at the tube inlets then take the form

$$\hat{p} = \varepsilon\mathrm{i}k^{-1}\mathcal{Z}_1\partial_\nu\hat{p}. \tag{11.55}$$

With the expansion of the angular frequency, or equivalently the wavenumber, as in (11.34), the leading and first-order boundary conditions are

$$\varepsilon^0 : \qquad \hat{p}_0 = 0, \tag{11.56a}$$

$$\varepsilon^1 : \qquad \hat{p}_1 = \mathrm{i} k_0^{-1} \mathcal{Z}_1(k_0) \partial_\nu \hat{p}_0, \tag{11.56b}$$

which is based on an expansion of the impedance as

$$\mathcal{Z}(k) = \varepsilon \mathcal{Z}_1(k_0) + \varepsilon^2 \mathcal{Z}_1'(k_0) k_1 + O(\varepsilon^3), \qquad \text{as } \varepsilon \to 0. \tag{11.57}$$

Next, we multiply the complex conjugate of (11.35) with $\hat{p}_1$, (11.36) with $\hat{p}_0^*$, and subtract the former from the latter. Using the fact that the unperturbed eigenvalue is real (because the leading-order problem is self-adjoint), we obtain

$$\hat{p}_0^* \nabla \cdot (c^2 \nabla \hat{p}_1) - \hat{p}_1 \nabla \cdot (c^2 \nabla \hat{p}_0^*) = -2\omega_0 \omega_1^{\mathrm{bc}} |\hat{p}_0|^2, \tag{11.58}$$

where we added the superscript 'bc' to ω_1 to indicate that this results from the perturbed boundary conditions. We integrate the above equation over the domain and use Green's theorem to convert the volume integrals on the left hand side into surface integrals, viz.,

$$\int_{\partial V} c^2 \hat{p}_0^* \partial_\nu \hat{p}_1 \mathrm{d}A - \int_{\partial V} c^2 \hat{p}_1 \partial_\nu \hat{p}_0^* \mathrm{d}A = -2\omega_0 \omega_1^{\mathrm{bc}} ||\hat{p}_0||_2^2, \tag{11.59}$$

where ∂V represents the boundary of the domain and ∂_ν the derivative normal to the surface. The surface integrals vanish on the whole of ∂V, with the exception of the tube inlets, because we have either homogeneous Dirichlet or Neumann conditions for $\hat{p}_0$ and also for $\hat{p}_1$. (The conditions at those parts of the boundary which are not perturbed are enforced at each order in ε.) Moreover, the first surface integral on the left hand side vanishes also on the tube inlets according to the unperturbed boundary condition (11.56a). Hence, we have

$$\int_{\text{tube inlets}} c^2 \hat{p}_1 \partial_\nu \hat{p}_0^* \mathrm{d}A = 2\omega_0 \omega_1^{\mathrm{bc}} ||\hat{p}_0||_2^2. \tag{11.60}$$

Using now the first-order boundary conditions on the tube inlets (Eq. (11.56b)) and $\omega_0 = k_0/c$, the eigenvalue correction can be written as

$$\omega_1^{\mathrm{bc}} = \frac{\mathrm{i}}{2\omega_0^2 ||\hat{p}_0||_2^2} \int_{\text{tube inlets}} c^3 \mathcal{Z}_1(\omega_0) |\partial_\nu \hat{p}_0|^2 \mathrm{d}A. \tag{11.61}$$

We note that this is consistent with the observation that the impedance of a passive boundary, i.e., one that does not generate energy, must have a non-negative real part (Rienstra 2006). For if we have $\operatorname{Re} \mathcal{Z}_1(\omega_0) < 0$, then $\operatorname{Im} \omega_1^{\mathrm{bc}} < 0$, and the eigenvalue correction is destabilizing.

Equation (11.61) holds only for a degeneracy-preserving perturbation, but this is not a restriction in our case because the tubes have all the same inlet impedance. In principle, an analogous procedure as in Section 11.4.2 can be used to investigate asymmetric boundary perturbations which unfold the eigenvalue degeneracy. In our case, the relevant modes

are plane in the tubes and, therefore, (11.61) is simple to evaluate because the pressure gradient is constant on the integration surface.

Total eigenvalue correction

Since we considered only first-order corrections of the individual contributions (i) heat release feedback, (ii) modal volume damping, and (iii) boundary radiation, the total eigenvalue correction ω_1^{tot} is simply given by the sum of the three

$$\omega_1^{\text{tot}} = \omega_1^{q} + \omega_1^{\text{vd}} + \omega_1^{\text{bc}}. \tag{11.62}$$

The results based on the perturbation method are compared to those obtained from the network model in Section 11.5.1.

11.5 Some modeling results

We present a few results of the frequency-domain network-type model, developed in Section 11.3, to get an idea of its capabilities. More computational results based on this model will be presented in the next chapter, in conjuction with the experimental data. In addition to that, the model will be also used in Section 12.3 to design a stabilizing controller. We also compare the results from the perturbation method, described in Section 11.4, with those from the network model.

For the tube transfer function parameters (see Eqs. (11.13) and (11.14)), we use $c_k = 1.15$ and $c_{\tau.\text{ref}} = 0.29\,\text{ms}$ and a temperature increase $(\Delta T)_{\text{ref}} = 50\,\text{K}$. As indicated, we consider these as reference values and use them in most computations. While we can take c_k to be a constant, c_τ and ΔT depend on the heating grid power. The dependence of c_τ on the input power is based on the fact that the non-dimensional heating grid response to flow perturbations must be a function of the Strouhal number $Sr = \omega l_{\text{gr}}/\bar{u}$, where l_{gr} is a characteristic length of the grid cross section. Then from (11.13), we have $c_\tau \sim l_{\text{gr}}/\bar{u}$, and the bulk velocity depends on the temperature increase because the mean flow is convection induced. These reference values as well as the variation of c_τ and ΔT with heating power originate from measurements of the temperature increase as a function of the electrical power input. This is discussed in the experimental part in the next chapter (Section 12.2). The constant transfer function gain c_k was chosen such that the model results are consistent with the experimental observations.

An increase in the heating grid power in the model has two effects on the relevant modes up to 600 Hz: (i) a continuous increase of the mode frequencies and (ii) a continuous increase of the growth rates. These effects simply result from a higher speed of sound and larger unsteady expansion due to an increased normalized temperature ratio. Since these are only quantitative changes, and we cannot expect the model to be quantitatively accurate in every aspect (cf. Section 11.6), we stick to the reference parameters as given above for all model calculations, also those in the next chapter. We only make an exception when considering a non-uniform heating power distribution around the circumference.

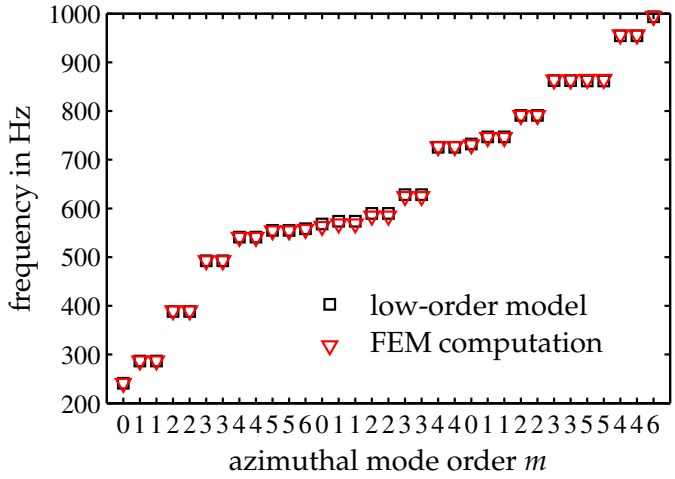

Figure 11.6: Acoustic eigenfrequencies of the annular Rijke tube configuration and corresponding azimuthal mode order m for a temperature increase of 50 K; model and Helmholtz solver results are compared.

11.5.1 Comparison of cold eigenfrequencies with finite element computations

We compare the eigenfrequencies of the annular Rijke tube configuration computed with the model to those obtained with a finite element Helmholtz solver[11] (Fig. 11.6). No dynamic heat release was taken into account at this point, but the reference temperature jump of 50 K across the heating grids, representative of that observed in the experiment (see Chapter 12), was included. The end correction at the tube inlets was explicitly modeled by an elongated duct in the finite element geometry. Due to the rotational symmetry of the set-up, the Helmholtz solver does not need to compute the whole geometry. We make use of quasi-periodic Floquet–Bloch boundary conditions so that only one segment (one-twelfth, in our case) needs to be considered. This approach is illustrated in Appendix B on the basis of an elementary thermoacoustic model problem.

The eigenfrequencies obtained from the network model compare well with the finite element computation. This demonstrates that the purely acoustic properties have been represented correctly with the approach described in Section 11.3. Since the boundary conditions at the up- and downstream end of our configuration are open, all modes have at least a half-wave structure in axial direction. Moreover, only the axisymmetric modes and those with azimuthal orders being an integer multiple of 6 are not degenerate (cf. Section 11.2). The modal density between 500 and 600 Hz is particularly high (Fig. 11.6). Azimuthal modes of order 4, 5, and 6 in this frequency range were found to be unstable in the stability analysis (see below). The pressure patterns in the annular duct corresponding to these modes are shown in Fig. 11.7 (computed with the Helmholtz solver). The angular location of the pressure nodes and antinodes is arbitrary for azimuthal orders 4 and 5 because these modes are degenerate (cf. Section 11.2).

[11] Comsol Multiphysics (Version 3.3), `http://www.comsol.com`

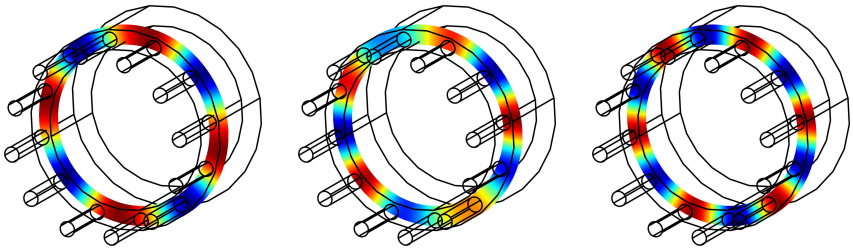

Figure 11.7: Pressure patterns corresponding to the acoustic modes of the annular Rijke tube with azimuthal orders 4, 5, and 6 at eigenfrequencies 541, 554, and 557 Hz (from left to right)

11.5.2 Linear stability

The linear stability characteristics for the experimental system were computed with the low-order model with and without including the heat release transfer function (11.13). The reference temperature jump of 50 K across the heat sources was used for this calculation. Figure 11.8 shows the complex eigenvalues determined from Eq. (11.17). Negative imaginary parts correspond to instability. Without including feedback from the heat release, all eigenvalues lie in the stable half-plane. This results from the modal damping in the annulus (cf. Eq. (11.25)) and the radiation from the tube inlets (Eq. (11.22)). The imaginary part of the eigenvalues grows with mode number because both damping mechanisms increase with frequency. All eigenvalues with frequencies larger than 600 Hz were strongly damped, also for the case with heat release feedback, and are thus not shown.

The heat release destabilizes all eigenvalues in the 600 Hz range. Most strongly affected is a group of modes around 550 Hz with zero or small negative imaginary part. These eigenvalues correspond to azimuthal mode orders $m = 4$, 5, and 6 (with increasing frequency). Since these three modes are of first longitudinal order, they are all axial half-waves. As we will see in the next section, the theoretical assessment of the stability of the modes agrees well with the experiment, and modes of higher axial order do not play a significant role. Therefore, whenever we use one of the terms '5th-order azimuthal mode', '4th azimuthal mode', or '$m = 6$ mode' or something similar, we implicitly refer to that circumferential mode which is of first longitudinal order.

As evident from Fig. 11.8, the growth rates of the unstable modes are rather small. This is because, as mentioned in Section 11.4, the acoustic source character of the normalized heat release perturbation is proportional to the normalized temperature increase $T_{\mathrm{ds}}/T_{\mathrm{us}} - 1$. Compared to a flame, the temperature increase across a heating grid is much smaller. For the computational results shown above, we used $T_{\mathrm{ds}} - T_{\mathrm{us}} = 50\,\mathrm{K}$. However, the 5th- and 6th-order azimuthal modes, which are identified as unstable in Fig. 11.8, are found to be strongly oscillating in the experiment and thereby confirm these results, as will be shown in the next chapter.

11.5.3 Comparison of results from network model and perturbation method

The eigenvalues for the model system with heat release feedback computed from the perturbation scheme are shown in Fig. 11.9 (a). Results for a circumferentially uniform heat

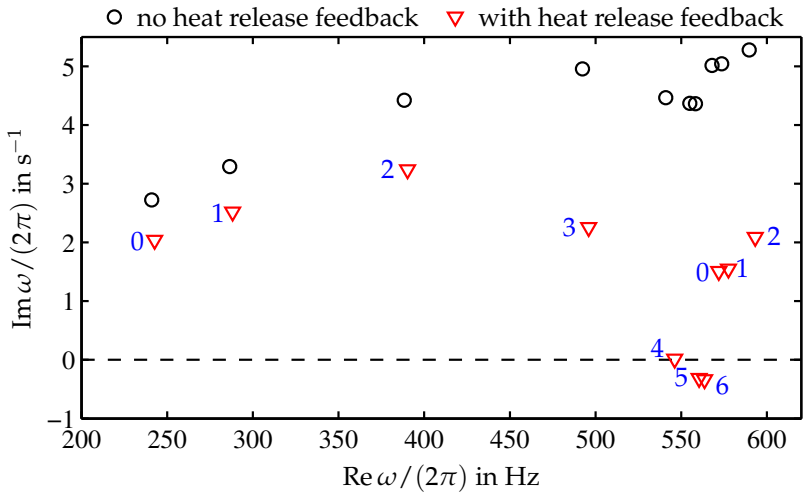

Figure 11.8: Eigenvalues of the annular Rijke tube computed with the low-order model for a temperature increase of 50 K. Results with and without feedback from the heat release are shown. Numbers indicate azimuthal mode order.

release transfer function (C_{12}) and for a modulated transfer function gain (C_4) are displayed. In case of the C_4 pattern, the transfer function gain in the individual tubes is modulated according to $|\mathcal{F}_n| = s_n|\mathcal{F}|$, where $\mathcal{F}$ is the heat release transfer function in the symmetric case, and the modulation pattern is given by

$$\boldsymbol{s} = \left[1/3 \;\; 4/3 \;\; 4/3 \;\; 1/3 \;\; 4/3 \;\; 4/3 \;\; 1/3 \;\; 4/3 \;\; 4/3 \;\; 1/3 \;\; 4/3 \;\; 4/3\right]^T. \tag{11.63}$$

Hence, every third heat source has reduced gain, but the mean value is identical to the symmetric case. For the perturbation method, we used the acoustic modes that were computed with the Helmholtz solver (see Section 11.5.1) as unperturbed zeroth-order solution. Since the end correction of the tube inlets was explicitly accounted for in the geometry of the finite element model, we used only the real part of the Levine–Schwinger impedance (2.10) in the calculation of the eigenvalue correction due to boundary damping (Eq. (11.61)).

From the discussion in Section 11.2, we know that degenerate modes with azimuthal orders being a multiple of 2 should split in this case, whereas for all modes with azimuthal order different from that, the C_4 perturbation preserves the degeneracy. The results from the perturbation method are fully consistent with this. In the 600 Hz range considered, modes with azimuthal orders 2 and 4 split, while all other degeneracies are sustained. In fact, the eigenvalues which are not split by the symmetry reduction are not affected at all. The 6th-order azimuthal mode is distinct also in the C_{12} case and therefore cannot split. Moreover, the gain-modulation-induced splitting is an essentially destabilizing process because one of the split modes has a larger and one a smaller growth rate compared to the fully symmetric C_{12} case. This effect can also be verified experimentally by modulating the heating grids of the annular Rijke tube with a C_4 pattern, as will be shown in Section 12.2.

The analogous results but computed from the low-order model described in Section 11.3 are plotted in Fig. 11.9 (b). We consider the C_{12} case first. In comparison to the perturbation method, the growth rates are smaller, in particular for those modes which are most destabilized. An analysis of the individual contributions of the perturbations from the

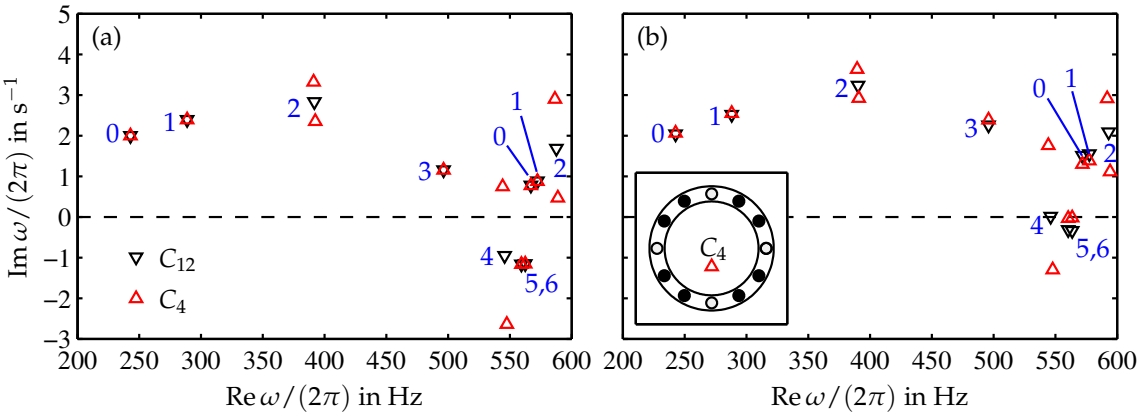

Figure 11.9: Comparison of perturbation method and network model results. Eigenvalues for a fully symmetric heat release feedback (C_{12}) and for one with a circumferential modulation of the transfer function gain according to a C_4 pattern. Results from computations with (a) perturbation method and (b) network model. The inset in frame (b) depicts the gain modulation pattern of the heat release feedback for the C_4 case. Numbers indicate azimuthal mode order.

self-adjoint part of the modes, i.e., (i) modal damping in the annulus, (ii) radiation from the tube inlets, and (iii) feedback from the heat release, reveals that it is effect (iii) which causes the discrepancy between the results from network model and perturbation method. This analysis can be performed because the individual contributions can be switched off in both calculation methods. However, the perturbation method assumes the feedback from the heat release to be small, in contrast to the network model. Therefore, we consider the results from the latter to be more accurate.

Qualitatively, both methods give very similar results. In particular, the mode splitting due to the reduction in symmetry by the C_4 pattern is consistent. One qualitative difference is that while the perturbation method predicts the non-split modes to be unaffected by the gain modulation, the results from the low-order model show a small influence, e.g., for the 5th and 6th azimuthal modes. Accordingly, this must be a higher-order effect.

11.6 Discussion

The low-order model results agree quantitatively well with those computed using the Helmholtz solver for the case with no heat release feedback. This demonstrates that the acoustics are correctly represented. Low-order model and perturbation method also show qualitatively similar results. The disagreement can be traced back to the fact that the perturbation method is only of first order in the heat release feedback. On the other hand, destabilization of the modes through the heat release and the selection of the most unstable modes agree well. With respect to asymmetries in the heat release response and the associated eigenvalue splitting, both methods give similar results.

As we will see in the next chapter, the network model results are consistent with measurement data from the experimental set-up. Mode stability, the effect of asymmetries, and the impact of feedback control agree with the experiments. On the other hand, the model cannot be considered quantitatively accurate in every aspect. An exact prediction of the

growth rates, for instance, and along the same lines, an accurate determination of the stability border is likely beyond its capabilities. Such quantitative predictions are inherently difficult, even with a model exclusively based on experimental data (Bothien et al. 2010).

In the network model, we assumed a constant temperature downstream of the heat source. This is only an approximation. Due to heat losses to the walls, the temperature decreases in downstream direction. Evidently, this effect is stronger for higher heating powers. Moreover, if we apply non-uniform heating powers around the circumference, the temperature field will also vary with the angular coordinate, which we do not take into account by means of the analytical eigenfunction expansion used in the network model. In principle, non-uniform temperature fields can be included either by using numerically computed eigenfunctions in the network model or directly in the framework of the perturbation method. However, this obviously requires the specification of the complete temperature field, which would have to be acquired experimentally or numerically. This was not done in the present work.

Chapter 12

Experimental Analysis and Control of Azimuthal Instabilities

Transformation to modal coordinates
In the experimental investigation of the annular Rijke tube, the acoustic pressure is measured with 12 microphones equally spaced along the circumference at a fixed axial location upstream of the heating grids (see Figs. 10.1 and 10.2). Similarly, the frequency domain model developed in Section 11.3 yields the eigenfunction pressure distribution in the 12 tubes at the heat sources. Although the axial locations of measurement and model output are not exactly the same, the circumferential distribution of the pressure is identical. Considering the modal nature of the pressure field and the fact that only a few modes were found to be unstable in the linear analysis (Section 11.3), a transformation of the vectors of measured and calculated pressure distributions into coordinates properly representing the modal structure is appropriate. For this purpose, we introduce unitary transformation matrices $\mathbf{B}_N$ of dimension $N \times N$ whose columns are a discrete representation of the circumferential mode shapes. We leave N variable because we want to use the same basis for the actuation space when applying control, which is of lower dimension. We consider two types of bases for even N:

basis (i) is a standing wave basis, in which the columns of $\mathbf{B}_N$ have elements $w_0 1$, $w_1 \cos\varphi_n$, $w_1 \sin\varphi_n, \ldots, w_{N/2}\cos N/2\varphi_n$, with $\varphi_n = 0 \ldots 2\pi(N-1)/N$. The coefficients w_i are introduced to make the basis vectors orthonormal so that $\mathbf{B}_N$ is unitary. This is achieved by choosing $w_0 = w_{N/2} = \sqrt{N}$ and $w_1 \ldots w_{N/2-1} = \sqrt{N/2}$. We used this basis already in Section 11.3.3 for the determination of the modal content of the modeled eigenfunction.

basis (ii) is a rotating wave basis, in which the columns of $\mathbf{B}_N$ have elements $c_e \exp[-\mathrm{i}\varphi_n N/2], c_e \exp[-\mathrm{i}\varphi_n(N/2-1)], \ldots, c_e \exp[\mathrm{i}\varphi_n(N/2-1)]$, with $c_e = 1/\sqrt{12}$. $\mathbf{B}_N$ is essentially the unitary Fourier matrix.

We will denote both bases by $\mathbf{B}_N$ because whenever we refer to it, it will equally hold for both.

The pressure coordinates in the modal basis represent the coefficients of the modal pressure distribution. We obtain the modal coefficients by projecting the measured or

calculated pressure vector $\hat{\boldsymbol{p}}$ on the modal basis vectors, hence

$$\hat{\boldsymbol{p}}_m = \mathbf{B}_N^{\dagger}\hat{\boldsymbol{p}}. \tag{12.1}$$

Since basis (i) is real, it can be applied to frequency- as well as time-domain pressure vectors. This is not so for the complex basis (ii). The modal basis vectors have a non-vanishing imaginary part, and therefore, the quadrature component of $\boldsymbol{p}$ is also necessary to determine the associated modal coefficients.

Note here that with an orthonormal basis, the amplitudes of the modal coefficients are larger than the maximum pressure amplitude in the tubes by a factor of $\sqrt{N/2}$ for $m = 1 \ldots 5$ and $\sqrt{N}$ for $m = 0, 6$.

A note on terminology and notation
We refer to the quantities obtained from a modal decomposition of the time-domain pressure signals as *modal coefficients* and denote them by a_m. A superscript c, s indicates the reference to a standing wave basis, either cosine or sine component. a_5^c, for instance, represents the $\cos 5\varphi$ component in the measured pressure vector $\boldsymbol{p}$. For the rotating wave basis, we use superscripts $+$ and $-$ to indicate counter-clockwise and clockwise spinning components, respectively. The modal coefficients typically oscillate at the resonance frequencies of their associated modes.

We define *modal amplitudes* as the oscillation amplitudes of the modal coefficients and denote them by $\hat{a}_m$, as the Fourier transform. For a steady-state oscillation, we determine the modal amplitudes either by Fourier transform or through the RMS, the latter if the signal is sufficiently narrow-band. In the transient case, we obtain $\hat{a}_m$ as the magnitude of the analytic signal $a_m + \mathrm{i}\mathcal{H}[a_m]$, again assuming the signal is narrow-band. In addition, we label an mth-order azimuthal mode of sine or cosine type by s_m and c_m; clockwise and counter-clockwise components are labeled by e_m^-, and e_m^+. Particular basis vectors in $\mathbf{B}_N$ are referred to as $\boldsymbol{b}_m^{c,s}$ and $\boldsymbol{b}_m^{\pm}$.

12.1 Self-excited oscillations

Consistent with the linear stability analysis based on the low-order model, azimuthal modes of orders 5 and 6 were observed in the experiment for a certain range of input powers. Figure 12.1 shows the average amplitude of the modal coefficients for a variation in the input power. For azimuthal orders 1–5, the effective amplitude $(\hat{a}_m^{c2} + \hat{a}_m^{s2})^{1/2}$ is plotted. All heating grids were driven with identical power. No instability is observed for input powers smaller than 1500 W. With increasing heating power, the 6th-order azimuthal mode becomes unstable. Its amplitude grows with an increase in the electrical power up to about 1700 W. The 5th azimuthal mode starts to grow and dominates for higher power values. At an input power of 2000 W, the $m = 6$ mode is almost completely suppressed. For larger powers, however, this mode remains significant, although the 5th-order mode is clearly dominant. The strong suppression of the $m = 6$ mode around 2000 W was a reproducible feature. Also note that the amplitude of the 5th azimuthal mode increases continuously with input power, which clearly corresponds to a supercritical bifurcation. Regarding the temporal evolution, when the heating grid power is switched on, the $m = 6$ mode

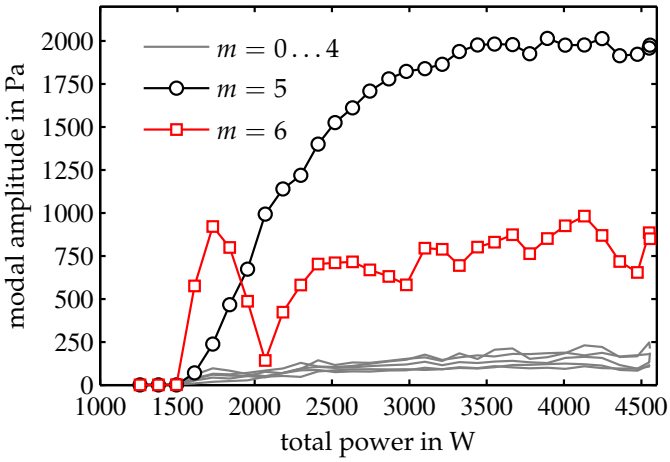

Figure 12.1: Measured modal amplitudes for varying total input power

is actually growing much faster and is limited and then reduced in amplitude through the 5th-order azimuthal mode (not shown). The modes with azimuthal order lower than 5 only have a small contribution to the measured pressure signals.

For exemplary purposes, the amplitude spectrum of one of the pressure signals is shown in Fig. 12.2. The data corresponds to a total input power of 3200 W. A strong peak, extending more than four orders of magnitude above the background noise, is visible around 560 Hz. At this scale, the frequencies corresponding to the 5th and 6th and the stable 4th azimuthal modes cannot be distinguished. A few harmonics are also present.

A more detailed view of the dominant frequency content of the pressure oscillations is given in Fig. 12.3. The data corresponds to total input powers of 1700 and 2100 W (cf. Fig. 12.1). A peak with small magnitude is visible between 520 and 530 Hz. This corresponds to the $m = 4$ mode that was found to be marginally stable in the low-order model. Two stronger frequency components are found around 540 and 550 Hz. The location of the peaks slightly increases with input power due to the larger speed of sound downstream

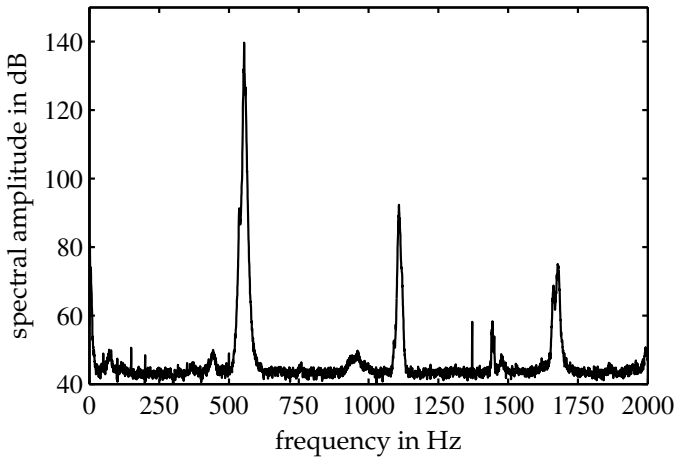

Figure 12.2: Pressure amplitude spectrum measured in one tube for a total input power of 3200 W

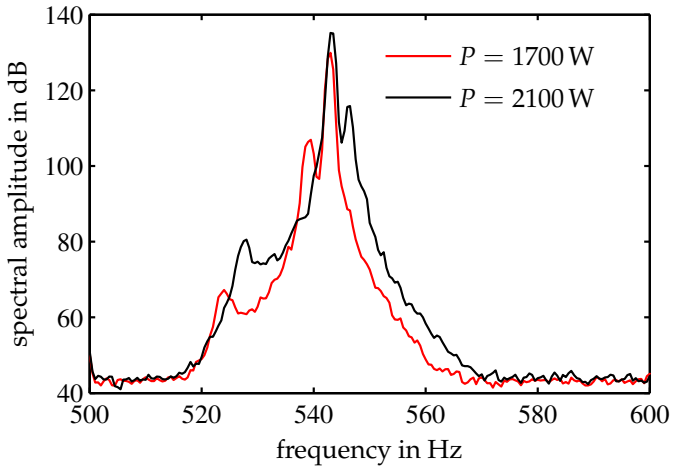

Figure 12.3: Pressure amplitude spectra measured in one tube for input powers of 1700 and 2100 W with the $m = 6$ and $m = 5$ mode being dominant, respectively

of the heat source. The spacing of the two dominant peaks is only 3–4 Hz, which also compares well with the model results (Fig. 11.8). For an input power of 1700 W, the peak with the higher frequency is about an order of magnitude larger. On comparison with Fig. 12.1, we find this spectral component to be associated with the $m = 6$ mode. At 2100 W, the 5th-order azimuthal mode clearly dominates. The reason for the two unstable modes being in such close proximity is that the tubes, in which the heating grids are mounted, favor oscillations in this frequency range. However, the annular duct is still necessary to couple the dynamics in the tubes. Without annulus, no self-excited oscillations were observed.

The simultaneous oscillation of two instability modes is not often observed in thermoacoustic investigations. The common explanation is that the oscillation of the "more unstable" mode suppresses the growth of the weaker one. In our case, the presence of two unstable modes with significant amplitudes is clearly related to the close proximity of their associated oscillation frequencies (see also Fig. 12.3). However, a closer inspection of the temporal evolution of the modal amplitudes showed that the weaker $m = 6$ mode did not have a constant amplitude. It was growing and decaying, seemingly randomly, on a much larger time scale than the actual oscillation. A growth in amplitude was always associated with a decay of the $m = 5$ mode. Thus, there was a continuous competition between the two modes rather than two coexisting oscillations with constant amplitudes.

The azimuthal instability modes observed in annular combustion chambers can be either standing or rotating in angular direction or be a mixture of both (Krebs et al. 2002; Schuermans et al. 2006; Staffelbach et al. 2009). In the present case, the nature of the oscillation patterns is more difficult to assess due to the two coexisting modes. A careful investigation of the time traces of the 12 pressure sensors showed that the $m = 6$ mode was always of standing type. This was expected, since this mode is not degenerate, and therefore, rotating wave solutions do not exist in the linear regime. Schuermans et al. (2006) showed that the saturation in the heat release response at high amplitudes favors rotating wave solutions. We conjecture, however, that this does not apply to azimuthal modes which are not degenerate.

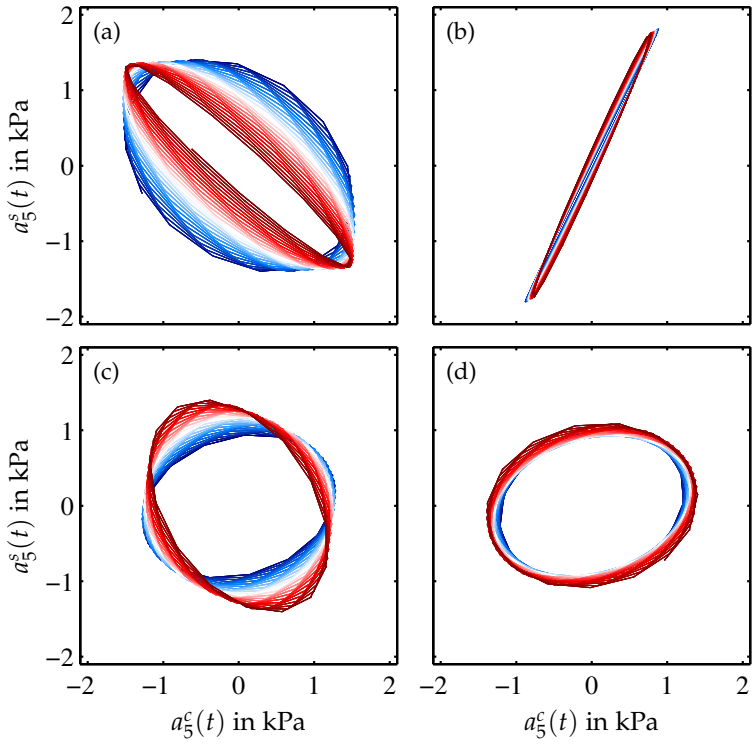

Figure 12.4: Phase-plane trajectories in a_5^c–a_5^s space. Colors from blue to red via white indicate increasing time. Each trajectory in (a)–(d) corresponds to a different period of time with an interval of 49 milliseconds; the data is sampled at 2^{13} Hz. Total electric power 3000 W.

The 5th-order azimuthal mode is degenerate so that spinning and standing oscillation patterns are possible. No information can be gained from the stability analysis because all linear combinations of the two basis functions spanning the degenerate eigenspace are equivalent. The postprocessing of the experimental data showed that the $m = 5$ mode was not of definite standing or rotating type. In terms of the $\cos m\varphi$–$\sin m\varphi$ basis, azimuthally standing components are associated with in-phase modal coefficients a_m^c and a_m^s. Conversely, a purely rotating solution has modal coefficients which are in quadrature but have identical magnitudes (Evesque et al. 2003). Thus, the nature of the 5th azimuthal mode can best be visualized by means of a phase plane with the coefficients of the cosine and sine modes as coordinates. A circumferentially standing wave is then represented by a straight line whose slope determines the angular location of the pressure nodes, and a purely spinning wave corresponds to a circle.

Figure 12.4 shows four exemplary results, which correspond to the same operating conditions (total power of 3000 W) but different time intervals. Apparently, the 5th-order azimuthal mode is neither distinctly spinning nor standing. In fact, it does not exhibit any stationary characteristic at all. Figure 12.4 (b), for instance, clearly corresponds to a circumferentially standing wave, whereas Fig. 12.4 (c) and (d) represent essentially rotating modes. A transition between different oscillation patterns can be observed in frame (a). Qualitatively similar characteristics were also present at other input powers, for which the $m = 5$ mode was unstable.

Similar information is gained by studying the spin ratio Δ_m^{sp}, as proposed by Evesque et al. (2003). The spin ratio represents the relative contribution of the energy in the rotating component to the total acoustic energy in an mth-order azimuthal mode. For a pair of counter-clockwise and clockwise spinning modes with (complex) coefficients a_m^+ and a_m^-, the spin ratio is given by

$$\Delta_m^{\mathrm{sp}} = \frac{(1 - |a_m^+/a_m^-|)^2}{(1 + |a_m^+/a_m^-|)^2}. \tag{12.2}$$

In contrast to the $\cos m\varphi$–$\sin m\varphi$ basis, the modal coefficients a_m^+ and a_m^- cannot be obtained simply by projecting the measured pressure signals $\boldsymbol{p}$ on the rotating wave basis. This is because the latter is complex, and as a consequence, the quadrature component of $\boldsymbol{p}$ must be included in the projection. In a postprocessing step, this poses no serious difficulty because the quadrature component is simply obtained from the Hilbert-transformed signal. Essentially, this amounts to augmenting $\boldsymbol{p}$ with a quadrature component so that the signal is proportional to $\mathrm{e}^{\mathrm{i}\omega t}$. Then the modal coefficients of the rotating basis are computed from a projection of the analytic signals corresponding to the measured pressures, viz.,

$$a_m^{\pm} = (\boldsymbol{b}_m^{\pm})^{\dagger} \boldsymbol{p}_{\mathrm{a}}, \tag{12.3}$$

where $\boldsymbol{p}_{\mathrm{a}} = \boldsymbol{p} + \mathrm{i}\mathcal{H}[\boldsymbol{p}]$. Alternatively, we can obtain the coefficients of the rotating wave basis from the analytic signals of the coefficients of the standing wave basis. Since the pressure distribution associated with a certain mth-order azimuthal mode must be identical in the two bases, we have

$$\hat{a}_m^c w_m \cos m\varphi + \hat{a}_m^s w_m \sin m\varphi = \hat{a}_m^+ c_e \, \mathrm{e}^{-\mathrm{i}m\varphi} + \hat{a}_m^- c_e \, \mathrm{e}^{\mathrm{i}m\varphi}, \tag{12.4}$$

where w_m and c_e are the normalization coefficients of the two bases. Thus, the coefficients of the two bases can be transformed according to

$$\begin{bmatrix} \hat{a}_m^+ \\ \hat{a}_m^- \end{bmatrix} = \frac{w_m/c_e}{2} \begin{bmatrix} 1 & \mathrm{i} \\ 1 & -\mathrm{i} \end{bmatrix} \begin{bmatrix} \hat{a}_m^c \\ \hat{a}_m^s \end{bmatrix}, \tag{12.5}$$

which can be equally applied to the corresponding analytic signals (because $\boldsymbol{p}$ is narrowband).

The spin ratio computed from the pressure signals corresponding to the measurements shown in Fig. 12.4 does not take a stationary value but varies between 0 and 1 (Fig. 12.5). This represents purely standing and spinning waves, respectively, apparently appearing in a random fashion. Such complex behavior is somewhat unexpected. Experimental and numerical investigations on unstable annular thermoacoustic systems (Section 10.1) typically show one distinct standing-to-spinning-wave ratio (which may depend on the initial conditions). Yet, we also note that such detailed information on the acoustic mode type is often omitted. A possible explanation for the seemingly random characteristics in the present case is the following. As shown by Schuermans et al. (2006), rotating and standing waves correspond to stable fixed points and saddles, respectively, in wave-amplitude phase space. The stable manifold of the saddle separates the basins of attraction for the two (clockwise and counter-clockwise) rotating solutions. For certain initial conditions, the solution trajectory may first be attracted to the saddle, along the stable manifold, and

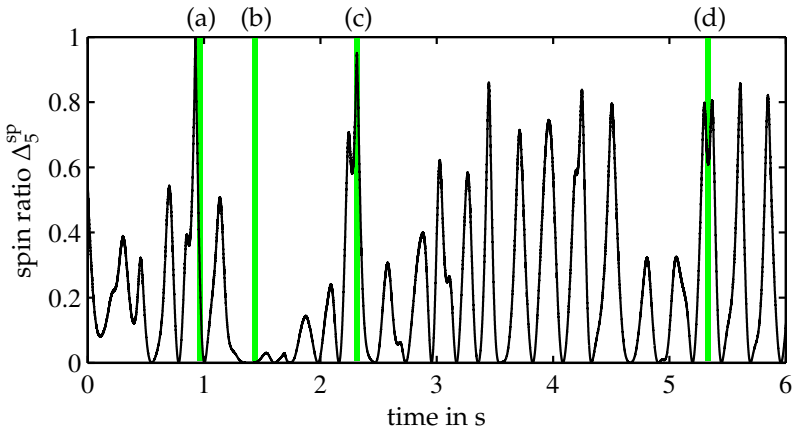

Figure 12.5: Spin ratio of the 5th azimuthal mode for a total input power of 3000 W. Green stripes correspond to time intervals of frames (a)–(d) in Fig. 12.4.

spend some time in the vicinity of this unstable equilibrium, before eventually approaching one of the two stable fixed points. As mentioned by Schuermans et al. (2006), this process may take some time. We consider now the effect of noise on the dynamics in this phase space. The state of the mode will be continuously relocated and, given a sufficiently large noise level, may even jump between the basins of attraction of the two rotating solutions. The mean flow is laminar and, accordingly, there is no real noise contribution in the system. However, the simultaneous presence of the 6th azimuthal mode can be considered as a random component driving the dynamics of the $m = 5$ mode.

12.2 The effect of an asymmetric power distribution

An azimuthal variation of burner and flame properties in an annular combustion chamber, either through geometrical changes (Berenbrink & Hoffmann 2000; Krüger et al. 2001) or burner group staging (Kokanović et al. 2006; Noiray et al. 2010), can have a stabilizing influence on the pressure oscillations. We mimic this effect in the annular Rijke tube through an azimuthal variation of the power that is supplied to each heating grid. Changing the geometry of a burner or the equivalence ratio with which it is supplied typically changes the flame response. An analogous effect is obtained when varying the power of a heating grid. To reflect this in the model, we need to determine the variation of the heat release response parameters with the grid's input power.

In general, varying the grid's input power has an impact on the gain as well as on the phase of the tube transfer function $\mathcal{F}_n$. Higher power leads to an increase in the downstream temperature and in the mean velocity (because it is convection induced). Since the heat release response of the grid is a function of the Strouhal number, the effect of a change in the supplied power can be estimated based on measured temperatures and the associated mean velocities for different heating powers. The measured temperature increase across one of the heating grids as a function of the input power is displayed in Fig. 12.6. The data can be well represented by the trial-and-error correlation

$$\Delta T/\mathrm{K} = 2.1 \times (P_{\mathrm{single}}/\mathrm{W})^{2/3}, \tag{12.6}$$

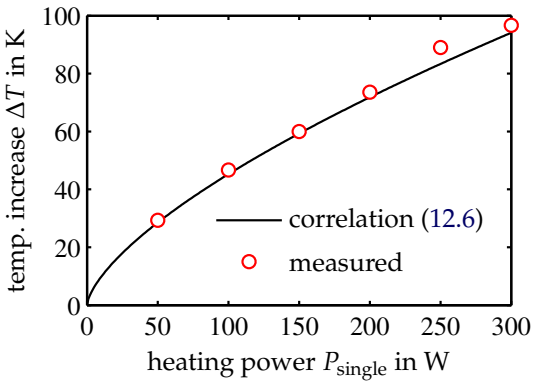

Figure 12.6: Temperature increase across a heating grid as a function of the input power. Measured data and correlation (12.6) are shown.

where the index 'single' indicates that this is the power to one grid only. Assuming that the grid's input power is transferred to the air with ideal efficiency, and using the mean bulk energy balance, we have for the mean velocity upstream of the grid

$$\bar{u}_{\text{us}} = \frac{1}{A\rho_{\text{us}}c_p}\frac{P_{\text{single}}}{\Delta T}, \tag{12.7}$$

which can be calculated as a function of the input power by using (12.6).

According to Lighthill (1954), the characteristic time of the grid's wire in the heat release transfer function (11.13) can be calculated as $c_\tau = 0.2\,d_{\text{w}}/\bar{u}$, where d_{w} is the wire diameter. Opposed to that, Kopitz found from direct numerical simulations a constant of proportionality of 0.4. For our calculations, we employ the latter value. Moreover, since the heating grids are made from flat wire (see Section 10.3), we use the corresponding hydraulic diameter $d_{\text{h}} = 0.49\,\text{mm}$ (which certainly is a crude approximation). For a reference temperature increase $(\Delta T)_{\text{ref}} = 50\,\text{K}$, we obtain from (12.6) and (12.7) a reference velocity of $\bar{u}_{\text{us.ref}} = 0.67\,\text{m}\,\text{s}^{-1}$. This yields a characteristic time for the heat transfer from the wire of $c_{\tau\text{.ref}} = 0.29\,\text{ms}$, as claimed in Section 11.5. Then we can express the effect of a variation of the input power on the heat release transfer function in tube n, $\mathcal{F}_n$, through

$$\frac{(\Delta T_{\text{single}})_n}{(\Delta T)_{\text{ref}}} = \left(\frac{P}{P_{\text{ref}}}\right)^{2/3} \quad \text{and} \quad \frac{c_\tau}{c_{\tau\text{.ref}}} = \left(\frac{P_{\text{single}}}{P_{\text{ref}}}\right)^{-1/3}. \tag{12.8}$$

We take into account the effect of a change in the temperature increase on the unsteady expansion resulting from heat release fluctuations, but do not model the circumferential temperature distribution that results from an azimuthal variation of the input power, as discussed in Section 11.6.

An azimuthal variation of the heat release transfer functions does not necessarily have a positive effect on thermoacoustic stability. Nominally degenerate azimuthal modes can be split if the system's symmetry group is reduced in a particular way through the introduced circumferential variation (cf. Section 11.2). To illustrate this effect, we investigate two patterns of azimuthal "staging": one has a 4-fold rotational symmetry (denoted by C_4) with reduced power at every third heating grid, and the other one has a 3-fold rotational symmetry (denoted by C_3) with groups of two heating grids alternating in lower and higher electric power. The staging patterns are visualized in Fig. 12.7. In all results shown in this section, the total electric power is held constant at 2900 W. To quantify the strength

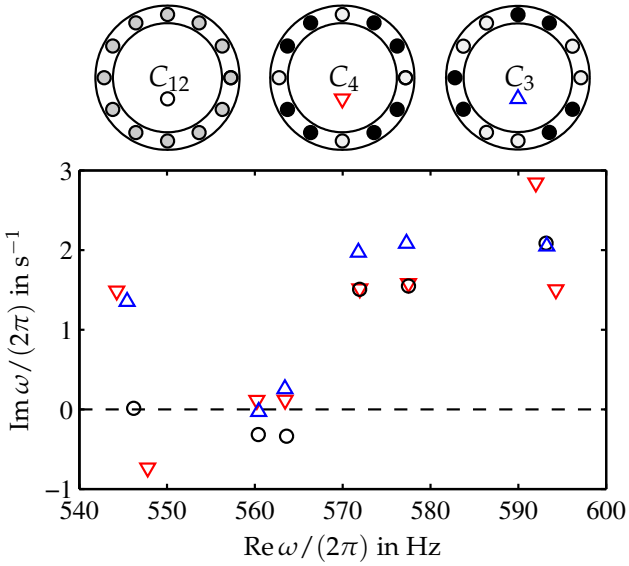

Figure 12.7: Visualization of the nominal power distribution and of the two staging patterns with associated eigenvalues; darker circles indicate higher electric power. The eigenvalues of the C_4 and the C_3 case correspond to $\sigma = 1$ and $\sigma = 1.5$, respectively.

of the circumferential modulation, we define the asymmetry parameter σ as

$$\sigma = \frac{\Delta P}{P_{\text{mean}}}, \tag{12.9}$$

where ΔP is the difference in electric power supplied to the two types of heating grids in one staging pattern, and P_{mean} is the mean power (which is held constant).

Since only three independent power sources are used for the 12 grids (see Section 10.3), it is not possible to realize arbitrary heating power distributions along the circumference and, at the same time, exploit the full range of electrical power available. For the C_3 staging pattern, for instance, it is already necessary to connect 6 of the heating grids to one power source. Therefore, the maximum total power that can be used is reduced by a factor depending on the particular staging pattern.

We discuss the model results for the two staging patterns first. The system eigenvalues for the reduced symmetry groups C_4 and C_3 and the corresponding staging patterns are shown in Fig. 12.7. For comparison, the eigenvalues for the original fully symmetric case (C_{12}) are also plotted. For clearness, only the frequency range between 540 and 600 Hz is shown. We consider the effect of the C_4 staging pattern first. Here, $\sigma = 1$ has been used for the computations. The $m = 4$ mode, degenerate in the baseline case with a frequency of 546 Hz and marginally stable, splits into two distinct modes as a result of the reduction in symmetry. As already noted in Section 11.5.3, this is an essentially destabilizing effect because one of the split modes has a larger imaginary part, whereas the other moves down into the unstable half plane. The modes of azimuthal order 5 and 6 at 560 and 564 Hz, which are dominant in the fully symmetric case, are slightly stabilized. The mode with a frequency of 593 Hz in the baseline case also splits because it is of 2nd azimuthal order. However, both $m = 2$ split modes remain stable. The unfolding of the degeneracy of the

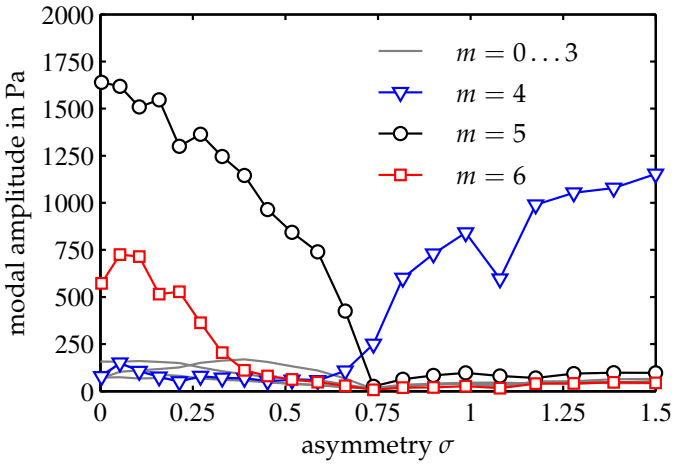

Figure 12.8: Measured modal amplitudes as a function of the asymmetry parameter σ for a C_4 staging pattern; total power input 2900 W.

4th- and 2nd-order azimuthal modes is consistent with the symmetry arguments introduced in Section 11.2. Thus, based on the linear analysis, we summarize the effect of the C_4 staging pattern as a slight stabilization of the nominally unstable $m = 5$ and $m = 6$ modes at the cost of a significant destabilization of one of the $m = 4$ split modes.

The results of the C_3 staging pattern with $\sigma = 1.5$ are univocal: all modes are either stabilized or affected only insignificantly (also those which are not shown in Fig. 12.7). However, the damping of the 5th-order azimuthal mode is only slightly increased so that it remains marginally stable. It is important to note here that no destabilizing splitting of the 6th-order azimuthal mode occurs because this mode is already distinct in the baseline case due to the 12-fold rotational symmetry. Different values of the asymmetry parameter σ have been used for the computation of the two staging cases because the experiments showed an effect of the C_4 pattern already at $\sigma = 1$ whereas the stabilizing influence of the C_3 pattern could be observed only for $\sigma > 1.3$ (see below).

To assess the effect of the reduced circumferential symmetry in the experiment, measurements were performed with a constant total power of 2900 W while varying the distribution to the 12 heating grids according to the C_4 and C_3 staging patterns. The measured modal amplitudes as a function of the asymmetry parameter σ are shown in Figs. 12.8 and 12.10, respectively. At $\sigma = 0$, only the 5th and 6th-order azimuthal modes are oscillating, with the former dominating. This corresponds to the case already considered before. Increasing the asymmetry according to the C_4 pattern (Fig. 12.8) leads to a continuous decrease in the amplitudes of the 5th- and 6th-order azimuthal modes. At $\sigma = 0.75$ both of these modes are stabilized. However, at the same time, the $m = 4$ mode is destabilized and grows in amplitude with a further increase of σ. These results correspond well with the eigenvalue analysis for $\sigma = 1$ (Fig. 12.7).

Since for the C_4 staging pattern, the $m = 4$ modes are not degenerate any more, they have a distinct pressure pattern along the circumference. Hence, we can compare the modeled circumferential pressure distribution (Eq. (11.19)) corresponding to the unstable $m = 4$ mode with the measured pressure distribution. This comparison is presented in Fig. 12.9. For completeness, the pressure pattern of the stable split mode is also shown. The measured and modeled pressure patterns both correspond to $\sigma = 1$. The experimental

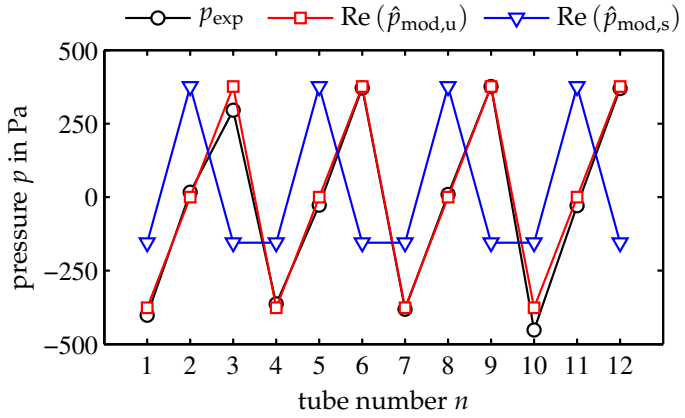

Figure 12.9: Modeled and measured pressure distributions in the tubes corresponding to the 4th-order azimuthal mode for $\sigma = 1$, C_4 staging pattern. Heating grids in tubes 2, 5, 8, and 11 have a reduced power input. The stable ($\hat{p}_{mod,s}$) and the unstable ($\hat{p}_{mod,u}$) $m = 4$ split modes are shown.

observations confirm the model results. Clearly, the selected pressure pattern identified in the measured data corresponds to the computed unstable mode. The reason for this pattern being more unstable is that the pressure nodes are arranged such that they coincide with the locations of the heating grids with reduced power (and thus, smaller transfer function gain). The measured pressure data represents an arbitrary snapshot. Since the modeled pressure distribution is an eigenfunction, its amplitude is undetermined. In Fig. 12.9, the amplitude of the computed pressure pattern has been scaled such that it matches the experimentally determined magnitudes.

An increase in σ according to the C_3 pattern (Fig. 12.10) results in a decrease in the amplitude of the 5th-order azimuthal mode. In contrast, the $m = 6$ mode is not damped by the asymmetry. It increases in amplitude, quite significantly around $\sigma \approx 0.6$, and settles on a constant level for $\sigma = 0.7$–1. Increasing the asymmetry parameter further, both modes are eventually stabilized at $\sigma = 1.3$. The fact that both modes become stable

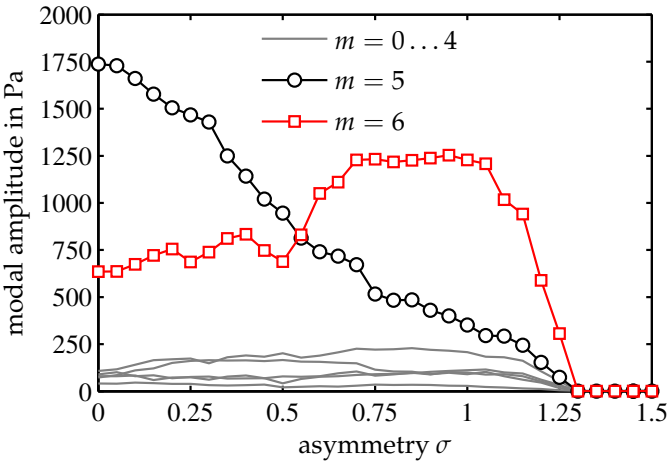

Figure 12.10: Measured modal amplitudes as a function of the asymmetry parameter σ for a C_3 staging pattern; total power input 2900 W.

at the same value of the asymmetry parameter indicates significant interaction even at low amplitudes. The eigenvalue analysis for this staging pattern with $\sigma = 1.5$ (Fig. 12.7) showed the $m = 6$ mode to be stabilized and the $m = 5$ mode to be marginally stable. This does not fully correspond to the experimental data but points in the same direction.

12.3 Feedback control

Controlling thermoacoustic instabilities in annular domains is markedly different from the purely longitudinal case. This is related to the higher complexity of the acoustic field and the multiple sources of heat release present. In a longitudinal test-rig, for instance, a single sensor signal is sufficient for control, whereas for an annular configuration, this is not the case. The pressure nodes associated with longitudinal acoustic modes are fixed. If neither actuator nor sensor is located in a node of the unstable mode, the oscillation can be measured as well as affected, and thus, control is possible, in principle. (There are other factors which may impede this task, such as actuator bandwidth and authority.) Degenerate azimuthal modes, in contrast, have the necessary degree of freedom to evade control if only a single sensor or a single actuator is used. The same holds true if only one damping device (a Helmholtz resonator, say) is attached to an annular chamber (Stow & Dowling 2003). As explained in Section 11.2, the degenerate eigenvalue splits, and only one of the split modes is stabilized. Feedback control with only a single sensor or a single actuator will have the same effect.

We consider the stabilization of the unstable azimuthal modes in the annular Rijke tube as a classical feedback control problem as shown in Fig. 12.11. The open-loop plant transfer function $\mathbf{H}(\omega)$ maps the 6 actuator commands (the input to the speakers' amplifiers) to the 12 pressure signals (left frame in Fig. 12.11). To stabilize the system, the 12 pressure signals are fed back to the 6 speaker commands via the control transfer function $\mathbf{K}(\omega)$ (right frame in Fig. 12.11). As indicated in Fig. 12.11, we will not attempt to control the complete system but only the unstable modes. This is referred to as *modal control* and is explained in detail in Section 12.3.2. The definition of open-loop and closed-loop transfer function that we use in the following is according to Fig. 12.11.

12.3.1 Including actuation in the model

The model developed in Section 11.3 does not include the effect of actuation and, hence, is only able to represent free oscillations of the homogeneous system (the eigensolutions). To design a stabilizing controller $\mathbf{K}$, we need the plant transfer functions $\mathbf{H}$, which map the control signals to the sensor signals, i.e., $\hat{\boldsymbol{p}} = \mathbf{H}(\omega)\hat{\boldsymbol{e}}$. To obtain $\mathbf{H}$, we have to model how the speakers influence the system. Extending the model from Section 11.3 to include actuation is not difficult because the whole acoustic field is already accounted for. Also, since the speakers are mounted to the tubes, we only need to consider the effect on the respective plane wave amplitudes; the three-dimensional nearfield is restricted to a rather small region due to the high cut-on frequencies of the non-planar tube modes. We thus model the effect of a speaker in one of the tubes as a 2×2 transfer matrix with infinitesimal

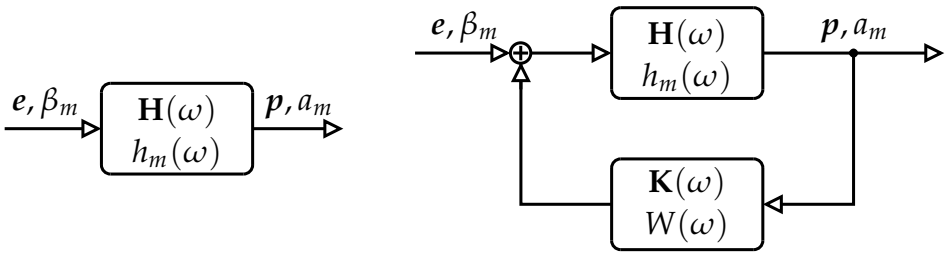

Figure 12.11: Definition of open- and closed-loop transfer functions for feedback control in the annular Rijke tube. Left: open-loop transfer function; right: closed-loop transfer function. $\mathbf{H}$ is the 6×12 plant transfer function that maps the 6 actuator signals $\boldsymbol{e}$ to the 12 microphone signals $\boldsymbol{p}$. $\mathbf{K}$ is the 12×6 control transfer function that relates the 12 microphone signals to the 6 actuator commands. The scalar variables β_m and a_m are the modal coefficients of the actuator command and the pressure signals, respectively. $h_m(\omega)$ is the modal plant transfer function and relates the modal coefficients of the actuator signals to the modal pressure coefficients. $W(\omega)$ is the compensator transfer function that is used for modal control. β_m, h_m and W are defined in Section 12.3.2

axial extent and volume source. Hence, we have the coupling relations

$$\hat{p}_b = \hat{p}_a, \tag{12.10a}$$

$$\hat{u}_b = \hat{u}_a + g(\omega)\hat{e}, \tag{12.10b}$$

where subscripts a and b indicate evaluation up- and downstream of the actuator location, and $g(\omega)$ is the speaker transfer function. The term 'speaker transfer function' is a bit fuzzy because it does not clearly define what effects are included. We therefore understand Eq. (12.10) to be the actual definition of g. As such, it includes the effect of the amplifiers, the speakers, all parts involved in the mounting mechanism, and the nearfield source characteristics. The transfer function g also depends on the entire system the speaker is attached to as a result of the back impedance (e.g., Marx et al. 2006). Therefore, it is not possible to measure g in an isolated set-up, a Multi-Microphone tube, say, and simply transfer the result.

We also need to account for the fact that the measured signals are not identical with the pressure directly at the heat source but at a small distance upstream (see Fig. 10.1). This is, however, not difficult because we can model this effect by using elementary plane wave theory. We merely need to add two duct elements (in each tube) with the appropriate length so that we obtain the pressure at the microphone locations and represent the actuation effect at the proper axial position. The model then takes the form as shown in Fig. 12.12. The admittance matrix, as defined in Section 11.3.4, now represents the upstream part only up to the microphone positions. The plane wave propagation between the microphones and the heat sources is simply modeled with duct transfer matrices. Likewise, the impedance matrix accounts for the annular section and the array of tubes (see Sections 11.3.5 and 11.3.6) down to the axial location of the speakers. A second duct transfer matrix models the distance between the actuators and the heat sources.

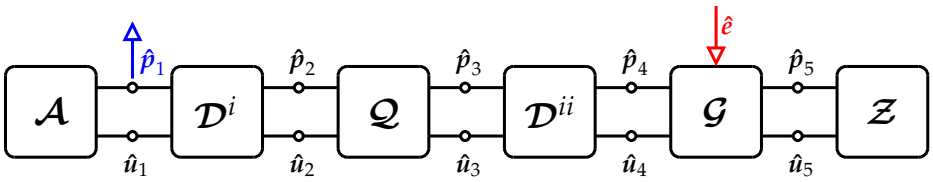

Figure 12.12: Network model representation of the annular Rijke tube accounting for proper sensor and actuator locations. $\mathcal{Q}$ maps upstream to downstream pressures and velocities via $\mathbf{X}$ and $\mathbf{I}+\mathcal{F}$, respectively. $\mathcal{D}^i$ and $\mathcal{D}^{ii}$ represent duct transfer matrices in each tube, and $\mathcal{G}$ models the actuator response. The open-loop transfer function of the system is defined through $\hat{\boldsymbol{p}}_1 = \mathbf{H}(\omega)\hat{\boldsymbol{e}}$.

Denoting the duct transfer matrix elements by $T_{ij}^{i,ii}$, the open-loop transfer function can be written as

$$\mathbf{H}(\omega) = \left[(T_{12}^{ii}\mathbf{I} - \mathcal{Z}T_{12}^{ii}\mathbf{I})\mathbf{X}(T_{11}^{i}\mathbf{I} + T_{12}^{i}\mathcal{A}) + (T_{12}^{ii}\mathbf{I} - \mathcal{Z}T_{22}^{ii}\mathbf{I})(\mathbf{I}+\mathcal{F})(T_{21}^{i}\mathbf{I} + T_{22}^{i}\mathbf{I}\mathcal{A})\right]^{-1}\mathcal{Z}\mathcal{G}, \tag{12.11}$$

where $\mathcal{G}$ is a 12×6 actuator transfer function that distributes the control signal to every second tube, hence

$$\mathcal{G}_{kl}(\omega) = \begin{cases} g(\omega), & k = l \ \wedge \ k \text{ odd}, \\ 0, & \text{else}. \end{cases} \tag{12.12}$$

12.3.2 Modal control

Designing a controller for the plant transfer function is not straightforward due to its multiple-input–multiple-output nature. In principle, H_∞-loop-shaping techniques can be used for this task. In the present case, however, the plant transfer function is simply too complex, essentially due to its transcendental character, so that these methods cannot be applied directly. Truncation to a finite-dimensional model would be required. On the other hand, controlling the pressure signals directly may not be the most effective way. Since we know which modes are unstable, a more sensible approach can be adopted by controlling the actual modes, as proposed by Schuermans et al. (2003) and Morgans & Stow (2007). For multiple unstable modes, this method requires one controller for each; however, these are only single-input–single-output systems, and designing a stabilizing control law is straightforward.

An additional advantage from a more fundamental point of view is that by being able to suppress individual modes rather than stabilizing the complete system, we are able, e.g., to study the growth of each mode unimpeded by the presence of the others. This can also be of practical value. Consider for instance the oscillation amplitudes of the 5th and 6th azimuthal modes in Fig. 12.1. For large input powers, the $m = 5$ mode has a distinctly larger oscillation amplitude than the $m = 6$ mode. In the case of the latter being acceptable and the former not, applying dampers designed to suppress the $m = 5$ mode may actually increase the oscillation amplitude of the $m = 6$ mode significantly because both modes interact nonlinearly. By how much the amplitude of the 6th azimuthal mode will grow is difficult to predict due to the nonlinear nature of the interaction.

Modal plant transfer functions

To obtain the modal model, we first project the open-loop plant model

$$\hat{\boldsymbol{p}} = \mathbf{H}(\omega)\hat{\boldsymbol{e}} \tag{12.13}$$

on the modal basis $\mathbf{B}_{12}$, viz.,

$$\mathbf{B}_{12}^{\dagger}\hat{\boldsymbol{p}} = \mathbf{B}_{12}^{\dagger}\mathbf{H}(\omega)\hat{\boldsymbol{e}}. \tag{12.14}$$

Next we represent the actuation vector in modal coordinates of the six-dimensional actuation space

$$\hat{\boldsymbol{e}} = \mathbf{B}_6\hat{\boldsymbol{e}}_m, \tag{12.15}$$

where $\mathbf{B}_6$ is a 6×6 matrix whose columns correspond to the continuous standing or rotating wave basis evaluated at the circumferential locations of the speakers. Since we only have six actuators, aliasing effects are introduced when considering modes up to azimuthal order 6, which will be necessary to control the unstable modes. Actuating an $m = 5$ mode will simultaneously excite modes of azimuthal order 1, and the forcing pattern for $m = 6$ is identical to that of $m = 0$. However, the aliasing effect cannot destabilize these lower modes because the sensor signals have an angular resolution up to $m = 6$, and hence do not cause backfolding up to this circumferential order. Therefore, feedback for the aliased modes is not established; they experience merely an open-loop forcing by the aliased feedback signal for the unstable modes with $m = 5$ and $m = 6$. Furthermore, no interference of the two unstable modes is generated. This can be directly inferred from the modal plant transfer function, as we will see in the following.

Combining (12.14) and (12.15), we obtain the modal plant transfer functions with

$$\hat{\boldsymbol{p}}_m = \mathbf{H}_m(\omega)\hat{\boldsymbol{e}}_m, \quad \mathbf{H}_m(\omega) = \mathbf{B}_{12}^{\dagger}\mathbf{H}(\omega)\mathbf{B}_6. \tag{12.16}$$

Since our nominal system has a C_{12} symmetry, which is reflected by the symmetry of the plant transfer function matrix $\mathbf{H}$, the circumferential modes decouple for the most part, and cross-talk is only introduced through the aliasing effect associated with insufficient spatial resolution of the actuators. As a result of this strong decoupling, the modal plant transfer function matrix $\mathbf{H}_m$ has only a few non-zero elements as opposed to $\mathbf{H}$, which is fully populated (but highly symmetric).

The structure of the modal plant transfer function matrix for the standing and the rotating wave basis are shown in Fig. 12.13. We consider the standing wave basis (left) first. Up to the third-order cosine mode, the system is diagonal, and every pressure mode can be directly actuated with the corresponding speaker pattern. The third-order sine mode cannot be actuated at all. This is because the speakers are located in the nodes of the associated pressure distribution. Obviously, this deficiency could be resolved by changing the coordinate origin. Then, however, the cosine mode could not be actuated or both modes would be excited simultaneously. Either way, with only six speakers, it is not possible to control the complete $m = 3$ eigenspace, a direct result of Shannon's sampling theorem. Since the 3rd-order azimuthal modes were not among the unstable ones, this shall not be of further concern. Actuating the unstable 5th and 6th azimuthal modes is always accompanied by an excitation of 1st- and 0th-order modes, respectively, due to backfolding.

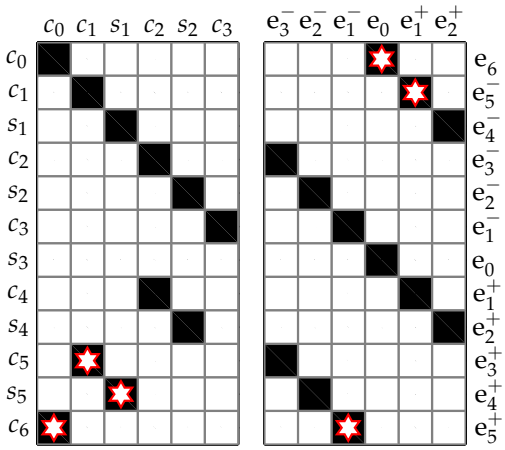

Figure 12.13: Non-zero elements of the modal open-loop plant transfer function $\mathbf{H}_m$ with respect to a standing (left) and a rotating basis. c_m and s_m correspond to cosine and sine modes of mth azimuthal order, and $e_m^{\pm}$ is a shorthand notation for $e^{\pm im\varphi}$. Stars indicate unstable modes.

We have a similar picture for the rotating wave basis (Fig. 12.13, right). The 3rd-order azimuthal modes can be actuated but only both spinning directions simultaneously. This again impedes control of the complete $m = 3$ eigenspace.

To design a suitable control law for stabilizing the unstable 5th- and 6th-order azimuthal modes, we consider only the associated non-zero elements of $\mathbf{H}_m$ (those marked by stars in Fig. 12.13). These are the transfer functions $h_m^{c,s}(\omega)$ which relate the modal amplitudes of the actuation commands $\hat{\beta}_m^{c,s}$ to those of the modal pressure amplitudes $\hat{a}_m^{c,s}$ (see Fig. 12.11), hence

$$\hat{a}_m^{c,s} = h_m^{c,s}(\omega)\hat{\beta}_m^{c,s}, \quad \text{where} \quad h_m^{c,s}(\omega) = (\boldsymbol{b}_{12.m}^{c,s})^{\dagger}\mathbf{H}_m(\omega)\boldsymbol{b}_{6.m}^{c,s}, \tag{12.17}$$

and $\boldsymbol{b}_{12.m}^{c,s}$ and $\boldsymbol{b}_{6.m}^{c,s}$ are the columns in matrices $\mathbf{B}_{12}$ and $\mathbf{B}_6$ associated with mode $m^{c,s}$.

Schuermans et al. (2003) and Stow & Dowling (2009) propose, in case of a fully symmetric system, to obtain a modal model for a particular mode by making an ansatz based on this mode only. While this is generally a valid procedure because the modes are decoupled in a symmetric system, we found this approach to be inaccurate for azimuthal modes of higher-order, which are of particular interest here. The acoustic nearfield at the tube–annular-duct transitions has a quantitative influence on the eigenfrequencies. For the 4th, 5th, and 6th azimuthal modes, with eigenfrequencies around 550 Hz, the resonance frequencies of the corresponding single-mode models were found to be different from those obtained from the full model (taking into account annular duct circumferential modes up to order 20) by 10–20 Hz. However, when representing the annular duct, not all azimuthal orders contribute to a certain system mode. In fact, only those that fold back due to aliasing have an effect in addition to the actual circumferential mode order. In case of an mth-order azimuthal system mode, these are the circumferential wavenumbers $lN \pm m$, $l = 1, 2\ldots$, for a configuration with N heat sources. Hence, the additional computational effort compared to a single-mode approach is clearly acceptable in view of a higher accuracy.

Calibration of the actuator response

As explained in Section 12.3.1, the open-loop plant model needs to be calibrated with respect to the actuator response. Since the transfer function of the loudspeakers, including the acoustic characteristics of the connecting parts, is not known, and moreover, cannot be

Table 12.1: Speaker parameters identified from experimental data

C_{sp}	$\omega_{\mathrm{sp}}/(2\pi)$	ζ_{sp}	τ_{sp}	l_{sp}
$484\,\mathrm{m\,s^{-2}\,V^{-1}}$	143 Hz	$0.18\,\mathrm{s^{-1}}$	0.6 ms	35 mm

measured directly, we identify this relation from response measurements in the full setup. These measurements are performed in cold conditions because an accurate identification is not possible in the presence of self-excited oscillations (Morgans & Dowling 2007). However, the actuator transfer function does not change with a temperature increase, and therefore, this approach is permissible.

Several ways of calibrating the actuator response are possible. For example, excitation with a single speaker can be used so that the speaker transfer function can be identified by investigating the response of each of the 12 microphones. This would have to be done for all speakers, in principle, to exclude any individual irregularities. As we intend to apply a modal control scheme, it is only important that the modal response is accurately represented in the model. For this reason, we identify the actuator transfer function based on experimentally determined modal response data. This is done by first driving the six speakers according to a distinct modal pattern, e.g., $e_j(t) = \cos(5\,\varphi_j)s(t), j = 1\ldots6$, for the cosine part of the $m = 5$ mode, where $s(t)$ is an identification waveform (we use a chirp signal), and φ_j corresponds to the angular locations of the speakers. Then the vector of measured pressure signals is projected on the respective circumferential mode in the measurement signal space to obtain the modal coefficient $a_m^{c,s}(t)$. After transformation to the frequency domain, the modal transfer function is calculated as $h_m^{c,s} = \hat{a}_m^{c,s}/\hat{e}_m^{c,s}$.

Now we have to identify the speaker transfer function $g(\omega)$, implicitly defined through (12.10), such that the respective element in the modeled modal transfer function $\mathbf{H}_m(\omega)$ matches the corresponding measured $h_m^{c,s}$ as accurately as possible in the relevant frequency range. We model the speaker transfer function as

$$g(\omega) = C_{\mathrm{sp}}\,\frac{\mathrm{i}\omega}{-\omega^2 + 2\mathrm{i}\zeta_{\mathrm{sp}}\omega + \omega_{\mathrm{sp}}^2}\,\mathrm{e}^{-\mathrm{i}\omega\tau_{\mathrm{sp}}}\,\sec(\omega l_{\mathrm{sp}}/c) \tag{12.18}$$

with parameters ω_{sp}, ζ_{sp}, τ_{sp}, and l_{sp}. The form of the speaker transfer function represents the typical high-pass character with slightly pronounced lower resonance frequency ω_{sp}, damping coefficient ζ_{sp}, and an additional delay τ_{sp}; C_{sp} is a constant amplification factor. The delay can be partially attributed to the low-pass filter of the microphone amplifier. To account for the short connecting tube (see Figs. 10.1 and 10.2), an additional reciprocal cosine term was added, which represents the acoustic transmission of the particle velocity along the tube. The parameters in (12.18) are then chosen such that the correspondence between measurement and model is as good as possible. The identified speaker parameters are summarized in Tab. 12.1.

Measured and modeled modal transfer functions for the 5th and 6th azimuthal modes, at cold conditions, for which the parameters in (12.18) were identified, are shown in Fig. 12.14. For the $m = 5$ mode, the measured sine and cosine parts are both shown. In principle, the modal transfer function of the sine and the cosine part should be identical; the model satisfies this, but it is advisable to confirm this property from the experimental

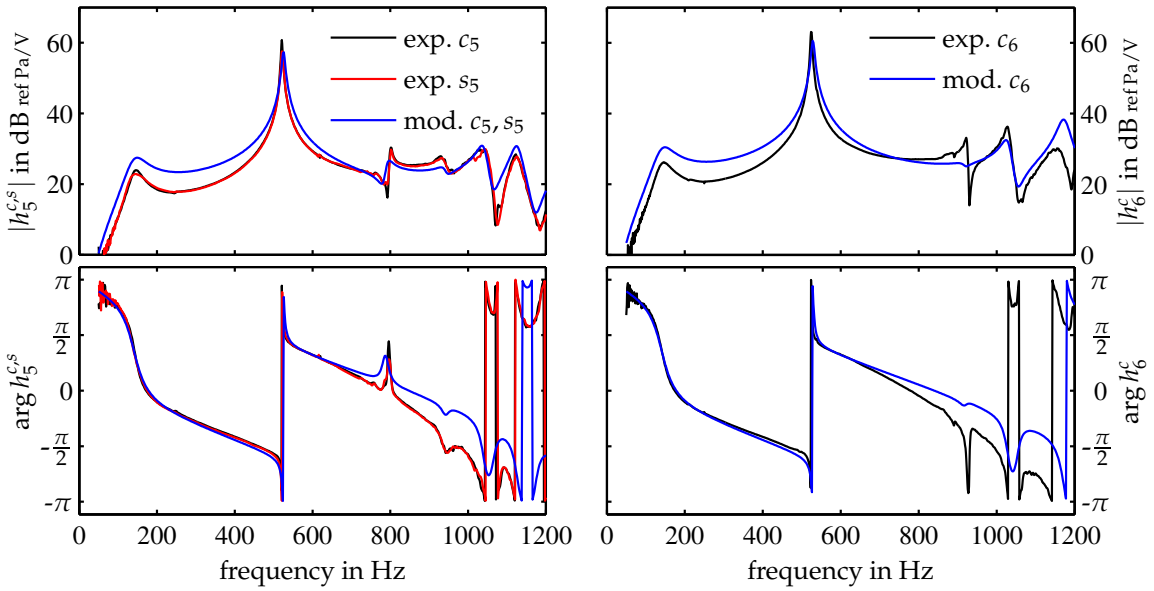

Figure 12.14: Measured and modeled modal transfer functions for the 5th (left) and the 6th azimuthal modes; heating grids off. c_m and s_m correspond to the cosine and the sine part, respectively.

data, too. The measured responses of the sine and the cosine part of the $m = 5$ mode essentially collapse. The modeled transfer functions also agree well with the measured data. Resonances corresponding to the unstable modes are represented accurately, and the phase matches up to about 700 Hz. At higher frequencies, the measured phase lag is progressive. This is not captured by the model, but phase accuracy at higher frequencies is not required for successful control. We also note that the width of the resonance peak, which is a measure for the modal damping, agrees reasonably well for modeled and measured results.

Phase-lead compensator design

In Section 11.5.2 we already identified the unstable modes from our model computations (Fig. 11.8). The instability can also be found in the open-loop transfer function with activated heating grids (Fig. 12.15). Assuming the system is characterized by a second-order oscillator around the resonance frequency, a phase increase by π indicates instability (Morgans & Dowling 2007), which is clearly the case. We also note from the open-loop transfer functions in Fig. 12.15 that additional loop-shaping is not necessary. In fact, as a result of the modal decomposition, the plant transfer functions have a high response only at the unstable mode frequency.

This type of instability can be stabilized, for example, with a phase-lead or a phase-lag compensator (Morgans & Dowling 2007). A principle difference between the two compensators is that high gain is introduced at large frequencies by the former and at small frequencies by the latter. Morgans & Dowling argued, in case of a longitudinal combustion system, that the phase-lag compensator is more suitable because high frequency noise is not amplified. Since our system is essentially noise-free and we do not want to destabilize lower modes (these are less damped than the higher modes), we use a phase-lead compensator, whose gain is small for low frequencies.

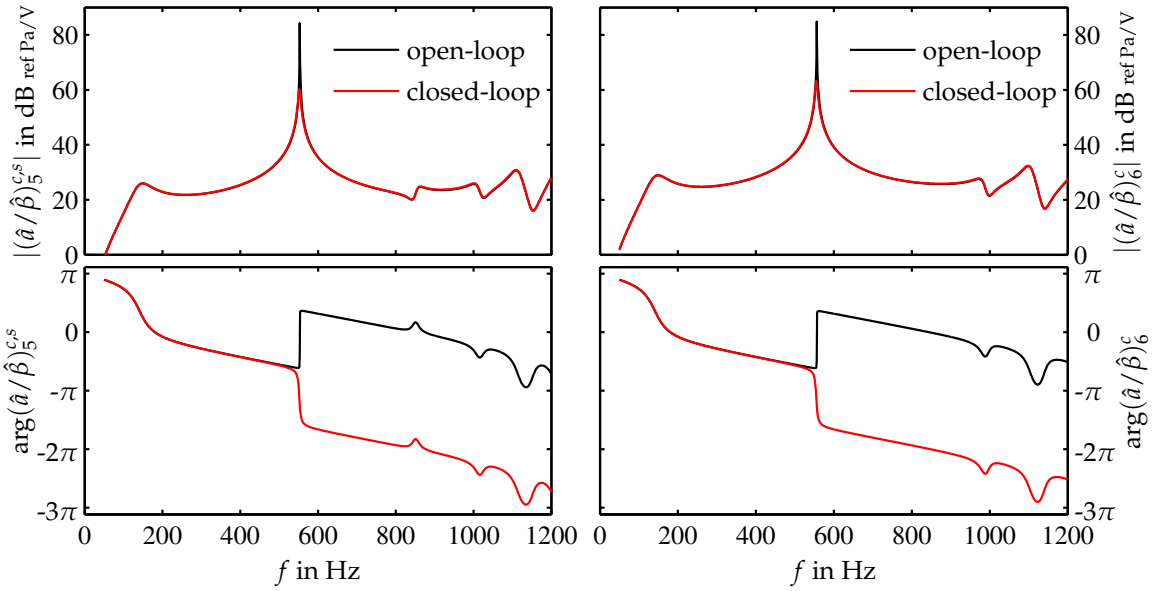

Figure 12.15: Modeled open- and closed-loop transfer functions for the 5th (left) and the 6th azimuthal modes. For the closed-loop case, a compensator gain of 6 has been used.

The standard phase-lead compensator has the transfer function

$$W(\omega) = C_{\mathrm{pl}} \frac{1 + a_{\mathrm{pl}} \tau_{\mathrm{pl}}\, \mathrm{i}\omega}{1 + \tau_{\mathrm{pl}}\, \mathrm{i}\omega}, \tag{12.19}$$

where $a_{\mathrm{pl}} > 1$ is the high-frequency gain, and the maximum phase increase occurs at $\omega = (\sqrt{a}_{\mathrm{pl}}\tau_{\mathrm{pl}})^{-1}$; C_{pl} is the compensator gain. Using $a_{\mathrm{pl}} = (5/2)^2$ and τ_{pl} such that the maximum phase increase occurs at 550 Hz, which is approximately the average oscillation frequency in the unstable heating power regime, both the 5th and the 6th azimuthal modes can be stabilized using the same control parameters. The modal control command is then computed from the modal pressure coefficients according to

$$\hat{\beta}_m^{c,s} = W(\omega)\hat{a}_m^{c,s}, \tag{12.20}$$

and the control matrix $\mathbf{K}(\omega)$ (Fig. 12.11) is given by

$$\mathbf{K}(\omega) = \sum_{c_5,s_5,c_6} \boldsymbol{b}_{6.m}^{c,s} W(\omega) (\boldsymbol{b}_{12.m}^{c,s})^{\dagger}. \tag{12.21}$$

With this form, all unstable modes are controlled. Naturally, we can exclude elements from the sum in (12.21) to control only part of the unstable subspace, which we will also do later on.

The stabilizing effect of the phase-lead compensator is apparent in the modeled closed-loop transfer functions (Fig. 12.15). The phase increase by π across the resonance frequency in the open-loop case is now a phase decrease, which indicates stability. In addition, the response peak is significantly reduced. The effect of control on the system eigenvalues is displayed in Fig. 12.16. For a compensator gain of $C_{\mathrm{pl}} = 6$, both unstable eigenvalues can be moved into the stable half-plane individually. In case of the 5th-order

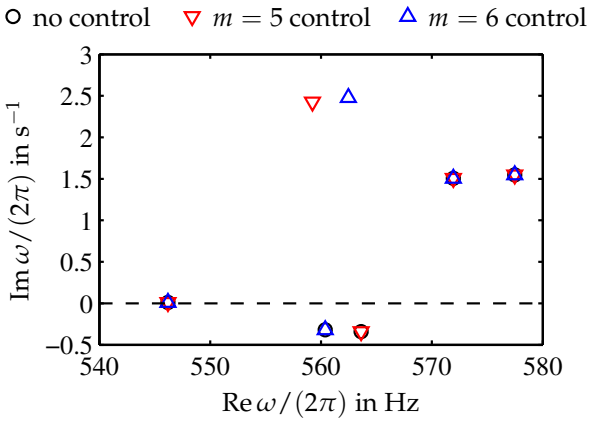

Figure 12.16: Effect of control on system eigenvalues with a compensator gain of 6. For $m = 5$, both unstable eigendirections are controlled.

azimuthal mode, both unstable eigendirections are controlled (with two individual compensators). The now stable eigenvalue is then still degenerate. If only one direction in the unstable $m = 5$ subspace is controlled, the degenerate eigenvalue splits, and the uncontrolled part remains in the lower half-plane at its original location (not shown).

12.3.3 Application of modal control

To apply the control scheme in the experiment, modal decomposition and recombination, and the phase-lead compensators were implemented on a control board (DS1103, dSpace) via Simulink. The sampling frequency was set to 9 kHz.

Complete stabilization

First, we apply control to all unstable modes simultaneously, i.e., we use two independent compensators of the form (12.19) for a basis of the unstable 5th azimuthal mode and one for the 6th azimuthal mode. For the degenerate $m = 5$ mode, we used the standing wave basis; using the rotating wave basis is more difficult and is discussed in the next paragraph. Identical control parameters were set for all unstable modes with a compensator gain of 6. Figure 12.17 presents results from the experimental application of the modal controller at an input power of 3 kW. After control for all unstable modes is activated, the instability is quickly diminished (Fig. 12.17, left). A spectral peak amplitude reduction of nearly 80 dB is achieved (Fig. 12.17, right). The small peak close to the nominally unstable frequencies corresponds to the 4th azimuthal mode, which was found to be marginally stable in the linear analysis (Fig. 11.8); no control was applied for this mode.

Control of standing and spinning subspaces

The unstable 5th azimuthal mode is degenerate, and therefore, the associated eigenspace is two-dimensional. This mode can be completely suppressed by controlling a basis of the unstable eigenspace, as shown in the preceding paragraph. If this basis is orthogonal, the two controllers can be independent. Furthermore, it is possible to control only a part of the unstable eigenspace. With respect to the standing wave basis, we can, for instance, only control the cosine part of the $m = 5$ mode. In this case, the sine part remains unstable and will be oscillating.

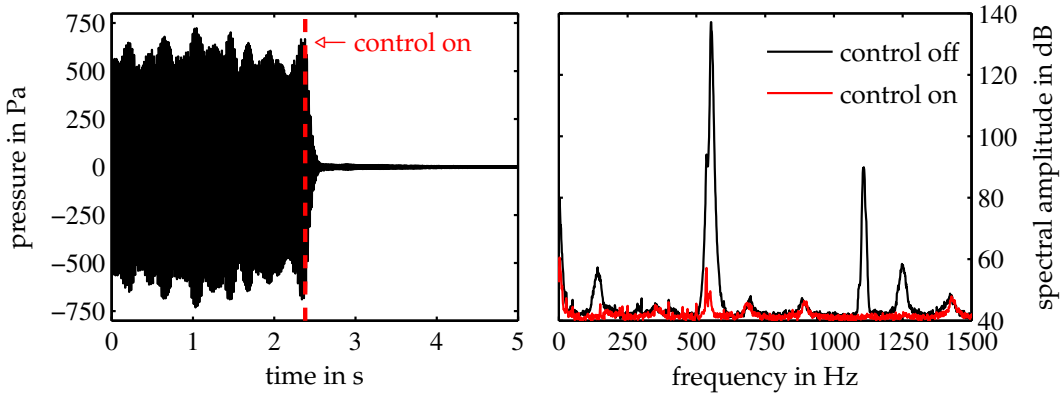

Figure 12.17: Application of the modal control scheme in the experiment. Histories of the 12 measured pressure signals (left) and amplitude spectra of one of the pressure signals for the uncontrolled and the controlled case (right). (The pressure spectra for all microphone signals are similar.)

Similarly, we can use a spinning basis with clockwise- and counter-clockwise-rotating wave components $\mathrm{e}^{\mathrm{i}m\varphi}$ and $\mathrm{e}^{-\mathrm{i}m\varphi}$. As mentioned at the beginning of this chapter, this basis is complex, and therefore, the quadrature component of the real pressure signals also needs to be taken into account in the control scheme. Accordingly, the input to the control transfer function matrix $\mathbf{K}(\omega)$ (Fig. 12.11) must be the analytic signal $\boldsymbol{p}_\mathrm{a} = \boldsymbol{p} + \mathrm{i}\mathcal{H}[\boldsymbol{p}]$. Computation of the analytic signal in a postprocessing step is a standard procedure, but in a control application, $\boldsymbol{p}_\mathrm{a}$ has to be available at run time. Various causal Hilbert filters are available from the signal processing literature (e.g., Mirta & Kaiser 1993, Chap. 13); however, these always introduce an additional time lag. In principle, the analytic signal can be generated with the time-lagged Hilbert transform by delaying the real component by the same amount, but an additional time lag is undesirable for control applications. In the present work, we therefore generate a narrow-band Hilbert transform by simply using a delay such that the pressure signals are phase-shifted by $\pi/2$ at the frequency of the unstable mode. This procedure is permissible because the signal is distinctly narrow-band (see Fig. 12.2). With a control board sampling frequency of 9 kHz, a quadrature phase shift at 560 Hz (which is sufficiently close to the $m = 5$ and $m = 6$ modes) is thus achieved by a discrete delay of four sampling steps.

Figure 12.18 shows results from the application of the control scheme described above. The unstable 6th-order azimuthal mode is suppressed at all times. In addition, only one basis function of the unstable $m = 5$ mode is controlled. By stabilizing, for example, only the cosine part, we obtain an almost perfect sine distribution (red curve in Fig. 12.18). Conversely, we can control the sine part only; this results in the blue curve. When controlling only one spinning direction, a perfectly rotating mode is observed (which spins in the uncontrolled direction).

Further results for the control of individual unstable subspaces corresponding to the 5th-order azimuthal mode are presented in Fig. 12.19. In the time intervals indicated, different components of the $m = 5$ mode are controlled; the information is summarized in Tab. 12.2. The $m = 6$ mode is, again, controlled at all times. For $t < t_1$, all unstable modes are controlled. At t_1, control of a_5^s (the sine component of the $m = 5$ mode) is ceased. This mode now starts to grow exponentially and settles on an approximately

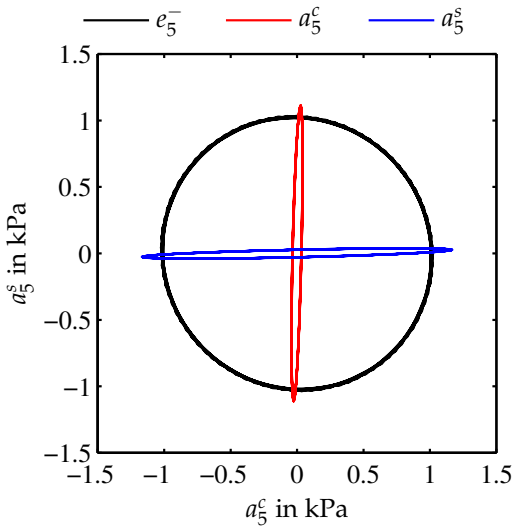

Figure 12.18: Standing-wave-basis modal amplitudes for different types of partial subspace control. The 6th azimuthal mode is always controlled; in addition, the mode indicated in the legend is also controlled. The length of each trajectory corresponds to a time interval of 40 ms.

constant oscillation level. In the spinning wave basis (Fig. 12.19 (a)), the amplitudes of the two eigenfunction coordinates are equal, as necessary to produce a standing wave pattern. With respect to the standing wave basis (Fig. 12.19 (b)), only the a_5^s component has a non-zero amplitude. At t_2, control is switched to the spinning wave basis, targeting only the clockwise rotating a_5^- component. As a result, only the amplitude of the counter-clockwise rotating wave, a_5^+, is non-zero (Fig. 12.19 (a)). In the standing wave basis, this corresponds to equal amplitudes of the two components (but with a phase shift of $\pi/2$). At t_3, control is again switched to the standing cosine component with amplitude a_5^c. Between t_4 and t_5, all unstable modes are controlled. Individual control of the unstable subspaces corresponding to the amplitudes a_5^s and a_5^+ is applied at times t_5–t_6 and t_7–t_8 and between t_6 and t_7, respectively. Similar results as in case of control of the complement modes are evident.

The spin ratio Δ_5^{sp}, as defined in Eq. (12.2), is plotted in Fig. 12.19 (c). When the 5th-order azimuthal mode is completely controlled, or the amplitudes have not yet attained a significant level, the spin ratio cannot be computed in a sensible manner. This is represented by the random variation of Δ_5^{sp} between 0 and 1. However, whenever the oscillation amplitude is non-vanishing, the spin ratio gives a clear indication whether the mode is standing or rotating.

We consider now frame (d) in Fig. 12.19, which displays the normalized low-pass filtered sum of the 12 squared pressure signals for the different control cases. The plot shows the quantity $E = N^{-1} \sum_{n=1}^{N} \mathrm{LP}[p_n^2]/(\rho c^2)$, which is representative of the oscillation energy in the system ($\mathrm{LP}[\cdot]$ is a low-pass filter). If the energy in the controlled modes is neglected, this term is identical to the squared sum of the oscillating modes (because the modal bases are unitary). We note that the oscillation energy is significantly larger in case of a spinning mode by approximately a factor of two. Incidentally, this is also evident from frame (b) when comparing the modal amplitudes between t_2 and t_3 with those between t_3 and t_4. The modal amplitudes in case of the standing and the spinning mode limit cycle are almost equally high. However, both standing wave amplitudes are non-zero when the wave is rotating, and since the pressure field is a superposition of the modal contributions, the oscillation energy is higher in this case.

Table 12.2: Annotation to Fig. 12.19. Time intervals for which particular modes are controlled.

time	$t < t_1$	t_1–t_2	t_2–t_3	t_3–t_4	t_4–t_5	t_5–t_6	t_6–t_7	t_7–t_8	$t > t_8$
control	a_6, a_5^c, a_5^s	a_6, a_5^c	a_6, a_5^-	a_6, a_5^c	a_6, a_5^c, a_5^s	a_6, a_5^s	a_6, a_5^+	a_6, a_5^s	a_6, a_5^c, a_5^s

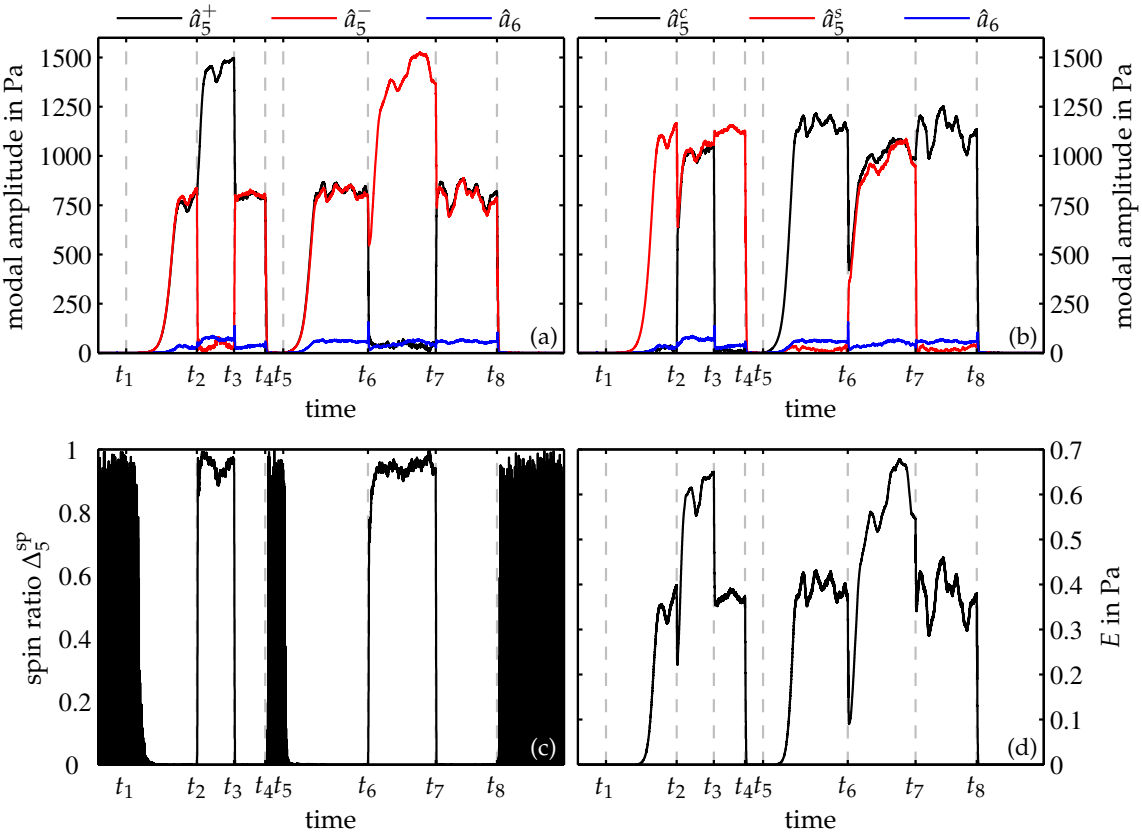

Figure 12.19: Transient variation of subspace control; (a) spinning-wave-basis modal amplitudes, (b) standing-wave-basis modal amplitudes, (c) spin ratio, and (d) equivalent of oscillation energy. A total time interval of 30 seconds is shown.

The reason for the oscillation energy to be higher for the rotating mode is difficult to assess because the limit cycle amplitude is determined by the nonlinear response of the heat source, information on which we do not have available. Yet, it is reasonable to assume that the nonlinearity is essentially of saturation type. In case of the rotating mode, all heating grids experience identical velocity oscillation amplitudes; only the phase is different. Therefore, the oscillations in all tubes enter the saturation level at the same amplitude. This is different for the standing wave mode. Only tubes located at circumferential pressure antinodes experience the maximum velocity oscillations bounded by the saturation level, whereas those close to nodes hardly see any perturbations at all. Therefore, the rotating mode is more effective in distributing the fluctuation energy among all tubes while complying with the saturation level at each heating grid.

As a last application of the modal control scheme, we determine the linear growth rates of the unstable modes. This is achieved by first suppressing all modes and then deactivating control for one mode at a time. The logarithm of the modal amplitudes for this

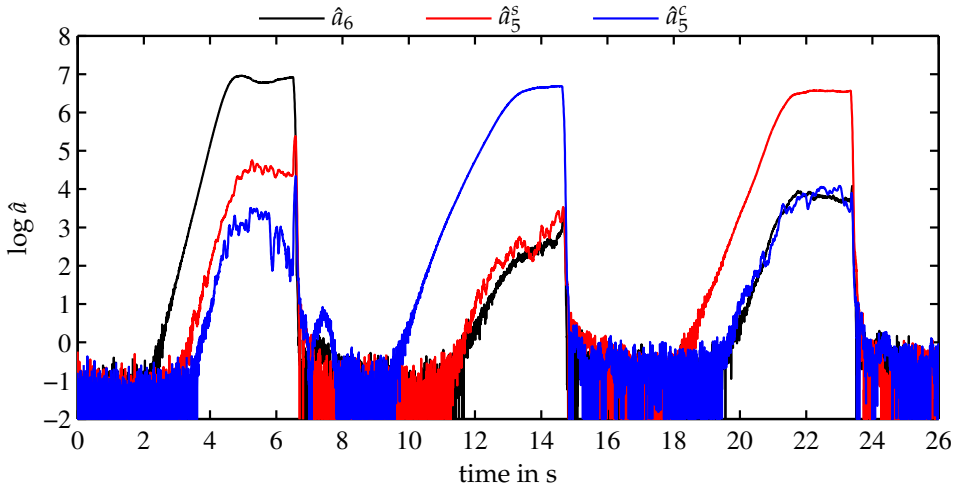

Figure 12.20: Investigation of the linear growth of the unstable modes. All modes are controlled initially. Control is deactivated for one mode at a time. The plot shows the magnitude of the analytic signals of the modal coefficients. A total input power of 3000 W has been used.

procedure is shown in Fig. 12.20. Here, the modal amplitudes were computed from the modal coefficients as the magnitude of the corresponding analytic signals. A total input power of 3000 W was used for this case. The stage of linear growth can be recognized in Fig. 12.20 as a linear increase in the logarithm of the modal amplitude. An evaluation of the slope for small amplitudes yields the growth rates $-\mathrm{Im}\,\omega/(2\pi)$, which we determine as 0.55 s^{-1}, 0.35 s^{-1}, and 0.37 s^{-1} for the a_6, the a_5^s, and a_5^c modes, respectively. These values compare reasonably well with those obtained from our model computation, although for the experimental data, the $m = 6$ mode has a somewhat larger growth rate. The two $m = 5$ modes have nearly identical growth rates, confirming the theory in that both eigendirections are equally unstable.

During the control experiments, we also noted that for total input powers larger than 3000 W, the 4th azimuthal mode was indeed marginally stable. By activating control for the unstable $m = 5$ and $m = 6$ modes, which is an impulsive action, the $m = 4$ mode was excited and could be observed to be oscillating at a rather low level. However, this oscillation was distinct, with the other modes being controlled, and persisted for significant periods of time. The amplitude varied, but only very slowly.

12.4 Concluding discussion

In this chapter, we performed an experimental study of the annular Rijke tube. Consistent with linear stability analysis, the 5th and 6th azimuthal modes were unstable. For the degenerate $m = 5$ mode, no distinct standing or spinning pattern was established. We conjectured that this can be attributed to the simultaneous presence of the $m = 6$ mode, which can be interpreted as a random noise component for the 5th azimuthal mode. As Schuermans et al. (2006) have shown, it is the saturation nonlinearity in the heat release response that promotes the spinning wave pattern. Since, in our case, the growth rates are

very small, the nonlinearity is weak, and the effect on the degenerate $m = 5$ eigenspace may not be strong enough to cause a distinct splitting into the two rotating modes.

We investigated the effect of an asymmetric power distribution on the stability of the azimuthal modes. Two staging patterns were applied, one with a C_4 and one with a C_3 symmetry. The C_4 pattern reduced the oscillation amplitudes of the nominally unstable $m = 5$ and $m = 6$ modes but, at the same time, destabilized the 4th azimuthal mode. This destabilization could be attributed to a splitting of the mode (which was marginally stable in the symmetric case) as a result of the reduced symmetry. With the C_3 pattern, a full stabilization could be achieved because no weakly damped modes were split. These observations were consistent with results from the low-order model.

The asymmetry we applied in this study was quite strong (σ up to 1.5), but this is only because the parameters of the heat release transfer function vary only weakly with the electrical input power. For premixed flames in annular combustion chambers, we expect that less asymmetry in the operating parameters is needed to generate a noticeable effect in the transfer function. Another possibility is to use different burners or a different internal fuel staging to achieve a significant circumferential variation of the transfer function properties (Noiray et al. 2010).

Based on a decomposition of the pressure field into the individual azimuthal contributions, we set up a modal control scheme utilizing six speakers around the circumference. This allowed for efficient control, for only the unstable subspace is considered. Three independent controllers were used, one for each unstable mode. A full suppression of the pressure oscillations could be achieved, reducing the spectral peak amplitude by almost four orders of magnitude. Furthermore, the unstable modes could be controlled individually, which allows to study them in isolated form.

Conclusions and Outlook

Combustion oscillations are one of the main issues for gas turbines operating in lean premixed mode. This dynamic phenomenon manifests itself in large fluctuations of the pressure and the flow field and effectively constrains the operating envelope of the engine so that optimal efficiency, power output, and emission levels cannot be achieved. Fundamental knowledge on thermoacoustic instabilities, modeling tools to predict their occurrence, and methods for their control are needed to advance gas turbine technology to higher efficiency and lower emissions. The present work has contributed to this task in the following ways.

In the first part of this thesis, we studied combustion instabilities in an atmospheric test-rig and successfully applied different control methodologies. We introduced a multiple actuator scheme for more flexible control, in which acoustic forcing and secondary fuel injection were used in a combined mode. This strategy was shown to maintain significantly reduced pressure oscillation levels, while consuming a minimum amount of pilot fuel. Since actuator limitations are one of the major issues preventing the application of active control solutions to industrial applications (Dowling & Morgans 2005), combining the advantages of different forcing mechanisms is a useful approach.

Quantitatively accurate modeling of realistic combustor configurations is not possible today. Therefore, model-free adaptive control schemes are particularly attractive. We applied a two-parameter extremum-seeking scheme in a test-rig combustor and demonstrated that the controller was able to find the pulsation minimum in parameter space. Instabilities were successfully mitigated at different operating conditions, and control could be maintained even for a transient variation of the preheat temperature. Peak amplitude reductions in the unsteady combustor pressure of up to 40 dB were achieved.

Control of combustion instabilities is an attractive problem from an academic point of view because it involves so many different disciplines. However, what prevents the transition of these methods to industry is not the lack of control concepts or test-rig demonstrations but the actuator issue. Further research should be focused on robust, high-bandwidth actuators, preferably to modulate the main or some secondary fuel flow. Fluidic oscillators, which have no moving parts and are, therefore, extremely robust, are attractive for this task and were shown to be capable of controlling thermoacoustic pulsations recently (Guyot et al. 2009). Although only suitable for open-loop excitation, coupling this type of actuator to an adaptive scheme, like the one presented in Section 5, so that amplitude and/or frequency of the oscillator are tuned, appears to be a promising approach.

We investigated subcritical instabilities in the combustor test-rig and demonstrated triggering of limit-cycle oscillations in a linearly stable system and hysteresis with respect

to variations in the operating parameters. This is a crucial contribution in light of recent findings on the non-normal character of thermoacoustic dynamics. The possibility of triggering instabilities in linearly stable systems is not accounted for in most stability analyses. To assess the importance of these transient aspects in the system dynamics, precise experimental statements about the nature of the instability (linear or subcritical) are indispensable.

The hydrodynamic–acoustic coupling approach presented in Part II, was demonstrated to be an efficient tool for modeling thermoacoustic instabilities in the low-Mach-number long-wavelength regime and for exploring suitable control scenarios. We validated the method on the basis of an experimental investigation of an elementary thermoacoustic configuration. Even though the flame was relatively simple in this case, the principal methodology has been proven to provide results which compare well with measurement data. Two control schemes were applied in a configuration with a more complex flame and showed that the stabilizing influence known from various experiments could be well captured by the coupled method.

Although not considered in this thesis, the two-way coupling is also suitable to represent annular combustors. In this case, the circumferential component of the acoustic pressure gradient causes a transversal acceleration of the flame, an effect which is not well understood presently. These extensions are currently in development, and test computations show that multiple flames in an annular set-up, coupled to a reduced-order representation of the azimuthal acoustic field, establish a rotating mode limit-cycle oscillation.

Another possible application of this approach are aeroacoustic instabilities in ducted systems associated with side-branch resonators. The phenomenon is very similar to thermoacoustic oscillations from a systems point of view. The combination pipe system–shear layer can become linearly unstable and exhibit self-sustained oscillations (Kriesels et al. 1995). Here, the feedback is induced by the unsteady shear layer shed from the side branch's rim and impinging on the trailing edge. This type of configuration is often associated with low-Mach-number flows and long acoustic wavelengths of the unstable modes and can be modeled with low-order methods essentially identical to those used for combustion instabilities (see, e.g., Martínez-Lera et al. 2009). Linear stability considerations as well as describing function based analyses have been applied but, to our knowledge, no computation of a complete duct system in a limit-cycling state has been performed yet.

To narrow the gap between elementary studies in longitudinal configurations (which are abundant) and full-scale applications in annular geometries, we devised a surrogate system for studying thermoacoustic instabilities associated with azimuthal modes (Part III). This system has a well-defined, simple, and generic set-up, in which heating grids mimic the flames in an annular combustion chamber. In experimental investigations, we found unstable modes of azimuthal orders 5 and 6. We have shown that these instabilities can be suppressed by a circumferential modulation of the heat sources. This is an effect which cannot be studied in "single-burner" configurations. However, care has to be taken that the circumferential variation of the heat sources does not cause a splitting of nominally degenerate, lightly damped modes, as this was found to be an essentially destabilizing effect. Assessing under what circumstances degenerate modes are split requires to determine the effect of azimuthal non-uniformities on system symmetry.

In addition to the experimental analysis of the annular system, we developed a low-order system model. The results obtained from this model were consistent with the experimental observations. Mode stability and the effect of a circumferential variation of the heating power could be correctly predicted. Although we used the developed modeling tools only for our surrogate system, application to annular combustor configurations is also possible. Furthermore, the model was employed to design a controller based on a modal decomposition of the pressure field. This controller was successfully applied in the experimental set-up and achieved a complete stabilization of all nominally unstable modes. Moreover, control of only parts of the unstable subspace was possible so that purely standing and purely spinning modes could be established.

In the present work, we applied only active control to mitigate the instabilities in the annular set-up. However, passive solutions, such as Helmholtz dampers, are still favored by the gas turbine industry. The most effective placement of a set of, possibly different, dampers (which may be in the order of 10–20 in number, Lepers et al. 2005) to stabilize a particular mode is a non-trivial undertaking, and tests utilizing full-scale annular combustion chambers are costly and time-consuming. Principal investigations addressing this question can be carried out in our simplified set-up.

Appendix A

Experimental Decomposition of the Plane Wave Mode

Plane wave decomposition is a method with which a one-dimensional acoustic field in a homogeneous duct can be stripped into up- and downstream propagating components. The experimental realization of this technique in thermoacoustic systems, based on multiple axially distributed measurements of the acoustic pressure, is now typically called the Multi-Microphone-Method. It is the key technique for the experimental identification of the acoustic and thermoacoustic properties of the elements in a low-order thermoacoustic model. This applies to transfer matrices and possibly associated source terms, but also to the acoustic boundary conditions. In addition to that, the acoustic velocity, that is required for flame transfer function measurements, can be determined with this method if multiple microphone measurements are available upstream of the flame. Originally, the wave decomposition goes back to Seybert & Ross (1977) and Chung & Blaser (1980) who used it for the characterization of absorptive materials and mufflers. Only two microphones were used, which is the minimum requirement. Poinsot et al. (1986) extended the decomposition method to make use of several microphones for the measurement of the reflection coefficient of a premixed flame. The direct experimental characterization of transfer matrices of thermoacoustic elements is due to Heckl (1990) for a heating grid and Paschereit et al. (2002) for a swirl-stabilized premixed flame. It is also possible to determine the actuator characteristics for active control applications in terms of its plane wave response (Bothien et al. 2007), which is particularly useful for model-based control approaches (see, e.g., Gelbert et al. 2008).

In a homogeneous (constant cross-section and temperature) duct with a uniform plug flow at low Mach number, the frequency-domain plane wave acoustic field can be written as (Munjal 1987)

$$\hat{p} = \hat{f}_0 \, \mathrm{e}^{-\mathrm{i}k^+ x} + \hat{g}_0 \, \mathrm{e}^{\mathrm{i}k^- x}, \tag{A.1a}$$

$$\hat{u} = \hat{f}_0 \, \mathrm{e}^{-\mathrm{i}k^+ x} - \hat{g}_0 \, \mathrm{e}^{\mathrm{i}k^- x}, \tag{A.1b}$$

where $\hat{f}_0$ and $\hat{g}_0$ are the complex amplitudes of the down- and upstream traveling waves (the Riemann invariants at $x = 0$) and $k^\pm = \omega/(c \pm \mathrm{M})$ are the associated wavenumbers of the plane mode (neglecting visco-thermal damping). The pressure has been scaled by the characteristic impedance ρc, but we denote it simply by p for convenience. For frequencies

below the cut-on frequency for the first azimuthal mode, only this part of the pressure field propagates; all other non-planar components decay exponentially.

We consider now N pressure measurements at different axial locations x_n and their associated Fourier transforms $\hat{\boldsymbol{p}} = [\hat{p}_1 \dots \hat{p}_N]^T$. Applying (A.1a) at every x_n, we obtain a linear system of equations that can be written in matrix–vector form as

$$\hat{\boldsymbol{p}} = \mathbf{M} \begin{bmatrix} \hat{f}_0 \\ \hat{g}_0 \end{bmatrix}, \tag{A.2}$$

where the propagation matrix $\mathbf{M}$ is given by

$$\mathbf{M} = \begin{bmatrix} \mathrm{e}^{-\mathrm{i}k^+x_1} & \mathrm{e}^{\mathrm{i}k^-x_1} \\ \vdots & \vdots \\ \mathrm{e}^{-\mathrm{i}k^+x_N} & \mathrm{e}^{\mathrm{i}k^-x_N} \end{bmatrix}. \tag{A.3}$$

For $N \geq 2$, Eq. (A.2) can be solved (in a least squares sense if N is strictly larger than 2) for the wave amplitudes $\hat{f}_0$ and $\hat{g}_0$ if the pressure phasors $\hat{\boldsymbol{p}}$ are known, viz.,

$$\begin{bmatrix} \hat{f}_0 \\ \hat{g}_0 \end{bmatrix} = \mathbf{M}^+ \hat{\boldsymbol{p}}. \tag{A.4}$$

In (A.4), $\mathbf{M}^+$ is a pseudoinverse of $\mathbf{M}$. Evidently, the determination of the Riemann invariants at the reference location, $\hat{f}_0$ and $\hat{g}_0$, will be more robust against any measurement errors if N is large.

In principle, this method can be applied in a turbulent combustor without any external forcing. The stochastic source terms associated with turbulence provide for excitation of the acoustic field. However, significantly higher accuracy is achieved when using a broadband forcing signal, or even single-frequency excitation, with a speaker. In this case, the pressure phasors $\hat{p}_n$ can be replaced with the forcing-correlated contribution only, $\hat{p}_n^e$, say. This can be obtained from the scaled cross-spectrum of the pressure and the excitation signal as

$$\hat{p}_n^e = \frac{\overline{\hat{p}_n \hat{e}^*}}{\sqrt{\overline{\hat{e}\hat{e}^*}}}, \tag{A.5}$$

where the overbar denotes an ensemble average.

The procedure explained above essentially determines the complete pressure field in the duct applied to. With the Riemann invariants known at the reference location, acoustic pressure and velocity can be computed at an arbitrary location by making use of (A.1). This is called the Multi-Microphone-Method. Using only microphones to determine the plane wave acoustic field has the advantage that no velocity probe is necessary. Measuring the acoustic particle velocity (associated with small amplitudes) directly is difficult and, therefore, error prone. This applies in particular to the burnt side of the flame.

The error in the wave decomposition can be estimated on the basis of the normalized mean squared deviation

$$\delta_{\mathrm{dev}} = \frac{||(\mathbf{I} - \mathbf{M}\mathbf{M}^+)\hat{p}||_2^2}{||\hat{p}||_2^2}, \tag{A.6}$$

where $||(\cdot)||_2^2$ denotes the square of the Euclidean 2-norm. It is important to recognize that this represents only the deviation between the assumed form of the pressure field and the measured pressure phasors. Depending on the microphone positions x_n and the speed of sound, the propagation matrix $\mathbf{M}$ can be badly conditioned so that small errors in $\hat{p}$ are amplified and lead to meaningless results for $\hat{f}_0$ and $\hat{g}_0$. This is, e.g., the case for low frequencies and small microphone spacings.

Appendix B

Computation of Annular Thermoacoustic Modes Based on the Solution in a Reference Cell

Acoustic and thermoacoustic modes in an annular configuration can be computed from a single reference cell. For this to work, we have to require that all cells are identical. We need our system to feature a discrete rotational symmetry of order N, where N is the number of cells (burners, say). Under these circumstances, the method yields exact results. Here, exact refers to the solution of the full annular configuration. We used this method to compute the acoustic modes of the annular Rijke tube configuration in Part III for the case with no heat release feedback. Thermoacoustic modes including heat release feedback can be calculated with this method as well, as we will show in the following on the basis of a simple model problem.

The method rests on Bloch's theorem, that is used in quantum mechanics and solid state physics for the computation of dispersion curves and bandgaps in crystal solids. To illustrate this method, we consider an elementary model system related to an annular combustion chamber and show that the Bloch-type solution can be taken directly from a well-known example in quantum mechanics, the Kronig–Penney model (see, e.g., Griffiths 1995 or the original article by Kronig & Penney 1931).

We consider the one-dimensional configuration shown in Fig. B.1. N heat sources (all identical) are arranged in a ring. The spacing between two adjacent sources shall be identical as well. We can take this model to be a very simplistic representation of flames in an annular combustion chamber with no axial and radial variations. If we further assume a constant temperature along the circumference and consider heat sources with point support, the frequency-domain pressure field (scaled by the characteristic impedance) is governed by

$$\hat{p}''(\varphi) + k^2 \hat{p}(\varphi) = -\mathrm{i}k \frac{\gamma - 1}{\gamma P_0} \sum_{n=1}^{N} \hat{q} \delta(\varphi - n\Delta\varphi), \tag{B.1}$$

where the prime denotes differentiation with respect to φ, $\Delta\varphi = 2\pi/N$ is the spacing between the heat sources, and we have rescaled the wavenumber with the radius R of the ring so that $k = \omega R/c$ now represents a Helmholtz number. Due to the ring structure, we have boundary conditions of periodicity, viz., $\hat{p}(\varphi + 2\pi) = \hat{p}(\varphi)$.

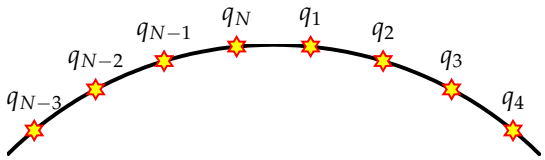

Figure B.1: A periodic arrangement of N heat sources in a ring

To close Eq. (B.1), we need to relate $\hat{q}$ to the acoustic field, and a traditional choice would be to make it a linear function of the gradient of $\hat{p}$, i.e., of the acoustic velocity. However, in this configuration, the gradient of $\hat{p}$ corresponds to the circumferential acoustic velocity. Excitation of a compact monopole-type source by a long-wave transverse velocity oscillation is unphysical for symmetry reasons. For simplicity, we therefore assume the heat source to be a linear function of the pressure. We can actually reason that the pressure will be related to an in-plane (axial) component of the velocity by some transfer function. We hence relate the heat source through a transfer function f to the pressure

$$\frac{\gamma-1}{\gamma P_0}\,\hat{q} = f(k)\hat{p} \tag{B.2}$$

and abbreviate the right hand side of (B.1) so that we can write

$$\hat{p}'' + k^2\hat{p} = -V(\varphi,k)\hat{p}, \tag{B.3}$$

where the "potential" V is given by

$$V(\varphi,k) = \mathrm{i}kf(k)\sum_{n=1}^{N}\delta(\varphi - n\Delta\varphi). \tag{B.4}$$

Equation (B.3) is identical to the time-harmonic Schrödinger equation with (scaled) potential V and energy eigenvalue k^2. In case of the Schrödinger equation, the potential V does typically not depend on the eigenvalue. This makes, however, no difference for the derivation of the solution. The important point is that the potential is periodic in φ, with fundamental period $2\pi/N$. In quantum mechanics, Eq. (B.3) determines the admissible energy eigenvalues and associated wave functions in a one-dimensional, periodic crystal lattice where the nuclei generate the Dirac comb potential.[1]

By invoking now the Floquet–Bloch theorem (Griffiths 1995), the problem can be restricted to a single reference cell (e.g., $\varphi \in [0, 2\pi/N]$) with quasi-periodic boundary conditions

$$\hat{p}(\varphi + \Delta\varphi) = \mathrm{e}^{\mathrm{i}b\Delta\varphi}\,\hat{p}(\varphi), \tag{B.5}$$

where b is the Bloch wavenumber. Speaking in terms of solid state physics, the Bloch wavenumber is restricted to the reciprocal unit cell (the first Brillouin zone), i.e., $b \in$

[1] In their original article, Kronig & Penney (1931) actually considered a periodic rectangular potential with certain width and height. However, in the limit of infinitely thin pulses (which they also considered), this is equivalent to the Dirac comb.

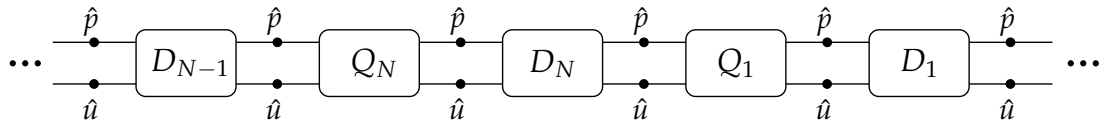

Figure B.2: Network model of the ring configuration

$(-N/2, N/2]$. An alternative formulation of the Floquet–Bloch theorem is that there are solutions of (B.3) which have the decomposition

$$\hat{p}(\varphi) = \mathrm{e}^{\mathrm{i}b\varphi}\, v(\varphi), \tag{B.6}$$

where $v(\varphi)$ is periodic with period $2\pi/N$. The theorem does not say that all solutions must have this form, and for degenerate modes, this is indeed not the case. We can, however, construct all solutions from solutions which have the form (B.6). For example, a degenerate azimuthal mode can have a circumferential variation like $\cos m\varphi$, which does not satisfy (B.6) for any admissible value of the Bloch wavenumber b. Yet, we can reconstruct this solution from two other solutions which have the form (B.6) (one with positive b and one with negative b) and share the same eigenvalue. Evidently, the degenerate eigenfunctions we compute based on a reference cell with Floquet–Bloch boundary conditions are of traveling wave form. In Section 11.2, we found that traveling waves with an azimuthal order that is equal to a half-integer multiple of the order of the symmetry group may not exist. In this case, the quasi-periodic boundary conditions (B.5) simply reduce to conditions of symmetry or skew-symmetry. (The former if the mode order is a full-integer multiple and the latter in case of a half-integer multiple.)

Following Griffiths (1995), the dispersion relation for the eigenvalues of (B.3) can be obtained by requiring that the solution is continuous everywhere and the first derivative has a jump complying with the Dirac comb. Then the eigenvalues k of our problem are solutions of

$$\cos(b\Delta\varphi) - \cos(k\Delta\varphi) + \frac{\mathrm{i}}{2} f(k) \sin(k\Delta\varphi) = 0. \tag{B.7}$$

Since we also have 2π-periodicity, b can only take discrete values $b = 0, \pm 1, \pm 2, \ldots$ Note that the sign of b makes no difference in (B.7); it does, however, in (B.5). The corresponding eigenfunctions can be easily obtained because, from (B.3), we find them to be simple harmonic waves with a jump in the gradient of $\hat{p}$ at $n\Delta\varphi$ that is equal to $f(k)\hat{p}(n\Delta\varphi)$. Based on the solution in the reference cell, the pressure field in the whole domain can be obtained by (repeated) application of (B.5).

Before discussing the meaning of (B.7) in the context of circumferential thermoacoustic instabilities, we consider an alternative way of modeling this problem. Since the configuration in Fig. B.1 is completely one-dimensional and the heat sources are modeled as infinitely thin, we can represent it with network methods in an *exact* way. To do this, we connect N duct and heat release elements in series that eventually connect to themselves (Fig. B.2).

The duct elements account for the wave propagation between two adjacent heat sources

$$D = \begin{bmatrix} \cos(k\Delta\varphi) & -\mathrm{i}\sin(k\Delta\varphi) \\ -\mathrm{i}\sin(k\Delta\varphi) & \cos(k\Delta\varphi) \end{bmatrix}, \tag{B.8}$$

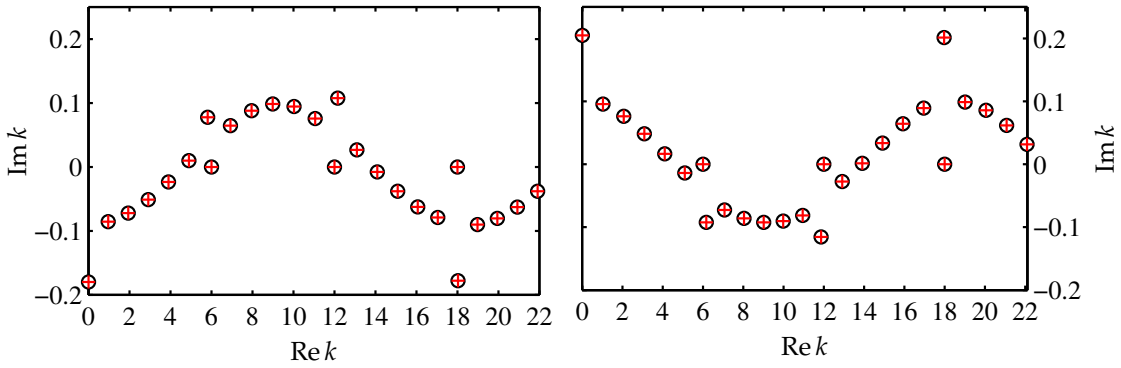

Figure B.3: Eigenvalues of the Kronig–Penney model with $N = 12$, $\tau = 0.34$, and $n = 0.1$ (left), respectively $n = -0.1$ (right). Black circles correspond to solutions of (B.7) and red crosses to solutions of (B.11).

and the Q elements for the jump in acoustic velocity resulting from the pressure induced heat release

$$Q = \begin{bmatrix} 1 & 0 \\ f(k) & 1 \end{bmatrix}. \tag{B.9}$$

Due to the 2π-periodicity, the acoustic field connects to itself after N duct–heat-release combinations, and we can evaluate pressure and velocity at an arbitrary position in the network to find

$$\begin{bmatrix} \hat{p}_n \\ \hat{u}_n \end{bmatrix} = (DQ)^N \begin{bmatrix} \hat{p}_n \\ \hat{u}_n \end{bmatrix}. \tag{B.10}$$

Hence, only non-trivial solutions exist if the dispersion relation

$$\det |(DQ)^N - \mathbf{I}| = 0 \tag{B.11}$$

is satisfied.

To produce numerical results, we choose the most common heat release transfer function, an n–τ model, $f(k) = n\,\mathrm{e}^{-\mathrm{i}k\tau}$. Here, τ is a non-dimensional time lag related to the dimensional form by c/R. The eigenvalues of the dispersion relations (B.7) and (B.11) for $N = 12$, $\tau = 0.34$, and $n = \pm 0.1$ are shown in Fig. B.3. In our one-dimensional setting, the real part of k roughly corresponds to the azimuthal mode order.

The first thing we should mention is that the range of azimuthal mode orders shown in Fig. B.3 is actually quite large and exceeds even the cell-width > wavelength limit; but it is still interesting to see the stability of these modes as well. The stability ($\mathrm{Im}\,k > 0$) or instability of the modes can be simply related to a pressure-in-phase-with-heat-release condition. Another noticeable feature is the eigenvalue splitting that occurs for azimuthal mode orders with non-zero integer multiples of $N/2$. This is consistent with the symmetry considerations in Section 11.2. All other eigenvalues corresponding to non-zero azimuthal mode orders are degenerate. For integer multiples of $N/2$, one of the split eigenvalues has identically zero imaginary part. It is straightforward to see why this is so. If the azimuthal mode order is a multiple of $N/2$, then there is always one eigenfunction that has nodes at $\varphi = n\Delta\varphi$, i.e., at the locations of the heat sources. Since the sources are driven by the local pressure, the source term is identically zero for these cases. The other

eigenfunction associated with the eigenvalue having non-zero growth rate has an antinode at the positions of the heat sources. The sign of the growth rate then depends on the phase of the exponential in the heat release transfer function $f(k)$. From (B.7) we note that for $b = 0$, $k = 0$ is a solution. Associated with this is only the trivial solution $\hat{p} = 0$. The eigenvalues computed from the network model dispersion relation (B.11) are identical to those obtained from the solution of (B.7), as evident in Fig. B.3.

Although we illustrated the approach only for a simple model system, it can be applied for complex cases as well. The only requirement is the rotational symmetry of the entire configuration. If this is given, however, the computational savings can be significant.

Bibliography

ABU-ORF, G. M. & CANT, R. S. (1996). "Reaction rate modelling for premixed turbulent methane-air flames." In: *Proceedings of the Joint Meeting of the Portuguese, British and Swedish Sections of the Combustion Institute*, Madeira, Spain.

ANANTHKRISHNAN, N., DEO, S., & CULICK, F. E. C. (2005). "Reduced-order modeling and dynamics of nonlinear acoustic waves in a combustion chamber." *Combust. Sci. Technol.*, **177**(2):221–248.

ARIYUR, K. B. & KRSTIĆ, M. (2002). "Slope seeking and application to compressor instability control." In: *Proceedings of the 41st IEEE Conference on Decision and Control*, pp. 3690–3697. Las Vegas, NV.

ARIYUR, K. B. & KRSTIĆ, M. (2003). *Real-Time Optimization by Extremum-Seeking Control*. John Wiley & Sons, Hoboken, NJ.

ARMITAGE, C. A., BALACHANDRAN, R., MASTORAKOS, E., & CANT, R. S. (2006). "Investigation of the nonlinear response of turbulent premixed flames to imposed inlet velocity oscillations." *Combust. Flame*, **146**:419–436.

AUER, M. P., GEBAUER, C., MÖSL, K. G., HIRSCH, C., & SATTELMAYER, T. (2005). "Active instability control: Feedback of combustion instabilities on the injection of gaseous fuel." *J. Eng. Gas Turbines Power*, **127**:748–754.

AYOOLA, B. O., BALACHANDRAN, R., FRANK, J. H., MASTORAKOS, E., & KAMINSKI, C. F. (2006). "Spatially resolved heat release rate measurements in turbulent premixed flames." *Combust. Flame*, **144**(1–2):1–16.

BALACHANDRAN, R., AYOOLA, B. O., KAMINSKI, C. F., DOWLING, A. P., & MASTORAKOS, E. (2005). "Experimental investigation of the nonlinear response of turbulent premixed flames to imposed inlet velocity oscillations." *Combust. Flame*, **143**(1–2):37–55.

BALASUBRAMANIAN, K. & SUJITH, R. I. (2008*a*). "Non-normality and nonlinearity in combustion–acoustic interaction in diffusion flames." *J. Fluid Mech.*, **594**:29–57.

BALASUBRAMANIAN, K. & SUJITH, R. I. (2008*b*). "Thermoacoustic instability in a Rijke tube: Non-normality and nonlinearity." *Phys. Fluids*, **20**(4):044103.

BALLENTINE, L. E. (1998). *Quantum Mechanics: A Modern Development*. World Scientific, Singapore.

BANASZUK, A., JACOBSON, C. A., KHIBNIK, A. I., & MEHTA, P. G. (1999*a*). "Linear and nonlinear analysis of controlled combustion processes. Part I: Linear analysis." In: *Proceedings of the 1999 IEEE International Conference on Control Applications*, pp. 199–205.

BANASZUK, A., JACOBSON, C. A., KHIBNIK, A. I., & MEHTA, P. G. (1999*b*). "Linear and nonlinear analysis of controlled combustion processes. Part II: Nonlinear analysis." In: *Proceedings of the 1999 IEEE International Conference on Control Applications*, pp. 206–212.

BANASZUK, A., ZHANG, Y., & JACOBSON, C. A. (2000). "Adaptive control of combustion instability using extremum-seeking." In: *Proceedings of the American Control Conference*, pp. 416–422. Chicago, Illinois.

BANASZUK, A., ARIYUR, K. B., & KRSTIĆ, M. (2004). "An adaptive algorithm for control of combustion instability." *Automatica*, **40**:1965–1972.

BANASZUK, A., MEHTA, P. G., JACOBSON, C. A., & KHIBNIK, A. I. (2006). "Limits of achievable performace of controlled combustion processes." *IEEE Trans. Control Syst. Technol.*, **14**(5):881–895.

BECHERT, D. W. (1980). "Sound absorption caused by vorticity shedding, demonstrated with a jet flow." *J. Sound Vib.*, **70**(3):389–405.

BECKER, R., KING, R., PETZ, R., & NITSCHE, W. (2007). "Adaptive closed-loop separation control on a high-lift configuration using extremum seeking." *AIAA J.*, **45**:1382–1392.

BELLOWS, B. & LIEUWEN, T. (2004). "Nonlinear response of a premixed combustor to forced acoustic oscillations." AIAA paper 2004-0455.

BELLOWS, B. B., BOBBA, M. K., FORTE, A., SEITZMANN, J. M., & LIEUWEN, T. (2007*a*). "Flame transfer function saturation mechanisms in a swirl-stabilized combustor." *Proc. Combust. Inst.*, **31**:3181–3188.

BELLOWS, B. B., BOBBA, M. K., SEITZMANN, J. M., & LIEUWEN, T. (2007*b*). "Nonlinear flame transfer function characteristics in a swirl-stabilized combustor." *J. Eng. Gas Turbines Power*, **129**:954–961.

BELLUCCI, V., FLOHR, P., & PASCHEREIT, C. O. (2004). "Numerical and experimental study of acoustic damping generated by perforated screens." *AIAA J.*, **42**(8):1543–1549.

BENARD, N., MOREAU, E., GRIFFIN, J., & CATTAFESTA III, L. N. (2010). "Slope seeking for autonomous lift improvement by plasma surface discharge." *Exp. Fluids*, **48**(5):791–808.

BENOIT, L. & NICOUD, F. (2005). "Numerical assessment of thermo-acoustic instabilities in gas turbines." *Int. J. Numer. Methods Fluids*, **47**:849–855.

BERENBRINK, P. & HOFFMANN, S. (2000). "Supression of dynamic combustion instabilities by passive and active means." ASME paper 2000-GT-0079.

BIAGIOLI, F. (2006). "Stabilization mechanisms of turbulent premixed flames in strongly swirled flows." *Combust. Theor. Model.*, **10**(3):389–412.

BIAGIOLI, F., GÜTHE, F., & SCHUERMANS, B. (2008). "Combustion dynamics linked to flame behaviour in a partially premixed swirled industrial burner." *Exp. Therm. Fluid Sci.*, **32**(7):1344–1353.

BLOXSIDGE, G. J., DOWLING, A. P., HOOPER, N., & LANGHORNE, P. J. (1988*a*). "Active control of reheat buzz." *AIAA J.*, **26**(7):783–790.

BLOXSIDGE, G. J., DOWLING, A. P., & LANGHORNE, P. J. (1988*b*). "Reaheat buzz: an acoustically coupled combustion instability. Part 2. Theory." *J. Fluid Mech.*, **193**:445–473.

BOHN, D. & DEUKER, E. (1993). "An acoustical model to predict combustion driven oscillations." *20th International Congress on Combustion Engines*. London, UK.

BOTHIEN, M. R., MOECK, J. P., & PASCHEREIT, C. O. (2007). "Time domain modelling and stability analysis of complex thermoacoustic systems." *Proceedings of the Institution of Mechanical Engineers, Part A: Journal of Power and Energy*, **221**(5):657–668.

BOTHIEN, M. R., MOECK, J. P., & PASCHEREIT, C. O. (2008). "Active control of the acoustic boundary conditions of combustion test rigs." *J. Sound Vib.*, **318**(4–5):678–701.

BOTHIEN, M. R., MOECK, J. P., & PASCHEREIT, C. O. (2010). "Comparison of linear stability analysis with experiments by actively tuning the acoustic boundary conditions of a premixed combustor." *J. Eng. Gas Turbines Power*, **32**(12):121502 (10 pages).

CAMPOS-DELGADO, D. U., SCHUERMANS, B. B. H., ZHOU, K., PASCHEREIT, C. O., GALLESTEY, E., & PONCET, A. (2003). "Thermoacoustic instabilities: Modeling and control." *IEEE Trans. Control Syst. Technol.*, **11**(4):429–447.

CANDEL, S. (2002). "Combustion dynamics and control: Progress and challenges." *Proc. Combust. Inst.*, **29**(1):1–28.

CANDEL, S. M. (1992). "Combustion instabilities coupled by pressure waves and their active control." *Symp. (Int.) Combust.*, **24**:1277–1296.

CHU, B.-T. (1965). "On the energy transfer to small disturbances in fluid flow (Part I)." *Acta. Mech.*, **1**(3):215–234.

CHUNG, J. Y. & BLASER, D. A. (1980). "Transfer function method of measuring in-duct acoustic properties." *J. Acoust. Soc. Am.*, **68**(3):907–913.

CLAVIN, P., PELCÉ, P., & HE, L. (1990). "One-dimensional vibratory instability of planar flames propagating in tubes." *J. Fluid Mech.*, **216**:299–322.

COHEN, J. M. & BANASZUK, A. (2003). "Factors affecting the control of unstable combustors." *J. Propul. Power*, **19**(5):811–821.

CORREA, S. M. (1992). "A review of NOx formation under gas-turbine combustion conditions." *Combust. Sci. Technol.*, **87**:329–362.

CREMER, L. (1971). "The second annual Fairey lecture: The treatment of fans as black boxes." *J. Sound Vib.*, **16**(1):1–15.

CRIGHTON, D. G., DOWLING, A. P., FFOWCS WILLIAMS, J. E., HECKL, M. A., & LEPPINGTON, F. A. (1992). *Modern Methods in Analytical Acoustics: Lecture Notes*. Springer-Verlag, Berlin.

CROCCO, L. & CHENG, S.-I. (1956). *Theory of combustion instability in liquid propellant rocket motors*. AGARDograph No. 8. Butterworths Scientific Publications.

CULICK, F. E. C. (1966). "Acoustic oscillations in solid propellant rocket chambers." *Appl. Acoust.*, **12**:113–126.

CULICK, F. E. C. (2006). "Unsteady motions in combustion chambers for propulsion systems." RTO AGARDograph AG-AVT-039.

DAVIES, P. O. A. L. & HOLLAND, K. R. (2004). "The measurement and prediction of sound waves of arbitrary amplitude in practical flow ducts." *J. Sound Vib.*, **271**(3–5):849–861.

DE GOEY, L. P. H., VAN MAAREN, A., & QUAX, R. M. (1993). "Stabilization of adiabatic premixed flames on a flat flame burner." *Combust. Sci. Technol.*, **92**(1):201–207.

DÖBBELING, K., KNÖPFEL, H. P., POLIFKE, W., WINKLER, D., STEINBACH, C., & SATTELMAYER, T. (1994). "Low NOx premixed combustion of MBtu fuels using the ABB double cone burner (EV Burner)." ASME paper 94-GT-394.

DÖBBELING, K., HELLAT, J., & KOCH, H. (2007). "25 years of BBC/ABB/ALSTOM lean premix combustion technologies." *J. Eng. Gas Turbines Power*, **129**:2–12.

DOWLING, A. P. (1995). "The calculation of thermoacoustic oscillations." *J. Sound Vib.*, **180**(4):557–581.

DOWLING, A. P. (1997). "Nonlinear self-excited oscillations of a ducted flame." *J. Fluid Mech.*, **346**:271–290.

DOWLING, A. P. (1999). "A kinematic model of a ducted flame." *J. Fluid Mech.*, **394**:51–72.

DOWLING, A. P. & MORGANS, A. S. (2005). "Feedback control of combustion oscillations." *Annu. Rev. Fluid Mech.*, **37**(2):151–182.

DOWLING, A. P. & STOW, S. R. (2003). "Acoustic analysis of gas turbine combustors." *J. Propul. Power*, **19**(5):751–764.

DUCRUIX, S., DUROX, D., & CANDEL, S. (2000). "Theoretical and experimental determinations of the transfer function of a laminar premixed flame." *Proc. Combust. Inst.*, **28**(1):765–773.

DUROX, D., SCHULLER, T., NOIRAY, N., & CANDEL, S. (2009). "Experimental analyis of nonlinear flame transfer functions for different flame geometries." *Proc. Combust. Inst.*, **32**(1):1391–1398.

EROGLU, A., FLOHR, P., BRUNNER, P., & HELLAT, J. (2009). "Combustor desgin for low emissions and long lifetime requirements." ASME paper GT2009-59540.

ESCUDIER, M. (1987). "Confined vortices in flow machinery." *Annu. Rev. Fluid Mech.*, **19**:27–52.

EVESQUE, S. & POLIFKE, W. (2002). "Low-order acoustic modelling for annular combustors: Validation and inclusion of modal coupling." ASME paper GT-2002-30064.

EVESQUE, S., POLIFKE, W., & PANKIEWITZ, C. (2003). "Spinning and azimuthally standing acoustic modes in annular combustors." AIAA paper 2003-3182.

FFOWCS WILLIAMS, J. E. (1984). "Anti-sound." *Proc. R. Soc. London*, **A 395**:63–88.

FLEIFIL, M., ANNASWAMY, A. M., GHONEIM, Z. A., & GHONIEM, A. F. (1996). "Response of a laminar premixed flame to flow oscillations: A kinematic model and thermoacoustic instability results." *Combust. Flame*, **106**(4):487–510.

FUNG, Y.-T., YANG, V., & SINHA, A. (1991). "Active control of combustion instabilities with distributed actuators." *Combust. Sci. Technol.*, **78**:217–245.

GELB, A. (ed.) (1974). *Applied Optimal Estimation*. M.I.T. Press, Cambridge, MA.

GELBERT, G., MOECK, J. P., BOTHIEN, M. R., KING, R., & PASCHEREIT, C. O. (2008). "Model predictive control of thermoacoustic instabilities in a swirl-stabilized combustor." AIAA paper 2008-1055.

GHONIEM, A. F., PARK, S., WACHSMAN, A., ANNASWAMY, A., WEE, D., & ALTAY, H. M. (2005). "Mechanism of combustion dynamics in a backward-facing step stabilized premixed flame." *Proc. Combust. Inst.*, **30**(2):1783–1790.

GIAUQUE, A., NICOUD, F., & BREAR, M. (2007). "Numerical assessment of stability criteria from disturbance energies in gaseous combustion." AIAA paper 2007-3425.

GÖTTGENS, J., MAUSS, F., & PETERS, N. (1992). "Analytic approximation of burning velocities and flame thicknesses of lean hydrogen, methane, ethylene, ethane, acetylene, and propane flames." *Symp. (Int.) Combust.*, **24**:129–135.

GRAY, R. M. (2006). "Toeplitz and circulant matrices: A review." *Foundations and Trends in Communications and Information Theory*, **2**(3):155–239.

GRIFFITHS, D. J. (1995). *Introduction to Quantum Mechanics*. Prentice-Hall, Upper Saddle River, NJ.

GUSTAVSEN, B. & SEMLYEN, A. (1999). "Rational approximation of frequency domain responses by vector fitting." *IEEE Trans. Power Delivery*, **14**(3):1052–1061.

GÜTHE, F. & SCHUERMANS, B. (2007). "Phase-locking in post-processing for pulsating flames." *Meas. Sci. Technol.*, **18**:3036–3042.

GÜTHE, F., LACHNER, R., SCHUERMANS, B., BIAGIOLI, F., GENG, W., INAUEN, A., SCHENKER, S., BOMBACH, R., & HUBSCHMIDT, W. (2006). "Flame imaging on the ALSTOM EV-burner: thermo acoustic pulsations and CFD-validation." AIAA paper 2006-437.

GUYOT, D., BOTHIEN, M. R., MOECK, J. P., & PASCHEREIT, C. O. (2007). "Active control of combustion instability using fuel flow modulation." *Proc. Appl. Math. Mech.*, **7**:4090015–16.

GUYOT, D., PASCHEREIT, C. O., & RAGHU, S. (2009). "Active combustion control using a fluidic oscillator for asymmetric fuel flow modulation." *Int. J. Flow Control*, **1**(2):155–166.

HABER, L. C., VANDSBURGER, U., SAUNDERS, W. R., & KHANNA, V. K. (2000). "An examination of the relationship between chemiluminescent light emission and heat release rate under non-adiabatic conditions." ASME paper 2000-GT-0121.

HAMERMESH, M. (1989). *Group Theory and its Application to Physical Problems*. Dover Pubs., New York.

HATHOUT, J. P., FLEIFL, M., ANNASWAMY, A. M., & GHONIEM, A. F. (2002). "Combustion instability active control using periodic fuel injection." *J. Propul. Power*, **18**(2):390–399.

HECKL, M. A. (1988). "Active control of the noise from a Rijke tube." *J. Sound Vib.*, **124**(1):117–133.

HECKL, M. A. (1990). "Non-linear acoustic effects in the Rijke tube." *Acustica*, **72**:63–71.

HERMANN, J. & HOFFMANN, S. (2005). "Implementation of active control in a full-scale gas-turbine combustor." In: T. Lieuwen & V. Yang (eds.), *Combustion Instabilities in Gas Turbine Engines*, vol. 210 of *Progress in Astronautics and Aeronautics*, pp. 611–634. AIAA Inc.

HIBSHMAN, J. R., COHEN, J. M., BANASZUK, A., ANDERSON, T. J., & ALHOLM, H. A. (1999). "Active control of pressure oscillations in a liquid-fueled sector combustor." ASME paper 99-GT-215.

HIGGINS, B., MCQUAY, M. Q., LACAS, F., ROLON, J. C., DARABIHA, N., & CANDEL, S. (2001). "Systematic measurements of OH chemiluminescence for fuel-lean, high-pressure, premixed, laminar flames." *Fuel*, **80**:67–74.

HIRSCH, C., FANACA, D., REDDY, P., POLIFKE, W., & SATTELMAYER, T. (2005). "Influence of the swirler design on the flame transfer function of premixed flames." ASME paper GT2005-68195.

HUANG, X. (2001). *Development of Reduced-Order Flame Models for Prediction of Combustion Instability*. Ph.D. thesis, Virginia Tech, Blacksburg, VI.

HUANG, Y. & YANG, V. (2009). "Dynamics and stability of lean-premixed swirl-stabilized combustion." *Prog. Energy Combust. Sci.*, **35**(4):293–364.

HUBBARD, S. & DOWLING, A. P. (2001). "Acoustic resonances of an industrial gas turbine system." *J. Eng. Gas Turbines Power*, **123**:766–773.

HUBER, A. & POLIFKE, W. (2009). "Dynamics of practical premixed flames, Part I: model structure and identification." *Int. J. Spray Combust. Dyn.*, **1**(2):199–228.

HUBER, A., ROMANN, P., & POLIFKE, W. (2008). "Filter-based time-domain impedance boundary conditions for CFD applications." ASME paper GT2008-51195.

ILLINGWORTH, S. J. & MORGANS, A. S. (2008). "Adaptive control of combustion instabilities in annular combustors." ASME paper GT2008-50436.

INTERNATIONAL ENERGY AGENCY (2009). "Key world energy statistics 2009." http://www.iea.org/publications/free_new_Desc.asp?PUBS_ID=1199.

ISELLA, G., SEYWERT, C., CULICK, F. E. C., & ZUKOSKI, E. E. (1997). "A further note on active control of combustion instabilities based on hysteresis." *Combust. Sci. Technol.*, **126**:381–388.

JOHNSON, C. E. (2006). *Adaptive Control of Combustion Instabilities Using Real-Time Modes Observation*. Ph.D. thesis, Georgia Institute of Technology.

JOHNSON, C. E., NEUMEIER, Y., LUBARSKY, E., LEE, J. Y., NEUMAIER, M., & ZINN, B. T. (2000). "Suppression of combustion instabilities in a liquid fuel combustor using a fast adaptive control algorithm." AIAA paper 2000-0476.

JONES, C. M., LEE, J. G., & SANTAVICCA, D. A. (1999). "Closed-loop active control of combustion instabilities using subharmonic secondary fuel injection." *J. Propul. Power*, **15**(4):584–590.

KAESS, R., POLIFKE, W., POINSOT, T., NOIRAY, N., DUROX, D., SCHULLER, T., & CANDEL, S. (2008). "CFD-based mapping of the thermo-acoustic stability of a laminar premix burner." In: *Proceedings of the Summer Program 2008*, pp. 289–302. Center for Turbulence Research, Stanford University.

VAN KAMPEN, J. F., KOK, J. B. W., & VAN DER MEER, T. H. (2007). "Efficient retrieval of the thermo-acoustic flame transfer function from a linearized CFD simulation of a turbulent flame." *Int. J. Numer. Methods Fluids*, **54**(9):1131–1149.

KIM, K., KASNAKOĞLU, C., SERRANI, A., & SAMIMY, M. (2009). "Extremum seeking control of subsonic cavity flow." *AIAA J.*, **47**(1):195–205.

KING, R., BECKER, R., FEUERBACH, G., HENNING, L., PETZ, R., NITSCHE, W., LEMKE, O., & NEISE, W. (2006). "Adaptive flow control using slope seeking." In: *Proceedings of the 14th IEEE Mediterranean Conference on Control Automation*. Ancona, Italy.

KLEIN, R. (1995). "Semi-implicit extension of a Godunov-type scheme based on low Mach number asymptotics I: One-dimensional flow." *J. Comput. Phys.*, **121**:213–237.

KNOOP, P., CULICK, F. E. C., & ZUKOSKI, E. E. (1997). "Extension of the stability of motions in a combustion chamber by nonlinear active control based on hysteresis." *Combust. Sci. Technol.*, **123**(1):363–376.

KOKANOVIĆ, S., GUIDATI, G., TORCHALLA, S., & SCHUERMANS, B. (2006). "Active combustion control system for reduction of NOx and pulsation levels in gas turbines." ASME paper GT2006-90895.

KOMAREK, T. & POLIFKE, W. (2010). "Impact of swirl fluctuations on the flame response of a perfectly premixed swirl burner." *J. Eng. Gas Turbines Power*, **132**:061503 (7 pages).

KOPITZ, J. (2007). *Kombinierte Anwendung von Strömungssimulation, Netzwerkmodellierung und Regelungstechnik zur Vorhersage thermoakustischer Instabilitäten*. Ph.D. thesis, Technische Universität München.

KOPITZ, J. & POLIFKE, W. (2008). "CFD-based application of the Nyquist criterion to thermo-acoustic instabilities." *J. Comput. Phys.*, **227**:6754–6778.

KOPITZ, J., HUBER, A., SATTELMAYER, T., & POLIFKE, W. (2005). "Thermoacoustic stability analysis of an annular combustion chamber with acoustic low order modeling and validation against experiment." ASME paper GT2005-68797.

KREBS, W., WALZ, G., & HOFFMANN, S. (1999). "Thermoacoustic analysis of annular combustor." AIAA paper 99-1971.

KREBS, W., WALZ, G., FLOHR, P., & HOFFMANN, S. (2001). "Modal analyis of annular combustor: Effect of burner impedance." ASME paper 2001-GT-0042.

KREBS, W., FLOHR, P., PRADE, B., & HOFFMANN, S. (2002). "Thermoacoustic stability chart for high-intensity gas turbine combustion systems." *Combust. Sci. Technol.*, **174**(7):99–128.

KREBS, W., BETHKE, S., LEPERS, J., FLOHR, P., PRADE, B., JOHNSON, C., & SATTINGER, S. (2005). "Thermoacoustic design tools and passive control: Siemens Power Generation approaches." In: T. Lieuwen & V. Yang (eds.), *Combustion Instabilities in Gas Turbine Engines*, vol. 210 of *Progress in Astronautics and Aeronautics*, pp. 89–112. AIAA Inc.

KRIESELS, P. C., PETERS, M. C. A. M., HIRSCHBERG, A., WIJNANDS, A. P. J., IAFRATI, A., RICCARDI, G., PIVA, R., & BRUGGEMAN, J. C. (1995). "High amplitude vortex-induced pulsations in a gas transport system." *J. Sound Vib.*, **184**(2):343 – 368.

KRONIG, R. D. & PENNEY, W. G. (1931). "Quantum mechanics of electrons in crystal lattices." *Proc. R. Soc. London*, **130**:499–513.

KRSTIĆ, M. & WANG, H.-H. (2000). "Stability of extremum seeking feedback for general nonlinear dynamic systems." *Automatica*, **36**:595–601.

KRÜGER, U., HÜREN, J., HOFFMANN, S., KREBS, W., FLOHR, P., & BOHN, D. (2001). "Prediction and measurement of thermoacoustic improvements in gas turbines with annular combustion systems." *J. Eng. Gas Turbines Power*, **123**:557–566.

LACARELLE, A., MOECK, J. P., PASCHEREIT, C. O., GELBERT, G., KING, R., LUCHTENBURG, D. M., NOACK, B. R., KASTEN, J., & HEGE, H.-C. (2010). "Modeling the fuel/air mixing to control the pressure pulsations and NOx emissions in a lean premixed combustor." In: R. King (ed.), *Active Flow Control II, Notes on Numerical Fluid Mechanics and Multidisciplinary Design*, vol. 108, pp. 307–321. Springer-Verlag Berlin.

LANG, W., POINSOT, T., & CANDEL, S. (1987). "Active control of combustion instability." *Combust. Flame*, **70**(3):281–289.

LANGHORNE, P. J. (1988). "Reaheat buzz: an acoustically coupled combustion instability. Part 1. Experiment." *J. Fluid Mech.*, **193**:417–443.

LAUER, M. & SATTELMAYER, T. (2010). "On the adequacy of chemiluminescence as a measure for heat release in turbulent flames with mixture gradients." *J. Eng. Gas Turbines Power*, **132**:061502 (8 pages).

LEIBOVICH, S. (1978). "The structure of vortex breakdown." *Annu. Rev. Fluid Mech.*, **10**:221–246.

LEPERS, J., KREBS, W., PRADE, B., FLOHR, P., POLLAROLO, G., & FERRANTE, A. (2005). "Investigation of thermoacoustic stability limits of an annular gas turbine combustor test-rig with and without Helmholtz resonators." ASME paper GT2005-68246.

LEVINE, H. & SCHWINGER, J. (1948). "On the radiation of sound from an unflanged circular pipe." *Phys. Rev.*, **73**(4):383–406.

LIEUWEN, T. (2003). "Modeling premixed combustion–acoustic wave interactions: A review." *J. Propul. Power*, **19**(5):765–781.

LIEUWEN, T., TORRES, H., JOHNSON, C., & ZINN, B. T. (2001). "A mechanism of combustion instability in lean premixed gas turbine combustors." *J. Eng. Gas Turbines Power*, **123**(1):182–189.

LIEUWEN, T. C. (2002). "Experimental investigation of limit-cycle oscillations in an unstable gas turbine combustor." *J. Propul. Power*, **18**(1):61–67.

LIEUWEN, T. C. & YANG, V. (eds.) (2005). *Combustion Instabilities in Gas Turbine Engines*, vol. 210 of *Progress in Astronautics and Aeronautics*. AIAA, Inc.

LIGHTHILL, M. J. (1952). "On sound generated aerodynamically. I. General theory." *Proc. R. Soc. London*, **A 211**:564–587.

LIGHTHILL, M. J. (1954). "The response of laminar skin friction and heat transfer to fluctutations in the stream velocity." *Proc. R. Soc. London*, **A 224**:1–23.

LINDSTEDT, R. P. & VÁOS, E. M. (1999). "Modeling of premixed turbulent flames with second moment methods." *Combust. Flame*, **116**(4):461 – 485.

LIPATNIKOV, A. N. & CHOMIAK, J. (2002). "Turbulent flame speed and thickness: phenomenology, evaluation, and application in multi-dimensional simulations." *Prog. Energy Combust. Sci.*, **28**:1–74.

LJUNG, L. (1999). *System Identification: Theory for the User*. Prentice Hall, Upper Saddle River, NJ, second edn.

LOHRMANN, M. & BÜCHNER, H. (2004). "Scaling of stability limits in lean premixed combustors." ASME paper GT2004-53710.

LUCCA-NEGRO, O. & O'DOHERTY, T. (2001). "Vortex breakdown: a review." *Prog. Energy Combust. Sci.*, **27**(4):431–481.

MARTIN, C. E., BENOIT, L., SOMMERER, Y., NICOUD, F., & POINSOT, T. (2006). "Large-eddy simulation and acoustic analysis of a swirled staged turbulent combustor." *AIAA J.*, **44**(4):741–750.

MARTÍNEZ-LERA, P., KARTHIK, B., SCHRAM, C., FÖLLER, S., KAESS, R., & POLIFKE, W. (2009). "Low-order modeling of a side branch at low mach numbers." AIAA paper 2009-3263.

MARX, D., MAO, X., & JAWORSKI, A. (2006). "Acoustic coupling between the loudspeaker and the resonator in a standing-wave thermoacoustic device." *Appl. Acoust.*, **67**:402–419.

MATALON, M. (2007). "Intrinsic flame instabilities in premixed and nonpremixed combustion." *Annu. Rev. Fluid Mech.*, **39**:163–191.

MATVEEV, K. I. & CULICK, F. E. C. (2003). "A study of transition to instability in a Rijke tube with axial temperature gradient." *J. Sound Vib.*, **264**(3):689–706.

MCINTOSH, A. C. (1991). "Pressure disturbances of different length scales interacting with conventional flames." *Combust. Sci. Technol.*, **75**:287–309.

MCMANUS, K., HAN, F., DUNSTAN, W., BARBU, C., & SHAH, M. (2004). "Modeling and control of combustion dynamics in industrial gas turbines." ASME paper GT2004-53872.

MCMANUS, K. R., POINSOT, T., & CANDEL, S. (1993). "A review of active control of combustion instabilities." *Prog. Energy Combust. Sci.*, **19**(1):1–29.

MELLING, T. H. (1973). "The acoustic impedance of perforates at medium and high sound pressure levels." *J. Sound Vib.*, **29**(1):1–65.

MERK, H. J. (1957*a*). "Analysis of heat-driven oscillations of gas flows. I. General considerations." *Appl. Sci. Res.*, **6**(4):317–336.

MERK, H. J. (1957*b*). "Analysis of heat-driven oscillations of gas flows. II. On the mechanism of the Rijke-tube phenomenon." *Appl. Sci. Res.*, **6**(5–6):402–420.

MERK, H. J. (1958). "Analysis of heat-driven oscillations of gas flows. III. Characteristic equation for flame-driven oscillations of organ-pipe type." *Appl. Sci. Res.*, **7**(2–3):175–191.

MILLER, P. D. (2006). *Applied Asymptotic Analysis*, vol. 75 of *Graduate Studies in Mathematics*. American Mathematical Society, Providence, RI.

MIRTA, S. K. & KAISER, J. F. (eds.) (1993). *Handbook for Digital Signal Processing*. John Wiley & Sons, Inc., New York.

MOECK, J. P., BOTHIEN, M. R., & PASCHEREIT, C. O. (2007*a*). "An active control scheme for tuning acoustic impedances." AIAA paper 2007-3540.

MOECK, J. P., ENGEL, R., & PASCHEREIT, C. O. (2007*b*). "Passive control of combustion induced noise in an auxiliary bus heating system." In: *Proceedings of the 14th International Congress on Sound and Vibration*. Cairns, Australia.

MOECK, J. P., OEVERMANN, M., KLEIN, R., PASCHEREIT, C. O., & SCHMIDT, H. (2009). "A two-way coupling for modeling thermoacoustic instabilities in a flat flame Rijke tube." *Proc. Combust. Inst.*, **32**(1):1199–1207.

MOECK, J. P., SCHARFENBERG, C., PASCHEREIT, C. O., & KLEIN, R. (2010). "A zero-Mach solver and reduced order acoustic representations for modeling and control of combustion instabilities." In: R. King (ed.), *Active Flow Control II, Notes on Numerical Fluid Mechanics and Multidisciplinary Design*, vol. 108, pp. 291–306. Springer-Verlag Berlin.

MONGIA, H., HELD, T., HSIAO, G., & PANDALAI, R. (2003). "Challenges and progress in controlling dynamics in gas turbine combustors." *J. Propul. Power*, **19**(5):822–829.

MORGANS, A. S. & DOWLING, A. P. (2007). "Model-based control of combustion instabilities." *J. Sound Vib.*, **299**:261–282.

MORGANS, A. S. & STOW, S. R. (2007). "Model-based control of combustion instabilities in annular combustors." *Combust. Flame*, **150**(4):380–399.

MORSE, P. M. & FESHBACH, H. (1953). *Methods of Theoretical Physics, Parts I & II*. McGraw-Hill, New York.

MÜNCH, M. (2008). "MOLOCH – Ein Strömungsverfahren für inkompressible Strömungen – Technische Referenz 1.0." Tech. Rep. 109, Potsdam Institute for Climate Impact Research (PIK).

MUNJAL, M. L. (1987). *Acoustics of Ducts and Mufflers*. John Wiley & Sons, Inc., New York.

MURUGAPPAN, S., GUTMARK, E. J., & ACHARYA, S. (2000). "Application of extremum seeking controller for suppression of combustion instabilities in spray combustion." AIAA paper 2000-1025.

NAIR, S. & LIEUWEN, T. (2005). "Acoustic detection of blowout in premixed flames." *J. Propul. Power*, **21**(1):32–39.

NAJM, H. N., PAUL, P. H., MUELLER, C. J., & WYCKOFF, P. S. (1998). "On the adequacy of certain experimental observables as measurements of flame burning rate." *Combust. Flame*, **113**(3):312–332.

NAYFEH, A. H. & BALACHANDRAN, B. (1995). *Applied Nonlinear Dynamics*. John Wiley & Sons, New York.

NEUNERT, U. (2009). *Thermoakustische Untersuchung einer Reisemobilheizung*. Ph.D. thesis, Technische Universität München.

NICOUD, F. & POINSOT, T. (2005). "Thermoacoustic instabilities: Should the Rayleigh criterion be extended to include entropy changes?" *Combust. Flame*, **142**:152–159.

NICOUD, F., BENOIT, L., SENSIAU, C., & POINSOT, T. (2007). "Acoustic modes in combustors with complex impedances and multidimensional active flames." *AIAA J.*, **45**(2):426–441.

NOIRAY, N., DUROX, D., SCHULLER, T., & CANDEL, S. (2007). "Passive control of combustion instabilities involving premixed flames anchored on perforated plates." *Proc. Combust. Inst.*, **31**(1):1283–1290.

NOIRAY, N., DUROX, D., SCHULLER, T., & CANDEL, S. (2008). "A unified framework for nonlinear combustion instability analysis based on the flame describing function." *J. Fluid Mech.*, **615**:139–167.

NOIRAY, N., DUROX, D., SCHULLER, T., & CANDEL, S. (2009). "A method for estimating the noise level of unstable combustion based on the flame describing function." *Int. J. Aeroacoust.*, **8**(1&2):157–176.

NOIRAY, N., BOTHIEN, M., & SCHUERMANS, B. (2010). "Analytical and numerical analysis of staging concepts in annular gas turbines." In: *Proceedings of the Int'l Summer School and Workshop on Non-Normal and Nonlinear Effects in Aero- and Thermoacoustics*. Technische Universität München.

OEVERMANN, M., SCHMIDT, H., & KERSTEIN, A. R. (2008). "Investigation of autoignition under thermal stratification using linear eddy modeling." *Combust. Flame*, **155**(3):370 – 379.

PALIES, P., DUROX, D., SCHULLER, T., MORENTON, P., & CANDEL, S. (2009). "Dynamics of premixed confined swirling flames." *C. R. Mec.*, **337**:395–405.

PALIES, P., DUROX, D., SCHULLER, T., & CANDEL, S. (2010). "The combined dynamics of swirler and turbulent premixed swirling flames." *Combust. Flame*, **157**(9):1698–1717.

PANKIEWITZ, C. & SATTELMAYER, T. (2003). "Time domain simulation of combustion instabilities in annular combustors." *J. Eng. Gas Turbines Power*, **125**:677–685.

PASCHEREIT, C. O. & GUTMARK, E. (2002). "Proportional control of combustion instabilities in a simulated gas turbine combustor." *J. Propul. Power*, **18**(6):1298–1304.

PASCHEREIT, C. O. & GUTMARK, E. (2008). "Combustion instability and emission control by pulsating fuel injection." *J. Eng. Gas Turbines Power*, **130**:011012 (8 pages).

PASCHEREIT, C. O., GUTMARK, E., & WEISENSTEIN, W. (1998). "Structure and control of thermoacoustic instabilities in a gas-turbine combustor." *Combust. Sci. Technol.*, **138**:213–232.

PASCHEREIT, C. O., GUTMARK, E., & WEISENSTEIN, W. (1999*a*). "Coherent structures in swirling flow and their role in acoustic combustion control." *Phys. Fluids*, **11**:2667–2678.

PASCHEREIT, C. O., GUTMARK, E., & WEISENSTEIN, W. (1999*b*). "Control of thermoacoustic instabilities in a premixed combustor by fuel modulation." AIAA paper 99-0711.

PASCHEREIT, C. O., GUTMARK, E., & WEISENSTEIN, W. (2000). "Excitation of thermoacoustic instabilities by interaction of acoustics and unstable swirling flow." *AIAA J.*, **38**(6):1025–1034.

PASCHEREIT, C. O., FLOHR, P., & SCHUERMANS, B. (2001). "Prediction of combustion oscillations in gas turbine combustors." AIAA paper 2001-0484.

PASCHEREIT, C. O., SCHUERMANS, B., POLIFKE, W., & MATTSON, O. (2002). "Measurement of transfer matrices and source terms of premixed flames." *J. Eng. Gas Turbines Power*, **124**(2):239–247.

PASCHEREIT, C. O., SCHUERMANS, B., BELLUCCI, V., & FLOHR, P. (2005). "Implementation of instability prediction in design: ALSTOM approaches." In: T. Lieuwen & V. Yang (eds.), *Combustion Instabilities in Gas Turbine Engines*, vol. 210 of *Progress in Astronautics and Aeronautics*, pp. 445–480. AIAA Inc.

PELCÉ, P. & ROCHWERGER, D. (1992). "Vibratory instability of cellular flames propagating in tubes." *J. Fluid Mech.*, **239**:293–307.

PERACCHIO, A. A. & PROSCIA, W. M. (1999). "Nonlinear heat-release/acoustic model for thermoacoustic instability in lean premixed combustors." *J. Eng. Gas Turbines Power*, **121**:415–421.

PERRIN, R. (1977). "A group theoretical approach to warble in ornamented bells." *J. Sound Vib.*, **52**(3):307–313.

PERRIN, R. & CHARNLEY, T. (1973). "Group theory and the bell." *J. Sound Vib.*, **31**(4):411–418.

PETERS, N. (1992). "Fifteen lectures on laminar and turbulent combustion." ERCOFTAC Summer School 1992, RWTH Aachen.

POINSOT, T., LE CHATELIER, C., CANDEL, S. M., & ESPOSITO, E. (1986). "Experimental determination of the reflection coefficient of a premixed flame in a duct." *J. Sound Vib.*, **107**(2):265–278.

POINSOT, T., BOURIENNE, F., CANDEL, S., ESPOSITO, E., & LANG, W. (1989). "Suppression of combustion instabilities by active control." *J. Propul. Power*, **5**(1):14–20.

POINSOT, T., YIP, B., VEYNANTE, D., TROUVÉ, A., SAMANIEGO, J. M., & CANDEL, S. (1992). "Active control: an investigation method for combustion instability." *J. Phys. III France*, **2**:1331–1357.

POLIFKE, W. & GENTEMANN, A. (2003). "Order and realizability of impulse response filters for accurate identification of acoustic multi-ports from transient CFD." In: *Proceedings of the 10th International Congress on Sound and Vibration*. Stockholm, Sweden.

POLIFKE, W., KOPITZ, J., & SERBANOVIC, A. (2001*a*). "Impact of the fuel time lag distribution in elliptical premix nozzles on combustion stability." AIAA paper 2001-2104.

POLIFKE, W., PONCET, A., PASCHEREIT, C. O., & DÖBBELING, K. (2001*b*). "Reconstruction of acoustic transfer matrices by instationary computational fluid dynamics." *J. Sound Vib.*, **245**(3):483–510.

POLIFKE, W., FISCHER, A., & SATTELMAYER, T. (2003). "Instability of a premix burner with nonmonotonic pressure drop characteristic." *J. Eng. Gas Turbines Power*, **125**:20–27.

PUTNAM, A. A. (1971). *Combustion-driven oscillations in industry*. American Elsevier Publishing Company, New York.

RAUN, R. L., BECKSTEAD, M. W., FINLINSON, J. C., & BROOKS, K. P. (1993). "A review of Rijke tubes, Rijke burners and related devices." *Prog. Energy Combust. Sci.*, **19**(4):313–364.

RAYLEIGH, J. W. S. (1878). "The explanation of certain acoustical phenomena." *Nature*, **18**:319–321.

RICHARDS, G. A., THORNTON, J. D., ROBEY, E. H., & ARELLANO, L. (2007). "Open-loop active control of combustion dynamics on a gas turbine engine." *J. Eng. Gas Turbines Power*, **129**(1):38–48.

RIENSTRA, S. W. (2006). "Impedance models in time domain including the extended Helmholtz resonator model." AIAA paper 2006-2686.

RIENSTRA, S. W. & HIRSCHBERG, A. (2006). "An introduction to acoustics." Tech. rep., TU Eindhoven. IWDE 92-06.

RILEY, A. J., PARK, S., DOWLING, A. P., EVESQUE, S., & ANNASWAMY, A. M. (2004). "Advanced closed-loop control of an atmospheric gaseous lean-premixed combustor." *J. Eng. Gas Turbines Power*, **126**:708–716.

ROOK, R. (2001). *Acoustics in Burner-Stabilised Flames*. Ph.D. thesis, TU Eindhoven.

ROOK, R., DE GOEY, L. P. H., SOMERS, L. M. T., SCHREEL, K. R. A. M., & PARCHEN, R. (2002). "Response of burner stabilized flat flames to acoustic perturbations." *Combust. Theor. Model.*, **6**(2):223–242.

ROWLEY, C. W. (2002). *Modeling, Simulation, and Control of Cavity Flow Oscillations*. Ph.D. thesis, California Institute of Technology.

ROWLEY, C. W. & WILLIAMS, D. R. (2006). "Dynamics and control of high-Reynolds-number flow over open cavities." *Annu. Rev. Fluid Mech.*, **38**:251–276.

ROWLEY, C. W., WILLIAMS, D. R., COLONIUS, T., MURRAY, R. M., & MACMYNOSKI, D. G. (2006). "Linear models for control of cavity flow oscillations." *J. Fluid Mech.*, **547**:317–330.

RUPP, J., CARROTTE, J., & SPENCER, A. (2010). "Interaction between the acoustic pressure fluctuations and the unsteady flow field through circular holes." *J. Eng. Gas Turbines Power*, **132**(6):061501 (9 pages).

SATTELMAYER, T. (2003). "Influence of the combustor aerodynamics on combustion instabilities from equivalence ratio fluctuations." *J. Eng. Gas Turbines Power*, **125**:11–19.

SATTELMAYER, T. & POLIFKE, W. (2003). "Assessment of methods for the computation of the linear stability of combustors." *Combust. Sci. Technol.*, **175**:453–476.

SATTELMAYER, T., FELCHLIN, M. P., HAUMANN, J., HELLAT, J., & STYNER, D. (1992). "Second-generation low-emission combustors for ABB gas turbines: Burner development and tests at atmospheric pressure." *J. Eng. Gas Turbines Power*, **114**:118–125.

SCHADOW, K. C. & GUTMARK, E. (1992). "Combustion instability related to vortex shedding in dump combustors and their passive control." *Prog. Energy Combust. Sci.*, **18**(2):117–132.

SCHIMEK, S., MOECK, J. P., & PASCHEREIT, C. O. (2010). "An experimental investigation of the nonlinear flame response of an atmospheric swirl-stabilized premixed flame." ASME paper GT2010-22827.

SCHMID, P. J. (2007). "Nonmodal stability theory." *Annu. Rev. Fluid Mech.*, **39**:129–162.

SCHMID, P. J. & HENNINGSON, D. S. (2001). *Stability and transition in shear flows*. Springer, New York.

SCHMIDT, H. & JIMÉNEZ, C. (2010). "Numerical study of the direct pressure effect of acoustic waves in planar premixed flames." *Combust. Flame*, **157**(8):1610–1619.

SCHMITT, P., POINSOT, T., SCHUERMANS, B., & GEIGLE, K. P. (2007). "Large-eddy simulation and experimental study of heat transfer, nitric oxide emissions and combustion instability in a swirled turbulent high-pressure burner." *J. Fluid Mech.*, **570**:17–46.

SCHNEIDER, G., ARIYUR, K. B., & KRSTIĆ, M. (2000). "Tuning of a combustion controller by extremum seeking: A simulation study." In: *Proceedings of the 39th IEEE Conference on Decision and Control*, vol. 5, pp. 5219–5223.

SCHREEL, K. R. A. M., ROOK, R., & DE GOEY, L. P. H. (2002). "The acoustic response of burner-stabilized flat flames." *Proc. Combust. Inst.*, **29**(1):115–122.

SCHUERMANS, B. (2003). *Modeling and Control of Thermoacoustic Instabilities*. Ph.D. thesis, EPF Lausanne, Switzerland.

SCHUERMANS, B., BELLUCCI, V., & PASCHEREIT, C. O. (2003). "Thermoacoustic modeling and control of multi burner combustion systems." ASME paper 2003-GT-38688.

SCHUERMANS, B., BELLUCCI, V., FLOHR, P., & PASCHEREIT, C. O. (2004*a*). "Thermoacoustic flame transfer function of a gas turbine burner in premix and pre-premix combustion." AIAA paper 2004-0456.

SCHUERMANS, B., BELLUCCI, V., GUETHE, F., MEILI, F., FLOHR, P., & PASCHEREIT, C. O. (2004*b*). "A detailed analysis of thermoacoustic interaction mechanisms in a turbulent premixed flame." ASME paper GT2004-53831.

SCHUERMANS, B., LUEBCKE, H., BAJUSZ, D., & FLOHR, P. (2005*a*). "Thermoacoustic analysis of gas turbine combustion systems using unsteady CFD." ASME paper GT2005-68393.

SCHUERMANS, B., LUEBCKE, H., & FLOHR, P. (2005*b*). "Analysis of combustion instabilities using unsteady CFD with frequency dependent impedances." In: *Proceedings of the 12th International Congress on Sound and Vibration*. Lisbon, Portugal.

SCHUERMANS, B., PASCHEREIT, C. O., & MONKEWITZ, P. (2006). "Non-linear combustion instabilities in annular gas-turbine combustors." AIAA paper 2006-0549.

SCHUERMANS, B., GUETHE, F., PENNELL, D., GUYOT, D., & PASCHEREIT, C. O. (2009). "Thermoacoustic modeling of a gas turbine using transfer functions measured at full engine pressure." ASME paper GT2009-59605.

SCHULLER, T., DUCRUIX, S., DUROX, D., & CANDEL, S. (2002). "Modeling tools for the prediction of premixed flame transfer functions." *Proc. Combust. Inst.*, **29**(1):107–113.

SCHULLER, T., DUROX, D., & CANDEL, S. (2003). "A unified model for the prediction of laminar flame transfer functions: comparisons between conical and V-flame dynamics." *Combust. Flame*, **134**(1-2):21–34.

SEARBY, G. & ROCHWERGER, D. (1991). "A parametric acoustic instability in premixed flames." *J. Fluid Mech.*, **231**:529–543.

SENSIAU, C., NICOUD, F., & POINSOT, T. (2008). "Computation of azimuthal combustion instabilities in an helicopter combustion chamber." AIAA paper 2008-2947.

SENSIAU, C., NICOUD, F., & POINSOT, T. (2009). "A tool to study azimuthal standing and spinning modes in annular comustors." *Int. J. Aeroacoust.*, **8**(1–2):57–68.

SEUME, J. R., VORTMEYER, N., KRAUSE, W., HERMANN, J., HANTSCHK, C.-C., ZANGL, P., GLEIS, S., VORTMEYER, D., & ORTHMANN, A. (1998). "Application of active combustion instability control to a heavy duty gas turbine." *J. Eng. Gas Turbines Power*, **120**:721–726.

SEYBERT, A. F. & ROSS, D. F. (1977). "Experimental determination of acoustic properties using a two-microphone random-excitation technique." *J. Acoust. Soc. Am.*, **61**(5):1362–1370.

SKULINA, D. J. (2005). *A Study of Non-linear Acoustic Flows at the Open End of a Tube using Particle Image Velocimetry*. Ph.D. thesis, University of Edinburgh.

SMITH, K. O. & BLUST, J. (2005). "Combustion instabilities in industrial gas turbines: Solar Turbines' experience." In: T. Lieuwen & V. Yang (eds.), *Combustion Instabilities in Gas Turbine Engines*, vol. 210 of *Progress in Astronautics and Aeronautics*, pp. 29–41. AIAA Inc.

STAFFELBACH, G., GICQUEL, L. Y. M., & POINSOT, T. (2009). "Large eddy simlation of self-excited azimuthal modes in annular combustors." *Proc. Combust. Inst.*, **32**(2):2909–2916.

STOW, S. & DOWLING, A. P. (2004). "Low-order modelling of thermoacoustic limit cycles." ASME paper GT2004-54245.

STOW, S. R. & DOWLING, A. P. (2003). "Modelling of circumferential modal coupling due to Helmholtz resonators." ASME paper GT2003-38168.

STOW, S. R. & DOWLING, A. P. (2009). "A time-domain network model for nonlinear thermoacoustic oscillations." *J. Eng. Gas Turbines Power*, **131**:031502 (9 pages).

STOW, S. R., DOWLING, A. P., & HYNES, T. P. (2002). "Reflection of circumferential modes in a choked nozzle." *J. Fluid Mech.*, **467**:215–239.

SUBRAMANIAN, P., MARIAPPAN, S., SUJITH, R. I., & WAHI, P. (2010). "Application of numerical continuation to bifurcation analysis of Rijke tube." In: *Proceedings of the Int'l Summer School and Workshop on Non-Normal and Nonlinear Effects in Aero- and Thermoacoustics*. Technische Universität München.

SYRED, N. (2006). "A review of oscillation mechanisms and the role of the precessing vortex core (PVC) in swirl combustion systems." *Prog. Energy Combust. Sci.*, **32**(2):93–161.

THUMULURU, S. K. & LIEUWEN, T. (2009). "Characterization of acoustically forced swirl flame dynamics." *Proc. Combust. Inst.*, **32**(2):2893–2900.

TIRIBUZI, S. (2006). "Very rough grid approach for CFD modelling of thermoacoustic oscillations inside an annular premixed combustor." ASME paper GT2006-90055.

TIRIBUZI, S. (2007). "Numerical assessment of SCAP: A passive system of preventing thermoacoustic oscillations in gas turbine annular combustors." ASME paper GT2007-28063.

TRAN, N., DUCRUIX, S., & SCHULLER, T. (2009). "Damping combustion instabilities with perforates at the premixer inlet of a swirl burner." *Proc. Combust. Inst.*, **32**(2):2917–2924.

TREFETHEN, L. N. & BETCKE, T. (2006). "Computed eigenmodes of planar regions." In: *Recent advances in differential equations and mathematical physics*, vol. 412 of *Contemp. Math.*, pp. 297–314. Amer. Math. Soc., Providence, RI.

TYAGI, M., CHAKRAVARTHY, S. R., & SUJITH, R. I. (2007). "Unsteady combustion response of a ducted non-premixed flame and acoustic coupling." *Combust. Theor. Model.*, **11**(2):205–226.

U. S. ENERGY INFORMATION ADMINISTRATION (2010). "International energy outlook 2010." http://www.eia.doe.gov/oiaf/ieo/highlights.html.

WANG, H.-H. & KRSTIĆ, M. (2000). "Extremum seeking for limit cycle minimization." *IEEE Trans. Autom. Control*, **45**(12):2432–2437.

WANG, H.-H., YEUNG, S., & KRSTIĆ, M. (2000). "Experimental application of extremum seeking on an axial-flow compressor." *IEEE Trans. Control Syst. Technol.*, **8**(2):300–309.

WANGHER, A., SEARBY, G., & QUINARD, J. (2008). "Experimental investigation of the unsteady response of premixed flame fronts to acoustic pressure waves." *Combust. Flame*, **154**(1–2):310–318.

WICKER, J. M., GREENE, W. D., KIM, S.-I., & YANG, V. (1996). "Triggering of longitudinal combustion instabilities in rocket motors: Nonlinear combustion response." *J. Propul. Power*, **12**(6):1148–1158.

WIDENHORN, A., NOLL, B., & AIGNER, M. (2008). "Impedance boundary conditions for the numerical simulation of gas turbine combustion systems." ASME paper GT2008-50445.

WU, X., WANG, M., MOIN, P., & PETERS, N. (2003). "Combustion instability due to the nonlinear interaction between sound and flame." *J. Fluid Mech.*, **497**:23–53.

YU, K. H., WILSON, K. J., & SCHADOW, K. C. (1998). "Liquid-fueled active instability suppression." *Symp. (Int.) Combust.*, **27**:2039–2046.

ZHOU, K., DOYLE, J. C., & GLOVER, K. (1996). *Robust and Optimal Control*. Prentice Hall, Upper Saddle River, NJ.

ZHU, M., DOWLING, A. P., & BRAY, K. N. C. (2005). "Transfer function calculations for aeroengine combustion oscillations." *J. Eng. Gas Turbines Power*, **127**(1):18–26.

ZINN, B. T. (1970*a*). "A theoretical study of non-linear damping by Helmholtz resonators." *J. Sound Vib.*, **13**(3):347–356.

ZINN, B. T. (1970*b*). "A theoretical study of nonlinear combustion instability in liquid-propellant rocket engines." *AIAA J.*, **6**(10):1966–1972.

ZINN, B. T. & LIEUWEN, T. C. (2005). "Combustion instabilities: Basic concepts." In: T. C. Lieuwen & V. Yang (eds.), *Combustion Instabilities in Gas Turbine Engines*, vol. 210 of *Progress in Astronautics and Aeronautics*, pp. 3–24. AIAA Inc.